Online ISSN : 2395-602X
Print ISSN : 2395-6011
www.ijsrst.com

International e-Conference on Recent Trends in Nano-Materials and Its Applications 2021(RTNA-2021)

Organised by

Department of Physics in Collaboration with
Internal Quality Assurance Cell (IQAC)
Sangola Taluka Shetkari Shikshan Prasarak
Mandal Sangola's Vidnyan Mahavidyalaya, Sangola
Tal-Sangola, Dist-Solapur, MH-413307, India

VOLUME 9, ISSUE 2, MARCH-APRIL-2021

INTERNATIONAL JOURNAL OF SCIENTIFIC RESEARCH IN SCIENCE AND TECHNOLOGY

Email : editor@ijsrst.com Website : http://ijsrst.com

International e-Conference on Recent Trends in Nano-Materials and Its Applications-2021 (RTNA-2021)

9th-10th April, 2021

In Association with
International Journal of Scientific Research in Science and Technology
Print ISSN: 2395-6011 Online ISSN : 2395-602X
Volume 9, Issue 2, March-April-2021
International Peer Reviewed, Open Access Journal

Organised by

Department of Physics in Collaboration with Internal Quality Assurance Cell (IQAC)
Sangola Taluka Shetkari Shikshan Prasarak Mandal Sangola's
Vidnyan Mahavidyalaya, Sangola
Tal-Sangola, Dist-Solapur, MH-413307, India
Affiliated to Punyashlok Ahilyadevi Holkar Solapur University, Solapur, Maharashtra, India

Published By
Technoscience Academy
(The International Open Access Publisher)

website: www.technoscienceacademy.com

Resource Persons

Prof. P. S. Patil
Pro Vice-Chancellor, ShivajiUniversity, Kolhapur

Dr. MassimilinoGalluzzi
Materials Interfaces Center, Shenzhen Institute of Advanced Technology, Chinese Academy of Sciences, China

Dr. Ing. FlorianJ. Stadler
College of Materials Science and Engineering, Shenzhen University, China

Organizing Committee

Dr. S. B. Jundale
Principal

Mr. B. B. Navale
Head of Dept.

Dr. S. S. Dhasade
IQAC Coordinator

Dr. J. V. Thombare
Convener

Mr. A. M. Kambale
Organizing Secretary

CONTENTS

International e-Conference on Recent Trends in Nano-Materials and Its Applications-2021
In Association with International Journal of Scientific Research in Science and Technology
Volume 9 | Issue 2 | Print ISSN: 2395-6011 | Online ISSN: 2395-602X (www.ijsrst.com)

Synthesis of ZnO Nanostructure by Calotropis Procera Leaf Extract: Green Approach and its Antibiofilm Activity

Abhinay Mandawade, Laxmi Sonawane, Ganesh Kande, Sana Khan, Lalita Jondhale, Pratibha Loke*
Department of Physics and Electronics, Karmveer Shantarambapu Kondaji Wavare Arts, Science and Commerce College Cidco, Nashik 422008, Maharashtra, India

ABSTRACT

Zinc oxide (ZnO) is group II-VI binary compound with direct and wide band gap inorganic compound semiconductor material whose absorption in the near UV spectral region with band gap of (3.37 eV at 300 K), large free-exciton binding energy (~60 meV). Calotropis procera plant effectively used as antifungal agent as well as it contains various bioactive compound such as phenolic, terpenoids, polysaccharides, flavonoids and other proteins. The synthesized sample has been characterized by X-ray diffraction (XRD) reveals that hexagonal crystal structure and no any other peaks were observed in the pattern which is an indication of formation of pure phase of ZnO. UV-Vis-Diffused reflectance Spectroscopy (UV-DRS) shows absorption edge at 368 nm with corresponding energy band gap is 3.36 eV, which confirms the formation of ZnO. Field emission scanning electron microscope (FE-SEM) shows a spherical shape of morphology and X-ray dispersive X-ray analysis (EDAX) gave information about the presence of Zn and O elements in the samples. Synthesized sample explored of candila albicans biofilm it shows about 30% inhibition of biofilms.

Keywords : ZnO, Green Synthesis, Calotropis Procera, Biofilm, Candila Albicans.

I. INTRODUCTION

ZnO nanostructures have gain the great attention for its potential applications in various fields like varistors, gas sensors, field emitters and solar cells [1]. Green synthesis method make uses of practically pollutant free chemicals to synthesis nanomaterials and hold the use of compassionate solvents such as water, natural extracts [2]. In the biological or green synthesis methods which includes the uses of plant extract, fungi, microbes, and extracts of fruit and vegetables are precious for the synthesis of metal and metal oxide nanoparticles (NPs) [3]. In worldwide research many reports are available for green synthesis of ZnO NPs mediated by plant extract such as Azadirachta indica [3], Artocarpus gomezianus [4], Orange fruit peel extract [5], Moringa oleifera leaf [6], Maple leaf [7], Plectranthus amboinicus [8], Phyllanthusniruri [9], Brown marine alga Sargassum muticum [10]. The green synthesized ZnO NPs are explored for different applications such as photocatalytic activity [2], antibacterial activity [4], toxicity [11], therapeutic efficiency [12], pharmacological activity[13] and insecticidal activity [14].

Green synthesis or biological method there are some advantages such as low-cost precursors, less time, high impurity product; handling process is costly equipments over chemical methods [2]. Generally, the nanoparticle synthesis involve use of chemicals and

toxic reducing agents that are toxic and lead to non-eco-friendly by-products. Increasing interest in minimization or elimination of such hazardous chemicals as well as awareness towards green chemistry and other biological processes have led researchers to formulate an environmentally benign approach for the synthesis of nanoparticles [20].

In recent years, with the ever-increasing application of antibiotics, glucocorticoids, immune suppressants, and interventional and surgical procedures uses various catheters. Candida species are one of the most common opportunistic pathogens that causes fungal infection in humans. Candida albicans (C. albicans) can forms a biofilms on surfaces such as urinary catheters, blood vessels, catheter, orthopedic implants and joint prostheses. Biofilms formed on different surfaces by C. albicans are inhibited by nanoparticles such as Se [19] MgO [16], $ZnFe_2O_4$@Ag [17], Ag [15] and Gold [18].

II. MATERIALS AND METHODS:

Calotopis procera leaves were collected from Nashik (India). Zinc Acetate was purchased from sigma laboratory Pvt. Ltd. Nashik (India). All the chemicals were of analytical grade and uses as it is without further purification. All the solution was prepared in distilled water. All glassware used for the preparation of ZnO NPs were properly washed with distilled water and dried in hot oven.

2.1. Synthesis of ZnO NPs –

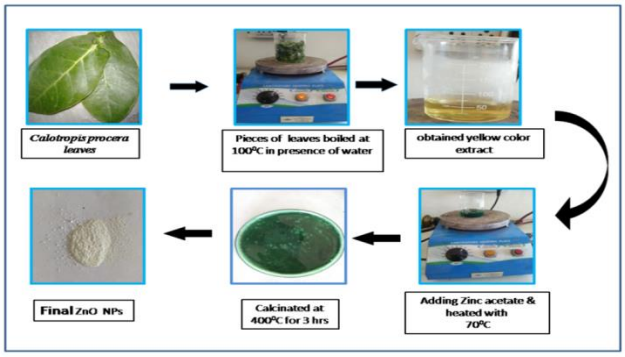

Schematic of Synthesis of ZnO NPs

Initially fresh 2 gm leaves of Calotropis Procera were washed then chopped with small pieces. The chopped leaves boiled at 100^0 C for 10 min subsequently the obtained extract filtered with whatmann filter paper no1. The filtrated solution was centrifuged at 1500 rpm for 5 min to remove heavy biomaterials. For fabrication of the ZnO NPs, 50 mL of extract added in 50 mL of distilled water and heated 70^0C for 10 min. Zinc acetate (6gm) added into hot extract with then further constant magnetic stirring for 1 hr. The obtained solution was evaporated till dryness. Finally it was kept in the muffle furnace at 400 ^{0}C for 3 hours, further white colour ZnO NPs are obtained.

2.2. Antibiofilm Assay –

Typically the procedure adapted from [25] the 100µL of 10^7 cells/mL of Candida albicans grown overnight in yeast peptone dextrose broth in presence of water were added into 96 well polystyrene plate and incubated for 3 hours for adherence of cells. The un-adhered cells were gently washed with phosphate buffer saline (PBS). The different concentrations (0–100 µg/L) of ZnO NPs were added to each well, and incubated for 24 hours at 37 ^{0}C. After 24 hours of incubations, the medium supernatant was removed, and the biofilm formed wash gently with PBS and further incubated with 100 µL of 5 mg/mL MTT (3-(4,5 Dimethylthiazol-2-yl)- 2,5-Diphenyltetrazolium Bromide) solution. After 6 hours of incubations.

2.3. Material Characterizations -

The X-ray diffraction pattern of as synthesized sample was recorded in the 2θ range of 10^o–80^0 at a scanning rate of 2^0 /min using Miniflex 600 making Rigaku Japan with a monochromator and Ni-filtered Cu Kα = 1.5406 Å). The ultraviolet-visible (UV-Vis) spectroscopy study was carried out by Shimadzu in the range of 200 to 800 nm. The Fourier transform infrared spectrum was recorded by Shimadzu. The Scanning electron microscope images were captured

by FESEM : FEI Nova Nano SEM 450 with an ultra high resolution low voltage imaging and unique low vacuum capabilities. In EDAX analysis was recorded by EDS : Bruker XFlash 6I30.

III. RESULTS AND DISCUSSION

3.1 XRD analysis –

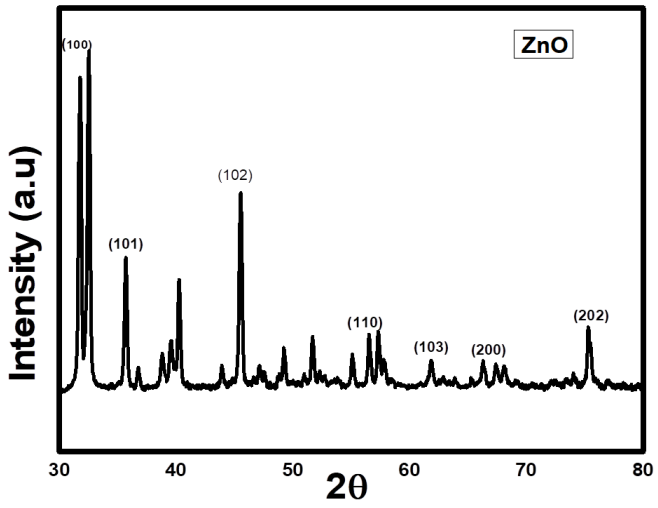

Figure 1 - XRD pattern of synthesized ZnO NPs

The crystal structure information obtained from X-ray diffraction (XRD) technique. Figure 1 shows the XRD pattern which was taken along with 2θ vs intensity. The diffraction peaks appeared at 2θ = 31.79^0, 35.80^0, 45.52^0, 56.43^0, 61.74^0, 66.35^0 and 75.27^0 with corresponding crystal planes are (100), (101), (102), (110), (103), (200) and (202) respectively they are well matches with hexagonal wurtzite structure of ZnO, the PCPDF no. is 00-036-1451 [2].

3.2 UV-Visible Diffuse Reflectance Spectroscopy (UV Vis –DRS):

The UV-Vis-DRS spectrum of ZnO NPs as shown in figure 2. The spectrum indicates the edge located at around 368 nm which corresponds to ground excitonic peak of ZnO NPs. The energy band gap calculated and which was found to be 3.36 eV. The purity of the ZnO NPs are confirmed by the non existence of other absorption peaks in the spectrum.

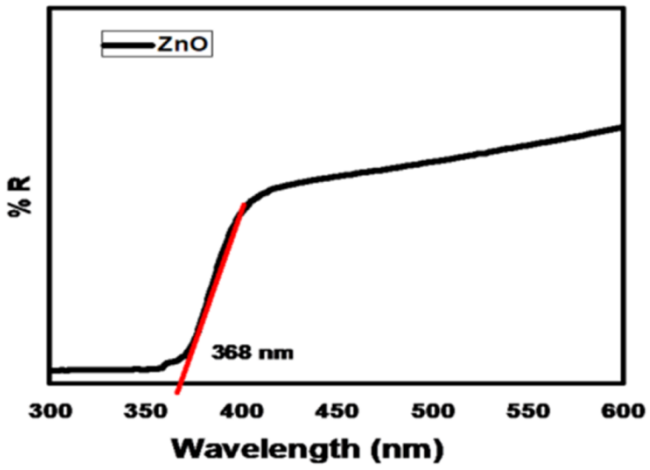

Figure 2 - DRS spectrum of synthesizes ZnO NPs

The minimum wavelength required to promote electron depends upon the band gap energy (E_g) of the ZnO and the E_g is calculated by using Eq.

$$E_g = \frac{hc}{\lambda} - - - - - (1)$$

Where h is planks constant (6.626×10^{-34} J-s) c is speed of light (3×10^8 ms^{-1}) and absorption edge in nm. By putting the values 'h' and 'c' in Eq (1) we obtain the following equation,

$$E_g = \frac{1240}{\lambda} - - - - (2)$$

λ = 368 nm from ZnO UV-Vis-DRS spectrum The band gap energy of ZnO was found to be 3.3eV [2]

3.3 FT-IR analysis –

The ZnO NPs was synthesized by green synthesis method as shown in the above figure. The range of FT-IR scanned from 4000 to 400 cm^{-1} in the % of Transmission mode. In Figure 3(a) The FT-IR spectrum shows the absorption peak in the region in 1630 cm^{-1} it corresponds to an aromatic ring. The weak absorption observed at 2208 due to C≡C streaching vibration. The broad band at 3300-3490cm^{-1} implies the O-H streaching .The broad FT-IR bands are 650, 1650, 2208, 3400 cm^{-1} shows presence of alkyl halide, alkene, alkyne, amine confirms to leaf extract are stabilizing ZnO NPs. In Figure 3(b) FT-IR spectrum of ZnO NPs peak appeared in lower energy region between 250 and 500 cm^{-1}.

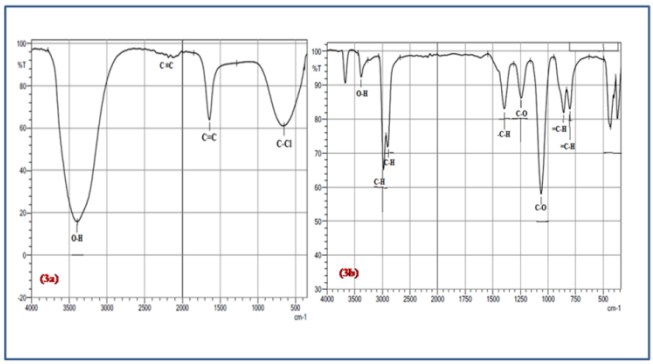

Figure 3(A) aqueous leaf extract of Calotropis Procera
Figure 3(B) Synthesized ZnO NPs

[1]. The absorption band at ~3350 cm^{-1} is observed, which is the corresponding to O-H streaching of surface adsorbed water molecule and the band ~ 3190 cm^{-1}[2].

3.4 FESEM analysis –

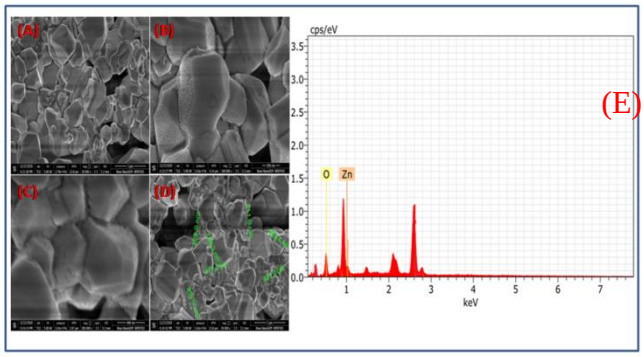

Figure (A-D) FESEM Images Figure (E) EDAX Graph

The Field Emission Scanning Electron Microscopy gives a surface morphology. As shown in Figure 4 (A-D) the hexagonal cube like structure of synthesized ZnO. The various ranges are used to analyze the morphology of ZnO such as 1µm, 500 nm, and 400 nm Energy dispersive X-ray analysis confirms the presence of Zn and O elements without any other impurities as shown in the Figure 4 (E).

Antibiofilm Activity –

Schematics of biofilm formation of candida albicans on the surface with different steps are referred from [19] with various modification as shown In Figure 5 (A) (1) candida cells as a part of a various mixed microbial community.(2) The attachment of candida to host surfaces of different medical devices via surface adhesion or coaggregation with bacteria (3) Insufficient host defense leads to abundance of Candida occurs in different morphological forms. (4) Hyphal cells in epithetiall biofilms support tissue by Candida albicans. (5) Finally tissue invension, yeast cells spread in the blood vessels and are open to the immune cells. In Fig 5(B) the synthesized ZnO NPs are used for Candida albicans biofilms inhibition. ZnO NPs shows inhibition in Figure :5(B) with 20×10^5 cells/mL were added 31.2 µg/mL to each well of the 96-well polystyrene plates, 45×10^5 cells/mL were added 62.5 µg/mL to each well of the 96-well polystyrene plates. 55×10^5 cells/mL were added 125 µg/mL to each well of the 96-well polystyrene plates. It shows maximum inhibition about 25% of biofilms [21].

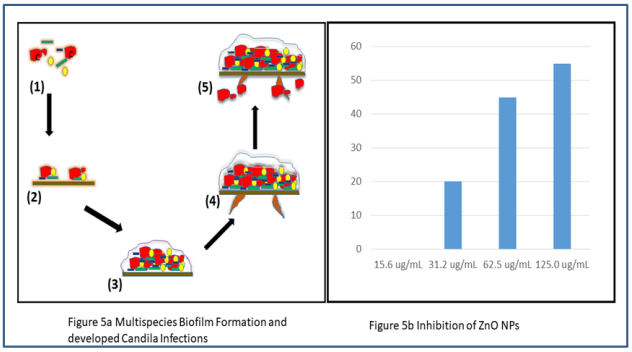

Figure 5a Multispecies Biofilm Formation and developed Candila Infections

Figure 5b Inhibition of ZnO NPs

IV. CONCLUSION

In summary, the synthesized sample has been characterized by X-ray diffraction (XRD) reveals that hexagonal crystal structure and no any other peaks were observed in the pattern which is an indication of formation of pure phase of ZnO. UV Visible spectroscopy of ZnO indicates absorption edge located at around 368nm. Field Emission Scanning Electron Microscopy (FESEM) along with Energy Dispersive X-Ray spectroscopy (EDAX) indicate the hexagonal shape of nanoparticles and presence of Zn & O element without any impurity. Field emission scanning electron microscope (FE-SEM) shows a

hexagonal shape of surface morphology and X-ray dispersive X-ray analysis (EDAX) gave information about the presence of Zn and O elements in the samples. ZnO NPs can be explored for treatment of cure various diseases such as bronchitis, dyspepsia, paralysis, swellings and intermittent fever. Nevertheless, it also reveals antifungal, antiviral, antibacterial, anticarcinogenic and anticandidal activities.

V. Acknowledgements –

Authors would like thanks to Principal Dr. J. D. Sonkhaskar, Head of Department Dr. P. G. Loke, Department of Physics and Electronics of KSKW Arts, Science and Commerce College, Uttamnagar, CIDCO, Nashik-422008 for giving instrument facilities to carry out this research work also thanks for their precious courage and valuable time.

VI. REFERENCES

[1]. Gnanasangeetha D, SaralaThambavani D. "One Pot Synthesis of Zinc Oxide Nanoparticles via Chemical and Green Method" Research Journal of Material Sciences, Vol 1(7), 1-8, (2013).

[2]. V. V. Gawade, N. L. Gavade, H. M. Shinde, S. B. Babar, et al.,"Green synthesis of ZnO nanoparticles by using Calotropis procera leaves for the photodegradation of methyl orange" J Mater Sci: Mater Electron, Vol 28, 14033–14039, (2017).

[3]. Artocarpus gomezianus, "Green synthesis, characterization and antimicrobial activities of Zinc Oxide nanoparticles from the leaf extract of Azadirachta indica (L.)" Vol 345, 329-336, (2015).

[4]. Tu Uyen Doan Thi, Trung Thoai Nguyen, Y Dang Thi, Kieu Hanh Ta Thi, et al., "Green synthesis of ZnO nanoparticles using orangefruit peel extract for antibacterial activities" Royal Society Of Chemistry Advances Vol 9, 10, 23899, (2020).

[5]. T. Lakshmikandhan, "Green synthesis and characterization of ZnO nanoparticles using calabash (crescentia cujete) extract", Malaya Journal of Matematik, Vol. S, No. 2, 4280-4288, (2020).

[6]. K. Elumalai, S. Velmurugan, S. Ravi, V. Kathiravan, et al., "Green synthesis of Zinc oxide nanoparticles using Moringa oleifera leaf extract and evaluation of its antimicrobial activity", Spectrochim. Acta Mol. Biomol. Spectrosc. 143, 158 (2015).

[7]. S. Vivekandhan, M. Schereiber, C. Mason, A.K. Mohanty,et al., "Maple leaf (Acersp) extract mediated green process for the functionalization of ZnO powders with silver nanoparticles" Colloids Surf. B 113, 169 (2014).

[8]. S. Vijayakumar, G. Vinoj, B. Malaikozhundan, S. Shanthi, et al.,"Plectranthus amboinicus leaf extract mediated synthesis of zinc oxide nanoparticles and its control of methicillin resistant Staphylococcus aureus biofilm and blood sucking mosquito larvae" Spectrochim. Acta Mol. Biomol. Spectrosc. 137, 886 (2015).

[9]. M. Anbuvannan, M. Ramesh, G. Viruthagiri, N. Shanmugam, et al., "Synthesis, characterization and photocatalytic activity of ZnO nanoparticles prepared by biological method" Acta Mol. Biomol. Spectrosc. 143, 304 (2015).

[10]. S. Azizi, M. B. Ahmad, F. Namvar, R. Mohamad, "Green biosynthesis and characterization of zinc oxide nanoparticles using brown marine macroalga Sargassum muticum aqueous extract" Mater. Lett. 116, 275 (2014).

[11]. V. N. Kalpana and V. Devi Rajeswari, "A Review on Green Synthesis, Biomedical Applications, and Toxicity Studies of ZnO NPs, Bioinorganic Chemistry and Applications" Volume 2018, 3569758, 1-12 (2018).

[12]. Khadeeja Parveen, Viktoria Banse, and Lalita Ledwani, "Green synthesis of nanoparticles:

Their advantages and disadvantages" American Institute of Physics 1724, 020048 (2016).

[13]. Ajay Kumar Meena, Mruthyumjaya Rao Meda, M M Rao "Ayurvedic uses and pharmacological activities of Calotropis procera Linn". Asian Journal of Traditional Medicines,1-10 6 2(2011).

[14]. Ramachandran Ishwaryaa, Baskaralingam Vaseeharana, Subramanian Kalyania, Balan Banumathi et al.,"Facile green synthesis of zinc oxide nanoparticles using Ulva lactuca seaweed extract and evaluation of their photocatalytic, antibiofilm and insecticidal activity" Journal of Photochemistry & Photobiology, B: Biology 178, 49–258 (2018).

[15]. Fanzhi Kong, Jiaying Wang, Rui Han, Shuaiqi Ji, et al., "Antifungal Activity of Magnesium Oxide Nanoparticles: Effect on the Growth and Key Virulence Factors of Candida Albicans,"Mycopathologia, 185(3):485-494. (2019)

[16]. Deepika Thakur, Saravanan Govindaraju, KyuSik Yun, Jin-Seo Noh, "The Synergistic E_ect of Zinc Ferrite Nanoparticles Uniformly Deposited on Silver Nanowires for the Biofilm Inhibition of Candida albicans," Nanomaterials, 9, 1431, (2019)

[17]. Shivkrupa D. Halbandge,Ashwini K. Jadhav, Priyanka M. Jangid,Amruta V. Shelar, "Molecular targets of biofabricated silver nanoparticles in Candida albicans," The Journal of Antibiotics, volume 72, 640–644, (2019)

[18]. Shakir Khan, Fahad Alam, Ameer Azam, Asad U Khan,"Gold nanoparticles enhance methylene blue–induced photodynamic therapy: a novel therapeutic approach to inhibit Candida albicans biofilm," International Journal of Nanomedicine, 3245–3257, (2012) .

[19]. Gregory Guisbiers, Humberto H. Lara, Ruben Mendoza-Cruz, Guillermo Naranjo, et al., "Inhibition of Candida albicans biofilm by pure selenium nanoparticles synthesized by pulsed laser ablation in liquids," Nanomedicine; 13(3): 1095–1103, (2017).

[20]. Shikha Dubey, Yogesh Chandra Sharma "Calotropis procera mediated one pot green synthesis of Cupric oxide nanoparticles (CuO-NPs) for adsorptive removal of Cr(VI) from aqueous solutions," Wiley Applied Organometallic Chemistry; 1 of 15, (2017).

[21]. Humberto H. Lara, Dulce G. Romero-Urbina, Christopher Pierce, Jose L. Lopez-Ribot "Effect of silver nanoparticles on Candida albicans biofilms: anultrastructural study"Journal OF Nanobiotechnology,1-12, (2015) .

International e-Conference on Recent Trends in Nano-Materials and Its Applications-2021
In Association with International Journal of Scientific Research in Science and Technology
Volume 9 | Issue 2 | Print ISSN: 2395-6011 | Online ISSN: 2395-602X (www.ijsrst.com)

Structural Properties of Mn Doped Zinc Oxide Nanopowders by Chemical Co-Precipitation

A.R. Babar[1*]

[1]Department of Physics, Shankarrao Mohite Mahavidyalaya, Akluj – 413101, India (Affiliated to Punyashlok Ahilyadevi Holkar Solapur University, Solapur) Maharashtra, India

ABSTRACT

Nanocrystalline tin oxide (SnO2) was synthesized using stannic chloride pentahydrate (SnCl4.5H2O) as a precursor in aqueous medium by chemical co-precipitation method. The influence of sintering temperature on the crystalline structure was studied. X-ray diffraction studies reveal that all powders exhibit tetragonal crystal structure. It is observed that crystallinity and crystallite size increases with sintering temperature. Various absorption bonds viz. Sn-O, O-Sn-O and O-H are observed from the FTIR study. The compositional analysis of SnO2 nanoparticles is studied using X-ray photoelectron spectroscopy (XPS). The symmetric spin orbit splitting of Sn 3d5/2 ground state and Sn 3d3/2 excited states is observed in XPS with sintering temperature while O 1s is recognized with O-2 state.

Keywords: Chemical co-precipitation, Tin oxide, XRD, crystallite size, FTIR, XPS.

I. INTRODUCTION

In this fast-paced world, nanotechnology has created a new industrial revolution globally and becomes a major topic in recent material research fields. Many countries have invested in nanotechnology due to its small in size with huge immense potential. It is well known and widely applied in many areas such as in nano finishing of functional textiles, biomedical, electronics, batteries, solar cells, chemical coatings and so forth. Nanotechnology creates structures that have excellent properties by controlling atoms and molecules, functional materials, devices and systems on the nanometer scale by involving precise placement of individual atoms of the size around 1 nm to 100 nm.

Mn- doped Zinc oxide nanoparticles has increased a lot of attention from the scientists and researchers to undergo this research interest due to its various applications in photocatalyst, chemical sensors, solar cells and optoelectronic devices. However, the doping efficiency was influenced by the strong tendency of the Mn dopant ions to segregate at the nanoparticles surfaces. The Mn doping transition metals in ZnO give the best results because Mn has the highest magnetic moment and has the most stable polarization regions. Some Zn can be substituted with Mn ions which can provide ferromagnetic properties [1-2]. Many studies have been conducted to produce ZnO including in the form of powder and film [3]. In general, Mn substitution into ZnO can be formed in the system of Zn1-xMnxO. Regarding the synthesis of nanoparticles, many experts due to its excellent

properties compared to other methods have chosen precipitation. Mn is preferred for the doping of ZnO due to the d electron of Mn can easily overlap with the ZnO's valence band as compared with other transition element. There are various studies shown that Mn doped semiconductors have influenced the physical, chemical and structural properties of undoped ZnO nanoparticles. For example, the optical properties of undoped ZnO nanoparticles especially on the tuning of the band gap can be greatly improved at the nanoscale by Mn doping. Practically, among other traditional synthetic methods, coprecipitation provides a simple route with low cost for large-scale production. Furthermore, such method also does not need expensive raw materials. Actually, the term "doped" is used to modify the optical or magnetic properties of the host by adding impurities ions against the host lattice (Figure 1).

In this paper, we report the effect of Mn dopant concentrations (1 to 5 at %) on the structural properties of Mn-doped ZnO nanoparticles.

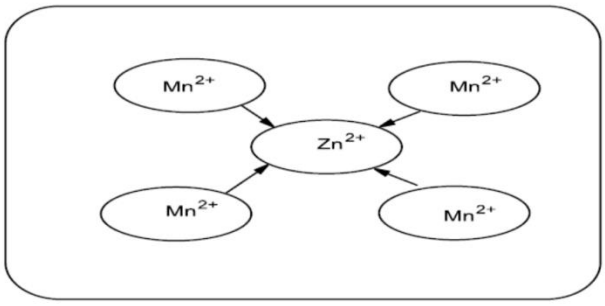

Figure 1: Mn-doped ZnO nanoparticles

II. EXPERIMENTAL:

Zinc oxide nanoparticles are synthesized using the wet chemical co-precipitation method. The precursors used in the synthesis ZnO are Zinc acetate dihydrate having purity 99%. The preparation conditions were carefully controlled. Double distilled water was used for solution preparation. Solution pH, considered using the relation between pH and concentrations of both the solutions was adjusted to neutral by adding aqueous ammonia to preserve the hydroxide phases of Zn and Mn. The homogeneous solution was prepared by thoroughly mixing both the solutions. White gelatinous precipitate formed, was filtered using Whatmann filter paper No. 17. The precipitate was washed thoroughly until traces of Cl were removed. It was further dried at ambient temperature and sintered at different temperatures within 400°C for 6h in air atmosphere.

III. RESULTS AND DISCUSSION:

Figure 2 & 3 shows the XRD patterns of undoped and 10 at % Mn-doped ZnO nanocrystalline powder. The sharp intense peaks of ZnO confirms the good crystalline nature of ZnO and the diffraction peaks can be indexed to a hexagonal wurtzite structured ZnO [4]. Furthermore, compared with the undoped ZnO, introduced manganese ions shift the diffraction peaks to higher angles by 0.17◦. Such changes are indeed to be expected if Mn ions replace Zn ions in the lattice, as the Mn ions have smaller ionic radii (0.66Å) than Zn ions (0.74Å). The shift degrees indicate decrease of lattice parameters. From Fig. 2 one can observe that the intensity of (101) diffraction plane increased slightly than that of pure ZnO [5].

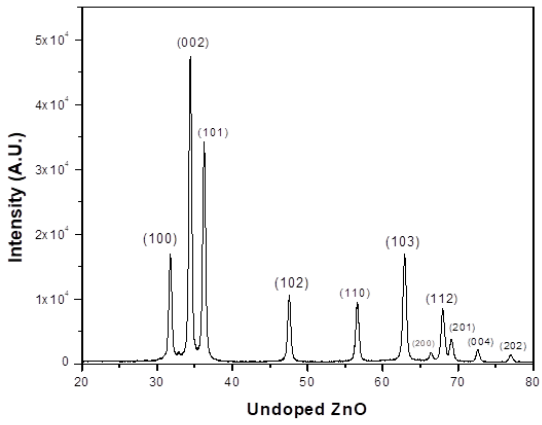

Fig. 2 XRD patterns of undoped ZnO nanocrystalline powder.

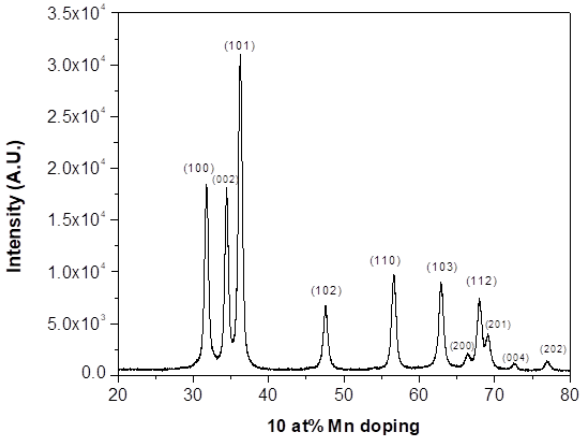

Fig. 3 XRD patterns of 10 at % Mn-doped ZnO nanocrystalline powder.

The crystallite size 'D' is calculated using Scherrer's formula,

$$D = 0.94\lambda / \beta \cos\theta$$

Where D is the crystallite size, β is the broadening of the diffraction line measured at half of its maximum intensity (rad) FWHM and λ is the x-ray wavelength (1.5405Å). It is seen that as doping increases the crystallite size increases up to 10 at% and tends to decrease afterwards as shown in Fig. 4.

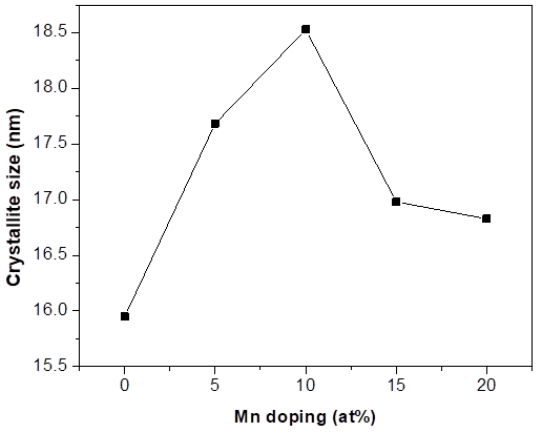

Fig. 4 Variation crystallite size with Mn doping.

Evaluation of the lattice parameters a, c as a function of Mn concentrations is shown in Fig. 5 & 6. As for Mn-doped nanocrystalline powder, the lattice parameters a & c calculated from the (101) a peak, the values of a & c are increases upto 10 at % doping and further decreases. The calculated lattice parameter are higher than the standard JCPDS parameter for bulk ZnO, a = b = 3.2498 Å and c = 5.2060 Å, respectively. Since the ionic radii of Zn^{2+} (0.74 Å) is smaller than that of Mn^{2+} (0.83 Å) and larger than that of Mn^{3+} (0.64 Å) [6].

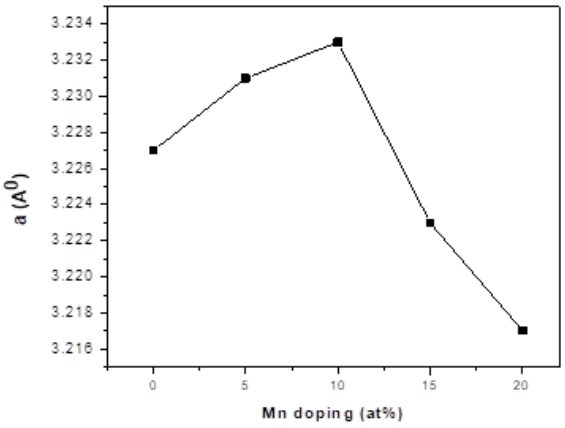

Fig. 5 Variation of lattice parameters 'a' function of Mn doping concentrations.

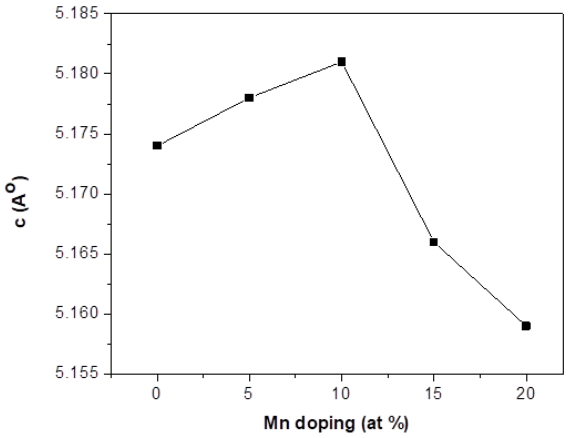

Fig. 6 lattice parameters 'c' as a function of Mn doping concentrations.

Fig. 7 shows the Williamson and Hall plot of our undoped as well as Mn-doped nanocrystalline ZnO particles. It is observed that the strain in Mn-doped samples decreases upto 10 at % Mn and further increases [7]. It is seen that more Mn content is introduced into the sample, the stronger tensile is, or more created compression stress. The change in structural properties of Mn-doped samples are due to

strain present in nanocrystals. The above study gives the idea of promising application of synthesized Mn-doped ZnO nanoparticles for optoelectronic devices.

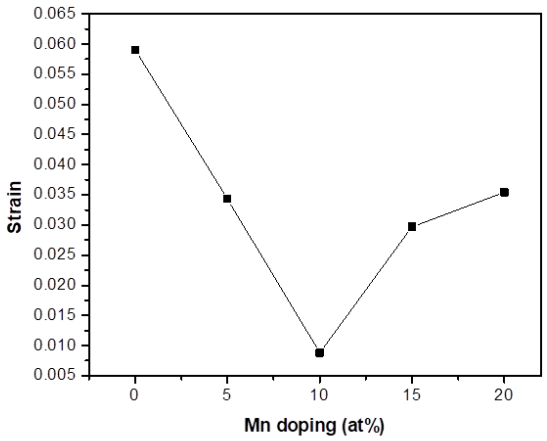

Fig. 7 Williamson and Hall plot of undoped as well as Mn-doped nanocrystalline ZnO nanoparticles.

IV. CONCLUSION

ZnO sample containing transition metal Mn synthesized by chemical co-precipitation method correspond to a hexagonal structure similar to that of undoped ZnO. The XRD measurement suggests that Mn atoms substitute Zn sites in the crystals without changing the wurtzite structure, but with the lattice parameters varying slightly with the extent of doping. XRD data showed that all the samples had a (002) preferential orientation perpendicular to the substrate. Crystallite size of the ZnO film was found to be decreased with Mn-doping. We also observed on doping the grain size reduces drastically reducing to nano-scale i.e., doping hinders the grain growth. No secondary phases were observed for the simple synthesis process adapted in the present work for the doped ZnO samples upto 20 at % of Mn doping.

V. REFERENCES

[1]. Jung S W, An S-J, Yi G-C, Jung C U, Lee S-I and Cho S 2002 Ferromagnetic properties of Zn1–xMnxO epitaxial thin films Applied Physics Letters 80 4561–3.

[2]. Sato K and Katayama-Yoshida H 2000 Material Design for Transparent Ferromagnets with ZnO Based Magnetic Semiconductors Japanese Journal of Applied Physics 39 L555–8.

[3]. Kim K J and Park Y R 2002 Spectroscopic ellipsometry study of optical transitions in Zn1–xCoxO alloys Applied Physics Letters 81 1420–24.

[4]. Jagriti Gupta, P.A. Hassana, K.C.Barick, Structural, photoluminescence, and photocatalytic properties of Mn and Eu co-doped ZnO nanoparticles Materials Today Proceedings 42 (2) 2021, 926-931.

[5]. P. Shunmug Sundaram, S. Stephen Rajkumar Inbanathan, G.Arivazhagan, Structural and optical properties of Mn doped ZnO nanoparticles prepared by co-precipitation methodPhysica B: Condensed Matter, 574 (2019) 411668.

[6]. Xu Li, Xinghu Zhu, Kangxin Jin, Dingyu yang, Study on structural and optical properties of Mn-doped ZnO thin films by sol-gel method Optical Materials 100 (2020)109657.

[7]. Raj Kamal Yadav & Pratima Chauhan, Estimation of lattice strain in Mn-doped ZnO nanoparticles and its effect on structural and optical properties, Indian Journal of Pure & Applied Physics, 57 (2019) 881-890.

International e-Conference on Recent Trends in Nano-Materials and Its Applications-2021
In Association with International Journal of Scientific Research in Science and Technology
Volume 9 | Issue 2 | Print ISSN: 2395-6011 | Online ISSN: 2395-602X (www.ijsrst.com)

Synthesis and Electrical Characterization of LSM Thin Films as Cathode for SOFC

B. S. Kamble[1*], U. M. Chougale[2], V. J. Fulari[2], R. K. Nimat[3]

[1]Department of Physics, D. B. J. College, Chiplun-415605, Maharashtra, India

[2]Department of Physics, Shivaji University, Kolhapur-416004, Maharashtra, India

[3]Department of Physics, Balasaheb Desai College, Patan-415206, Maharashtra, India

ABSTRACT

Lanthanum Strontium Manganite (LSM) thin films with 0.1, 0.2 and 0.3 mol % were synthesized by spray pyrolysis technique with optimized various spray parameters. These thin films were annealed at for 2 hours to exist in perovskite type structure. Frequency dependent dielectric properties were studied and impedance study was done at constant temperature. At low frequency dielectric constant attains high value and as frequency increases dielectric constant suddenly decreases and bears constant value. Impedance graphs with increased strontium content show decrease in the polarization resistance. The low polarization resistance makes these films as most proper cathode material for miniature SOFC to reduce operating temperature.

Keywords: LSM, Dielectric Constant, Impedance spectra, Cathode.

I. INTRODUCTION

Solid oxide fuel cell (SOFC) is one of an electrochemical device which generates efficient and pollution free clean power [1]. Magnetic-based perovskite oxides have attracted much attention for different technological applications that can be built through their special electronic and magnetic features. Strontium substituted lanthanum manganite (LSM) with general formula La1-xSrxMnO3-δ, is the most widely used cathode material for SOFC [2-4]. It has been reported that electrochemical reactions of cathode materials like LSM, with low oxygen vacancy concentration and low ionic conductivity, are limited to the three phase boundaries where gaseous oxygen in pores, electrons in catalytic materials and oxygen ions in electrolyte materials meet and react [5]. For efficient performance of SOFC, the roll of cathodic polarization became significant [6-7]. In this paper the LSM thin films were prepared by cost effective spray pyrolysis technique (SPT). Thin films of cathode materials which are small crystal particle were produced by SPT. The dielectric constant and impedance were taken by LCR meter with varying frequency.

II. EXPERIMENTAL MATERIALS

Lanthanum Nitrate hexahydrate (La (NO3).6H2O Loba Chmie), Strontium Nitrate (Sr(NO3)2 Loba Chmie) and Manganese Nitrate hexahydrate (Mn(NO3)3.6H2O-ALFA ASER)

Synthesis

LSM thin film were obtained by following procedure using spray pyrolysis technique (SPT).

Preparation of Thin films

Lanthanum Nitrate hexahydrate (La (NO3).6H2O LobaChmie), Strontium Nitrate (Sr (NO3)2 Loba chime) and Manganese Nitrate hexahydrate (Mn (NO3)3.6H2O-ALFA ASER) were dissolved in double distilled water. This precursor solution was used for SPT using glass nozzle with spray rate 3 ml/min on alumina substrates placed on hot plate having a temperature about , this leads to pyrolytic decomposition of these metallic salts and formation of Lanthanum Strontium Manganite thin film. The doping concentration can be maintained in precursor by addition of the strontium. The as prepared LSM thin films were annealed at for 2 hours.

The annealed films were used for measurement of dielectric constant and impedance spectroscopy. Actual impedance and phase angle were measured w. r. t. frequency from100 Hz to 5 MHz keeping 1mV amplitude of test signal by HIOKI LCR - Q meter simultaneously and real and imaginary impedance w.r.t. frequency was calculated

III. RESULTS AND DISCUSSION

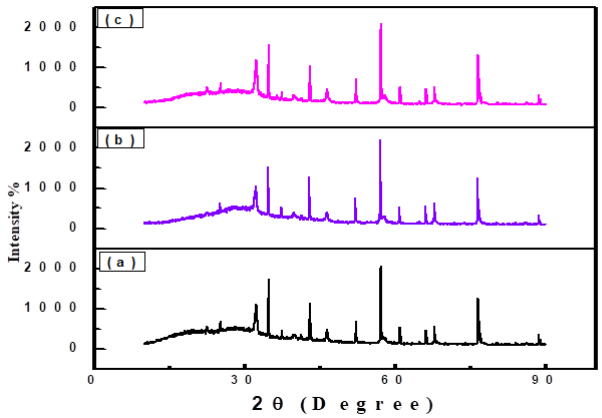

FESEM is the morphological analysis of the particle was done with the help of FESEM which is displayed in fig.1. From analysis of FESEM, it was observed that thin films had uniformly pores and well cling to the substrate. This type of porous material fulfils need of SOFC cathode for diffusion of oxygen to the interface for reduction reaction, which possess a high active surface area. As can be seen that the sample sintered at $750^{O}C$ the particles have spherical shape. It was found that perovskite phase formation took place after sintering at $750^{O}C$.

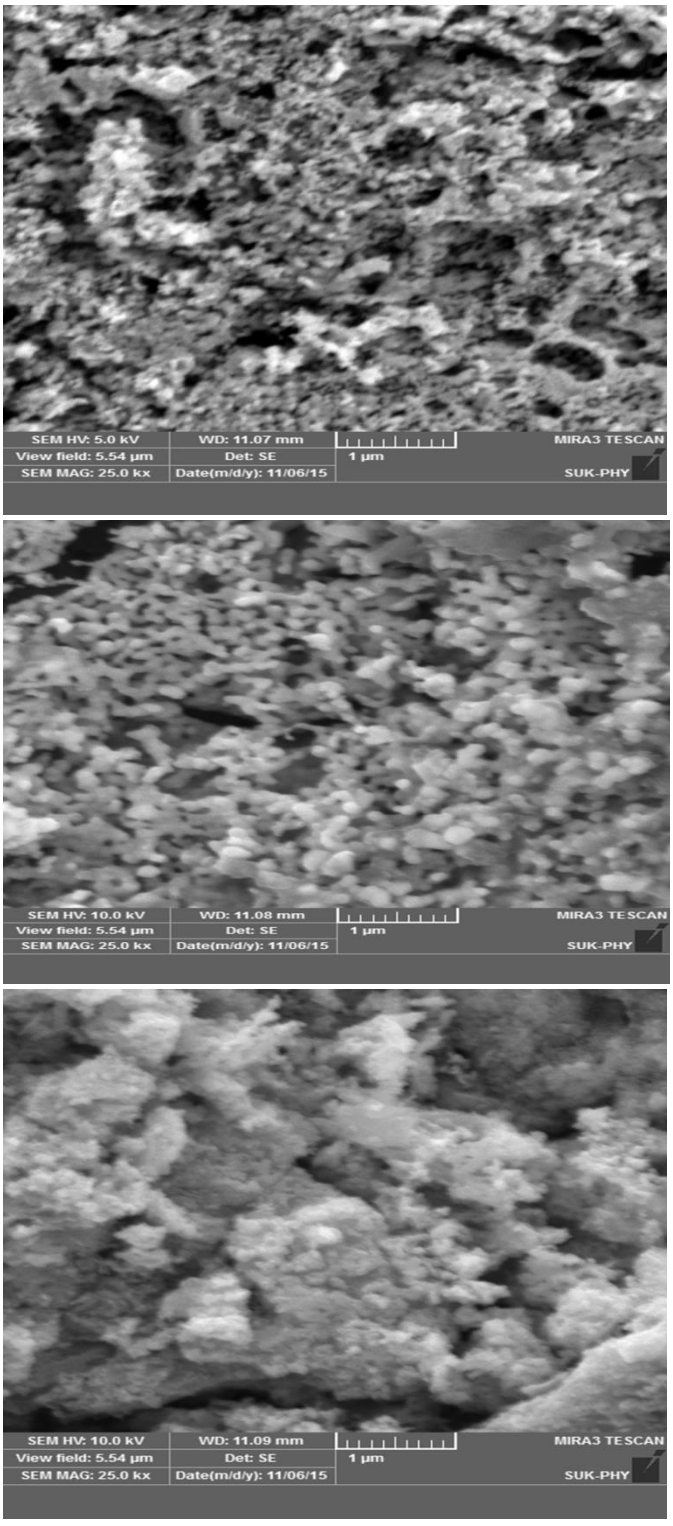

Fig.1 FESEM images of LSM thin films (a) X=0.1, (b) X = 0.2 and (c) X = 0.3

Dielectric Constant of thin films

It was observed that dielectric constant increased rapidly at very low frequency and it decreases rapidly with increasing frequency. The polarizability of molecules has greater value, higher the dielectric constant and atomic polarization remain constant at these (high) frequencies. On further increase in the frequency the magnitude of dielectric constant decreases very slowly and it is due to presence of interfacial polarization. At higher frequency dielectric constant attain constant value due to presence of space charge polarization. According to Maxwell-Wagner theory of interfacial polarization, the dielectric dispersion phenomenon was explained successfully [8], in consonance with the Koops theory [9].

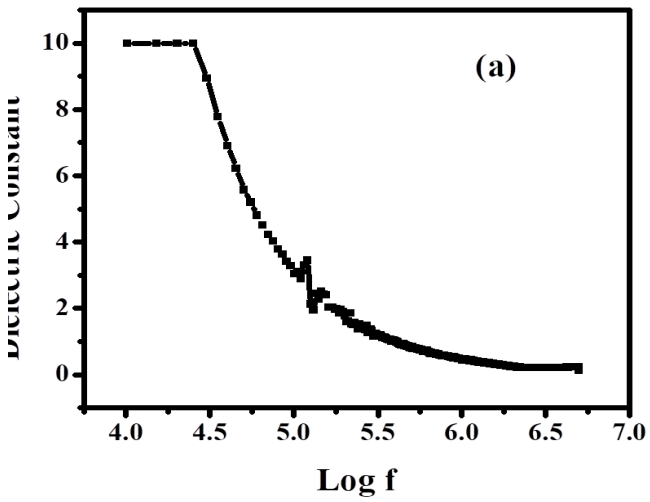

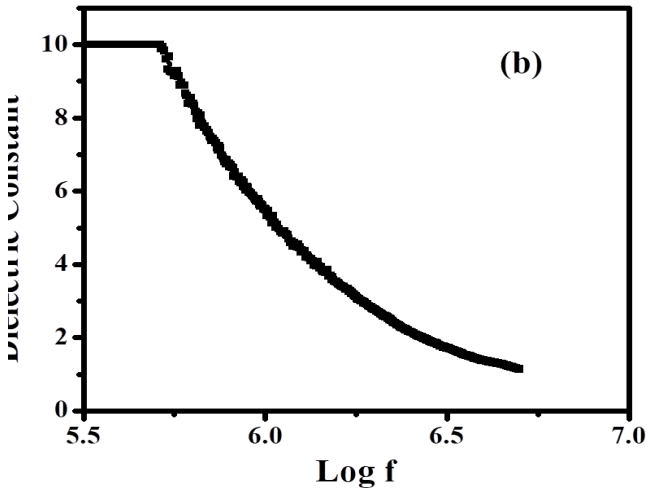

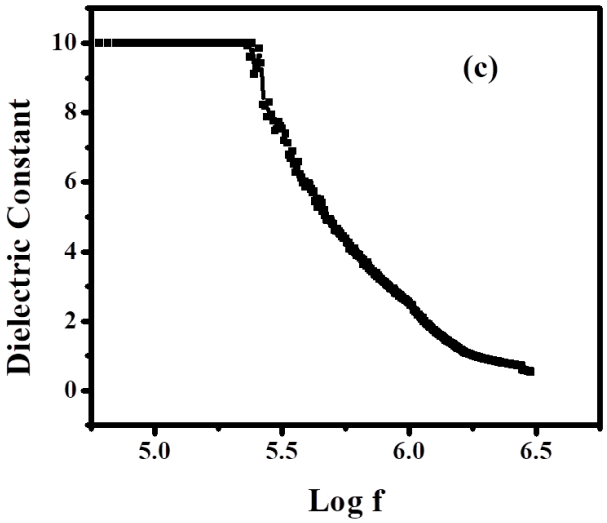

Fig.2 The Dielectric constant Vs frequency of LSM thin films (a) X=0.1, (b) X = 0.2 and (c) X = 0.3

Impedance spectroscopy of LSM thin films

To identify the contribution of grain, grain boundary and electrode, impedance spectroscopy has become significant. To determine impedance of cathode material, Nyquist diagram or Cole-Cole plot is used. To increase performance of FC at low operating temperature it is essential to decrease polarization resistance of the electrodes especially cathode material [10].

The electrical impedance spectra measured at room temperature and plotted by Nyquist plot for various strontium concentrations is depicted in fig.2. The high frequency intercepts on real axis of Nyquest plot, indicate the total specific ohmic resistance (Ro), and the distance between the lowest and highest frequency intercept corresponded to total area specific polarization resistance (Rp) from cathode. From above graph polarization resistance values were determined and are summarized in table.1. It is interpreted that by increasing strontium content polarization resistance decreases. This suggests that the electrode performance of LSM improves with increasing Sr2+ ion molar ratios [11]. At lower doping concentrations of strontium, grain boundaries primarily act as scattering site and potential barriers lead to reduced carrier mobility by increasing

impedance. At higher strontium doping concentrations, the impedance was decreased by the energy levels.

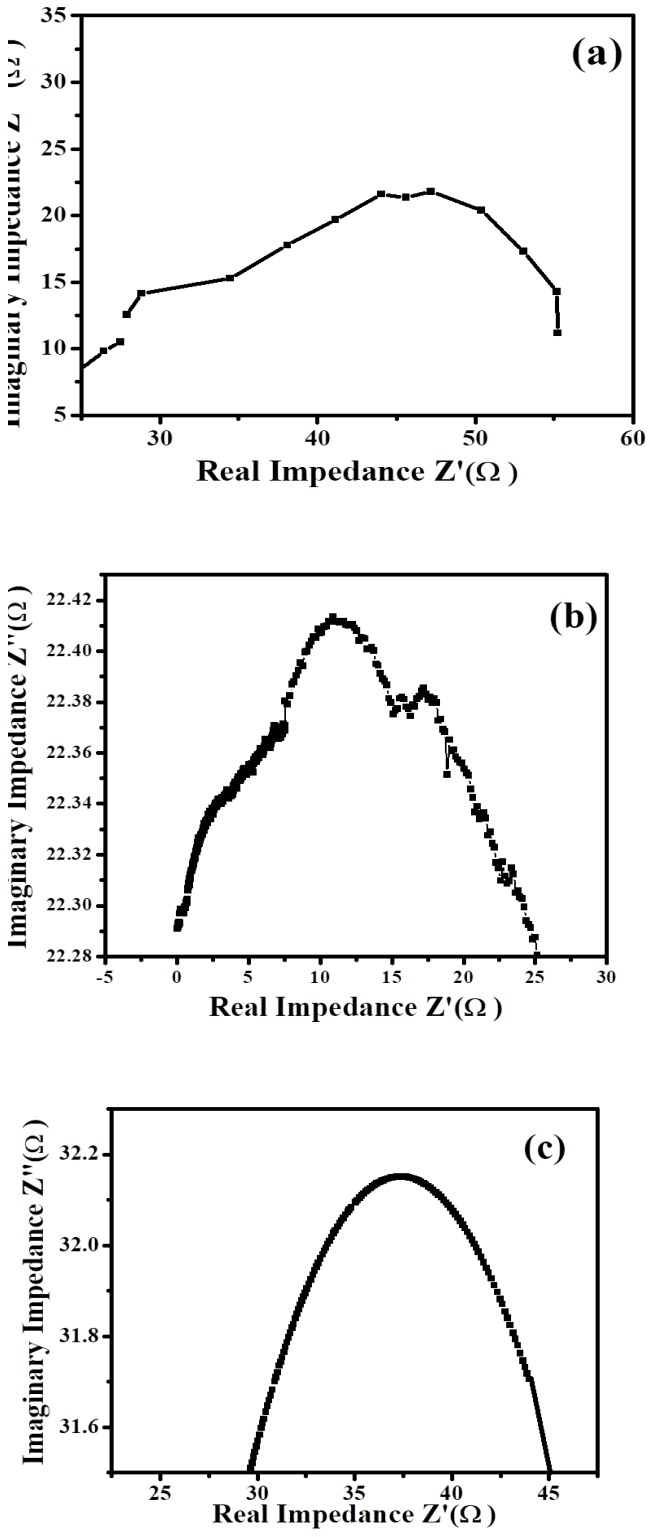

Fig. 3. Nyquist plots for LSM films (a) X =0.1, b) X = 0.2, (c) X = 0.3

Table 1 Ohmic and Polarization resistance

Strontium Concentration	Ohmic Resistance (Ro)	Polarization Resistance (Rp)
0.1	25X105 Ω cm2	30X105 Ω cm2
0.2	0 Ω cm2	25X105 Ω cm2
0.3	26X105 Ω cm2	18.5X105 Ω cm2

IV. CONCLUSION

The spray deposited LSM thin films attain higher value of dielectric constant due to accumulation of charges at low frequency. The magnitude of dielectric constant decreases when increasing frequency for all LSM samples. This suggests that LSM material exhibit semiconducting property. The low polarization resistance makes these films as most proper cathode material for miniatures SOFC to reduce operating temperature. Impedance spectra depict the role and contribution of grain, grain boundary and cathode material to overall dielectric characteristics of the electrode.

V. REFERENCES

[1]. Jiang S. P., Development of lanthanum strontium manganite perovskite cathode materials of solid oxide fuel cell: a review, J. Mater. Sci. 43 (21), (2008), 6799.

[2]. J. Chaichawong, K. Sato, H. Abe, K. Murata, T. Fukui, T. Charinpanitkul, W. Tanthapanichakoon, M. Naito, Formation of Strontium- doped Lanthanum Manganite La0.8Sr0.2MnO3 by mechanical milling without media ball, Adv. Powder Technol., 17, (2006), 613.

[3]. H. Taguchi, D. Matsuda, M. Nagao, K. tunihata, Y. Miyamoto, Synthesis of perovskite-type (La1-xSrx) MnO3(o-Less-Than-or-Equal to x-Less- than - or- Equal- to-0.3) at low

temperature, J. Am. Ceram. Soc., 72, (1992), 201.

[4]. D. P. Tarrago, C. d. F. malfalti, V. C. de Sousa, Influence of Fuel on Morphology of LSM powders obtained by solution combustion synthesis, Powder Technol. 269, (2015), 481.

[5]. A. J. Darbandi, T. Enz, H. Hahn, synthesis and characterization of Nanoparticulate films for intermediate temperature solid oxide fuel cells, Solid State Ionics, 180, (2009), 424.

[6]. E. P. Murray, T. Tsai, S. A. Bernett, Solid State Ionics, 110 (1998) 235.

[7]. T. Tsai, S. A. Bernett, Solid State Ionics J. Mater. Sci. 93 (1997) 207.

[8]. A. M. Abdeen, J. Magn. Magn. Mater. 192 (1999) 121.

[9]. C. M. Kanamadi, B. K. Chougule, J. Electroceram.15 (2005) 123.

[10]. S. Roy, S. B. Mujumdar, Synthesis and characterization of multiferroic composite thin films, Thesis (2011), IIT Kharagpur.

[11]. A. O. Turky, M. M. Rashid, A.M. Hassan, E. M. Elinaggar , M. Bechelany, Phys. Chem. Chem. Phys., 19, (2017), 6878.

International e-Conference on Recent Trends in Nano-Materials and Its Applications-2021
In Association with International Journal of Scientific Research in Science and Technology
Volume 9 | Issue 2 | Print ISSN: 2395-6011 | Online ISSN: 2395-602X (www.ijsrst.com)

Structural, Morphological and Compositional Properties of La^{3+} Substituted Li-Cd Ferrite by Co-Precipitation Method

B.B. Navale*[1] R.A. Bugad[2], J.V. Thombare[1], B.R.Karche[3]

[1]Vidnyan Mahavidyalaya Sangola Dist. -Solapur, Maharashtra 413307, India

[2]Sangola College Sangola, Dist. -Solapur, Maharashtra 413307, India

[3]Shankarrao Mohite Mahavidyalaya, Akluj, Dist.: Solapur, Maharashtra 413101, India

ABSTRACT

La^{3+} substituted Li-Cd ferrites (LLCF) with general formula $Li_{0.6}Cd_{0.4}La_{2y}Fe_{2-2y}O_4$ (where y = 0.0, 0.05) have been synthesized using co-precipitation method. The prepared sample was characterized by different physical and chemical characterization techniques for their structural and micro-structural properties. The X-ray diffraction (XRD) analysis was carried out to confirm the single-phase cubic spinel structure of La^{3+} substituted lithium cadmium ferrites. The crystallite size of LCF sample decreases from 49 nm to 45 nm for doped LLCF samples. The surface morphology of LLCF shows that the interlocked nanoparticles with average grain size varying from 200 nm to 150 nm. Also, energy dispersive analysis by X-ray (EDAX) shows the presence of all the metals in the exact composition as that of precursors used for preparation of samples.

I. INTRODUCTION

The formation of Ferrites is mixed metal oxide having iron oxide as main component [1]. As we know the ferrites have acquired a spinel structure. The general formula of a spinel can be written as AB_2O_4 [2]. Generally, in the normal spinel structure, the A cations are in the tetrahedral sites and the B cations are in the octahedral site. Otherwise, half of the B cations and all the A cations are randomly distributed in octahedral sites, resulting in the inverse spinel structure [3]. Nanoparticles of ferrites have been the subject of detailed study for their interesting optical, magnetic and electric properties which are significantly different from those of their bulk counterparts [4].

Magnetic properties of nanoparticles of LLCF find wide technological applications such as drug delivery, Spintronics, magnetic refrigeration and high density recording etc. [5-6]. Ferrites have numerous application in cores of audio frequency and high frequency transformer coils, electromagnetic wave absorption, magneto optical displays [7].

The addition of rare earth metal ions like La^{3+} introduces changes in the structure and texture. [8]. Pervoskite -type material lanthanum substituted ferrite and relative oxides are widely used in fuel cells [9]. Physical properties of nanocrystalline ferrites depend on their microstructure. The grain and grain boundary mainly determine the microstructure. Thus, the information regarding the physical parameters of these components leads to the understanding of the overall properties of the materials [10].

Till now, some researchers have been carried out about the preparation and magnetic properties of ferrite. But the effect of lanthanum doped on the structure, grain size, morphology and magnetic properties for La-Li-Cd ferrite was reported less. In this paper we have reported the structural, morphological and compositional properties of Lanthanum substituted Lithium Cadmium ferrites in detail.

II. EXPERIMENTAL

2.1. Synthesis of La^{3+} substituted Li-Cd ferrite

The $Li_{0.6}Cd_{0.4}La_{2y}Fe_{2-2y}O_4$ (where y=0.0, 0.05) were prepared by the oxalate co-precipitation method. The high purity starting materials $LiSO_4.7H_2O$, $CdSO_4.7H_2O$, $LaSO_4.7H_2O$ and $Fe_2SO_4.7H_2O$ were used for preparation of samples. All chemicals are in AR grade. These chemicals were weighted in desired stoichiometric proportion and dissolved in distilled water. The pH of the solution was maintained at 4.8 by drop wise addition of concentrated H_2SO_4. The resulting solution was heated at 80 ^{0}C for 1 h in order to complete the ionization of metal sulfates [11]. The precipitating regent was prepared in distilled water by adding required proportion of AR grade ammonium oxalate. The precipitating regent was added by drop into metal sulfate solution with constant stirring until the process of precipitation was completed. The process of precipitation can be explained by following chemical reaction.

$$LiSO_4 + 2H_2O + C_2O_4^- \rightarrow LiC_2O_4 2H_2O + SO_4^{2-} \text{ -- (1)}$$

$$CdSO_4 + 2H_2O + C_2O_4^- \rightarrow CdC_2O_4 2H_2O + SO_4^{2-} \text{ (2)}$$

$$FeSO_4 + 2H_2O + C_2O_4^- \rightarrow FeC_2O_4 2H_2O + SO_4^{2-} \text{ (3)}$$

$$LaSO_4 + 2H_2O + C_2O_4^- \rightarrow LaC_2O_4 2H_2O + SO_4^{2-} \text{ (4)}$$

The resultant precipitation was the solid solution of lithium oxalate, cadmium oxalate, lanthanum oxalate and ferrous oxalate. The precipitate along with solution was digested on sand bath for 1h in order to settle down the precipitate at the bottom of the beaker. The precipitate was filtered by Whatman filter paper no.41 using suction flask operating with the vacuum pump. The precipitate was thoroughly washed with distilled water in order to remove sulfate ions. The absence of sulfate ion in the filtrate was confirmed by barium chloride test. The co-precipitate product was dried and calcined at 450 ^{0}C for 5h in air. The calcined powders were milled in an agate mortar with AR grade acetone as a base. The powders were pre-sintered at 700 ^{0}C for 5h.The pre-sintered powders were pressed under hydraulic pressure of 5 tones /cm^3 to form pellet using polyvinyl alcohol as binder. Then pellets were finally sintered at 900 ^{0}C for 12h. The temperature was raised and cooled at the rate of 100 ^{0}C per hours. The sintering process had cause the atom to move to its lattice completely.

2.2. Characterizations

XRD patterns of all samples were recorded using a Philips X-Ray Diffractometer model PW 1710 using Cu K_α radiation (λ=1.5405 A^o) in the 2θ range of 20-80^o. Sintered pellets were polished optically and then broken into small pieces. These small pieces of pellets were gold coated using Sputter coating unit operating at a voltage of 1 kV. The micrograph of La^{3+} substituted Li-Cd ferrites were taken with the help of scanning electron microscope. EDAX carried out JSM-6380 LA with an attached kevex Delta system.

III. RESULTS AND DISCUSSIONS

3.1. XRD studies

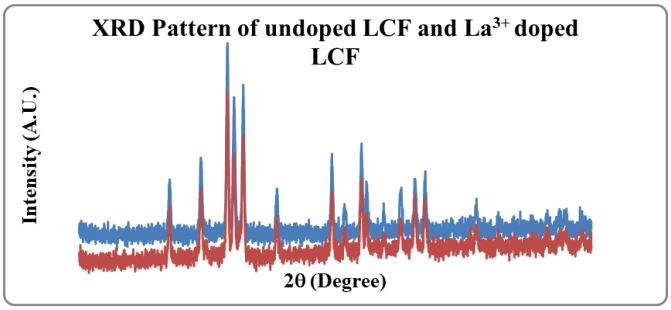

Fig.1: XRD pattern of undoped LCF and La^{3+} doped LCF.

Fig.1 shows the XRD patterns of composition $Li_{0.6}Cd_{0.4}La_{2y}Fe_{2-2y}O_4$ (where y = 0.0, 0.05, 0.1, 0.15,

0.20 and 0.25). The analysis of XRD patterns reveals that all the samples have single phase spinel cubic structure. The interplaner spacing was calculated using the relation (5);

$$d_{cal} = \frac{n\lambda}{2.\sin\theta} \quad \text{----- (5)}$$

The lattice constant was calculated using the relation (6);

$$a = d_{hkl} * \sqrt{\left(h^2 + k^2 + l^2\right)} \quad \text{---- (6)}$$

And the average crystallite size for all the LLCF samples from most intense peak (311) was determined by Debye Scherer formula (7);

$$D = \frac{0.9\lambda}{\beta\cos\theta} \quad \text{----- (7)}$$

where β is full width at half maxima, and θ is angle of diffraction. The crystallite size was found to be 49 nm to undoped sample and that of 45 nm for La^{3+} doped samples.

3.2. Surface morphological studies

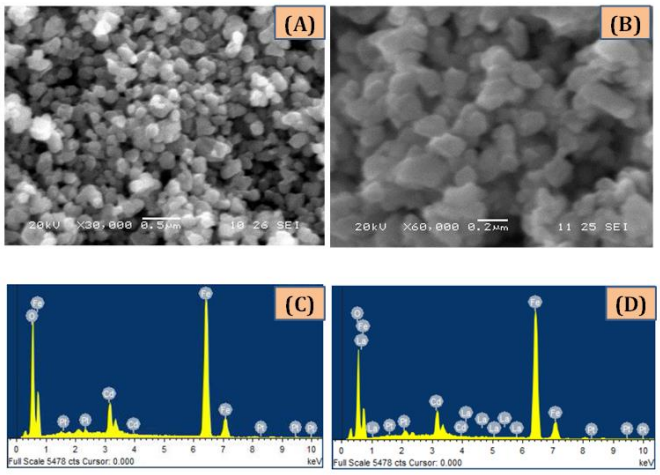

Fig.2: (A-B) SEM images of undoped LCF and La^{3+} doped LCF; (C-D) EDAX pattern of undoped LCF and La^{3+} doped LCF.

Fig.2 (A-B) shows the SEM images of composition $Li_{0.6}Cd_{0.4}La_{2y}Fe_{2-2y}O_4$ (where y = 0.0, 0.05). The measurement of grain size is counted by counting the number of grain boundaries intersected by a known measured length from the magnification [12]. It can be seen from the Fig.2 (A-B) that the average grain size is to be decreased upon Lanthanum doping. The variation in average grain size depends upon the grain growth mechanism involving diffusion coefficients, sintering temperature and concentration dissimilar ions [13].

3.3. EDAX studies

Two representatives EDAX spectra are shown in Fig. 2(C-D). Fig. 2(C) shows EDAX patterns of $Li_{0.6}Cd_{0.4}La_{2y}Fe_{2-2y}O_4$ System where y=0.00 and Fig. 2(D) shows EDAX patterns of $Li_{0.6}Cd_{0.4}La_{2y}Fe_{2-2y}O_4$ System where y=0.05. EDAX has been performed in order to study the compositional analysis of La substituted Li-Cd ferrite. EDAX analysis exhibits the elemental percentage of each element expected to be present in the La substituted Li-Cd ferrite sample. The heights of the peaks in the EDAX graphs represent the proportion of each element in the finally sintered La substituted Li-Cd ferrite. A change has been observed in the size and height of the peaks of all the La-substituted samples. With La^{3+} doping, the graph exhibits an increase in the height of the La peaks. In the present study, the Lanthanum is substituted for iron. Hence, the amount of iron decreases and this decrease in iron is observed in the peak height of Fe as shown in Fig. 2(D). The observed percentage of metals of each composition is consistent with the stoichiometry of the prepared samples.

IV. CONCLUSION

Lanthanum substituted lithium cadmium ferrite is cubic spinel ferrite. Nanocrystaline Lanthanum substituted lithium cadmium ferrite have been prepared by oxalate co-precipitation method at a pre-sintering temperature of 7000C for 5h and final sintering temperature of 9000C for 12h. The crystallite size decreases as a function La concentration. Crystallites size of all samples is found in the range of 49 nm - 45 nm. The microstructure of ferrite prepared by co-precipitation method consists of grain size in the range 200 to 150. The structure is compact with small amount of pores on the scale of crystallites.

V. REFERENCES

[1]. G. Kumar , M. Kanthwal, B.S. Chauhan & M. Singh. Indian J. Pure & Appl. Phy. 44 (2006) 930-934.

[2]. M Kaur, B.S.Randhawa, J. Singh, D. Utreja , J. Ceramics International. 39(2013) 325-328.

[3]. A. S. Vaingankar, S. A Patil, Sahashrabudhye, Trans. Indian. Inst. metals 34, 5 (1981) 387.

[4]. C. Wang, X. M. Zhang, X. F. Qian. J. Xie, W.Z.Wang and Y.T. Qian, Mater. Res. Bull., 33(1998) 1747.

[5]. P. C. Rajesh, Varma et.al, J. Alloys. Compd. 453 (2008) 29.

[6]. R.A. Bugad , T.R. Mane, C.S. Pawar B.R. Karche, Golden Research Thoughts 2 (2013)1-13.

[7]. S.N. Dolia, Solid State Phenomena, 171(2011) 79-91

[8]. Ishtiaq Ahmad, Muhammad Tahir Farid, Robina Kousar and Shahida. B. Niazi. World Appl. Sci. J. 22(6) (2013) 796-801.

[9]. N.Q. Mih, J. Am. Ceram. Soc. 76(1993) 563-588

[10]. S. Ghatak, M. Sinha, A.K. Meikap, S.K. Pradhan J. Mater. Res. Bull. 45 (2010) 954–960

[11]. A. B. Gadkari, T. J. Shinde, P. N. Vasambekar, J. Mater Sci: Mater Electron 21 (2010) 96-103.

[12]. B.R. Karche, B.V. Khasbarder, A.S. Vaingankar, Journal of Magntism and Magnetic Material, 168 (1997) 292

[13]. S.C. Watawe, U.A. Bamne and B.D. Sarwade, world scientific publishing Co. Pte. Ltd., Electromagnetic materials (pp 94-97)

International e-Conference on Recent Trends in Nano-Materials and Its Applications-2021
In Association with International Journal of Scientific Research in Science and Technology
Volume 9 | Issue 2 | Print ISSN: 2395-6011 | Online ISSN: 2395-602X (www.ijsrst.com)

Effect of Annealing On Structural, Morphological and Optical Properties of Cobalt Oxide Films

C. S. Pawar*, A. R. Babar

*Material Science Research Laboratory, Department of Physics, Shankarrao Mohite Mahavidyalaya, Akluj 413101, Maharashtra, India

ABSTRACT

Cobalt Oxide films have been successfully synthesized onto glass substrates by using novel M-CBD technique. The effect of annealing on the structural, morphological, optical properties and contact angle were studied using X-ray diffraction (XRD), scanning electron microscope (SEM), UV-Vis-NIR spectrophotometer and Digital Camera, respectively. X-ray diffraction pattern reveals annealed cobalt oxide films shows amorphous nature. The scanning electron microscopy images showed micro porous structure with very fine grains less than 50 nm in diameter. These films exhibited transmittance value of about 70 % in the visible and infra red range. The direct band gaps of cobalt oxide films was found to be in the range of 1.07–1.53 eV and 1.20 - 2.10 eV. Absorption coefficient ~ 104cm-1 were found for all the samples. Refractive indices vary from ~1.9 - 2.8 in the near infrared region. Surface wettability studied in contact with liquid interface, showed hydrophilic nature of annealed films as water contact angle was < 90o.

Keywords : Cobalt oxide, M-CBD, Thin film, X-ray diffraction, Morphology, Optical properties

I. INTRODUCTION

Most of the advances in the understanding of the properties of materials have been the outcome of a systematic observation of the materials properties, this is because of the fact that often small crystal or microstructural differences are associated with remarkable changes in physical properties. Thus, prior to the investigation of physical properties, it is very essential to pay attention to the structural, morphological and optical features and the relationship between crystal structure and various properties. In this regard, we have focused our research on cobalt oxides films and effect of annealing temperature on their properties.

Among the transition metal oxides, cobalt oxide is one of the most studied oxides because it exhibits several possible oxidation states Co^{2+}, Co^{3+}, and Co^{4+} and several types of coordinations, that is, tetrahedral, pyramidal, and octahedral. Consequently, cobalt oxides offer a wide field for the creation of many frameworks, not only stoichiometric oxides but also nonstoichiometric oxides, involving a mixed valency of cobalt and/or the presence of oxygen vacancies. It has three well-known polymorphs; the monoxide or cobaltous oxide (CoO), the cobaltic oxide (Co_2O_3) and the cobaltosic oxide or cobalt cobaltite (Co_3O_4). CoO is the final product formed when the cobalt compound or other oxides are calcinated to a sufficiently high temperature (1173 K). The pure CoO

is difficult to obtain, since it readily takes up oxygen even at room temperature to reform to a higher oxide. Cobaltic oxide (Co_2O_3) could be formed when cobalt compounds are heated at a low temperature in the presence of an excess of air. Co_2O_3 can be completely converted in to Co_3O_4 at temperature > 538 K. Co_2O_3 absorbs oxygen in sufficient quantity and transforms to a higher oxide Co_3O_4, with no change in the lattice structure [1]. Nano structured Co_3O_4, the most stable cobalt oxide with a spinel-type structure comprising both Co (II) and Co (III), is an important p-type semiconductor (direct band gaps at 1.5 and 2.0 eV respectively) [2, 3]

It is showed clear evidence for the existence of two band gap values of cobalt oxide [4]. Cobalt oxide thin films are promising candidates for various applications such as ion-storages [5], chemical sensors [6], solar thermal energy collectors [7] and electrochromic (EC) devices [8]. Black cobalt oxide is a selective coating material for high-temperature solar collectors [9]. The cobalt oxide coatings are superior to the black chrome coatings often used. Sensors electrochemical anodes [10] and newly invented application in super capacitors [11].

Various methods have been proposed to prepare Co_3O_4 films out of these M-CBD method has simple and inexpensive. The aim of the present work is to pay more attention to study influences of annealing temperature on the structural, morphological and optical behavior of cobalt oxide films prepared by M-CBD method.

II. EXPERIMENTAL

The films were deposited on glass substrate from cationic precursor of $CoCl_2$ complexed with ammonia, the H_2O_2 as anionic precursor. Doubled distilled water is placed alternately between the anionic and cationic precursor. The deposition was carried at room temperature with 40 sec time in cationic precursor and 15 sec time in anionic precursor. The films by this method are uniform and well adherent to the substrates. The prepared films were characterized by X-ray diffractometer (XRD) with cupper radiation (λ = 1.54 A˚) in the 2θ range from 20 to 80^0. The surface morphology was visualized using a JEOL-6360 scanning electron microscope (SEM). The optical properties were investigated within the wavelength range 300–1000 nm using UV–VIS-NIR spectrophotometer Systronics-119. The contact angle can be measured by using digital camera.

III. RESULTS AND DISCUSSION:

3.1. Cobalt oxide film formation:

Cobalt oxide films were obtained by immersing ultrasonically cleaned glass substrate into separately placed cationic and anionic precursors. The growth kinetics of a thin film deposition process is of the ion by ion type, which involves the ion-by –ion deposition at nucleation sites on the immersed surfaces.

0.4M Cobalt Chloride was used as a source of cobalt and aqueous ammonia (NH_4OH) solution (25% extra pure) was added with constant stirring to make it alkaline. Initially when aqueous ammonia solution was added in cobalt chloride solution.

$$Co^{2+} + NH_3 + H_2O + NO_3^- \rightarrow Co(OH)NO_3 \downarrow + NH_4^-$$

The excess of the reagent dissolves the precipitate, when hexamine cobaltate (II) ions are formed:

$$Co(OH)NO_3 \downarrow + 6NH_3 \rightarrow \left[Co(NH_3)_6\right]^{2-} + NO_3^- + OH^-$$

After immersion of substrate in the first bath cobalt hexamine complex get adsorbed on the surface of the substrate due to cohesive/Vander Walls/chemical attractive forces. The substrate is then immersed in a % H_2O_2 solution to convert the cobalt complex into cobalt oxy-hydroxide by the reaction, which can be represented as,

$$\frac{1}{2}[Co(NH_3)_6]^{2+} + 2\,(H_2O_2) \rightarrow CoO(OH) + 6NH_3 + 2H_2O \quad (3)$$

The CoO(OH) is very reactive with O_2 , and forms a higher oxide Co_3O_4 .

$$3Co^{III}O_{(S)} + 2\,OH^-(Sol) \rightarrow CO_3^{II,III}O_4(S) + 2e^- + H_2O \quad (4)$$

pale yellow dark brown

The Co_3O_4 product would formally be $Co^{II}O$ + $Co_2^{III}O_3$.

3.2. Structural Study:

X-ray diffraction study was carried out for the confirmation of phase and determination of crystal structure of Cobalt oxide film. Cobalt oxide films were characterized with X-ray diffraction in the 2θ range of 20^0 to 80^0. The annealing process generally produces the film free from the defects with improved crystallinity. **Fig. 1** shows XRD pattern of as deposited and annealed Cobalt oxide films at various temperatures on glass substrate. The presence of broad hump is due to the glass substrate. The as-deposited and annealed film did not show any distinct diffraction peak, which probably mean that the film consisted of amorphous cobalt oxy-hydroxide particles.

However at different annealing temperatures, the film did not show any diffraction peak. This revealed that the formed cobalt oxide is low crystalline. If the temperature of the treatment is less than 500^0C, all the films are amorphous or the mean crystalline size is too small to be detected by XRD analysis [12].

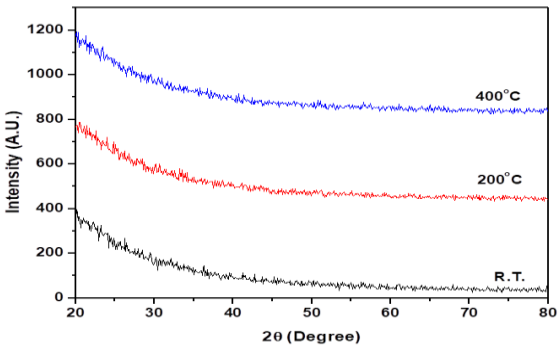

Fig. 1 Typical XRD pattern of cobalt oxide film at different annealing temperatures

3.3. Morphological study:

The influence of annealing temperature on the surface morphology of Cobalt oxide films is studied by scanning electron microscopy. **Fig. 2(a-f)** shows the SEM images of as deposited and annealed cobalt oxide films at 100, 200, 300, 400 and 500^oC at different magnifications (10,000× and 60,000×). At room temperature film reveals the relatively denser surface morphology consisting of smaller grains whereas the annealed at different temperatures represents rough surface with large grains. The film surface is well covered without any pinholes. It is clearly seen that the films have a heterogeneous surfaces. Coalescence of smaller grains of different sizes and shapes into bigger ones can be noticed when the annealed temperature increases. Also image shows a microporous structure with very fine spherical grains less than 50 nm in diameter. At higher temperature porosity decreases and there is growth of material, grain size increases means grains with some overgrown clusters and the crystallite size is increased as annealing temperature increases from 100^oC - 500^oC. Such type of surface morphology may offer increased surface area, feasible for supercapacitor applications.

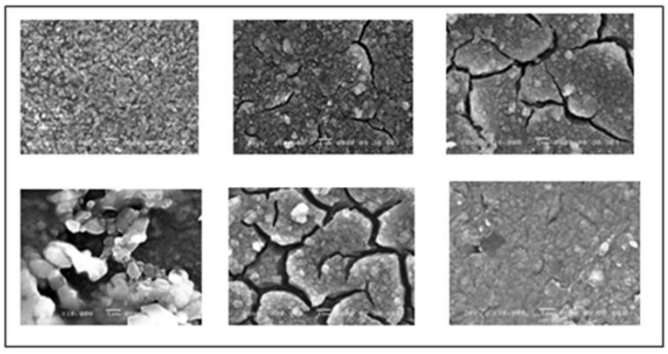

Fig. 2 SEM images of cobalt oxide film at different annealing temperatures (a) as deposited (b) annealed at 100oC (c) annealed at 200oC (d) annealed at 300oC (e) annealed at 400oC (f) annealed at 500oC

The quantitative composition of as deposited and annealed thin films on glass substrate was determined using energy dispersive X-ray analysis (EDAX) technique. A typical EDAX (which film) pattern is shown in **Fig.3.** The composition was 19.69:80.31atomic percentage of Co and O respectively. Also it is observed that as annealing temperature increases atomic percentage of Co is increases.

3.4. Optical studies:

Optical properties of cobalt oxide film were calculated with the help of optical absorption and transmission study. **Fig.4** shows the absorption spectra of cobalt oxide thin films at different annealing temperature. These spectra reveal that film has high absorbance (10^4 cm^{-1}). It is observed that absorption coefficient is very low for photon energy in the IR and visible region while suddenly increase in absorption coefficient in UV region. It is found that absorption coefficient is increases with increase in annealing temperature and absorption decreases with increase in wavelength. Also the increase in absorbance at lower wavelength side is attributed to the wide band gap of cobalt oxide. This could be because of increase in the density of states of holes with increase in annealing temperature.

Fig.5 shows the effect of annealing temperature on the optical transmittance of the cobalt oxide thin films. It is easily seen that the for particular wavelength transparency decreases with increasing the annealing temperature. This is due to the increase in particle size occurs with increasing heat treatment. The results indicate that the Cobalt oxide film at room temperature shows highest transparency (~ 40%) in the visible region. In contrast, UV transparency in the cobalt oxide films is much lower due to the low porosity of these non crystalline films. It is noted that the cobalt oxide film calcinated at 500^{0}C becomes condensed with larger particle size, which causes the high reflection of the light resulting in a dramatic loss of transparency. The results also confirm that the size of nano particles would influence light scattering and transmittance of the coated films [13]. Transmittance drastically decreases to zero at ~ 350 nm. The transmittance decreases as the annealing temperature increases is due to decrease in the band gap with carrier concentration.

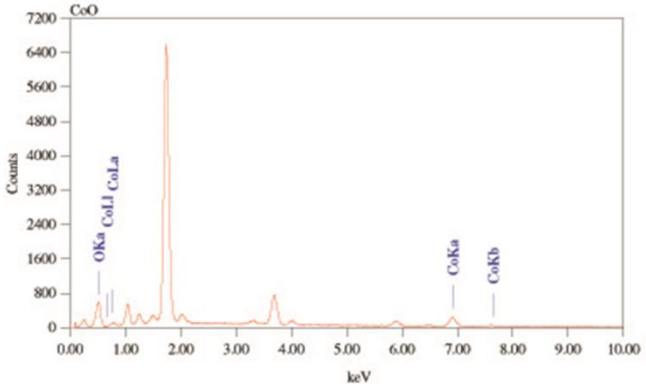

Fig. 3 Typical EDAX pattern of cobalt oxide film

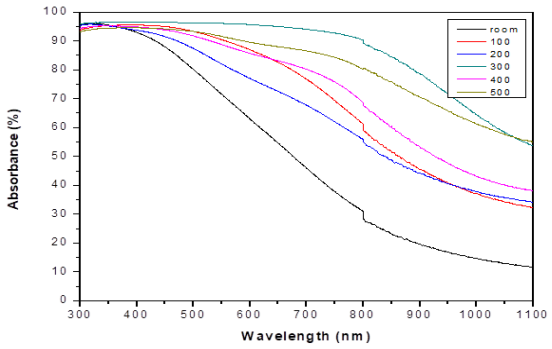

Fig. 4 Absorbance Spectra of cobalt oxide film at different annealing temperatures

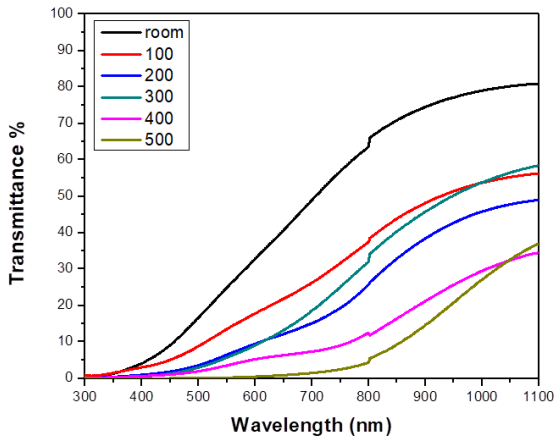

Fig. 5 Transmittance Spectra of cobalt oxide film at different annealing temperatures

Fig. 6 shows the plot $(\alpha h\upsilon)^2$ with $h\upsilon$ for a representative as deposited and annealed cobalt oxide thin films. It has been well established that for a large number of semiconductors the dependence of the absorption coefficient α, in the higher frequency region, upon the photon energy $h\upsilon$, for optically induced transitions, is given by the following classical expression [14]

$$\alpha h\upsilon = K (h\upsilon - E_g)^n \qquad (6)$$

Where Eg represents the optical band gap, hυ is the photon energy, K is constant depending upon the temperature, phonon energy, and n is an index which depends on nature of the electronic transition responsible for the absorption [15] etc. For allowed transition n = 1/2 and for allowed indirect transition n = 2. The extrapolation of the linear portion of curve at energy axis gives the optical band gap. The band gap energy at room temperature was found to be 1.53 eV and 2.10 eV.

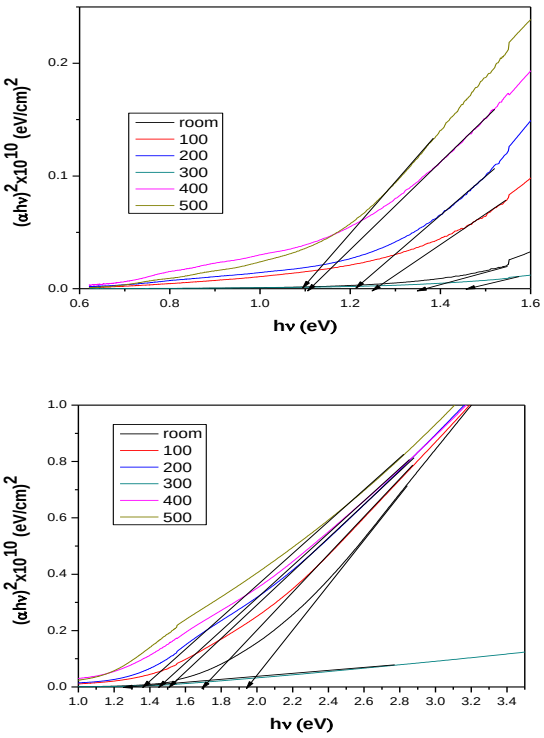

Fig. 6 Optical band gap variation at different annealing temperature

The band gap was found to be in the range of 1.07–1.53 eV and 1.20 - 2.10 eV for as deposited sample and for annealed sample at 100 – 500°C. The decrease in band gap with annealing temperature is probably to increase in grain size, leading to reduction in density of grain boundary trapping centre and improved crystallinity size and reduction of defect sites of the film. The decrease in optical band gap energy is generally observed in the annealed direct-transition-type semiconductor films. Bao and Yao [16] also reported a decrease in band gap with increasing annealing temperature for $SrTiO_3$ thin films, and suggested that a shift of the energy gap was mainly due to both the quantum- size effect and the existence of an amorphous phase in thin films.

Therefore, it is believed that both the increase in crystallite size and the reduction in amorphous phase cause the decrease in band gap of annealed Co_3O_4 films.

Fig. 8 shows the variation of refractive index (n) and extinction coefficient (K) with the wavelength. The magnitudes of the n and k are calculated by using the relationship.

$$R = \frac{(n-1)^2}{(n+1)^2} \quad \text{and} \quad K = \frac{\alpha\lambda}{4\pi} \tag{8}$$

From graph we can see that as annealing temperature of cobalt oxide film increases refractive index of the film increases. Also it is observed that as annealing temperature of cobalt oxide film increases value of K increases. Due to the high refractive index of cobalt oxide, it can be used as one of the layers in multilayer antireflection coatings, or as the outer layer of a dielectric pair coating to boost the reflectance of metals.

3.5. Contact angle measurement:

Fig. 9 (a-f) shows the water contact measurements for cobalt oxide films annealed at different temperatures. Interestingly, cobalt oxide exhibits hydrophilic behavior (60.73°), as water contact angle is < 90°. Generally, low water contact angle increases the electrochemical performance, where interfacial contact at electrolyte-electrode is important.

IV. CONCLUSION

Cobalt oxide films were synthesized by novel M-CBD method on the glass substrate. XRD shows amorphous nature. The surface morphological study revealed the total coverage of substrates at room temperature to 500 0C. Such surface morphology is useful to enhance the performance of

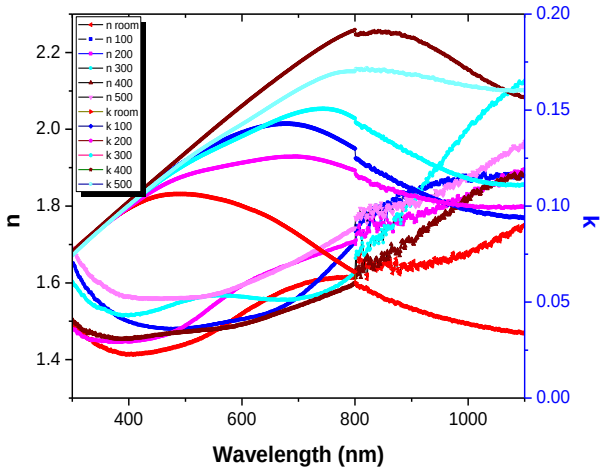

Fig. 8 variation of variation of refractive index (n) and extinction coefficient (K) with the wavelength for different annealing temperatures

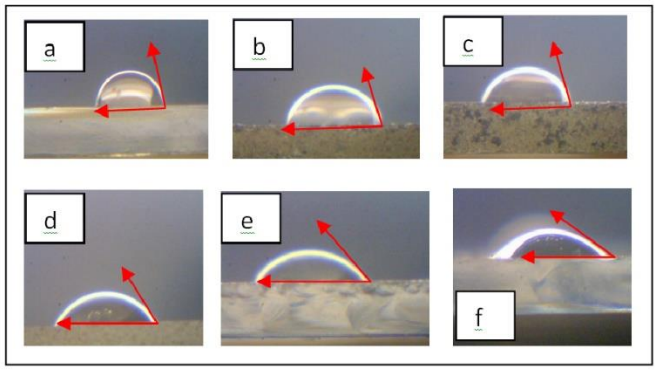

Fig. 9 Contact angles of cobalt oxide thin film at different annealing temperatures

(a) as deposited (b) 100oC (c) 200oC (d) 300oC (e) 400oC (f) 500oC

electrodes in alkaline batteries and supercapacitor like applications. High refractive index of cobalt oxide indicates that, it can be used as one of the layers in multilayer antireflection coatings. Contact angle measurement study confirms hydrophilic nature of annealed thin films.

V. REFERENCES

[1]. R.S. Young (Ed.), Cobalt, Its Chemistry Mutallurgy and Users, Reinhold Publ. Corp., New York, 1960.

[2]. F. Gu, C. Li, Y. Hu and L. Zhang, J. Cryst. Growth, 304 , (2007), 369.

[3]. S. G. Kandalkar, J. L. Gunjakar, C. D. Lokhande and O.S. Joo, J. Alloys Compd., 478, (2009),594.

[4]. I. J. Austin, B.D. Clay, C.E. Turner, J. Phys. C1 (1968) 1418.

[5]. S. G. Kandalkar, C.D. Lokhande, R.S. Mane, S.-H. Han, Appl. Surf. Sci. 253 (2007) 3952.

[6]. A . Cao, J. Hu, H. Liang, W. Song, L. Wan, X. He, X. Gao, S. Xia, J. Phys. Chem. B 110 (2006) 15858.

[7]. B. Pejova, A . Isahi, M. Najdoski, I. Grozdanov, Mater. Res. Bull. 36 (2001) 161.

[8]. C .G. Granqvist, Handbook of Inorgani c Electrochrom ic Mate rials, Elsevier, Amsterdam, 1995.

[9]. Abdel Hamid, Z., Abdel Aal, A., Schmuki, P. Surface and Interface Analysis 40 (2008) 1493

[10]. L. Yan, X.M. Zhang, T. Ren, H.P. Zhang, X.L. Wang, J.S. Suo, Chem. Commun. 8 (2002) 860.

[11]. H.K. Kim, T.Y. Seong, J.H. Lim, W.L. Cho, Y.S. Yoon, J. Power Source 102 (2001) 167.

[12]. R. Drasoven, S. Condurache Bota, Journal of Optoelectronics and advanced Materials Vol. 11 No. 12 Dec. (2009), 2141

[13]. M. A. Aegerter, N.A. Dahoudi, J. Sol–Gel Sci. Technol. 27 (2003) 81.

[14]. P. S. Patil, L.D.Kadam, and C.D.Lokhande, Thin Solid Films, 272, (1996), 29

[15]. J. TAUC, in "Amorphous and Liquid Semiconductor", edited by J. Tauc (Plenum, New York, 1974)

[16]. D. H. Bao and X. Yao, Naoki Wakiya, Kazuo Shinozaki, and Nobuyasu Mizutani, Applied Physics Letters, 79, (2001), 3767

International e-Conference on Recent Trends in Nano-Materials and Its Applications-2021
In Association with International Journal of Scientific Research in Science and Technology
Volume 9 | Issue 2 | Print ISSN: 2395-6011 | Online ISSN: 2395-602X (www.ijsrst.com)

Study of Growth parameters of Lithium Crystals by Single Diffusion Gel Method

Dadaji . V. Sonawane
Assistant professor, Department of physics, J.E.S. Arts, Science and Comm. College, Nandurbar, KBC North Maharashtra University, Jalgaon, Maharashtra, India

ABSTRACT

Single crystals of Lithium tartrate (C4H4O6Li2) Crystals were grown by single diffusion gel technique in a sodium meta silicate gel media at room temperature. Methanol used as solvent for lithium chloride. Optimum conditions were established for growth of good quality pure crystals. The effect of various parameters like were studied pH gel, gel density, concentration of inner and upper reactants. The Ethanol and methanol are used to dissolve lithium chloride. The good size of crystal are grown and The gel method is very simple and within the scope of the laboratory, method be utilized to synthesize crystals. The tartrate crystals have potentials applications such as dielectric, ferroelectric and piezoelectric. In the present work The Lithium tartrate crystal of white color, transparent are obtained, Needle shaped, dendrite crystal were grown [1-10]

Keywords: Gel Technique,Lithium tartrate Crystals,Various parameters (Gel density, pH, &Temperature.)

I. INTRODUCTION

Gel technique is the best technique for growing single crystals at ambient temperature, the compounds which are insoluble in water and decompose before melting can be easily grown by this technique. Due to very slow controlled rate of crystallization and non-turbulence during growth, good quality single crystals are obtained from this technique. The aim of the present work is to grow good quality single crystals of pure lithium tartrate in sodium metasilicate gel. Many researchers have grown the tartrate crystals of different elements having potential applications. The tartrate crystals have potentials applications such as dielectric, ferroelectric and piezoelectric.

1.1 CRYSTAL GROWTH-

The growth of crystal in the gel media is based on the diffusion of the reactant i.e. supernatant. Two techniques can be used for the process of diffusion of reactant in gel media.

1) Single diffusion technique and
2) Double diffusion technique

1.2 CHEMICAL REACTION –

The expected reaction taking place in this work is as below:

$$2LiCl + C_4H_6O_6 \Longrightarrow C_4H_4O_6Li_2 + 2HCl$$

II. EXPERIMENTAL PART

2.1. PREPARATION OF GEL –

The various concentrations of tartaric acid and those

of sodium metasilicate solutions were tried. The solution was added drop by drop with continuous stirring by using a magnetic stirrer till pH is reached in between 3.8 to 4.4. The acid was used for setting of the gel. The solution was then transferred to the corning glass tube. The mouth of the tube was covered by cotton plug. Initially, the mixture appeared to be quite transparent. The gel setting time was about 96 hours. It was observed that the period of setting also depends upon pH of the solvent. Table 1 .Shows optimum conditions to grow the crystals.

Table 1. Optimum conditions for growth of lithium tartrate crystals.

Sr.No	Various Process Parameter	Optimum conditions
1	Density of sodium meta silicate solution	1.04 g/cm^3
2	Volume of sodium meta silicate solution	18ml
3	Volume of tartaric acid	7 ml
4	Concentration lithium chloride	0.2 to 1M
5	pH	4.2
6	Concentration of tartaric acid	1 M
7	Environment temperature	25 to 30 °C
8	Solvent used	Ethanol or Methanol

2.2. EFFECT OF VARIOUS PARAMETERS ON CRYSTALS GROWTH

2.2.1. EFFECT OF GEL DENSITY-

As the gel densities increases, decrease in its transparency is observed like setting time of gel increases with decrease in density. The sodium meta silicate of density 1.04gm/cm^3.

Table 2. Effect of gel density on nucleation density.

Test tube No.	Tartaric acid 1M(ml)	Density of gel (gm/cm^3)	Number of nuclei formed	Observations
1	7	1.038	20	Nucleation process fast but very small crystals
2	7	1.040	24	Transport, well shinning
3	7	1.042	28	White, semitransparent
4	7	1.044	34	Big crystals formed
5	7	1.046	40	Small crystals

2.2.2. EFFECT OF CONCENTRATION OF REACTANTS –

Table 3. Volume of sodium metasilicate required for various concentration of tartaric acid

Test tube No	Concentration of tartaric acid (M)	Sodium meta silicate (ml)
1	1	18
2	1.25	22
3	1.5	25
4	1.75	28
5	2	32
6	2.5	36

(Volume of tartaric acid = 7 ml and pH=4.2)

Fig 1 Graph of sodium metasilicate vs concentration of tartaric acid

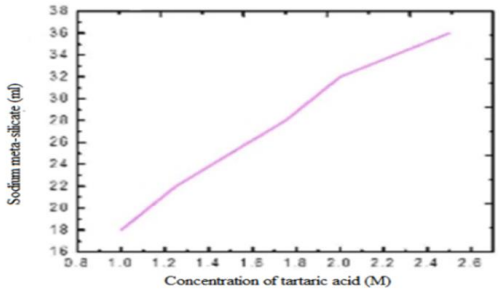

Fig.2. Graph of concentration of supernatants vs number of nuclei.

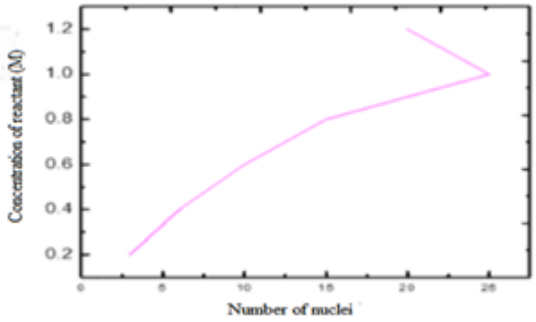

2.2.3. EFFECT OF CONCENTRATION OF SUPERNATANT –

Upper reactance from conc.0.2 to 1M where obtained dissolving LiCl in methanol solvent, It was added over the set gel. Very few nucleations were observed with very tiny size of the white crystals.

Table 4. Effect of concentration of supernatant (pH=4.4)

Test tube No.	Concentration of reactant above gel (Supernatant LiCl)M	No. of nuclei	Observations
1	0.2	3	Crystal size is very small.
2	0.4	6	Slight increase in crystal size
3	0.6	10	Star shaped well isolated crystal
4	0.8	15	Well isolated crystals of various shapes and size
5	1.2	20	Transparent whitish well isolated crystals.

III. RESULT AND DISCUSSION -

Crystals of lithium tartrate are whitish, semitransparent and star shaped . crystals having size 2.5 mm x 4.5mm and thickness of about 2.5 to 3 mm are obtained. Different parameters such as concentration of reactants, pH of gel, impurities in the solvent, gel setting time, gel aging time etc. have considerable effect on growth rate. However as the reactants percolates through the gel, the controlled reaction occurs below , at the depth of 3 to 4 cm. Hence good quality, semitransparent , well developed faces of crystals are observed.

IV. CONCLUSION

1. Gel method is very simple and within the scope of the laboratory, method be utilized to synthesize crystals, if optimum conditions are established.
2. The grown lithium tartrate crystal are white color good size of crystals are grown.
3. The supernatant solution prepared in methanol and ethanol gives good quality crystals.

V. REFERENCES

[1]. Henisch H.K“ Crystal growth in Gel”(1970)
[2]. Henisch H.K. “Crystals in Gel and Liesegang Rings” (1986)
[3]. Sawant D.K.Patil H.M. Bhavsar,D.S., Patil J.H. and Girase K.D.“Journal of scholars Research Library”3 (2011) 404-413.
[4]. Patil H.M. Sawant D.K, Bhavsar. D.S. Patil J.H.and Girase K.D.“Journal of.Therm. Anal.Calorim,” 107 (2012) 1031.
[5]. Krishnakumar V. and Dheivanalar S. Journal Raman Spectroscopy 40 (2009) 627-631.
[6]. Sawant.D.K. Ph.D.Thesis North Maharashtra University,Jalgaon (2012).
[7]. Sonawane S.S. Ph.D. Thesis. J.J.T. University Rajasthan (2017).
[8]. Ahmad Nazir and Kotru P.N.“ J. Crystal Growth” 24 (2014).
[9]. Nandre S.J. Ph.D. Thesis North Maharashtra University Jalgaon (2013).
[10]. Sawant D.K. Patil. H.M. Bhavsar.D.S. Patil. J.H.and Girase K.D. “Scholars Research Library Archives of Physics Research”,2 (2011) 67-73.

International e-Conference on Recent Trends in Nano-Materials and Its Applications-2021
In Association with International Journal of Scientific Research in Science and Technology
Volume 9 | Issue 2 | Print ISSN: 2395-6011 | Online ISSN: 2395-602X (www.ijsrst.com)

Study of Growth Parameters of Copper Tartrate Crystals by Single Diffusion Gel Method

Dadaji. V. Sonawane
Assistant professor, Department of physics, J.E.S. Arts, Science and Comm. College, Nandurbar, KBC North Maharashtra University, Jalgaon, Maharashtra, India

ABSTRACT

Copper tartrate crystals were grown by single diffusion gel technique in a sodium meta silicate gel media at room temperature. The optimum were established by varying different parameters. The effect of various parameters like were studied pH gel, gel density, concentration of reactants. The copper tartrate crystal of bluish color, semitransparent are obtained. Crystals of great interest from both solid state sciencs as well as technological point of view has been reported by many investigators using gel method. The purpose of the present paper is to report growth and influence of various parameters on the growth mechanism of crystals of copper tartrate in silica gel at ambient temperature. The optimum condition required for the growth of these crystal are worked out. [1-13]

Key words: Gel technique, copper tartrate crystals, Various parameters.

I. INTRODUCTION

Every citizen of the nation is enjoying the high standard of living due to recent developments of new materials. Every day pure and mixed crystals are added for practical and industrial purposes. Modern technological revolution was possible because of physical properties like ferroelectric, dielectric non-linear optical, piezoelectric, and semiconductor properties of the material. Therefore, we tried to develop novel materials for the above said applications. Herein, we have developed a methodology to grow the crystals of copper tartrate in silica gel medium in pure form. This chapter reports the complete study made on nucleation and growth of these crystals as a function of gel parameters like the specific gravity of the gel, pH, concentration of supernant solution, and concentration of tartaric acid.

II. MATERIALS AND METHODS

2.1. CHEMICAL REACTION –

The development of copper tartrate crystals is gained by reacting the copper chloride ($CuCl_2$) and tartaric acid.

The reaction is occurred as follow:

$$CuCl_2 + C_4H_6O_6 \longrightarrow CuC_4H_4O_6 + 2HCl$$

Copper chloride + Tartaric acid ⟶ Copper tartrate + waste product

2.2. PREPARATION OF SODIUM METASILICATE SOLUTIONS

Table 1. The data of density of sodium metasilicate solution.

Sr.No.	Various process parameters	Optimum conditions
1	Density of sodium meta silicate solution	1.04 g/cm^3
2	Concentration of tartaric acid	1 M
3	Volume of tartaric acid	7 ml
4	Concentration copper chloride	1 M

Concentration (gm/L)	Density (gm/cm^3)
20	1.038
22	1.040
24	1.042
26	1.044
28	1.046
30	1.048

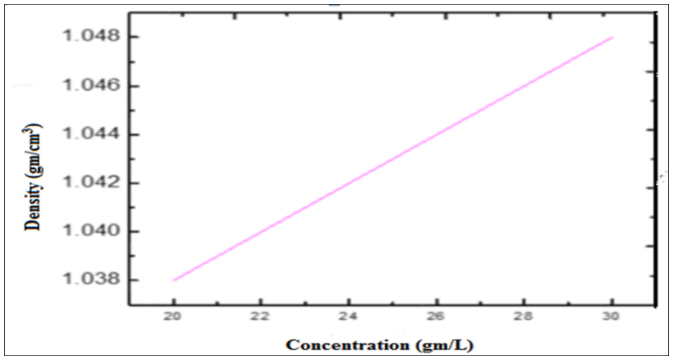

Fig. 1. Gel density vs concentration of sodium metasilicate.

2.3. PREPARATION OF GEL

Fig. 2. Experimental setup for growth of copper tartrate crystal

Table 2. The Optimum conditions for growth of copper tartrate crystals.

2.4. EFFECT OF VARIOUS PARAMETERS ON CRYSTAL GROWTH -

2.4.1. EFFECT OF GEL DENSITY –

Gels of various densities were prepared by mixing sodium meta silicate of specific density from 1.038 to 1.048 gm/cm^3 with one mole of tartaric acid at constant pH of 4.2. The transparency of gel decreases by increase in density of gel. It was also found that the nucleation density is got reduced with increase in gel density. This is attributed to the formation of smaller pore size into the dense gel.

Table 2 shows the effect of density on number of nuclei formation. In present work, best quality, well shining, transparent, various shape and size crystals were observed for density 1.040 gm/cm^3. Fig. 3 shows plot of gel density verses number of nuclei formation.

Table 3. Effect of gel density on nucleation density (pH=4.2, copper chloride solution $CuCl_2$ =1 M and tartaric acid =7ml)

Test tube No.	Tartaric acid 1M(ml)	Density of gel (gm/cm³)	Number of nuclei formed	Observations
1	7	1.038	22	Nucleation process fast but very small crystals.
2	7	1.040	26	Transparent, well shining.
3	7	1.042	32	Bluish, semitransparent.
4	7	1.044	35	Bigger crystals are formed
5	7	1.046	40	Good

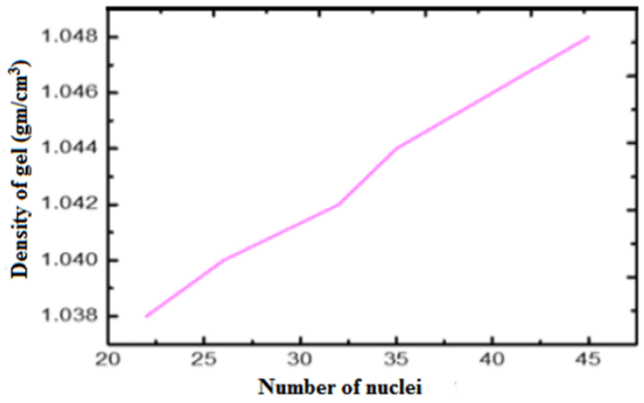

Fig. 3. Effect of gel density and the nuclei formation

2.4.2. EFFECT OF CONCENTRATION OF REACTANTS –

With increase in form of tartaric acid, volume of sodium meta silicate was required to adjust the pH value about 3.8 to 4.2 The fast growth rate at high concentration of tartaric acid resulted into dendrites growth. Table 4. gives the data of volume of sodium metasilicate required to adjust the pH at 4.2for 7ml tartaric acid. Fig. 4 shows the graph of volume of sodium meta silicate verses concentration of tartaric acid.

Fig. 4. Graph of sodium meta silicate

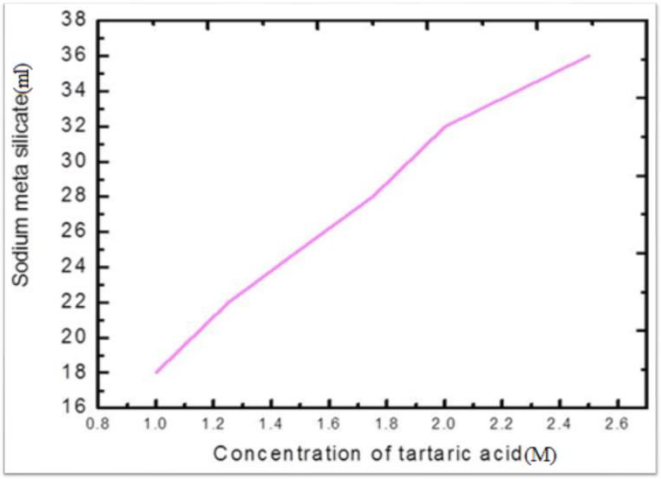

Table 4 Volume of sodium metasilicate required verse concentration of tartaric acid. for various concentration of tartaric acid

Test tube No.	Concentration of tartaric acid (1 to 2.5 M)	Sodium metasilicate (ml)
1	1	18
2	1.25	22
3	1.5	25
4	1.75	28
5	2	32
6	2.5	36

2.4.3. EFFECT OF CONCENTRATION OF SUPERNATANT –

Upper reactant concentration from 0.2 to 1.2 M were obtained by dissolving $CuCl_2$. At 0.8 M concentration of supernatant, transparent and semitransparent crystals were observed for the growth of good quality, large size and well faced crystals. All these observations are summarized in table 5. The linear nature of graph shows that the number of nuclei increased with respect to increase in concentration of supernant solution.

Table 5. Effect of concentration of supernatant

Test Tube No.	Conc. of reactant above gel	Number of Nuclei	Observations
1	0.2	5	Few nucleation's crystals size is very small
2	0.4	8	Slightly crystal size increased
3	0.6	12	Well shining crystals of various shape & size
4	0.8	18	Bluish crystals
5	1	25	Transparent and bluish color
6	1.2	30	Agglomeration of crystals

A. RESULT AND DISCUSSION

Crystals of copper tartrate are bluish, semitransparent and daimond shaped. crystals having size 3mm x 4mm and thickness of about 2 to 3 mm are obtained. Different parameters such as concentration of reactants, pH of gel, impurities in the solvent, gel setting time, gel aging time etc. have considerable effect on growth rate. However as the reactants percolates through the gel, the controlled reaction occurs below , at the depth of 3 to 4 cm. Hence good quality, semitransparent , well developed faces of crystals are observed.

III.CONCLUSION

The morphological changes of the crystals depend upon the growth conditions. Concentration of upper solvent and the pH of the gel played a vital role in molding the shape of these crystals. The studied crystals are of copper tartrate, The grown crystals have almost perfect shining surface structures.2)Copper tartrate-The concentration of tartaric acid (1M), pH(4.0-4.3),density of sodium metasilicate (1.04gm/cm3) and gel setting time (96 hours)

IV. REFERENCES

[1]. Shenoy P. Bangera K.VandShiva Kumar G.K"Cryst Res Technol."45(2010) 825.

[2]. Bhat Sushama, and Kotru P.N."Materials Chemistry and Physics" 39(1994)118.

[3]. John, M.V.Ittyachen,M.A"Cryst.Res.Technol."36(2001)141.

[4]. Parekh B.B. VyasR.M and Joshi M.J. "BullMaterSci."31(2008)143.

[5]. Toress M.E. Lopez and Peraza Stockel J. Yanes A.C., Gonzalez-Silgo, C.Ruiz-Perez .C, and P.A.J. Lorenzo-Luis, "Appli. Phys." 84(1998) 5729.

[6]. Sonawane.S.S .Nandre.S.J,Shitole.S.J.and Ahire.R.R."National Seminar on Advances in Nano-Structured Materials and Their Applications".(2013)

[7]. Patil.H.M. Ph.D.Thesis.North Maharashtra University. Jalgaon.(2014)

[8]. Nandre.S.J. Ph.D.Thesis North Maharashtra University. Jalgaon.(2013)

[9]. C. Balalakshmi and J Mani, "International Journal of Advance Research in Science and Engineering". 6(2017).

[10]. Knowledge Consortium of Gujarat,"Journal of Science". (2012)

[11]. Sawant. D. K. Patil H.M. and Bhavsar D.S. "Pelagia research library".2(2011) 63.

[12]. Nandre, S.J.Shitole S.J and Ahire.R.R. "Scholar research Library Archives of Physics Research"3 (2012)70.

[13]. Jethva.H.O.Dabhi.R.M. And Joshi,M.S.."Journal of Applied Physics."8(2016) 33-42 .

International e-Conference on Recent Trends in Nano-Materials and Its Applications-2021
In Association with International Journal of Scientific Research in Science and Technology
Volume 9 | Issue 2 | Print ISSN: 2395-6011 | Online ISSN: 2395-602X (www.ijsrst.com)

Study of Growth Parameters of Mixed Lithium- Copper Tartrate Crystals by Single Diffusion Gel Method

Dadaji. V. Sonawane

Assistant professor, Department of physics, J.E.S. Arts, Science and Comm. College, Nandurbar, KBC North Maharashtra University, Jalgaon. Maharashtra, India

ABSTRACT

Mixed Lithium-copper tartrate crystals were grown by single diffusion gel technique in a sodium meta silicate gel media at room temperature. The effect of various parameters like were studied pH gel, gel density, concentration of reactants & ethanol are used. Crystals having different morphologies and habits were obtained. The pH of the gel concentration of upper reactant 0.5 conc. of lower reactant 0.5 at room temp 30 c are found to be critical. In the present work few dendrite. Semitransparent faint bluish crystals of mixed copper lithium tartrate were obtained Maximum size of grown crystal was 1mmx2mmx2mm. The Lithium-copper tartrate crystal of whitish blue colour crystal, transparent are obtained.[1-21]

Keyword : Gel Technique, Mixed Lithium-Copper Tartrate, Various Parameters.

I. INTRODUCTION

It is well known fact that the doping of element significantly influences the physical and chemical properties of single crystal, which is of great interest from both solid state science and technological applications. Amongst the metal tartrates, lithium and copper tartrates have acquired interesting physical properties like, ferroelectric, piezoelectric, and non-linear optics. The doping of copper ions into lithium tartrate crystals affects the growth kinetics, morphology, shape size, perfection, unit cell dimensions, magnetic and thermal properties. Moreover, from the technological point of view, dopants play a crucial role to improve the growth kinetics, morphology and second harmonic properties of tartrate crystals. Considering the benefit of doped crystals, efforts have been made by researchers to grow the different types of tartrate crystals.

1.1. CHEMICAL REACTION –

The chemical reaction involved in crystal formation is shown below.

$$LiCl + CuCl + C_4H_6O_6 \longrightarrow LiCuC_4H_4O_6 + 2HCl$$

Lithium Chloride + Cuprous chloride + Tartaric acid $\longrightarrow$ Lithium Copper Tartrate

II. EXPERIMENTAL PART

2.1. Preparation of gel –

To prepare a good quality gel, we used various concentrations of tartaric acid and sodium metasilicate solutions (1.038 to 1.04 gm/cm^3). A 7ml of tartaric acid was taken in a beaker. A 1 M solution of sodium meta-silicate was added drop by drop under continuous stirring by using a magnetic stirrer till pH was reached to 3.8 to 4.4.The acid was used for setting of the gel. The solution was then transferred to the

corning glass tube. The mouth of the tube was covered by cotton plug. The gel setting time was one week. It was observed that the period of setting also depends upon pH of the final solution.

2.2. EFFECT OF VARIOUS PARAMETERS ON CRYSTAL GROWTH

2.2.1. EFFECT OF GEL DENSITY –

Gels of various densities were made by mixing sodium metasilicate of specific density from 1.038 to 1.04 gm/cm^3 with one mole tartaric acid at constant pH 4.2. It may be noted that rhombic shaped whitish-blue crystals of mixed lithium-copper tartrate were obtained with sodium meta silicate of density of 1.04 gm /cm^3. It was found that increase of gel density decreases the nucleation density. It is observed that as the growth of crystal increases with respect to increase in density of gel, as shown in Table 1. In present work, best quality, well semitransparentwere observed for 1.040gm/cm^{3}gel density.

Test tube No	Tartaric acid1M(ml)	Density of gel (gm/cm^3)	Number of nuclei formed	Observations
1	7	1.038	10	Nucleation process medium very small crystals.
2	7	1.040	21	Transparent
3	7	1.042	28	Faint bluish, semitransparent.
4	7	1.044	30	Bigger crystals are formed
5	7	1.046	38	Good some other small crystals

Table 1.Effect of gel density on nucleation density.

2.2.2. Effect of concentration of reactants –

As the concentration of tartaric acid was increased more volume of sodium meta silicate was required to adjust the require pH values of 3.8 to 4.2. By increasing the aging time the concentration of tartaric acid nucleation density also increased. The fast growth rate at high concentration of tartaric acid resulted into dendrites growth. We have optimized the sodium metasilicate solutions with respect to concentration of tartaric acid solution in order to adjust the pH 4.2. The optimized parameters and corresponding representative graph are shown in Table 2 and Fig. 1, respectively. We have obtained good quality crystals at 1 M concentration of tartaric acid under optimized condition.

Table 2 Volume of sodium metasilicate required for various concentration of tartaricacid

Test tube No.	Concentration of tartaric acid (1 to 2.5 M)	Sodium metasilicate (ml)
1	1	18.5
2	1.25	22.2
3	1.5	25.6
4	1.75	27.9
5	2	31.0
6	2.5	34

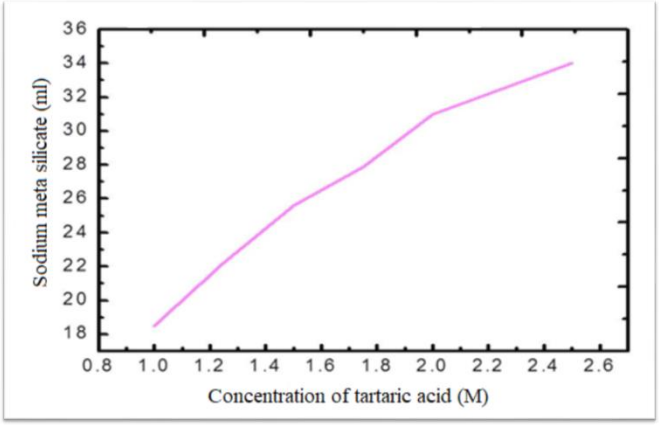

Fig. 1. Graph of Sodium metasilicate (ml) vs concentration of tartaric acid (M).

2.2.3. EFFECT OF TEMPERATURE -

During the growth study, we observed that the best temperature to grow the lithium-copper tartrate crystal is around 25-30 °C, and this temperature range is available in rainy and winter seasons. However, in

summer the ambient temperature is above 35-45 °C during day time that affecting the kinetic growth of the crystals.

III. RESULT AND DISCUSSION

It is observed that formation of crystal depends on the gel pH, higher the pH(pH>4.5) blocks the diffusing sites of the gel pores and may not be appropriate for the growth of single crystal even though there is release of HCL as by product which further reduces the effective value of the gel pH. On the other hand at gel pH value(pH<3.8) the growth of crystal may result. However it is observed that nucleation density becomes very high and it put limis on the size of crystal At h=4.2 well good quality crystal are observed. liesegang rings were observed. Thus high gel pH value(Ph>4.6) as well as low pH value(ph<3.8) does not gives fruitful result. In our experiments intermediate value of gel pH(3.0 to 4.2) is interesting. Under the optimum conditions established in the series of explained as earlier the crystal of mixed lithium-copper are observed basically inside the gel medium. The gel grown tartrate crystals are faint bluish colour

IV. CONCLUSION

1) Gel method is found to be suitable for the growth of mixed Cu-Litartrate crystals at room temp.
2) The gel grown tartrate crystals are faint bluish colour.
3) The maximum size of grown crystals was found to be 2 to 4 mm.
4) It was found that as pH increases, nucleation centers decreases.

V. REFERENCES

[1]. F.Jeau Rethinau, D. Arivuoli,S.Ramasamy and P.Ramasamy. "Material Research Bulletin" 29(1994)309-316.

[2]. Suresh Kumar B. and Rajendra BabuK. "Bull. Mater.Sci"30 (2007)349-355.

[3]. Rahimkutty M H, and Rajendra Babu K. "Bull. Mater.Sci".24 (2001)249.

[4]. Viji R K, GowriB and SahayaShajan X ."Indian Journal Phys".79(2005)1373.

[5]. Quasim I, Firdous A, Sahni N, Kotru P.N."Crystal Research and Technology" .44 (2009).

[6]. Gunter sperka.Inorganicachimica Acta,149(1988)149-150.

[7]. Ahmad Nazir and Kotru. P.N "Journals of crystal growth" 412(2015) 72-79

[8]. Nikolaj R. Ivanov."Institute of crystallography".12(2006).

[9]. Suresh Kumar B. and Rajendra Babu. K. "Bull. Mater.Sci".30(2007)349-355.

[10]. Patil N.S, Bachhav S.K. and Bhavsar D.S.Scholars. Research Library, "Archives of Applied Science Research", 6(1)(2014)45-51.

[11]. Mathivanan V. and Haris M. "Indian Journals of Pure and Applied Physics," 51(2013) 851-859.

[12]. Quasim I, Firdous A, Sahni N, Kotru P.N. "Crystal Research and Technology" 44. (2009).

[13]. Nandre,S.J. AhireR.R. and Shitole,S.J."Advance in applied science research." 2(2011) 134-139.

[14]. Ahmad Nazir, Kotru P.N."Journal of Crystal Growth".412(2015)720-721.

[15]. Patil N.S, Bachhav S.K. andBhavsarD.S.Scholars. Research Library,"Archives of Applied Science Research", 6(2014)45-51.

[16]. Patil N.S, Bachhav S.K. Kale M.S. and Bhavsar D.S. "Int. Journal of Engineering Research and Applications".4 (2014) 50-54.

[17]. Dhikale . M.D, Shitole .S.J. "International "Journal of chemical and physical science".7(2008).

[18]. Selvarajan P., Das B.N., "Journal Mater. Sci", 12(1993)1210.

[19]. Mathivanan V. andHaris M. "Indian Journals of Pure and Applied Physics," .51 (2013)254.

[20]. Nandre, S.J. Shitole and Ahire R.R. "Journal of Nano electron Phys".5 (2013)

[21]. Sawant .D.K. Ph.D.Thesis .North Maharastra University ,Jalgoan.(2012)

International e-Conference on Recent Trends in Nano-Materials and Its Applications-2021
In Association with International Journal of Scientific Research in Science and Technology
Volume 9 | Issue 2 | Print ISSN: 2395-6011 | Online ISSN: 2395-602X (www.ijsrst.com)

Single Crystal Growth and Study of Lithium Tartrate in Gel Method

Dadaji. V. Sonawane
Assistant professor, Department of physics, J.E.S. Arts, Science and Comm. College, Nandurbar, KBC North Maharashtra University, Jalgaon. Maharashtra, India

ABSTRACT

Single crystals of Lithium Tartrate were grown by single diffusion gel technique. Methanol used as solvent for lithium chloride .Optimum conditions were established for growth of good quality pure crystals. Effect of various growth parameters such as PH of the gel, concentration of inner reactants, concentration of upper reactants, gel density etc. The lattice parameters of lithium tartrate are almost matching with the JCPDS data. The crystals studied using XRD, FT-IR, and thermal analysis, (TGA & DTA) scanning electron microscope(SEM),, AES Were studied .Needle shaped and whitish colour, dentritic crystals were grown. [1-10]

Keywords : Gel Technique, Lithium Tartrate Crystals, Lithium Choride.

I. INTRODUCTION

Gel technique is the best technique for growing single crystals at ambient temperature, the compounds which are insoluble in water and decompose before melting can be easily grown by this technique. Due to very slow controlled rate of crystallization and non-turbulence during growth, good quality single crystals are obtained from this technique. The aim of the present work is to grow good quality single crystals of pure lithium tartrate in sodium metasilicate gel. Many researchers have grown the tartrate crystals of different elements having potential applications.The tartrate crystals have potentials applications such as dielectric, ferroelectric and piezoelectric.

1.1 CRYSTAL GROWTH

The growth of crystal in the gel media is based on the diffusion of the reactant i.e. supernatant. Two techniques can be used for the process of diffusion of reactant in gel media.

1) Single diffusion technique and 2) Double diffusion technique

The single diffusion technique was found to be most suitable for the growth of good quality crystals in present work. To grow the lithium tartrate crystals, we prepared different concentrations of LiCl solution in methanol or ethanol and used as a Supernant solution.

1.2 APPARATUS USED

1. Borosil glass test tube (25 cm in length and 2.5cm in diameter)
2. Magnetic stirrer
3. Various size beakers
4. Burettes and pipettes
5. Digital pH meter
6. Specific gravity bottle
7. Cotton

1.3 CHEMICALS Used –

The chemicals used for the growth of lithium tartrate crystals are commercial grade

1. Sodium metasilicate–(Na2SiO3.9H2O) (Loba chemicals)
2. Tartaric acid – A.R grade (C4H6O6) (Loba chemicals)
3. Lithium chloride –A.R grade 99.9% pure [LiCl]
4. Double distilled water for dilution
5. Methanol and ethanol

1.4 CHEMICAL REACTION –

The chemical reactions inside the gel can be expressed as

2Licl +C4O6H6 ⟶ (C4H4O6)Li

2+2HClLithium chloride + Tartaric acid → Lithium Tartarate

II. EXPERIMENTAL WORK

Gel was prepared by using tartaric acid and sodium metasilicate having different pH values. AR grade lithium chloride and tartaric acid were used as received. A 7ml of tartaric acid (1M) was taken in a small beaker. Sodium metasilicate solution of (1M) concentration was added drop by drop with constant stirring. ThepH of solution was maintained between 4 to 4.5. The solution was then transferred in the test tube (2.5cm diameter and 25cm length) then covered its mouth with cotton plug. It was transparent initially, after 2/3 days, it turns milky and gel converted into semisolid with little amount of water on the top of the surface.

After setting of hydro silica gel, allow the aging of the gel. Aging makes the gel harder and reduces the diameter of the capillaries present in the gel. A 1M concentration of LiCl solution was made by dissolving LiCl in methanol or ethanol. The solution was often poured slowly with the help of pipette. The height of the supernatant component should be 60-70% of the gel height. With time, lithium chloride diffuses in the gel and the crystals of lithium tartrate appears in the gel. This is called “single diffusion method”. In present work, lithium tartrate crystals were grown by single gel diffusion technique at various parameters. The crystal growth parameters were adjusted at optimum conditions to obtain full grown crystals. The solvents used to grow crystals played a vitally important role. In the present study, we used methanol or ethanol solvents to grow well-defined crystal in gel medium. An experimental set-up with working is shown in fig 1.

Fig. 1 Experimental set-up with working reaction during crystal growth in test tube.

PREPARATION OF GEL –

The various concentrations of tartaric acid and those of sodium metasilicate solutions were tried. The solution was added drop by drop with continuous stirring by using a magnetic stirrer till pH is reached in between 3.8 to 4.4. The acid was used for setting of the gel.

Table 1. Optimum conditions for growth of lithium tartrate crystals.

Sr.No	Various Process Parameter	Optimum conditions
1	Density of sodium meta silicate solution	1.04 g/cm^3
2	Volume of sodium meta silicate solution	18ml
3	Volume of tartaric acid	7 ml
4	Concentration lithium chloride	0.2 to 1M
5	pH	4.2
6	Concentration of tartaric acid	1 M
7	Environment temperature	25 to 30 °C
8	Solvent used	Ethanol or Methanol

III. MORPHOLOGY

Growth rate of the crystals is affected by parameters like pH and purity of reactance, gel setting time and aging time. Crystals of lithium tartrate are whitish, semitransparent and star shaped. Various types of crystals sizes with respect to supernant concentration were obtained, which is tabulated in Table 2.We have also taken the photographs of the grown crystals in test tube as well as on the graph paper to measure the dimension of the grown crystal and it is represented in Fig 42.The largest crystal size of 3 x 1 x 1 mm^3 was obtained at 0.8 M concentration of LiCl supernant solution. It is important to note that the obtained crystals are of good quality, semitransparent, and well developed. The optimum conditions for lithium tartrate crystals grown in silica gel are summarized in Table 2.

Table 2 Effect of habit, quality and size of lithium tartrate.

Lower reactant $C_4O_6H_6$ (ml)	Conc. of LiCl solution (1M)	pH	Habit	Quality	Size (mm)
7	0.4	4.2	Dendrite	Opaque	1 X 1 X1
7	0.6	4.2	Dendrite	Opaque	2 X 1 X1
7	0.8	4.2	Star shaped	Transparent, white, Good	3 X 1 X 1

Fig 2 Growth of lithium tartrate crystal in silica gel at various concentration of supernatants solution of (a) 0.4 M, (b) 0.6 M, (c) 0.8 M , and (d) & (e), Photographs of the grown crystals.

IV. RESULT AND DISCUSSION

Crystals of lithium tartrate are whitish, semitransparent and star shaped . crystals having size 2.5 mm x 4.5mm and thickness of about 2.5 to 3 mm are obtained. Different parameters such as concentration of reactants, pH of gel, impurities in the solvent, gel setting time, gel aging time etc. have considerable effect on growth rate. However as the reactants percolates through the gel, the controlled reaction occurs below , at the depth of 3 to 4 cm. Hence good quality, semitransparent , well developed faces of crystals are observed.

V. CONCLUSION

1. The grown lithium tartrate crystal are white

color good size of crystals are grown.

2. The supernatant solution prepared in methanol and ethanol gives good quality crystals.
3. Gel method is very simple and the colour is white.
4. within the scope of the laboratory, method be utilized to synthesize crystals, if optimum conditions are established.

VI. REFERENCES

[1]. Henisch H.K" Crystal growth in Gel"(1970)
[2]. Henisch H.K. "Crystals in Gel and Liesegang Rings" (1986)
[3]. Sawant D.K.Patil H.M. Bhavsar,D.S., Patil J.H. and Girase K.D."Journal of scholars Research Library"3 (2011) 404-413.
[4]. Patil H.M. Sawant D.K, Bhavsar. D.S. Patil J.H.and Girase K.D."Journal of.Therm. Anal.Calorim," 107 (2012) 1031.
[5]. Krishnakumar V. and Dheivanalar S. Journal Raman Spectroscopy 40 (2009) 627-631.
[6]. Sawant.D.K. Ph.D.Thesis North Maharashtra University,Jalgaon (2012).
[7]. Sonawane S.S. Ph.D. Thesis. J.J.T. University Rajasthan (2017).
[8]. Ahmad Nazir and Kotru P.N." J. Crystal Growth" 24 (2014).
[9]. Nandre S.J. Ph.D. Thesis North Maharashtra University Jalgaon (2013).
[10]. Sawant D.K. Patil. H.M. Bhavsar.D.S. Patil. J.H.and Girase K.D. "Scholars Research Library Archives of Physics Research",2 (2011) 67-73.

International e-Conference on Recent Trends in Nano-Materials and Its Applications-2021
In Association with International Journal of Scientific Research in Science and Technology
Volume 9 | Issue 2 | Print ISSN: 2395-6011 | Online ISSN: 2395-602X (www.ijsrst.com)

Synthesis and Characterization of Lithium Tartrate Single Crystals by Gel Technique

Dadaji. V. Sonawane
Assistant professor, Department of physics, J.E.S. Arts, Science and Comm. College, Nandurbar, KBC North Maharashtra University, Jalgaon, Maharashtra, India

ABSTRACT

In the present investigation, Lithium Tartrate crystals were grown in silica gel at ambient temperature. Methanol used as solvent for lithium chloride .Optimum conditions were established by varying various parameters such as pH of the gel solution, gel concentration, gel setting time, concentration of upper reactants, gel density etc. Crystals having different morphology were obtained. Whitish, shining, semitransparent, star shape, Needle shaped of lithium tartrate were obtained. The lattice parameters of lithium tartrate are almost matching with the JCPDS data. The crystal structure of compound was confirmed by powder X-ray powder diffraction, Atomic emission spectroscopy(AES) The crystals studied using XRD, FT-IR, and thermal analysis, (TGA & DTA), scanning electron microscope(SEM), Chemical analysis Were studied .Needle shaped and whitish colour, dentritic crystals were grown. [1-11]

Keywords : Gel technique, Lithium tartrate crystals, XRD & AES

I. INTRODUCTION

The Gel technique is the good technique for growing single crystals at room temperature, the compounds which are insoluble in water and decompose before melting can be easily grown by this technique. Due to very slow controlled rate of crystallization and non-turbulence during growth, good quality single crystals are obtained from this technique. The aim of the present work is to grow good quality single crystals of pure lithium tartrate in sodium metasilicate gel. Many researchers have grown the tartrate crystals of different elements having potential applications .The tartrate crystals have potentials applications such as dielectric, ferroelectric and piezoelectric

1.1. CHEMICAL REACTION

Growth of lithium tartrate crystals is gained by reacting the components lithium chloride (LiCl), and tartaric acid. The expected reaction taking place in this work is as below:

$$2LiCl + C_4H_6O_6 \longrightarrow C_4H_4O_6Li_2 + 2HCl$$

II. CHARACTERIZATION OF LITHIUM TARTRATE

The features of the crystal are important components of the study of crystals. This helps the crystal grower to assess the quality, nature and property of the crystals. A large number of experimental techniques exist to assess the composition quality and the presence of its constituent elements.

2.1. X-RAY DIFFRACTOMETRY (XRD)

The powder x-ray diffraction patterns for pure gel grown lithium tartrate crystals were recorded using powder method by Miniflex Rigaku, X-ray diffractometer at SAIF, IIT Powai. Computer program POWD was used to calculate (hkl) and'd' values of the recorded pattern. Calculated (hkl) and'd' values indicate orthorhombic crystals structure of lithium titrate crystals having lattice parameters of a = 6.7942 Å, b = 7.9807 Å and c = 5.2386 Å and volume (V) = 284.05 (Å)^3.

The unit cell parameters of the lithium tartrate crystals calculated by the computer program are shown in the table 1. The peaks obtained at 17.13, 20.26, and 21.40 corresponds to (110), (011), and (101) planes. The parameters fulfill the condition for orthorhombic system i.e. $a \neq b \neq c$ and $\alpha = \beta = \gamma = 90^o$. The recorded peaks are well matched to the JCPDS data card No. **01-0321** of lithium tartrate confirming the orthorhombic system .

Table 1. Unit cell parameters

Sr.No.	Lattice Parameters	Lithium Tartrate
1	System	Orthorhombic
2	a	6.7942 Å
3	b	7.9807 Å
4	c	5.2386 Å
5	V	284.05 (Å)^3

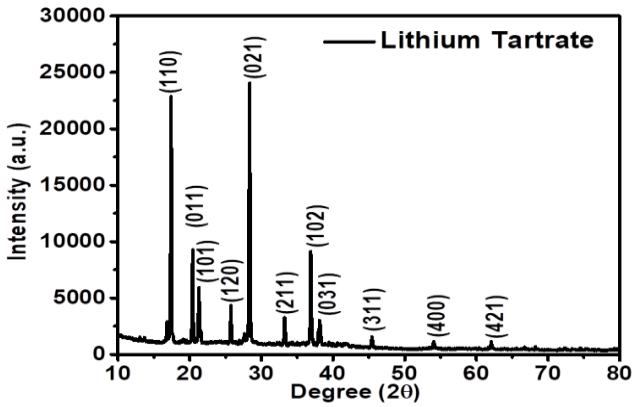

Fig 1. X-Ray diffraction pattern of lithium tartrate crystals grown by gel method

Table 2 Calculated and observed value of d-spacing

Peak no.	d-Spacing		Indices	2 θDegree	
	Obs.	Cal.	(h k l)	Obs.	Cal.
1	5.17	5.17	(1 1 0)	17.13	17.13
2	4.37	4.37	(0 1 1)	20.26	20.26
3	4.14	4.14	(1 0 1)	21.40	21.41
4	3.46	3.44	(1 2 0)	25.67	25.69
5	3.15	3.17	(0 2 1)	28.24	28.21
6	2.70	2.68	(2 1 1)	33.08	33.10
7	2.44	2.44	(1 0 2)	36.79	36.71
8	2.37	2.37	(0 3 1)	37.93	37.88
9	2.01	2.01	(3 1 1)	45.05	45.05
10	1.69	1.69	(4 0 0)	53.89	53.90
11	1.49	1.49	(4 2 1)	61.87	61.84

III. ELEMENTAL ANALYSIS

3.1. ATOMIC EMISSION SPECTROSCOPY (AES)

The peak corresponding to lithium could not be detected with the help of EDAX technique, as it has a low atomic number. So atomic emission spectroscopy (AES) technique was used to determine the presence of lithium in lithium tartrate crystals. By using this technique, the presence of lithium (Li) in the sample was confirmed[11].Analytical reports obtained for lithium tartrate crystals via Atomic Emission Spectroscopy is shown in table 3.s

Table 3. Percentage of sample (AES)

Sample	Li (%)
Li	2.95

IV. RESULT AND DISCUSSION

The crystals of lithium tartrate were characterized by XRD analysis. From these diffractogram, 'd' values were computed. From the XRD pattern it is noticed that the peaks obtained. We also found (101), (021),

and (102) lattice planes of lithium tartrate crystals at 2θ of 21.40, 28.81 and 36.51° , respectively. Moreover, apart from the individual lattice planes, we also obtained new peaks at 18.83, 23.11, 26.53, 34.51, 40.78, 48.19, 51.90 and 55.03 degree (2θ) exhibiting the planes (201), (141), (151), (171), (352), (313), (211) and (850), respectively. Calculated (hkl) and 'd' values indicate orthorhombic crystals structure of lithium tartrate crystals and having lattice parameters of a = 6.7942 Å, b = 7.9804 Å and c = 5.2386 Å and volume of unit cell, V = 284.05 $(Å)^3$.

V. CONCLUSION

There has been always a keen and competitive race to grow perfect single crystal with purity and tranceparancy. The good quality single lithium crystals of (3x1x1) and the atomic spectrum limited sample is used to determined it lelemetal composition. AES. The dopant concentration of lithium in the grown crystals is 29.8 ppm. Needle shaped and whitish colour, dentritic crystals were grown

VI. REFERENCES

[1]. Krishnakumar V. and Dheivanalar S. Journal Raman Spectroscopy 40 (2009) 627-631.
[2]. Ahmad Nazir and Kotru P.N." J. Crystal Growth" 24 (2014).
[3]. Sawant.D.K. Ph.D.Thesis North Maharashtra University,Jalgaon (2012).
[4]. Sonawane S.S. Ph.D. Thesis. J.J.T. University Rajasthan (2017).
[5]. Henisch H.K" Crystal growth in Gel"(1970)
[6]. Sawant D.K.Patil H.M. Bhavsar,D.S., Patil J.H. and Girase K.D."Journal of scholars Research Library"3 (2011) 404-413.
[7]. Patil H.M. Sawant D.K, Bhavsar. D.S. Patil J.H.and Girase K.D."Journal of.Therm. Anal.Calorim," 107 (2012) 1031.
[8]. Henisch H.K. "Crystals in Gel and Liesegang Rings" (1986)
[9]. Nandre S.J. Ph.D. Thesis North Maharashtra University Jalgaon (2013).
[10]. Sawant D.K. Patil. H.M. Bhavsar.D.S. Patil. J.H.and Girase K.D. "Scholars Research Library Archives of Physics Research",2 (2011) 67-73.
[11]. http://www.rsic.iitb.ac.in/icp-aes.html

International e-Conference on Recent Trends in Nano-Materials and Its Applications-2021
In Association with International Journal of Scientific Research in Science and Technology
Volume 9 | Issue 2 | Print ISSN: 2395-6011 | Online ISSN: 2395-602X (www.ijsrst.com)

Growth and Characterization of Copper Tartrate Crystal by Silica Gel Method

Dadaji. V. Sonawane

Assistant professor, Department of physics, J.E.S. Arts, Science and Comm. College, Nandurbar, KBC North Maharashtra University, Jalgaon, Maharashtra, India

ABSTRACT

In the present investigation, copper Tartrate crystals were grown in silica gel at ambient temperature. Distilled water used as solvent for copper chloride .Optimum conditions were established by varying various parameters such as pH of the gel solution, gel concentration, gel setting time, concentration of upper reactants, gel density etc. Crystals having different morphology were obtained. Bluish colour, semitransparent, diamond shaped, copper tartrate were obtained. The crystal structure of compound was confirmed by powder X-ray powder diffraction, Chemical analysis. The crystals studied using XRD, FT-IR, and thermal analysis, (TGA & DTA), scanning electron microscope (SEM), Chemical analysis Were studied .Needle shaped and bluish, semitransparent, well shining colour, Diamond crystals were grown. [1-17]

Keywords : Gel technique, Copper tartrate crystals, XRD & Chemical analysis.

I. INTRODUCTION

Every citizen of the nation is enjoying the high standard of living due to recent developments of new materials. Every day pure and mixed crystals are added for practical and industrial purposes. Modern technological revolution was possible because of physical properties like ferroelectric, dielectric non-linear optical, piezoelectric, and semiconductor properties of the material. Therefore, we tried to develop novel materials for the above said applications. Herein, we have developed a methodology to grow the crystals of copper tartrate in silica gel medium in pure form. This chapter reports the complete study made on nucleation and growth of these crystals as a function of gel parameters like the specific gravity of the gel, pH, concentration of supernant solution, and concentration of tartaric acid.

1.1 CHEMICAL REACTION –

The reaction is occurred as follow:

$CuCl_2 + C_4H_6O_6 \longrightarrow CuC_4H_4O_6 + 2HCl$

Copper chloride + Tartaric acid ⟶ Copper tartrate + waste product

II. CHARACTERIZATION OF GEL GROWN COPPER TARTRATE CRYSTALS

2.1. X-RAY DIFFRACTOMETRY (XRD)

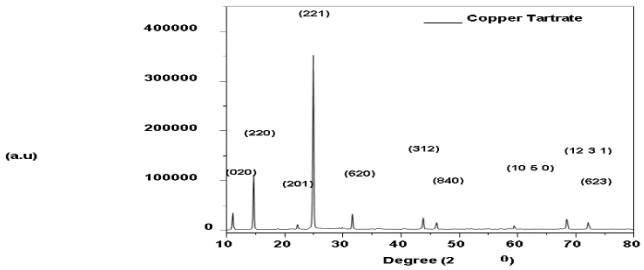

Fig. 1. X-Ray Diffraction of gel grown copper tartrate crystal.

X-ray diffractogram is useful in the analysis of crystal

structure, cell parameters' values, unit cell volume and lattice system , X-ray diffractogram of gel grown copper tartrate was recorded using powder rotation photograph method on 'Minislex Rigaku' X-ray diffractometer at department of Physics, Pratap College, Amalner. CuKα-radiation (wavelength λ=1.54051 Å) was used. The scanning speed was kept to 10^{o} min^{-1}. The recorded X-ray diffraction pattern is shown in Fig. 1. XRD pattern in shows very sharp peaks having high intensity which leads to extremely good crystalline perfection of the copper tartrate crystals. The lattice parameters of unit cells of copper tartrate is tabulated in the Table 1. From this powder diffraction data (hkl) values were computed. The computer program, POWD, (Integrative powder diffraction and indexing program version 2.2) was used to calculated (hkl) values.

The unit cell parameters, observed and calculated interplaner distance, and orientation of plane corresponding to 2θ obtained from the computer program are summarized in the Table 1 and 2. These parameters fulfill the condition for orthorhombic system i.e. $a \neq b \neq c$ and $\alpha = \beta = \gamma = 90^{0}$. The obtained data is in well agreement with the JCPDS data card no. 01-0158 of copper tartrate material.

Table 1. Lattice parameter for copper tartrate crystals.

C	Copper Tartrate
A	17.9058Å
B	16.0728Å
C	4.4232Å
V	1272.97 $(Å)^3$

Table 2 Calculated & observed value of d-spacing and (hkl) indices of copper tartrate crystal.

Peak	d-Spacing (Å)		Indices	2Θ Degree	
	Obs	Calc.	hkl	Obs	Calc.
1	8.0364	8.0364	(0 2 0)	11.00	11.00
2	5.9804	5.9804	(2 2 0)	14.80	14.80
3	3.9656	3.9656	(2 0 1)	22.40	22.40
4	3.5588	3.5562	(2 2 1)	25.00	25.02
5	2.7945	2.7976	(6 2 0)	32.00	31.96
6	2.0562	2.0567	(3 1 2)	44.00	43.99
7	1.9553	1.9553	(8 4 0)	46.40	46.40
8	1.5642	1.5643	(10 5 0)	59.00	59.00
9	1.3668	1.3671	(12 3 1)	68.60	68.59
10	1.3042	1.3043	(6 2 3)	72.40	72.39

III. CHEMICAL ANALYSIS

(INDIVIDUAL ANALYSIS OF COPPER) –

Copper tartrate is separated by routine method i.e.0.1 gm of copper tartrate was dissolved in dilute acidic solution and the copper was precipitated by passing H_2S gas in the solution. This was filtered by What Mann filter paper no.40. The precipitated was dried and ignited. Weight of copper residue was 0.028 g. The filtrate left after the precipitation of copper was used for analysis .

The filtrate was boiled to expel H_2S gas.

Theoretical percentage of copper (Cu).

Theoretically, in $CuC_4H_4O_6$ having molecular weight 211.62 gm,

The amount of Cu is 63.54 gm.

Percentage of copper = (63.54×100) ÷ 211.62 =30.02%

Practical percentage of copper:

Weight of sample =0.1g

Weight of the precipitate (Cu) = 0.028 g.

Percentage of copper = (0.028×100) ÷ 0.1

Percentage of copper = 28.0 %

Table 3.The result analysis of copper tartrate

Element	Theoretical value %	Practical value%
Copper(Cu)	30.02	28.0

IV. RESULT AND DISCUSSION

The crystals of copper tartrate were characterized by XRD analysis. From the XRD pattern it is noticed that the peaks obtained at 11.00, 14.80, 25.00, 31.95, and 43.35° are corresponds to the (020), (220), (221), (620), and (312) lattice planes of the copper tartrate crystals, respectively. Calculated (hkl) and 'd' values indicate orthorhombic crystals structure of copper tartrate crystals and having lattice parameters of a = 17.9058 Å, b = 16.0728 Å and c = 4.4232 Å and volume of unit cell, V = 1272.97 $(Å)^3$. We have used two different techniques to investigate the elemental composition present in the grown crystals. Specifically, we have used inductively coupled plasma atomic emission spectroscopy for lithium detection in lithium tartrate. We have also used energy dispersive X-ray analysis to identify the presence of copper in the copper tartrate. Theoritical value % of copper is 30 and observed value is 28.74

V. CONCLUSION

1. The gel grown copper tartrate crystals are bluish color.
2. The copper tartrate crystal is grown by simple gel method.
3. It was found that as pH increases, nucleation centers decreases
4. Theoretical value % of copper is 30 and observed value is 28.74

VI. REFERENCES

[1]. Shenoy P. Bangera K.VandShiva Kumar G.K"Cryst Res Technol."45(2010) 825.

[2]. Bhat Sushama, and Kotru P.N."Materials Chemistry and Physics" 39(1994)118.

[3]. John, M.V.Ittyachen,M.A"Cryst.Res.Technol."36(2001) 141.

[4]. Parekh B.B. VyasR.M and Joshi M.J. "BullMaterSci."31(2008)143.

[5]. Toress M.E. Lopez and Peraza Stockel J. Yanes A.C., Gonzalez-Silgo, C.Ruiz-Perez .C, and P.A.J. Lorenzo-Luis, "Appli. Phys." 84(1998) 5729.

[6]. Sonawane.S.S .Nandre.S.J,Shitole.S.J.and Ahire.R.R."National Seminar on Advances in Nano-Structured Materials and Their Applications".(2013)

[7]. Patil.H.M. Ph.D.Thesis.North Maharashtra University. Jalgaon.(2014)

[8]. Nandre.S.J. Ph.D.Thesis North Maharashtra University. Jalgaon.(2013)

[9]. C. Balalakshmi and J Mani, "International Journal of Advance Research in Science and Engineering". 6(2017).

[10]. Knowledge Consortium of Gujarat,"Journal of Science". (2012)

[11]. Sawant. D. K. Patil H.M. and Bhavsar D.S. "Pelagia research library".2(2011) 63.

[12]. Nandre, S.J.Shitole S.J and Ahire.R.R. "Scholar research Library Archives of Physics Research"3 (2012)70.

[13]. Jethva.H.O.Dabhi.R.M. And Joshi,M.S.."Journal of Applied Physics."8(2016) 33-42 .

[14]. Dave Mayuri P.Gandhi S.A. and Joshi V. "International Journal of Innovative Research in Science ,Engineering and Technology" .5(2016).

[15]. Sonawane. S.S. Ph.D. Thesis J.J.T.University. Rajasthan.(2017).

[16]. Patil Amit B. And Saraf. K.B. "National Seminar on Advances in Nano-Material and Their Applications"(2013) 91-97.

[17]. Sonawane, S.S. Nandre. S.J. Shitole, S.J. and Ahire. R.R. "National Seminar on Advances in Nano-Material and Their Applications"(2013)78-84.

International e-Conference on Recent Trends in Nano-Materials and Its Applications-2021
In Association with International Journal of Scientific Research in Science and Technology
Volume 9 | Issue 2 | Print ISSN: 2395-6011 | Online ISSN: 2395-602X (www.ijsrst.com)

Synthesis of Silver Nanoparticles Mediated by Dioscorea Bulbifera Tuber Extract for Antibiofilm Inhibition

G. K. Kande, S. I. Khan, A. S. Mandawade, L. D. Sonawane, L. J. Jondhale, P. G. Loke*
Department of Physics and Electronics, Karmveer Shantarambapu Kondaji Wavare, Arts, Science and Commerce College, Uttamnagar, CIDCO, Nashik, Maharashtra, India

ABSTRACT

In present study, we are reported green synthesis of silver nanoparticles (Ag NPs) by using Dioscorea bulbifera tuber extract. X-ray diffraction (XRD) shows that face centered cubic (FCC) crystal structure with average particle size 12nm. UV Vis Spectroscopy reveals strong surface plasmon resonance (SPR) peak at 430 nm which confirms optical property. Fourier Transform Infrared Spectroscopy (FTIR) shows strong peaks of phenolic and flavonoid groups present in the sample.Field Emission Scanning Electron Microscopy (FESEM) along with Energy Dispersive X-Ray Spectroscopy (EDAX) indicates the spherical shape of nanoparticles and presence of Ag element without any impurity. The synthesized Ag NPs are explored of Candida ablicans biofilms it shows maximum inhibition about 25% of biofilm and also it slow down the biofilm formation which may perhaps contribute to various applications in biomedical field.

Keywords : Silver nanoparticles, Dioscorea bulbifera,Green synthesis, Antibiofilm activity, Candida ablicans.

I. INTRODUCTION

In recent years nanomaterials have gained considerable interest owing to their widerange of properties.Green synthesis using plant extracts is an alternativefor hazardous chemicals which is efficient way to prepare nontoxic and ecofriendly metal nanoparticle[1].Many plants which used in recently for synthesis of silver NPs are Cucumis Prophetarum [2],Lysimachia Foenum-Graecum Hance [3], Achillea Millefolium L. [4], Elaeagnus Umbellate Extract (EU) [5], Neem, Onion and Tomato (NOT) [6], Cynara Scolymus (Artichoke) [7], Carica papaya [8], Caesalpinia digyna [9], etc.with applications phytochemistry and therapeutic potential, antimicrobial activities, antidiabetic activity, synergistic potential,phytochemical diversity, neuropharmacological activity, etc.In recent years research work has been doneby using Dioscorea bulbifera plant mediated nanoparticles and its applications such as gold [10], silver [10,11], copper [12], platinum–palladium bimetallic [13] nanoparticles.

Dioscorea bulbifera is special medicinal plant among the 600 species of the family of Dioscorea owing toits specific phytochemistry as well as supporting its general or worldwide application in therapeutics[14].Among various medicinal plants used in Ayurveda, Indian system of traditional medicine, Dioscorea bulbifera(D. bulbifera) is notable due to its multiple therapeutic potential. D. bulbifera is used as a complementary and alternative medicine in the tribal regions of India, Zimbabwe, South Africa and China [2, 21]. D. bulbiferaplant is rich in

polyphenolic compounds, especially flavonoids and catechin, which have distinct uses such as analgesic, anti-inflammatory, anti-hyperglycemic, antitumor activities, antioxidant and anti-diabetic as well asit isused for typical applications to ulcers, abscesses treatment of piles, chronic diarrhea, asthma, dry coughs, frequent or uncontrollable urination, diabetes, emotional instability and cancer.D. bulbifera tuber is having wide range of applications in medicine and traditional therapeutic treatments. Similarly, D. bulbifera plant is delivering medicinal applications such as herbal tonic which stimulates the stomach and spleen and exhibits effect on the lungs and kidneys as well [10, 15-17].

Biofilm serve as hides for disease and are often associated with high level antifungal resistance of the associated organisms.Candida species are among the most common opportunistic pathogens which causes various fungal infections in human. Candida ablicans (C. ablicans) can form a biofilms on different surfaces including blood vessels, catheters, and joint prostheses, stents, shunts, urinary catheters, and orthopedic implants [18]. C. ablicans mediated biofilms are inhibited by various nanoparticles including MgO NPs [18],$ZnFe_2O_4$@AgNWs [19],Ag NPs [20], Gold NPs [21], Se NPs [22], etc.

II. MATERIAL AND METHODS:

Silver nitrate ($AgNO_3$) 50% TECHNICAL grade was obtained from LOBA CHEMIE PVT. LTD. Dioscorea Bulbifera Tuber were collected from Dindori, Nashik, Maharashtra, India. For this synthesis we used double distilled water.

III. PLANT TUBER EXTRACT (DBTE):

Dioscorea Bulbifera Tuber
were collected and washed with double distilled water for several times.This Tuber grinded for fine powder. For 100 ml of water, we take 5gm of Tuber powder and then boiled it for 10min at 100°C. This boiled mixture filtered through Whatman paper no. 1 and placed at 4°C for further use.

Synthesis of Silver Nanoparticles using DBTE:

The synthesis process adapted from ref [10] with slight modifications the synthesis of Ag NPs by addition of 5 ml of DBTE (Dioscorea Bulbifera Tuber Extract) into 95 ml of 1mM $AgNO_3$ solution. The reaction was carried out in absence of light. The mixture was shaken at 40°C and 150rpm for 5 hrs in shaker. The synthesized sample centrifuged for 10 min with 5000 rpm and dried collected NPs. These Silver Nanoparticles used for further characterization.

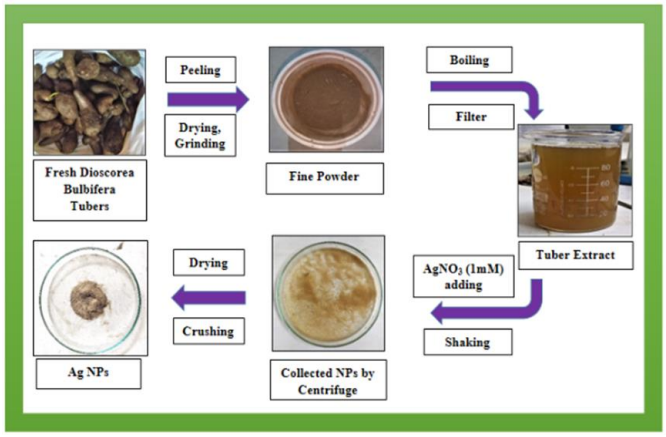

Fig.1: Schematic of DBTE synthesis

Antibiofilm Assay:

The antibiofilm assay protocol with slight modification as reported in [23], typically 100 µL of 10^7 cells/mL of Candida ablicansMTCC 227 in water were added into 96 wellpolystyrene plates and incubated for 3 hours for adherence of cells. The un-adhered cells were gently washedwith phosphate buffer saline (PBS). 100 µL of RoswellPark Memorial Institute (RPMI) medium containing different concentrations (0–100 µg/L) of Ag NPs wereadded to each well, and incubated for 24 hours at37°C. After 24 hours of incubations, the medium supernatant was removed, and the biofilm formed wasgently washed with PBS and further incubated with100 µL of 5 mg/mL MTT (3-(4,5 Dimethylthiazol-2-yl)-2,5-Diphenyltetrazolium Bromide) solution. After 6

hoursof incubations, 100 µL of dimethyl sulfoxide was added into each well and optical density was recorded on540 nm (Multimode Plate Reader, Thermo-Fisher, India).

Material Characterizations:

The X-ray diffraction pattern of as synthesized Ag NPs was recorded in the 2θrange of 10–80°at a scanning rate of 2°/min using Rikagu (Miniflex 600, Japan).The ultraviolet-visible (UV-Vis) spectroscopy study of Ag NPs was carried out by SHIMADZU Spectrophotometer in the range of 200 to 800 nm. The Fourier transform infrared spectrum was recorded by Fourier Transform Infra-red Spectrophotometer (FTIR),SHIMADZU IRAffinity-1. A drop of Ag NPs solution was placed on freshly prepared KBr disc and scanned between 500 - 4000 cm^{-1}. The scanning electronic microscopic images were captured by FESEM (FEI Nova NanoSEM- 450 instrument) with an EDS (Bruker XFlash-6I30). The Raman spectrum was recorded by Raman Spectrometer by RENISHAW Spectroscopy.

IV. RESULTS AND DISCUSSION:

X-ray Diffraction (XRD):

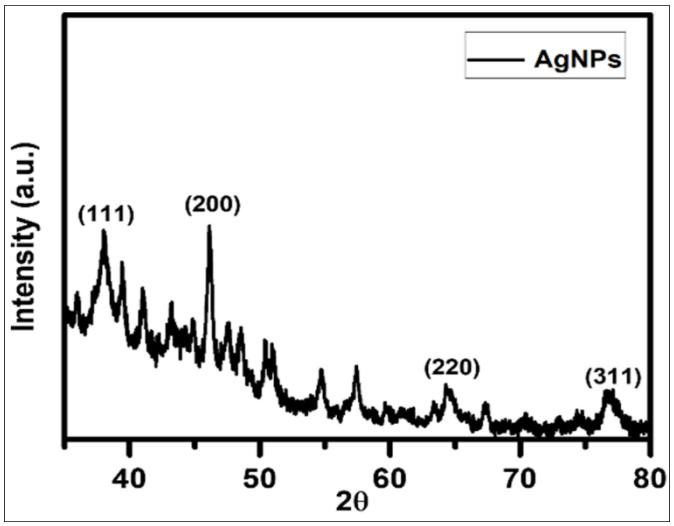

Fig.2: XRD Pattern of Ag NPs.

Figure (2)represents the X-ray diffraction (XRD) pattern of Ag NPs which well matches with the JCPSD (Joint Committee for Powder Diffraction Standard, data card no - 04-0783). The crystal planes (111), (200), (220) and (311) shows cubic crystalline phase with standard lattice constant to be 4.0862Å for Ag NPs and the observed lattice constant was found, (a=b=c)= 3.9314Å for the peak 2θ = 46.14° with corresponding crystal plane (200) [10]. The average particle size of Ag NPs was found 12nm which was calculated by using Debye Scherrer formula.

UV-Vis Diffuse Reflectance Spectroscopy Analysis:

Figure 3 shows UV-Vis spectra of DBTE (red colour) and Ag NPs (black colour) during formation of Ag NPs shows brown colour on incubation of silver nitrate with DBTE.UV-visible spectroscopy confirms the appearance of Ag NPs with strong surface plasmon resonance peak at 430nm[10]. Finally colour changes to dark brown which indicates formation of Ag NPs. DBTE powder do not shows any surface plasmon resonance peak.

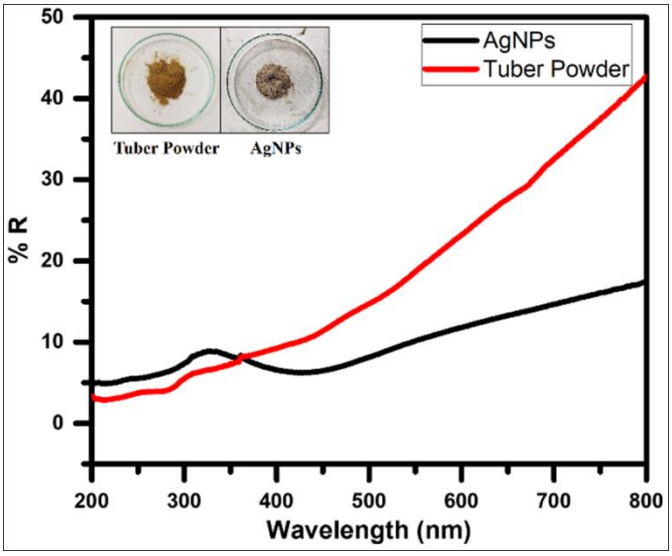

Fig.3: UV DRS of Tuber powder and Ag NPs

Fourier Transform Infra-Red (FT-IR) spectroscopic analysis:

Fourier Transform Infra-Red (FT-IR) spectroscopic analysis was performed to recognize the various functional groups present in the DBTE and Ag NPs as shown in the figure 4 (A) and 4 (B). FTIR spectra of DBTE shows the various key components like flavonoid and phenolic were observed in figure (4 A). The peaks observed at 1639, 1421, 1155, 1082 and 1026 cm^{-1} represents C=C stretch, O-H stretch, C-O

stretch, C-O stretch and C-N stretch. The broad and strong peak was found in DBTE at 3495 cm^{-1}, which is due to hydroxyl (-OH) group of phenols/alcohol.FT-IR spectra of silver nanoparticles (Ag NPs)(Fig: 4B) exhibited prominent peaks at 2926 cm^{-1}, 1649 cm^{-1} and 1442 cm^{-1}. It also shows different stretching vibration of bonds at different peaks; 3417 –O-H Stretch; 2137 cm^{-1} and 2075 cm^{-1} –N=C strong stretch; 1649 cm^{-1} –C=C and 1141 cm^{-1} –C-O strong stretch. Also peaks shows strong stretching of –O=C=O at 2347cm^{-1} and peak 1020 shows medium stretching of amine. The peak at 3417cm^{-1}gives a broad and very strong stretching corresponds to –O-H (Hydroxyl) group. Hence,the addition of silver showsthe band variations and strong stretching vibrations and bending [10].

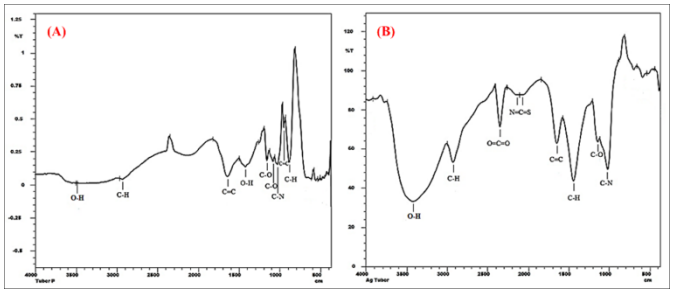

Fig.4: (A) FT-IR Spectra of Tuber powder and (B) FT-IR Spectra of Ag NPs.

Field Emission Scanning Electron Microscopy (FESEM):

The Field Emission Scanning Electron Microscopy (FESEM) gives information about the surface morphology. In figure 5 (A) shows various FESEM images at different resolution and magnification which shows the spherical shape of Ag NPs.Energy dispersive X-ray analysis (EDAX) as shown in the figure 5 (B) confirms presence of Ag without any impurity from figure 5 (C) shows the elemental mapping of Ag NPs with marked as green colour.

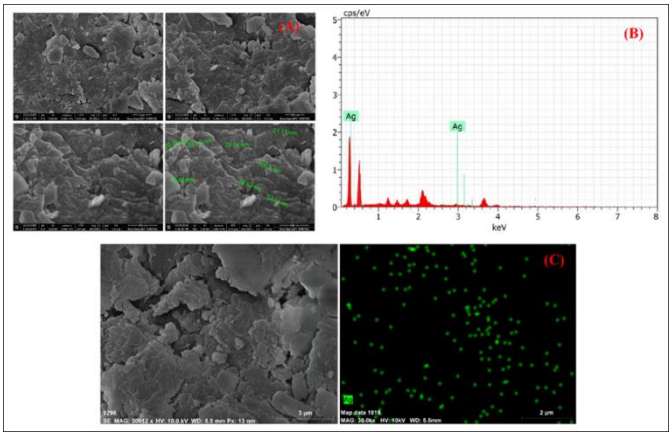

Fig.5: (A) FESEM of Ag NPs, (B) EDAX Pattern of Ag NPs and (C) EDAX Mapping of Ag NPs.

Raman Spectroscopy Analysis:

Figure 6 shows Raman spectrum of Ag NPs, the possible functional groups of biological capping molecules associated with stabilization of Ag NPs. The spectrum shows a strong and sharp peak at 239 cm^{-1}, which can be ascribed to the stretching vibrations of Ag–N and Ag–O bonds [24]. The very small vibrations of peak at 1366 and 1510 cm^{-1}respectively corresponding to symmetric and asymmetric C=O stretching vibrations of carboxylate group.

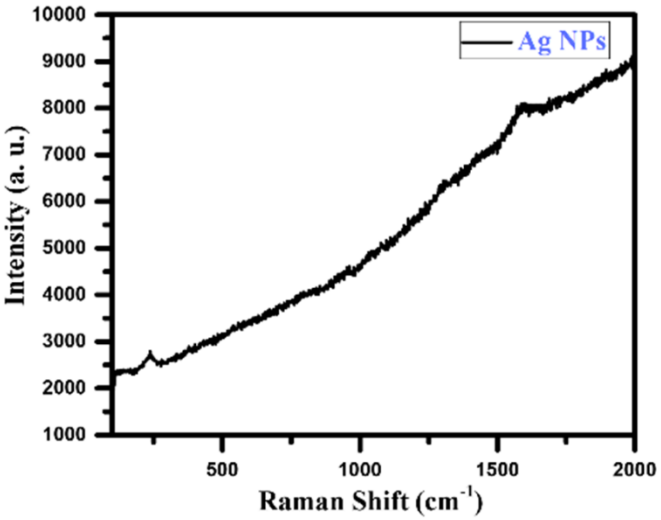

Fig.6: Raman Pattern of Ag NPs.

Antibiofilm Activity:

Figure 7(A) shows the Candida ablicans(C. ablicans)biofilm life cycle with various stages such as first stage with adherence of round yeast cells to a different surface,second stage with initiation of

biofilm formation in which cells are multiplied to form a basal layer of adhered cells,third stage including maturation of the biofilm and development of complex layers of polymorphic cells and forms extracellular matrix, in the last stage that is fourth stage where round yeast cells leave the mature biofilm to seed new sites to form dispersion [26].

The synthesized Ag NPs are explored forC. ablicans biofilms. Ag NPs shows inhibition in Fig.:7 (B),20 × 10^5cells/mL were added 15.6 µg/mL to each well of the 96-well polystyrene plates. Similarly, 25× 10^5cells/mL were added 62.5 µg/mL to each well of the 96-well polystyrene plates.It shows maximum inhibition about 25% of biofilm and also it slow down the biofilm formation which may perhaps contribute to various applications in biomedical field [25].

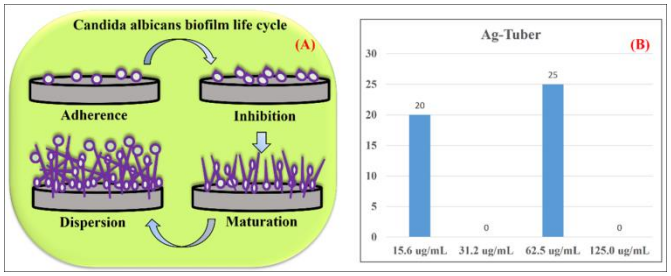

Fig.7:(A)C. ablicans biofilm life cycle,(B) Observed inhibition of Ag NPs.

V. CONCLUSION

In summary, plant mediated synthesis of nanoparticles have several advantages including facile, ecofriendly, nontoxic, cost-effective, biocompatible and so on. Ag NPs synthesized by green approach by using DBTE.X-ray diffraction (XRD) shows that face centered cubic (FCC) crystal structure with average particle size 12nm. UV Vis spectroscopy reveals strong surface plasmon resonance (SPR) peak at 430 nm which confirms optical property.Fourier Transform Infrared Spectroscopy (FTIR) shows strong peaks of phenolic and flavonoid groups present in the sample.Field Emission Scanning Electron Microscopy (FESEM) along with Energy Dispersive X-Ray Spectroscopy (EDAX) indicates the spherical shape nanoparticles and presence of Ag element without any impurity.From the Raman Spectra it was seen that the peak was observed at 239 cm-1 and after that the spectra goes on increasing. The synthesized sample explored of Candida ablicans biofilms, it shows maximum inhibition about 25% of biofilm.Ag NPs synthesized by using D. bulbifera plant tuber extract can be explored for various biomedical applications such as analgesic, anti-inflammatory, anti-hyperglycemic, antitumor activities and anti-diabetic etc.

Acknowledgements:

Authors would like thanks to the Principal Dr. J. D. Sonkhaskar and Head of the Department, Dr. P. G. Loke, Department of Physics and Electronics, KSKW Arts, Science and Commerce College, Uttamnagar, CIDCO, Nashik-422008, for providing laboratory and instrumentation facility.

VI. REFERENCES

[1]. T.Sinha, M. Ahmaruzzaman, P. Adhikari, R. Bora, (2017), "Green and Environmentally sustainable Fabrication of Ag-SnO2 nanocompostites and its multifunctional Efficacy As photocatalyst and Antibacterial and Antioxidant Agent," ACS sustainable Chem. Eng., 5, 4645-4655.

[2]. Hemlata, P.R. Meena, A.P. Singh, K.K. Tejavath, (2020), "Biosynthesis of Silver Nanoparticles Using Cucumis prophetarum Aqueous Leaf Extract and Their Antibacterial and Antiproliferative Activity against Cancer Cell Lines," ACS Omega,5, 10, 5520–5528.

[3]. Widsanusan Chartarrayawadee, Phattaraporn Charoensin, Juthaporn Saenma, Thearum Rin, et al. (2020), "Green synthesis and stabilization of silver nanoparticles using Lysimachia foenum-graecum Hance extract and their antibacterial activity," Green Process Synth 9: 107–118.

[4]. Huma Y., Ansar M., Khawaja Shafique A., M. Raffi, (2020), "Green synthesis of silver nanoparticles and their applications as an alternative antibacterial and antioxidant agents," Materials Science & Engineering C, 112,110901.

[5]. S. Ali, S. Perveen, M. Ali, et al., 2019,"Bioinspired morphology controlled silver nanoparticles for antimicrobial application,"Materials Science &Engineering C,108, 110421,2019.

[6]. K. Chand, M. Ishaque Abro, U. Aftab, A. Hussain Shah, et al. (2019), "Green synthesis characterization and antimicrobial activity against Staphylococcus aureus of silver nanoparticles using extracts of neem, onion and tomato," RSC Adv., 9, 17002.

[7]. Erdogan O, Abbak M, Demirbolat GM, Birtekocak F, Aksel M, Pasa S, et al. (2019), "Green synthesis of silver nanoparticles via Cynarascolymus leaf extracts: The characterization, anticancer potential with photodynamic therapy in MCF7 cells," PLoS ONE 14(6): e0216496.

[8]. S Renganathan et al., (2019), "Silver nanoparticle synthesis from carica papaya and virtual screening for anti-dengue activity using molecular docking,"Mater. Res. Express 6, 03, 5028.

[9]. M. S. Niloy, Md. M. Hossain, M. Takikawa, Md. S. Shakil, et al. (2020), "Synthesis of Biogenic Silver Nanoparticles Using Caesalpinia digyna and Investigation of Their Antimicrobial Activity and In Vivo Biocompatibility," ACS Appl. Bio Mater., 3, 11, 7722–7733.

[10]. S. Ghosh, S. Gaurav, A. Harke, M. Chacko and K. Joshi, et.al. (2016), "Dioscorea Oppositifodia Mediated Synthesis of Gold and Silver Nanoparticles with Catalytic Activity," J Nanomed & Nanotechnol, Volume 7:398, 2157-7439.

[11]. R. Uma Maheswari, A. Lakshmi Prabha, (2016), "Antibacterial Activity of Silver Nanoparticles Developed using nvitro Leaf Extracts of Dioscorea oppositifolia L," International Journal of Current Microbiology and Applied Sciences, Special Issue-3, pp. 75-81.

[12]. Ghosh S, More P, Nitnavare R, Jagtap S, Chippalkatti R, et.al. (2015), "Antidiabetic and Antioxidant Properties of Copper Nanoparticles Synthesized by Medicinal Plant Dioscorea bulbifera." J Nanomed Nanotechnol, S6: 007.

[13]. S. Ghosh, R. Nitnavare, A. Dewle, G. B Tomar, et.al. (2015), "Novel platinum–palladium bimetallic nanoparticles synthesized by Dioscorea bulbifera: anticancer and antioxidant activities," International Journal of Nanomedicine, 10, 7477–7490.

[14]. Ghosh S, Parihar VS, More P, Dhavale DD, Chopade BA (2015), "Phytochemistry and Therapeutic Potential of Medicinal Plant: Dioscorea bulbifera," Med chem 5: 160-172.

[15]. Poornima GN, Ravishankar RV (2007), "In vitro propagation of wild yams Dioscorea oppositifolia (Linn) and Dioscorea pentaphylla (Linn)," African Journal of Biotechnology 6: 2348-2352.

[16]. Ghosh S, Derle A, Ahire M, More P, Jagtap S, et.al. (2013), "Phytochemical analysis and free radical scavenging activity of medicinal plants Gnidiaglauca and Dioscorea bulbifera," Plos one 8: 12: e82529, 2013.

[17]. Sautour M, Mitaine-Offer AC, Lacaille-Dubois MA (2007), "The Dioscorea genus: a review of bioactive steroid saponins"J Nat Med.; 61(2); 91–101, 2007.

[18]. F. Kong, J. Wang, R. Han, S. Ji, et al. 2019, "Antifungal Activity of Magnesium Oxide Nanoparticles: Effect on the Growth and Key Virulence Factors of Candida ablicans,"Mycopathologia, 185(3):485-494.

[19]. D. Thakur, S. Govindaraju, KyuSik Yun, Jin-Seo Noh, (2019), "The Synergistic E_ect of Zinc Ferrite Nanoparticles Uniformly Deposited on Silver Nanowires for the Biofilm Inhibition of Candida ablicans," Nanomaterials, 9, 1431.

[20]. S. D. Halbandge, A. K. Jadhav, P. M. Jangid, A. V. Shelar, (2019), "Molecular targets of biofabricated silver nanoparticles in Candida ablicans," The Journal of Antibiotics, volume 72, pages 640–644.

[21]. S. Khan, F. Alam, A. Azam, A. U. Khan, (2012), "Gold nanoparticles enhance methylene blue–induced photodynamic therapy: a novel therapeutic approach to inhibit Candida ablicansbiofilm," International Journal of Nanomedicine,7, 3245–3257.

[22]. G. Guisbiers, H. H. Lara, R. Mendoza-Cruz, G. Naranjo, et al. 2017, "Inhibition of Candida ablicansbiofilm by pure selenium nanoparticles synthesized by pulsed laser ablation in liquids," Nanomedicine; 13(3): 1095–1103.

[23]. A. F. Shaikh, M. S. Tamboli, R. H. Patil, A. Bhan, 2019, "Bioinspired Carbon Quantum Dots: An Antibiofilm Agents," Journal of Nanoscience and Nanotechnology, Vol. 19, 2339–2345.

[24]. A. J. Kora1, S. R. Beedu, A. Jayaraman, 2012, "Size-controlled green synthesis of silver nanoparticles mediated by gum ghatti (Anogeissus latifolia) and its biological activity," Organic and Medicinal Chemistry Letters, 2:17.

[25]. Humberto H. Lara, Dulce G. Romero-Urbina, Christopher Pierce, Jose L. Lopez Ribot, et al., (2015), "Effect of silver nanoparticles on Candida ablicansbiofilms: an ultrastructural study," Lara et al. J Nanobiotechnol,13:91.

[26]. M. Gulati, C.J. Nobile, 2016, "Candida ablicansbiofilms: development, regulation, and molecular mechanisms," Microbes and Infection (2016), Volume 18, 5, 310-321.

International e-Conference on Recent Trends in Nano-Materials and Its Applications-2021
In Association with International Journal of Scientific Research in Science and Technology
Volume 9 | Issue 2 | Print ISSN: 2395-6011 | Online ISSN: 2395-602X (www.ijsrst.com)

Electrochemical Polymerization of Polypyrrole Thin Film by Potentiostatic Mode

J. V. Thombare[1]*, R. S. Gaikwad[1], P. M. Kharade[2], S. D. Patil[3], V. S. Shinde[4], S. S. Dhasade[1]

[1]Vidnyan Mahavidyalaya, Sangola, Tal-Sangola, Dist-Solapur, Maharashtra-413307, India
[2]Shankarrao Mohite Mahavidyalaya, Akluj, Dist-Solapur, Maharashtra, India
[3]Pratapsinh Mohite Mahavidyalaya, Karmala, Dist-Solapur, Maharashtra, India
[4]Baburao Patil College of Arts and Science, Anagar, Tal-Mohol, Dist-Solapur, Maharashtra, India

ABSTRACT

Polypyrrole thin films are prepared by electrodeposition. Here we have studied the film formation mechanism of polypyrrole thin films. The electrochemical oxidation of pyrrole makes a radical cation and di-cation. Initially, the concentration of radical cations is much higher than that of the neutral monomers which are near the electrodes, where, reactions are occurring and hence because of coupling di-cation forms. After losing two protons from di-cation again a neutral dimer is formed, which is then oxidized to radical cations, and so polymerization goes on. Polymerization and chain termination takes place in the gestation period.

Keywords : Electrodeposition, Potentiostatic Mode, Thin Films, Polypyrrole, etc.

I. INTRODUCTION

Electrochemical polymerization is the most widely used method in polypyrrole studies, offers many advantages [1-10]: it enables to produce an easily prepared polypyrrole with high conductivity, and in situ coating of polypyrrole on rather complex geometries. Electrochemical polymerization does not necessitate annealing at high temperature; therefore, it can be employed in flexible the devices such as dye sensitized solar cells (DSCs) [1], supercapacitors, etc. Polypyrrole films have been easily prepared either chemically or electrochemically. Polypyrrole is amorphous and conducting type conjugated polymer. Basically, polypyrrole has been made conductive by oxidation of the monomer i.e. pyrrole and conjugation have made with the anion. Due to conjugation with anion, the band gap energy of polypyrrole greatly reduced. Such conjugation with anion is called doping of polypyrrole by anion [11-12]. Polypyrrole has lots of distinct features related to electrical conductivity, electroactivity and high environmental stability, so it attracts widespread research interests [13].

Conducting polypyrrole shall be prepared electrochemically, by applying a potential across a solution containing the pyrrole to be polymerized and an electrolyte (supporting electrolyte), or chemically; using oxidants or cross-coupling catalysts. One of the advantages of electrochemical polymerization is that, the yielded polypyrrole electrodeposited in the form of film on the anode. However, anodic

electropolymerization has a serious shortcoming; the electro-generated polypyrrole presents structural irregularities due to polymer cross-linking [14]. Conducting polypyrrole is a promising electrode material for redox capacitors as, it is less expensive than other electrode materials, e.g., noble metal oxides [15].

This chapter deals with synthesis and characterization of polypyrrole films by potentiostatic mode of electrodeposition. The variation of current with voltage is studied with the help of linear sweep voltammetry and the deposition potential i.e. oxidation potential of polypyrrole is determined and polypyrrole films were deposited accordingly.

II. EXPERIMENTAL PROCESSES (POLYPYRROLE FILM FORMATION):

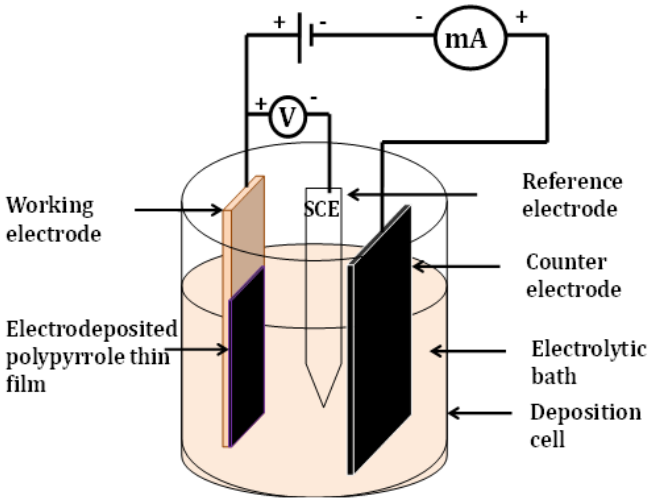

Fig. 1: Electrodeposition set up for synthesis of polypyrrole films

The room temperature deposition keeps away from the oxidation and corrosion of metallic substrates. Preparative parameters such as deposition potential, deposition time and concentration of the precursor optimized. In the typical synthesis, (0.1 M) pyrrole and (0.5 M) sulphuric acid are used as the monomer and electrolyte, respectively. Polypyrrole films were prepared on stainless steel substrates, at deposition potential of + 0.7 V vs SCE. The polypyrrole film was deposited on anode (stainless steel) and a pure graphite plate having nearly equal to area 4 cm^2 (Size:1 cm X 4 cm) of working electrode was used as a cathode, a saturated calomel electrode (SCE) was used as the reference electrode. A black colored polypyrrole film was obtained on the substrate as shown in Fig.1.

2.1. Substrate cleaning

Substrate cleaning is the breaking of the bonds between substrate and contaminants without detrimental the substrates. In thin film deposition process, substrate cleaning is an essential factor to get reproducible films as it affects the adherence, uniformity, smoothness and porosity of the films. The substrate cleaning process depends upon the nature of the substrate; degree of cleanliness required and nature of contaminates to be disinterested. The common contaminates are grease, oil particles, air borne dust, lint, adsorbed water etc. The stainless steel has been used as substrates. The following process has been assumed for cleaning the substrates.

1. The substrates were washed with detergent solution 'Molyclean' and then with water.
2. These substrates were boiled in chromic acid for about five minutes and then rinsed with distilled water.
3. These substrates were kept in NaOH solution to remove the acidic contaminations, washed with distilled water and cleaned ultrasonically.
4. Finally, the substrates were air dried.

III. RESULTS AND DISCUSSION

3.1 Mechanism of the Polymerization

In an electrochemical polymerization of pyrrole, the monomer pyrrole was dissolved in a solvent containing the anionic doping species such as H_2SO_4 (in present case), is oxidized at the surface of an electrode by application of an anodic potential (oxidation). The choice of the solvent and electrolyte is of particular importance in electrochemistry. Since, both solvent and electrolyte should be stable at the

oxidation potential of the monomer and provide an ionically conductive medium. Since pyrrole has a relatively low oxidation potential [16], electropolymerization shall be carried out in aqueous electrolytes.

As a result of the initial oxidation, the radical cation of the pyrrole is formed and reacts with other monomers present in solution to form oligomeric products and then the polymer. The extended conjugation in the polymer results in a lowering of the oxidation potential compared to the monomer. Therefore, the synthesis and doping of the polymer are generally done simultaneously. The anion is incorporated into the polymer to ensure the electrical neutrality of the film and at the end of the reaction, a polymeric film of controllable thickness is formed at the anode. The anode can be made of a variety of materials including platinum, gold, glassy carbon, stainless steel and tin doped indium oxide (ITO) coated glass. In the present work, we used the 304 stainless steel substrate as working electrode for deposition of polypyrrole thin film.

The electropolymerization is achieved by potentiostatic deposition mode corresponding to a constant potential applied at the surface of the electrode. The polymerization mechanism between chemical and electrochemical polymerization is different, only initial step is same i.e. generation of radical cations, which is shown in Fig.2. In this case, the concentration of radical cations is much higher than that of the neutral monomers which are near the electrodes, where, reactions are occurring and radical-radical coupling forms di-cation. Then di-cation loses two protons, generating a neutral dimer, which is then oxidized to radical cations, and so polymerization goes on. These radical cations, dimmers and trimmers are formed in the small "gestation period", before the polymerization [17].

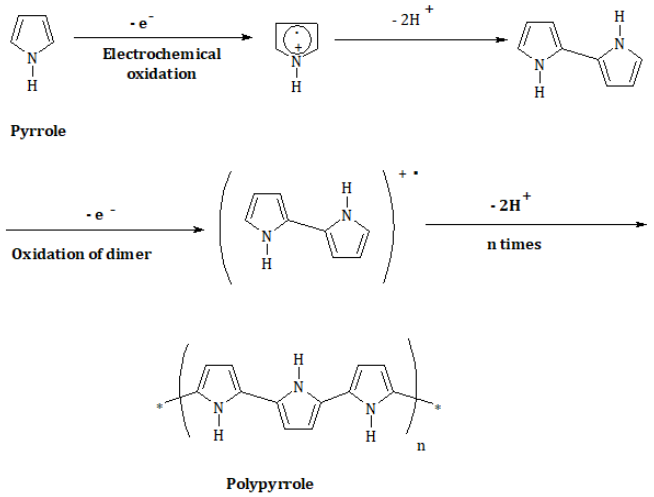

Fig.2: Polymerization mechanism of electrochemically synthesized polypyrrole films

IV. CONCLUSION

As per study, the electrodeposition of polypyrrole thin films at room temperature is easy process also there is no need of any sophisticated instruments. Also, with the help of electrodeposition we can control the film properties such as thickness, electrical conductivity etc. From electrochemical polymerization study we understand the formation of pyrrole ions, dimmers and so on i.e. formation of polymer chain.

V. REFERENCES

[1]. T. Makris, V. Dracopoulos, T. Stergiopoulos, P. Lianos, Electrochimica Acta, 56 (2011) 2004

[2]. R. Ramola, S. Chandra, J. Rana, R. Sonkawade, P. Kulriya, F. Singh, D. Avasthi, S. Annapoorni, Journal of Physics D: Applied Physics, 41 (2008) 115411

[3]. A. Ramanaviciene, W. Schuhmann, A. Ramanavicius, Colloids and Surfaces B: Biointerfaces 48 (2006) 159

[4]. Y. Cho, R. Borgens, Langmuir, 27 (2011) 6316

[5]. J. Lee, F. Serna, C. Schmidt, Langmuir 22 (2006) 9816

[6]. H. Bai, Q. Chen, C. Li, C. Lu, G. Shi, Polymer, 48 (2007) 4015

[7]. V. Misoska, J. Ding, J. Davey, W. Price, S. Ralph, G. Wallace, Polymer, 42 (2001) 8571 [8] A. Hussain, D. Saikia, F. Singh, D. Avasthi, A. Kumar, Nuclear Instruments and Methods in Physics Research B, 240 (2005) 834

[8]. I. Vermeir, N. Kim, P. Laibinis, Applied Physics Letters, 74 (1999) 3860

[9]. P. Somani, S. Radhakrishnan, Chemical Physics Letters, 292 (1998) 218

[10]. R. J. Waltman, J. Bargon, Candian Journal of Chemistry, 64 (1986) 76

[11]. N. K. Guimard, N. Gomez, C. E. Schmidt, Progress in Polymer Science, 32 (2007) 876 [13] Y. Lan, E. Wang, Y. Song, Y. Song, Z. Kang, L. Xu, Z. Li, Polymer, 47 (2006) 1480 [14] C. Aleman, J. Casanovas, J. Torras, O. Bertran, E. Armelin, R. Oliver, F. Estrany, Polymer, 49 (2008) 1066

[12]. A. Hussain, A. Kumar, Journal of Power Sources, 161 (2006) 1486

[13]. S. Sadki, P. Schottland, N. Brodiec, G. Sabouraud, Chemical Society Reviews, 29 (2000) 283

[14]. P. Chandrasekhar, Conducting polymers, Fundamentals and applications: a practical approach, Technology and Enginnering, Springer, 1999.

International e-Conference on Recent Trends in Nano-Materials and Its Applications-2021
In Association with International Journal of Scientific Research in Science and Technology
Volume 9 | Issue 2 | Print ISSN: 2395-6011 | Online ISSN: 2395-602X (www.ijsrst.com)

Conductivity Enhancement from $Li_{0.05}Zn_{0.95}O$ Nanostructures

L. M. Mahajan[1], S. C. Kulkarni[2], A. H. Bendale[3]

[1]Department of Electronics, K V N Naik Arts, Commerce and Science College, Nashik, Maharashtra, India
[2]Department of Electronic-Science, M.S.G. College, Malegaon-camp, Malegaon, Maharashtra, India
[3]K. K. Wagh Arts, Commerce Science and Computer Science College, Nashik, Maharashtra, India

ABSTRACT

Conductivity enhancement has been observed from ternary alloy compound of Li0.05Zn0.95O nanostructures. The influence of Lithium doping on electrical properties of sol-gel derived zinc oxide nanostructures was studied. Li0.05Zn0.95O Nanostructures were characterized. The XRD measurement exhibits single phase wurtzite structure along the (002) plane. The average particle size of pure ZnO and Li0.05Zn0.95O was found to be 36 nm and 30 nm respectively. Incorporation of Lithium, influenced the particle size. FESEM reveals the uniform rope type structure. The current-voltage characteristics obtained from semiconductor characterization system reveals that resistance of the nanostructures was found to be decreased with doping of Lithium. These results explore the applicability of Li0.05Zn0.95O nanostructures as a conducting oxide in electronic devices.

Keywords: Nanostructures; Li0.05Zn0.95O; sol-gel; XRD measurement.

I. INTRODUCTION

ZnO nanostructures have attracted much interest of researchers due to its useful structural and electrical properties. ZnO as a wide band gap material found to be promising candidate in many electronics applications such as thin film transistors [1], photo detectors [2] and light emitting devices [3]. These ZnO nanostructures can be fabricated by various kinds of fabrication methods, such as chemical bath deposition [4], spray pyrolysis [5], pulsed laser deposition [6], sol-gel process [7]etc. While the sol-gels based deposition of nanostructures offers reduction in the cost of fabrication and excellent compositional control [8].

In the present study, sol-gel deposition process is used for fabrication of nanostructures According to recent literature, by using sol-gel spin coating method Li doped ZnO nano structures were deposited on different types of substrate such as glass[9] and silicon[10]. The change in property of ZnO had been observed with doping. Present study reveals that the doping of Li changes grain size and conductivity.

II. EXPERIMENTAL

ZnO and $Li_{0.05}Zn_{0.95}O$ nano structures were deposited using sol-gel spin coating method. Zinc acetate dihydrate, methoxy ethanol, Lithium acetate, were used as a starting precursor. Solution was prepared for

0.4 moles of 5 at% Lithium. The solution was stirred on hot magnetic plate 50 minutes. After cooling of solution, it was used for spin coating deposition. With constant speed of rotation films were coated. The films were coated repeatedly get desired thickness. Pre and post heating treatment are given to samples after each coating and cooled down at room temperature. Samples were characterized for structural and electrical properties.

III. RESULTS AND DISCUSSION:

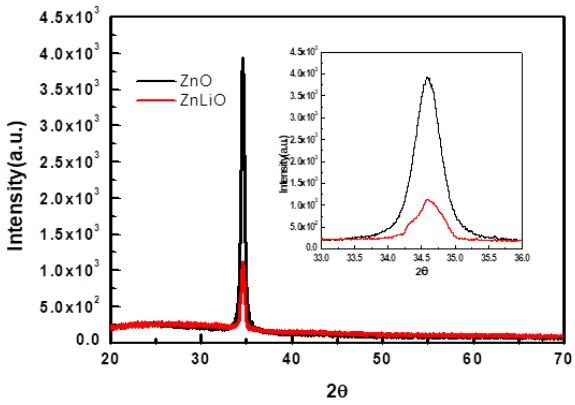

Fig. 1 XRD pattern of ZnO and $Li_{0.05}Zn_{0.95}O$ nanostructures. (Inset: Intensity of peak)

To investigate the crystal structure of deposited ZnO and $Li_{0.05}Zn_{0.95}O$ nano structures were characterized using X-ray diffractometer. Fig. 1 shows the XRD plot of ZnO and$Li_{0.05}Zn_{0.95}O$ nanostructures. Analysis clearly indicates single dominant peak corresponding to (002) plane at the 2Θ value of 34.58º. The doping of Lithium does not deteriorate the crystal structure. The average crystalline size of ZnO and $Li_{0.05}Zn_{0.95}O$ nanostructures has been estimated from Debye Scherrer equation[11].

$$D = \frac{0.9\lambda}{\beta\cos\theta} \qquad (1)$$

Where, D is the average crystalline size of the film. λ is the wave length of X-ray source(1.54059 Å), θ is the Bragg diffraction angle and β is the full width at half maximum intensity (FWHM)in radians. Average crystalline size estimated from XRD pattern and found to be 36.30 nm and 30.26 nm for ZnO and $Li_{0.05}Zn_{0.95}O$ nano structures respectively. Crystalline size decreased by Li doping. The diffraction angle of peak (002) is 34.58º and 34.59º for ZnO and $Li_{0.05}Zn_{0.95}O$ nanostructures respectively. Inset of fig. 1 shows the decrease in intensity with Li doping. The structural parameters of ZnO and $Li_{0.05}Zn_{0.95}O$ nanostructures were summarized in the table 1.

	Compound	2 θ (º)	FWHM (°)	Max. Intensity	Grain size D(nm)
Deposited samples	ZnO	34.58	0.23	3946.31	36.30
	Li0.05Zn0.95O	34.59	0.275	1150.46	30.26

Table 1: Structural parameters of ZnO and $Li_{0.05}Zn_{0.95}O$ nanostructures

Fig. 2 presents the FESEM images of ZnO and $Li_{0.05}Zn_{0.95}O$ nanostructures. Images of the films were taken at the scale of 10μm with magnification of 5,000 for ZnO and $Li_{0.05}Zn_{0.95}O$ nanostructures. Uniform rope type structure is retained for both the films with change in crystal size. The $Li_{0.05}Zn_{0.95}O$ nanostructures show denser morphology without visible voids and defects overall the surface.

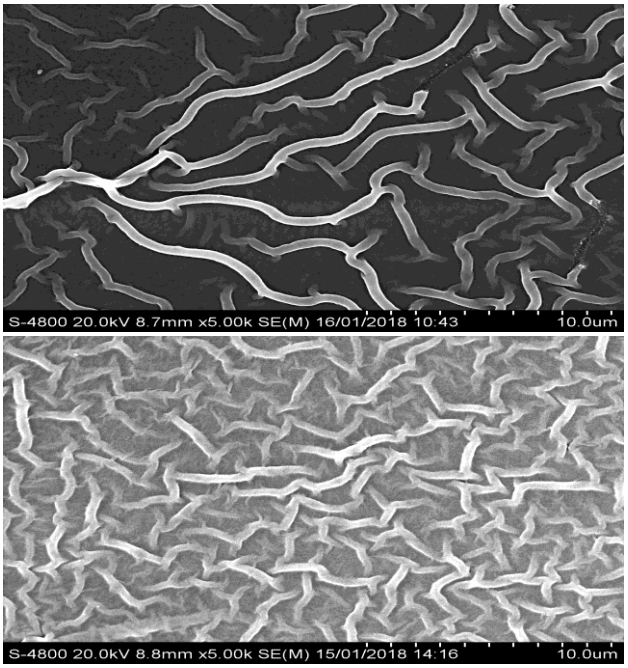

Fig.2 FESEM images of ZnO and $Li_{0.05}Zn_{0.95}O$ nanostructures.

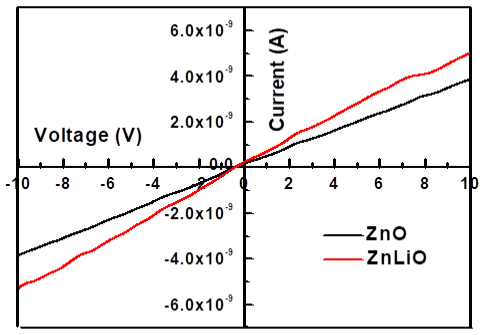

Fig. 4 I-V characteristics of ZnO and $Li_{0.05}Zn_{0.95}O$ nanostructures.

The electrical behavior of ZnO and $Li_{0.05}Zn_{0.95}O$ nanostructures was investigated by (I-V) Keithley instrument, which is realized in fig. 4. The characteristics were investigated for voltage between -10 V and 10 V. It was found to exhibit ohmic nature. The linear, ohmic nature showed the good quality of deposited $Li_{0.05}Zn_{0.95}O$ nanostructures. The doping of Lithium was an important factor to influence the current density with respect to bias voltage. The decrease in average resistance is observed with $Li_{0.05}Zn_{0.95}O$ nanostructures. The results revealed that conductivity of $Li_{0.05}Zn_{0.95}O$ nanostructures is higher than ZnO nanostructures due to decreasing grain size and increasing number of grain boundaries.

IV. CONCLUSION

In summary, the ZnO and Li0.05Zn0.95O nanostructures were synthesized by simple and inexpensive sol-gel spin coating technique on glass substrate. The XRD spectra reveals the crystalline quality ofLi0.05Zn0.95O nanostructures without any degradation of the wurtzite structure of the zinc oxide. The size of grains was found to decrease with Li incorporation in the ZnO nanostructures. The incorporation of Li in ZnO and decrease in size was confirmed through FESEM, which reflects uniform rope type structure. I-V characteristics analysis reveals increase in currant with doping of Lithium in ZnO nanostructures. The analysis and investigation lead successful incorporation of Li dopant in ZnO for conducting oxide in electronic devices.

V. REFERENCES

[1]. Shih CC, Lee WY, Chiu YC, Hsu HW, Chang HC, Liu CL, Chen WC (2016) Science report 6:20129

[2]. Gong M, Liu Q, Cook B, Kattel B, Wang T, Chan WL, Ewing D, Casper M, Stramel A, Wu JZ (2017) ACS Nano 11:4114-4123.

[3]. Lee H, Park I,KwakJ,Yoon DY, Lee C(2010) Applied physics letters 96:153306.

[4]. Al-Asadi AS, Henley LA, Ghosh S, Quetz A, Dubenko I, Pradhan N (2016) J. Appl. Phys. 119:084306- 084313.

[5]. Mani GK, Rayappan JBB (2014) Sensors and actuators B 198:125-133.

[6]. Guill GG, Palma MIM, Krishnan B, Avellaneda D, Castillo GA, DasRoy TK, Shaji S (2015) Materials chemistry and physics 162:561-570

[7]. Kasar CK, Sonawane US, Patil DS (2014) Applied Mechanics and Materials Vol. 481:45-48.

[8]. Boyraz C, Yesibas B, Arda L (2017) J Supercond Nov Magn, 30:1691-1698.

[9]. Meziane K, Elhichou A, Elhamidi A, Almaggoussi A, Chhiba M (2016) Journal of physics: conference series 758, 012019

[10]. Hsu HP, Lin DY, Lu CY, Ko TS, Chen HZ (2018) Crystals 8, 228.

[11]. Bindu P, Thomas S (2014) J.Theor Appl Phys 8:123-134.

International e-Conference on Recent Trends in Nano-Materials and Its Applications-2021
In Association with International Journal of Scientific Research in Science and Technology
Volume 9 | Issue 2 | Print ISSN: 2395-6011 | Online ISSN: 2395-602X (www.ijsrst.com)

Saccharum Officinarum Stem Extract Mediated Synthesis of Silver Nanoparticles: Green Approach

L. J. Jondhale, G. K. Kande, S. I. Khan, A. S. Mandawade, L. S. Sonawane, P. G. Loke*
Department of Physics and Electronics, Karmveer Shantarambapu Kondaji Wavare, Arts, Science & Commerce College, Uttamnagar, CIDCO, Nashik-422008, Maharashtra, India

ABSTRACT

Herein, we have studied fabrication of silver nanoparticles (Ag NPs) by using sugarcane or Saccharum Officinarum juice as green approach. Primary Ag NPs formation confirmed by using visual observations as a colour change from light yellow to dark brown also which further confirmed by UV-Vis spectroscopy shows strong absorption spectra with surface plasmon resonance (SPR) peak at 440 nm. X-ray diffraction (XRD) reveals that face centred cubic (FCC) crystal structure with the characteristic diffraction peaks at (111), (200), (220) and (311) and average nanoparticle size 18 nm. Fourier Transform Infrared Spectroscopy (FTIR) studies attributed that the hydrogen bonded O–H stretching vibration of phenol overlay on N–H stretching, C=O stretching owing to bio molecules which contain -COO groups. Field Emission Scanning Electron Microscopy (FESEM) along with Energy Dispersive X-Ray Spectroscopy (EDAX) specify that the spherical shape of synthesized Ag NPs as well as the spectra clearly shows strong signal peak at 2.8 keV corresponds to presence Ag element without any impurity. Raman Spectrum of the Ag NPs Peak shows strong and sharp band at 240cm^{-1} and stretching vibration of Ag-N and Ag-O bonds.

Keywords: Silver Nanoparticle, Saccharum Officinarum, Surface Plasmon Resonance, Green Synthesis And Raman Spectrum.

I. INTRODUCTION

In recent years, nanotechnology research is emerging as cutting-edge technology interdisciplinary with physics, chemistry, biology, material science and medicine. Biological or green synthesis methods are considered as safe, cost-effective, sustainable and environment friendly, facile and non-toxic [1-3]. Currently, researchers are focusing on the biological or green synthesis of nanoparticles by using microorganisms and plant extracts. Green synthesis of Ag NPs have been performed by using a variety of ways such as plant extract, microbial, cell biomass or cell free growth medium and biopolymers [4]. From last few years the great attention gained towards the plant extracts mediated green synthesis by using different plants such as Boerhaaviadiffusa [5], Tinosporacordifolia [6], Aloevera [7],Catharanthusroseus [8], Ocimumtenuiflorum [9], Azadirachta indica [10], Emblicaofficinalis [11], Cocosnucifera [12], Terminalia chebula[13] and Black Pepper[14].

The Saccharum Officinarum (S. Officinarum) or sugarcane is a well-known plant for sugar that is

sucrose which is a daily need recipe. Sugarcane have different applications which includes the bio-fuels, food products and carbon production. Owing to its richness, low cost, bio-degradable and recycling ability, S. Officinarum has been used for mass production of carbon based materials for natural precursor [15]. Sugarcane (S. Officinarum) extract mediated green synthesis of various nanostructures are reported as Ag-SnO_2[16], Ag [17-19], Au, Pt, Pd [20],carbon quantum dots (CQDs) [21], ZnO [22] and Si [23]. Various nanoparticles synthesized by using different components of sugarcane are used for wide range of applications such as photocatalytic activity [16], antioxidant activity, antibacterial activity [17], and biofilm formation [18].Green approach synthesized Ag NPs have been used for sensors for disease diagnosis [4],H_2O_2 sensor [24], heavy metal ion sensors [25] drugs delivery [26],radiation therapy [27] and ESR dosimetry [28].

II. MATERIALS AND METHODS:

Silver nitrate ($AgNO_3$) 50% TECHNICAL grade was obtained from LOBA CHEMIE PVT. LTD. Sugarcane or Saccharum Officinarum was collected by nearby market from Nashik, Maharashtra, India. For the complete synthesis double distilled water was used.

Synthesis of Silver Nanoparticles using Saccharum Officinarum:

The synthesis procedure of Ag NPs by using Sugarcane or Saccharum Officinarum(S. Officinarum) is adapted from [16] with little modifications. Fresh S. Officinarum juice was collected and filtered using Whatmanfilter paper no. 41. For synthesis addition of 25 ml of S. Officinarum Stem Extract into 150 ml of 0.01 M $AgNO_3$ solution. The solutions were maintained at pH 10 for further reaction. The mixture was refluxed with constant heating and stirring at 100 ^oC for 4 hrs. A dark brown coloured precipitate was observed. Subsequently it stabilized at room temperature for 24 hrs. The synthesized sample centrifuged for 20 min with 5000 rpm, washed well three times. The collected powder was desiccated at 60 ^oC and calcinated at 200 ^oC for 2 hrs.The final black colored Ag NPs are used for further characterization purpose (Fig. 1).

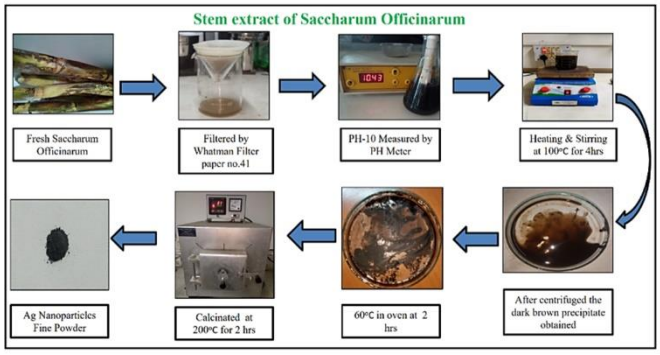

Fig.1: Schematic of Saccharum Officinarum synthesis

Material Characterizations:

The X-ray diffraction pattern of as synthesized Ag NPs was recorded in the 2θrange of 10–80^{o}at a scanning rate of 2^o/min using Rikagu (Miniflex600, Japan). The ultraviolet-visible (UV-Vis) spectroscopy study of Ag NPs was carried out by SHIMADZU Spectrophotometer in the range of 200 to 800 nm. The Fourier transform infrared spectrum was recorded by Fourier Transform Infra-red Spectrophotometer (FTIR), SHIMADZU IRAffinity-1. A drop of Ag NPs solution was placed on freshly prepared KBr disc and scanned between 400 - 4000 cm^{-1}. The scanning electronic microscopic images were captured by FESEM (FEI Nova NanoSEM- 450 instrument) with an EDS (Bruker XFlash- 6I30). The Raman spectrum was recorded by Raman Spectrometer by RENISHAW Spectroscopy.

III. RESULTS AND DISCUSSION:

X-ray Diffraction (XRD):

Saccharum Officinarum mediated Ag NPs XRD pattern as shown in the figure 2.The 2 theta peaks corresponding values are 38.13^o, 44.38^o, 64.61^o and 77.41^{o}with crystal planes are (111), (200),(220), and (311) respectively.From the crystal planes it confirms

the face centered cubic (FCC) crystalline structure of Ag NPs.The average nanoparticle size measured by using Debye-Scherrer equation and it was found to be 18nm [25]. The XRD pattern do not shows any impurity peaks which further confirm the purity of Ag NPs.

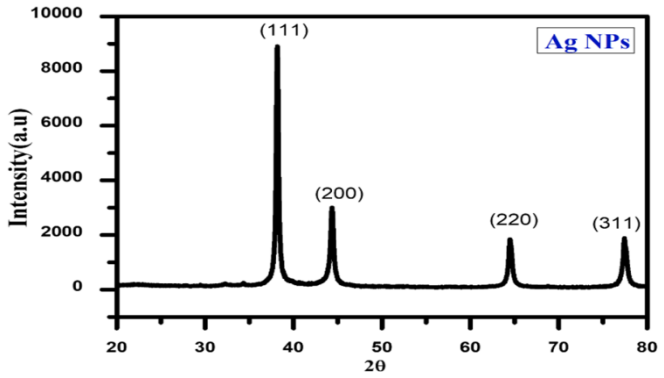

Fig.2: XRD Pattern of AgNPs.

UV-Vis Analysis:

The synthesis of Ag NPs by reduction of aqueous metal ions by using of S. Officinarum extract can easily studied UV-Vis spectroscopy technique. The absorbance spectra of reaction mixture containing aqueous solution of silver nitrate and extract of S. Officinarum shows dark brown color which confirms the formation of Ag NPs and it showed an absorbance peak at around 440 nm, which is characteristic feature of surface plasmon resonance (SPR)of Ag NPs [26] (Fig. 3).

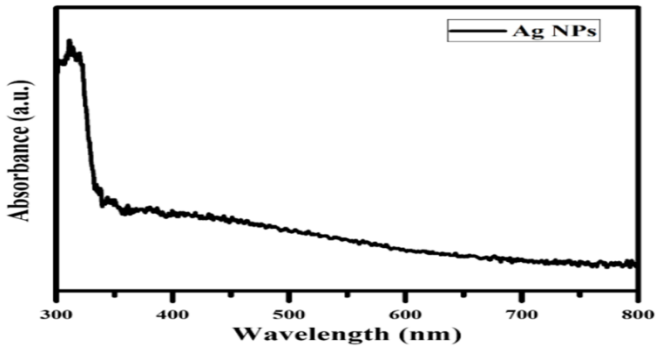

Fig.3: UV DRS of AgNPs

FTIR Spectroscopy:

The FTIR studies were carry out to identify the functional group. Sugar are the major components present in the S. Officinarum extract which might act as reducing agent to synthesize the Ag NPs. As shown in the figure 5 (A) and (B)the FTIR peaks for S. Officinarum juice and synthesized Ag NPs respectively. The FTIR spectra of the S. Officinarum extract peak shows flavonoid and phenolic were observed in Figure 5 (A) at 3375, 1625, 1265, 1045, 873 and 700 cm^{-1}, 3375 cm^{-1} represent O-H stretch , C=C stretch, C-O stretch, CO-O-CO stretch, C-H stretch, C=C stretch and hydroxyl (-OH) group of phenols/alcohol respectively. FTIR spectra of Ag NPs as shown in the figure 5 (B).It shows different stretching vibration at different peaks, 3358cm^{-1}, O-H stretch, 2331cm^{-1} C=N stretch, 1649cm^{-1} -C=C stretch, 929cm^{-1} =C-H & =CH stretch. The peak 3358cm^{-1} gives a strong stretching corresponding to O-H Stretch (Hydroxyl) group[16].

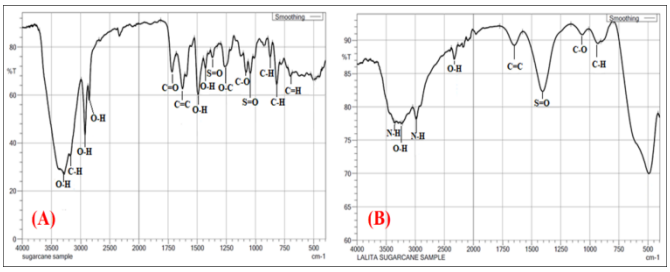

Fig.4: (A) FT-IR Spectra of Saccharum Officinarumand (B) FT-IR Spectra of AgNPs.

FESEM:

Field Emission Scanning Electron Microscopy(FESEM)technique used for surface morphology study of nanoparticles. The figure 5 (A) shows the spherical morphology of Ag NPs with slight agglomerations of nanoparticles as well as elemental mapping as shown in the figure 5 (A- d). Energy Dispersive X-ray Spectroscopy (EDAX) indicates presence of the Ag element at 3eV energy without any impurity as shown in the figure 5 (B).

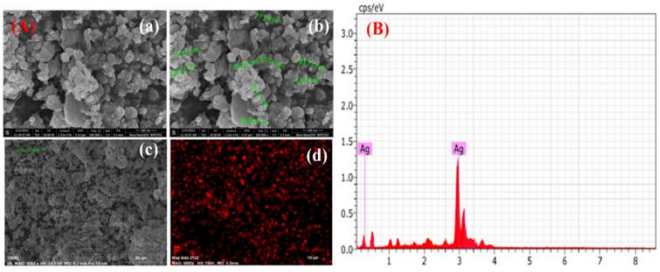

Fig.5: (A) FESEM of AgNPs,A) (d) EDAX Mapping of AgNPs. (B) EDAX Pattern of AgNPs

Raman Spectroscopy:

Raman spectrum of the Ag NPs was recorded spectrum shows the selective enhancement of Raman band of the various organic capping agents which was bound to the Ag NPs. In the figure 6 indicate higher intensity peak at 110 cm^{-1} and595 cm^{-1}.The peak shows a strong and sharp band at 240cm^{-1}, which can be ascribed to the stretching vibration of Ag-N and Ag-O bonds [21]. The formation of a chemical bond between Ag and amino nitrogen as well as silver and carboxylate groups of sugarcane molecules.

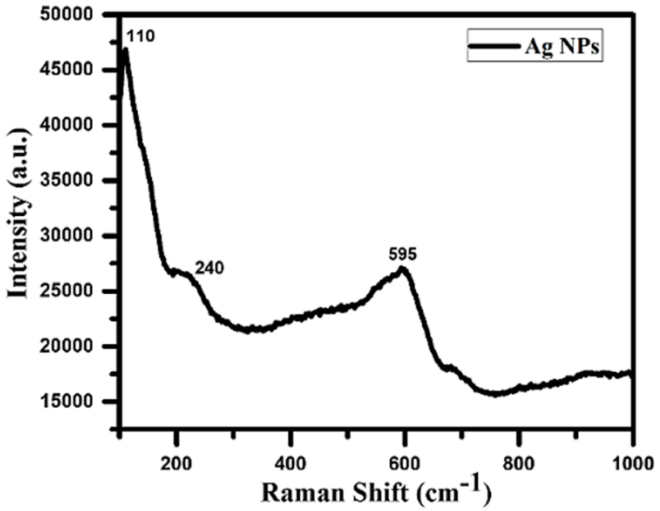

Fig.: 6 Raman Spectrum of AgNPs

IV. CONCLUSION

Green synthesis have several advantages including facile, ecofriendly, non-toxic, cost-effective, biocompatible, etc. X-ray diffraction (XRD) reveals that face centred cubic (FCC) crystal structure with the characteristic diffraction peaks at (111), (200), (220) and (311) and average nanoparticle size 18 nm. UV-Vis spectroscopy shows strong absorption spectra with surface Plasmon resonance (SPR) peak at 440 nm. Fourier Transform Infrared Spectroscopy (FTIR) studies attributed that the hydrogen bonded O–H stretching vibration of phenol overlay on N–H stretching, C=O stretching owing to bio molecules which contain -COO groups. Field Emission Scanning Electron Microscopy (FESEM) along with Energy Dispersive X-Ray Spectroscopy (EDAX) specify that the spherical shape of synthesized Ag NPs as well as the spectra clearly shows strong signal peak at 2.8 keV corresponds to presence Ag NPs without any impurity. Raman Spectrum of the Ag NPs Peak shows strong and sharp band at 240cm^{-1} and stretching vibration of Ag-N and Ag-O bonds.

Acknowledgement:

Author would like to thank to the Principal, Dr, J.D. Sonkhaskar, Head of Department, Dr. P. G. Loke, Department of Physics and Electronics, Karmveer Shantarambapu Kondaji Wavare, Arts, Science & Commerce College, Uttamnagar, CIDCO, Nashik-422008, for providing laboratory and instrumentation facility.

V. REFERENCES

[1]. Narayanan K.B., Sakthivel N.,(2010), "Biological synthesis of metal nanoparticles by microbes," Adv. Colloid Interface Sci., 2010, 153, 1–13.

[2]. Saifuddin N., Wong C.W., Nur-yasumira A.A., (2009), "Rapid biosynthesis of silver nanoparticles using culture supernatant of bacteria with microwave irradiation," E. J. Chem., 2009, 6, 61– 70.

[3]. Chaudhari P., Masurkar S, Shidore V., Kamble S., (2012), "Effect of biosynthesized silver nanoparticles on Staphylococcus aureus biofilm quenching and prevention of biofilm formation," Int. J. Pharm. Bio. Sci., 2012, 3, (1), 222 –229.

[4]. Sista Kameswara Srikar, Deen Dayal Giri, Dan Bahadur Pal, Pradeep Kumar Mishra, et al., (2016), "Green Synthesis of Silver Nanoparticles: A Review," Green and Sustainable Chemistry, 2016, 6, 34-56.

[5]. Vijaykumar P.P.N., Pammi S.V.N., KolluP.Satyanarayana K.V.V. Shameem U., (2014),"Green Synthesis and Characterization of Silver Nanoparticles Using Boerhaaviadiffusa

Plant Extract and Their Antibacterial Activity," Industrial Crops and Products, 52, 562-566.

[6]. Anuj, S.A. and Ishnava, K.B., (2013),"Plant Mediated Synthesis of Silver Nanoparticles Using Dried Stem Powder of Tinosporacordifolia, Its Antibacterial Activity and Its Comparison with Antibiotics," International Journal of Pharmacy and and Biological Sciences, 4, 849-863.

[7]. Chandran, S.P., Chaudhary, M., Pasricha, R., Ahmad, A., Synthesis of Gold Nanotriangles andSilver Nanoparticles Using Aloe Vera Plant Extract," Biotechnology Progress, 2006, 22, 577-583.

[8]. Mukunthan K.S., Elumalai E.K., Patel E.N.,Murty, V.R., (),"Catharanthusroseus: A Natural Source for Synthesis of Silver Nanoparticles," Asian Pacific Journal of Tropical Biomedicine, 1, 270-274.

[9]. Patil R.S., Kokate M.R., Kolekar, S.S., (2012),"Bioinspired Synthesis of Highly Stabilized Silver Nanoparticles Using Ocimumtenuiflorum Leaf Extract and Their Antibacterial Activity,"SpectrochimicaActa Part A: Molecular and Biomolecular Spectroscopy, 91, 234-238.

[10]. Tripathi A., Chandrasekaran N., Raichur A.M., Mukherjee A., (2009),"Antibacterial Applications of Silver Nanoparticles Synthesized by Aqueous Extract of Azadirachtaindica (Neem) Leaves," Journal of Biomedical Nanotechnology, 5, 93-98.

[11]. Ankamwar B., Damle C., Ahmad A.,Sastry M., (2005),"Biosynthesis of Gold and Silver Nanoparticles Using Emblicaofficinalis Fruit Extract, Their Phase Transfer and Transmetallation in an Organic Solution," Journal of Nanoscience and Nanotechnology, 5, 1665-1671.

[12]. Roopan S.M., Rohit M.G., RahumanA.A, Kamraj C., et al., (2013),"Low-Cost and Eco-Friendly Phyto-Synthesis of Silver Nanoparticles Using Coosnucifera Coir Extract and Its Larvicidal Activity," Industrial Crops and Products, 43, 631-635.

[13]. Edison, T.J.I. and Sethuraman, M.G., (2012),"Instant Green Synthesis of Silver Nanoparticles Using Terminaliachebula Fruit Extract and Evaluation of Their Catalytic Activity on Reduction of Methylene Blue," Process Biochemistry, 47, 1351-1357.

[14]. Shukla V.K., Singh R.P., Pandey, A.C., (2010),"Black Pepper Assisted Biomimetic Synthesis of Silver Nanoparticles," Journal of Alloys and Compounds, 507, L13-L16.

[15]. S.Thambiraj, D.Ravi Shankaran., (2016), "Green synthesis of highly fluorescent carbon quantum dots from sugarcane bagasse pulp," Applied Surface Science, 390, 435–443.

[16]. TanurSinha, M.D. Ahmaruzzaman, ParthaPradipAdhikari, Rekha Bora, (2017), "Green and Environmentally sustainable Fabrication of Ag-SnO2 nanocompostites and It's multifunctional Efficacy As photocatalyst and Antibacterial and Antioxidant Agent," ACS sustainable Chem. Eng. 2017, 5, 4645-4655.

[17]. KinniahPaulkumar, Gnanadhas Gnanajobitha, MahendranVanaja, ManickamPavunraj, et al., (2017), "Green synthesis of silver nanoparticle and silver based chitosan bionanocomposite using stem extract of Saccharum Officinarum and assessment of its antibacterial activity," Adv. Nat. Sci. Nanotechnol., 8, 03509, 9.

[18]. P. R. Chawdhari, S. A. Masurkar, V. B. Shidore, S. P. Kamble, (2012), "Biosynthesis of silver nanoparticles using sacchuramofficinarum and its antimicrobial activity," Micro and Nano Letters, 2012, 7, pp- 646-650.

[19]. ArunaJyothi Kora1, SashidharRaoBeedu, ArunachalamJayaraman, (2012), "Size-controlled green synthesis of silver nanoparticles mediated by gum ghatti (Anogeissuslatifolia) and its biological activity," Organic and Medicinal Chemistry Letters, 2:17.

[20]. MohdSayeedAkhtar, JitendraPanwar, YS Yun, (2012), "Biogenic synthesis of metallic nanoparticles by plant extracts," ACS Sustainable Chem. Eng., 1, 6, 591–602.

[21]. SurendranPandiyan, Lakshmanan Arumugam, Sakthy Priya Srirengan, Rameshkumar Pitchan, (2020), "Biocompatible Carbon Quantum Dots Derived from Sugarcane Industrial Wastes for Effective Nonlinear Optical Behavior and Antimicrobial Activity Applications,ACS Omega, 5, 47, 30363–30372.

[22]. D. Sharma, S. Kanchi, K. Bisetty, (2015), "Biogenic synthesis of nanoparticles: A review,"Arabia Journal of Chemistry,Volume 12, Issue 8, Pages 3576-3600.

[23]. NurKamilah Mohd, Nik Nur Atiqah Nik Wee, Alyza A. Azmi, (2017), "Green Synthesis of Silica Nanoparticles Using Sugarcane Bagasse," AIP Conference Proceedings 1885(1):020123-020131.

[24]. Tagad C.K., Dugasani S.R., Aiyer R., Park S., et al., (2013),"Green Synthesis of Silver Nanoparticles and Their Application for the Development of Optical Fiber Based Hydrogen Peroxide Sensor," Sensors and Actuators B: Chemical, 183, 144-149.

[25]. Kirubaharan C.J., Kalpana D., Lee Y.S., Kim A.R., et al., (2012),"Biomediated Silver Nanoparticles for the Highly Selective Copper(II) Ion Sensor Applications," Industrial and Engineering Chemistry Research, 51, 7441-7446.

[26]. Cheng, K.M., Hung, Y.W., Chen, C.C., Lin, C.C., et al., (2014),"Green Synthesis of Chondroitin SulfateCapped Silver Nanoparticles: Characterization and Surface Modification," Carbohydrate Polymers, 110, 195-202.

[27]. Lu R., Yang D., Cui D., Wang Z.,et al., (2012),"Egg White-Mediated Green Synthesis of Silver Nanoparticles with Excellent Biocompatibility and Enhanced Radiation Effects on Cancer Cells," International Journal of Nanomedicine, 7, 2101-2107.

[28]. Guidelli E.D., Ramos A.P., Zaniquelli M.E.D., Nicolucci P., et al., (2012),"Synthesis of Silver Nanoparticles Using DL-Alanine for ESR Dosimetry Applications," Radiation Physics and Chemistry, 81, 301-307.

International e-Conference on Recent Trends in Nano-Materials and Its Applications-2021
In Association with International Journal of Scientific Research in Science and Technology
Volume 9 | Issue 2 | Print ISSN: 2395-6011 | Online ISSN: 2395-602X (www.ijsrst.com)

Green Synthesis of Copper Nanoparticles Mediated By Dioscorea Bulbifera Tuber for Biofilm Inhibition

Laxmi Sonawane[1], Ram Sonawane[2], Abhinay Mandawade[1], Sana Khan[1], Ganesh Kande[1], Lalita Jondhale[1], Pratibha Loke*[1]

[1]Department of Physics and Electronics, Karmaveer Shantarambapu Kondaji Wavare, Arts, Science & Commerce College, Uttamnagar, CIDCO Nashik-422008, Maharashtra, India

[2]Department of Botany, Arts, Science & Commerce College, Dindori, Nashik-422008, Maharashtra, India

ABSTRACT

Herein, we report the synthesis of Cu NPs via green approach using Dioscorea bulbifera plant tuber extract. The as-synthesized products were characterized using X-ray diffraction (XRD) analysis reveals that confirmation of the face centered cubic (FCC) crystal structure without any impurity peaks with a lattice constant 0.3620 nm. Fourier Transform Infrared Spectroscopy (FTIR) shows the components like flavonoid and phenol were observed, which have contributed as surface capping agents for NPs. UV-visible spectroscopy shows that Cu NPs shows a strong surface Plasmon resonance absorption peak at 570 nm, which attributed to the formation of Cu NPs. Field emission scanning electron microscope (FE-SEM) exhibit a spherical shape of Cu NPs agglomerate morphology and Energy Dispersive X-ray analysis (EDAX) which confirm the presence of only Cu element without any impurities. Synthesized sample explored of Candida albicans biofilm and it shows about 20 % inhibition of biofilms.

Key words: Green synthesis, copper nanoparticles, Dioscorea bulbifera, biofilm and Candida albicans

I. INTRODUCTION

Nanomaterial's have unique properties that distinguish them from the corresponding bulk materials. The shape and size of metal nanoparticles influence their optical, catalytic and conductive properties [1]. Synthesis of nanoparticles through a green approach have been widely used because of its nontoxic, environment friendly and cost effective nature as compared with chemical as well as physical methods [2]. Copper nanoparticles (Cu-NPs) have applications such as super strong materials, antibacterial, sensors, catalysts, DNA binding, antimicrobial activity, antioxidants, industries and medicine [3]. There are several reports on plant mediated green synthesis of Cu NPs such as Eclipta prostrata leaves [4], Celastrus paniculatus Willd [5], Ageratum houstonianum Mill leaf [6], Cissus vitiginea [7], Juglans regia leaf [8], Lantana camara flower [9], Jatropha curcas leaves [10], Punica granatum [11] and Tea Leaf [12].

Dioscorea bulbifera is one of the unique medicinal plants among 600 species in the family Dioscoreaceae which has found its importance in traditional

medicine worldwide [13]. Among various medicinal plants used in Ayurveda, Indian system of traditional medicine as well as its multiple therapeutic potential [14]. Dioscorea bulbiferais used as alternative medicine in the various regions of India as well as Zimbabwe. Dioscorea bulbiferaplant tuber used as herbal tonic which further stimulates the stomach and spleen and also it shows effect on the lungs and kidneys. Tubers are also useful for to cure various activity such as dry cough, diabetes, asthma uncontrollable urination, poor appetite, chronic diarrhea, ulcers, anticancer, antioxidant, analgesic, and antinflammatory properties [15].

Biofilms are the bacterial groups firmly lodged in the extracellular matrices of polysaccharides, proteins, enzymes, and nucleic acids; thereby, facilitating anchorage to any surfaces irreversibly [16]. Candida albicans is considered as a major fungal pathogen of the humans causing considerable morbidity and mortality. Currently prescribed antifungal, antibiotics areoften failures in clinical situations, due to the development of multiple drug resistance, formation of drug resistant biofilms on biotic as well as abiotic surfaces and transformation from yeast to hyphal form morphology [17].

Antibiofilm Assay:

The procedure is taken from [18], typically 100µL of 107 cells/mL of Candida albicans in water were added into 96 well polystyrene plates and incubated for 3 hours for adherence of cells. The un-adhered cells were gently washed with phosphate buffer saline (PBS). 100 µL of Roswell Park Memorial Institute (RPMI) medium containing different concentrations (0–100 µg/L) of Cu NPs were added to each well, and incubated for 24 hours at37 oC. After 24 hours of incubations, the medium supernatant was removed, and the biofilm formed was gently washed with PBS and further incubated with100 µL of 5 mg/mL MTT (3-(4,5 Dimethylthiazol-2-yl)-2,5-Diphenyltetrazolium Bromide) solution. After few hours of incubations, 100 µL of dimethyl sulfoxide was added into each well and optical density was recorded.

II. MATERIALS AND METHODS:

Plant material and preparation of extract Dioscorea bulbifera tubers were collected from natural geographical landscape of Dindori, Nashik region Western Ghats of Maharashtra, India and were identified and authenticated by botanist from national research institute of basic Ayurvedic science, central council for research in Ayurveda and siddha, department of ayush, ministry of Health and family welfare, Government of India, New Delhi, Nehru garden, kothrud, pune, India assigning voucher specimen number 860 [19]. Washed tubers were sliced into small pieces and shade dried for 5-7 days followed by blending into fine powder. 10 g of finely ground tuber powder was boiled with 100 ml of sterile distilled water for 5 min in a 300 ml Erlenmeyer flask. The extract obtained was filtered through whatman filter paper No. 1 the filtered sample was collected and stored at 40C

Synthesis method –

Synthesis of Cu NPs was done with slight modification 10 ml of DBTE was added to 95 ml of 1.5 Mm aqueous CuSO4.5H2O solution and kept under shaking condition at 200 rpm and reduction of Cu2+ion.

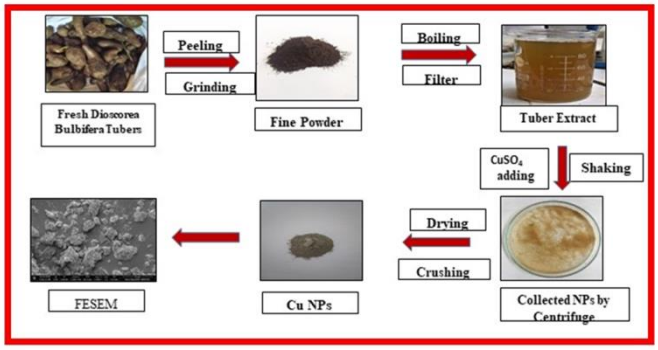

Schematics of synthesis of Cu NPs by green synthesis approach

III. RESULTS AND DISCUSSION:

1] XRD Studies

The X- ray diffraction XRD pattern of Cu NPs is shown in figure: (1). The diffraction intensities were recorded from 10 to 80o at 2θ angle, three characteristic peaks were observed at 2θ angles of 43°,50° and 74°, and these corresponds to the crystal planes (111), (200) and (220) which well matches with [Joint Committee on Powder Diffraction (JCPDS) 04-0784] The Cu NPs shows Face Center Cubic crystal structure [10].

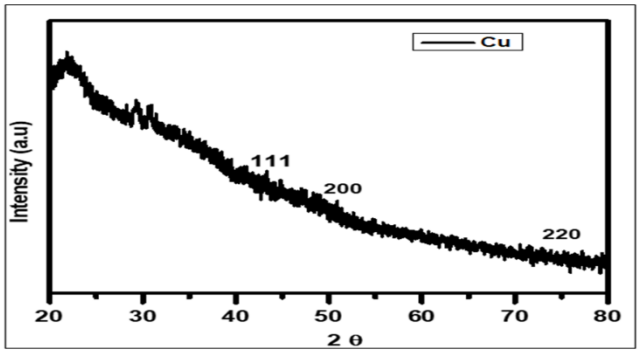

Fig 1 – XRD pattern of synthesized Cu NP

2] UV-Visible- Diffuse Reflectance (UV- Vis-DRS) Spectroscopy

From figure 2 shows the spectrum of Dioscorea bulbifera tuber powder and synthesized Cu NPs. The red spectrum indicates Dioscorea bulbifera tuber and synthesized Cu NPs shown black color. UV-Vis-DRS confirms the appearance of Cu NPs with strong surface plasmon resonance (SPR) peak at 570nm. The absorption band for Cu NPs has been reported to be in the range of 500-600 nm [20].

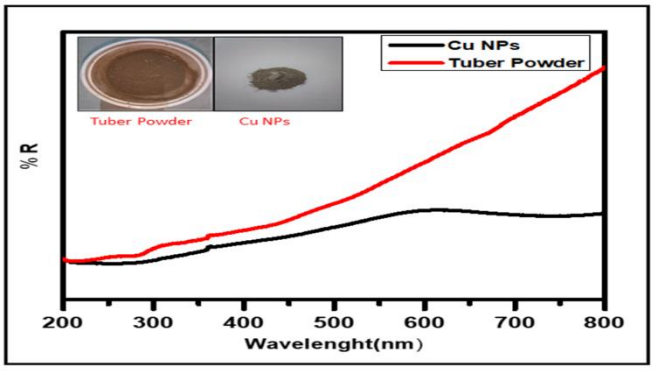

Fig 2 – DRS spectrum of synthesizes Cu NPs

3] Fourier transform infrared (FTIR) analysis:

FTIR technique is used to investigate the surface functional group of DBT powder (Dioscorea bulbifera tuber) as well as synthesized Cu NPs. FTIR spectra of DBT was recorded before synthesis and the peak shows the key components such as flavonoid and phenolic were observed in figure 3 (a): The peaks observed at 1639, 1421, 1155, 1082, and 1026 cm-1 represents C=C stretch, O-H stretch, C-O stretch and C-N stretch the broad and strong peak was found in DBT at 3495 cm-1, which is due to hydroxyl (-OH) group of phenols/alcohol.FTIR analysis also performed to recognize the various functional group present in Cu NPs mediated by Dioscorea bulbifera as shown in the figure 3(b): It also shows different stretching vibration of bands at different peaks; 3296 cm-1 O-H stretch; 2926 cm-1 C-H strong stretch vibration; 1622 cm-1 C=C variable stretch vibration; 1413 cm-1 –C-H variable bending vibration [14].

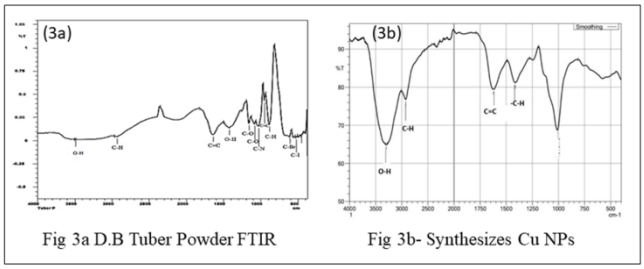

Fig 3a D.B Tuber Powder FTIR Fig 3b- Synthesizes Cu NPs

4] (FESEM)-EADX studies -

In figure 4 (A-D): The synthesized Cu NPs seems to show a cubic and hexagonal agglomerates surface morphology analyzed by Field Emission Scanning Electron Microscopy(FESEM). The Cu element presence also shown by elemental mapping as shwon in the figure 4 (E). The Energy Dispersive X-ray(EDAX) analysis show a signal corresponding to a significant presence of Cu element without any impurity peak as shown in figure 4 (F).

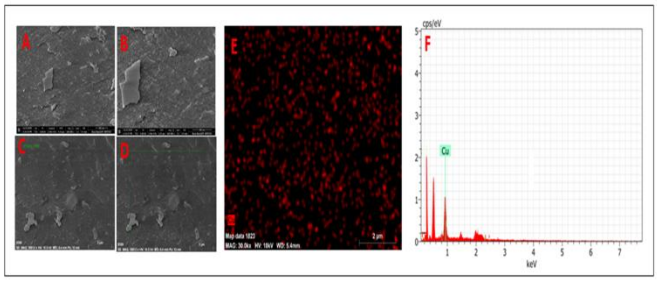

Fig 4(A-D): FESEM of CuNPs Fig 4(E): EDAX Mapping of CuNPs Fig 4 (F) EDAX Pattern ofCuNPs

[5] Antibiofilm Activity –

The schematics of biofilm formation of Candida albicans as shown in the figure 5 with various stages (i) culture medium surface with an adsorbed film of host proteins (blue colour). Initial yeast (red) contact the surface and adhesion to it. (ii) formation of the basal layers with micro colonies. (iii) completion of micro colony formation by addition of the upper and hyphal layer with extracellular matrix material (black) was formed. (iv) mature biofilms contain number of micro colonies with extracellular matrix material that surrounds both yeasts and hyphae (red). The two distinct layers such as a thin and basal region of densely packed yeast cells and an overlying thicker as well as more open hyphal layer. (v) mature biofilms which produces new spores (green) and disperse them [22].

The synthesized Cu NPs are explored for Candida albicans biofilms inhibition. CuNPs shows inhibition as shown in the in Figure 5 (b), 15 × 105 cells/mL were added 15.6 µg/mL to each well of the 96-well polystyrene plates. Similarly, 20 × 105 cells/mL were added 62.5 µg/mL to each well of the 96-well polystyrene plates. It shows maximum inhibition about 20% of biofilm also it slow down the biofilm formation which may various applications in biomedical field [23].

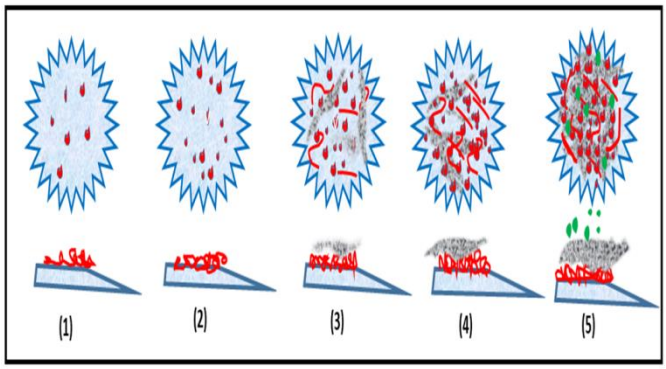

Fig 5(a): Stages in the formation of Candida albicans biofilm.

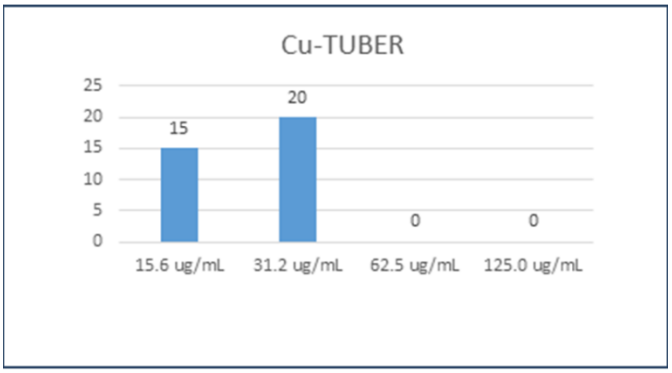

Fig 5(b) Inhibition of Cu NPs

IV. CONCLUSION

Green synthesis approach is an ecofriendly, non-toxic, facile and rapid approach. In present study we synthesized Cu NPs by plant extract Dioscorea bulbifera tuber. X-ray diffraction (XRD) analysis reveals that confirmation of the face centered cubic (FCC) crystal structure without any impurity peaks. UV-visible spectroscopy reveals a strong surface plasmon resonance absorption peak at 570 nm, which attributed to the formation of Cu NPs.

Fourier Transform Infrared Spectroscopy (FTIR) shows the components like flavonoid and phenol were observed, which have contributed as surface capping agents for NPs.Field emission scanning electron microscope (FE-SEM) exhibit a spherical shape of Cu NPs agglomerate morphology and Energy Dispersive X-ray analysis (EDAX) which confirm the presence of only Cu element without any impurities. Cu NPs are used for inhibition of fungal biofilm of Candida albicans which shows about 20 % reduction in biofilm. Cu NPs can be investigating for many biomedical activities such as antibacterial, antioxidant, analgesic, anti-inflammatory, antitumor activities and antidiabetic etc.

Acknowledgements –

Author would like to thanks to Principal Dr. J. D. Sonkhaskar, Head of Department Dr. P.G Loke, Department of Physics and Electronics of KSKW Arts, Science and Commerce College, Uttamnager, CIDCO,

Nashik-422008 for giving instrument facilities to carry out this research work also thanks for their precious courage and valuable time.

V. REFERENCES

[1]. E. J. Guidelli, A.P. Ramos, M. Elisabete, D. Zaniquelli, et al., "Green synthesis of colloids silver nanoparticles using natural rubber latex extracted from Hevea brasiliensis". Elsevie, (2011).

[2]. Zain, N. M., Stapley, A. G. F., et al., "Green Synthesis of Silver and Copper Nanoparticles using Ascorbic acid and Chitosan for Antimicrobial Applications", Carbohydrate Polymerscarbpol, (2014).

[3]. J. Suárez-Cerda, H. Espinoza-Gómez, G. Alonso-Nú ñez, I.A. Rivero, et al., "a green synthesis of copper nanoparticles using native cyclodextrins as stabilizing agents", Journal of Saudi Chemical Society,(2016).

[4]. Ill-Min Chung, AbdulRahman, Sampath Marimuthu, Arivarasan Vishnu Kirthi,kumar, et al., "Green synthesis of copper nanoparticles using Eclipta prostrata leaves extract and their antioxidant and cytotoxic activities,"Experimental and Therapeutic Medicine, (2017).

[5]. Suresh Chand Mali, Anita Dhaka, Chanda Kumari Githala, Rohini Trivedi, "Green synthesis of copper nanoparticles using Celastrus paniculatus Willd. leaf extract and their photocatalytic and antifungal properties", BiotechnologyReports, (2020).

[6]. Sandip Kumar Chandraker, Mishri Lal, Mithun Kumar Ghosh, Vivek Tiwari,"Green synthesis of copper nanoparticles using leaf extract of Ageratum houstonianum Mill. and study of their photocatalytic and antibacterial activities", IOP Publishing Ltd,(2020).

[7]. Shuang Wu, Shanmugam Rajesh Kumar, Malini Madasamy & Vanaja Mahendran "Green synthesis of copper nanoparticles using Cissus vitiginea and its antioxidant and antibacterial activity against urinary tract infection pathogens", Artificial Cells, Nanomedicine, and Biotechnology, (2020).

[8]. Marjan Asemani and Navideh Anarjan "Green synthesis of copper oxide nanoparticles using Juglans regia leaf extract and assessment of their physico-chemical and biological properties", DE GRUYTER, (2019).

[9]. Rakesh Chowdhury, Aslam Khan b and Md. Harunar Rashid,"Green synthesis of CuO nanoparticles using Lantana camara flower extract and their potential catalytic activity towards the aza-Michael reaction",RSC Adv., (2020).

[10]. Mithun Kumar Ghosh, Sanjay Sahu,a Indersh Guptaa and Tanmay Kumar Ghorai , "Green synthesis of copper nanoparticles from an extract of Jatropha curcas leaves: characterization, optical properties, CT-DNA binding and photocatalytic activity", RSC Adv., (2020).

[11]. P. Naga Padma, Syed Thanveer Banu and S. Chaitanya Kumari, "Studies on Green Synthesis of Copper Nanoparticles Using Punica granatum", Annual Research & Review in Biology (2018).

[12]. Jeevan Jyoti Mohindru, Umesh Kumar Garg,"Green Synthesis of copper nanoparticles using Tea leaf extract", International Journal of Engineering Sciences & Research Technology, (2017).

[13]. Ghosh S, Parihar VS, More P, Dhavale DD, et al., "Phytochemistry and Therapeutic Potential of Medicinal Plant: Dioscorea bulbifera"., Med chem, (2015).

[14]. Sougata Ghosh, Soham Jagtap,Piyush More, Usha J. Shete, et al., "Dioscorea bulbifera Mediated Synthesis of Novel AucoreAgshell Nanoparticles with Potent Antibiofilm and Antileishmanial Activity", Hindawi Publishing Corporation Journal of Nanomaterials, (2015).

[15]. Sougata Ghosh, Sonal P Gurav, Ashwini N Harke, Maliyackal Jini Chacko, "Dioscorea oppositifolia Mediated Synthesis of Gold and Silver Nanoparticles with Catalytic Activity", J Nanomed Nanotechnol, (2016).

[16]. Rabina Dumaru, Ratna Baral and Lok Bahadur Shrestha, et al.,"Study of bioflm formation and antibiotic resistance pattern of gram-negative Bacilli among the clinical isolates at BPKIHS, Dharan"Dumaru et al. BMC Res Notes, (2019).

[17]. Donlan, R. M. "Biofilm Formation: A Clinically Relevant Microbiological Process. Clinical Infectious Diseases", Healthcare Epidemiology, (2001).

[18]. Shivkrupa D. Halbandge, Ashwini K. Jadhav, Priyanka M. Jangid, Amruta V. Shelar, et al.,"Molecular targets of biofabricated silver nanoparticles in Candida albicans", The Journal of Antibiotics(2019)

[19]. Sougata Ghosh, Piyush More, Rahul Nitnavare, Soham Jagtap, et al., "Antidiabetic and Antioxidant Properties of Copper Nanoparticles Synthesized by Medicinal Plant Dioscorea bulbifera"Journal of J Nanomedicine & Nanotechnology(2015).

[20]. N. Nagar, V. Devra, "Green synthesis and characterization of copper nanoparticles using Azadirachta indica leaves", Materials Chemistry and Physics (2018).

[21]. Wenrui Gu, Dongmei Xu, Dongmei Guo, Liuping Zhang et al., "In vivo Models for Candida Albicans Biofilms Study", Journal of Microbiology and Biotechnology,(2016).

[22]. Humberto H. Lara, Dulce G. Romero-Urbina, Christopher Pierce, Jose L. Lopez-Ribot, et al., "Effect of silver nanoparticles on Candida albicans biofilms: an ultrastructural study," J Nanobiotechnol,(2015).

International e-Conference on Recent Trends in Nano-Materials and Its Applications-2021
In Association with International Journal of Scientific Research in Science and Technology
Volume 9 | Issue 2 | Print ISSN: 2395-6011 | Online ISSN: 2395-602X (www.ijsrst.com)

Mechanical Study of Pure and Zn^{2+} Doped Ammonium Dihydrogen Phosphate Crystal for Devise Applications

M.I.Baig[1], Mohd.Anis[2], M.D.Shirsat[3], Raje Shaikh B.B.[4], S.S.Hussaini[5*]

[1]Assistant Professor, Department of Physics, Prof Ram Meghe College of Engineering and Management, Amravati-444701, Maharashtra, India

[2]Assistant Professor, Department of Physics and Electronics, Maulana Azad College of Arts, Science and Commerce, Dr. Rafiq Zakaria Campus, Aurangabad-431001, Maharashtra, India

[3]Professor, RUSA Centre for Advanced Sensor Technology Department of Physics Dr. Babasaheb Ambedkar Marathwada University, Aurangabad-431004, Maharashtra, India

[4]Assistant Professor, Department of Physics, Government College of Arts & Science, Aurangabad-431001, Maharashtra, India

[5*]Associate Professor, Crystal Growth Laboratory, Department of Physics, Milliya Arts, Science and Management Science College, Beed-431122, Maharashtra, India

ABSTRACT

The present investigation explores the influence of metallic impurity on mechanical property of Ammonium dihydrogen phosphate (ADP) crystal to emphasize its utmost liability for futuristic device applications. The most commercially viable slow solvent evaporation method has been employed to grow the undoped and Zn2+ doped ADP (ADP-Zn) single crystals. Vickers micro hardness study has been employed to evaluate the role of metal in uplifting the hardness parameters of ADP crystal. The mechanical study of ADP-Zn crystal has been comparatively investigated with load ranging from 25g –100g.

Keywords: - Crystal growth, Microhardness study

I. INTRODUCTION

Ammonium dihydrogen phosphate (ADP) crystal has excellent property amongst the phosphate family due to its widespread applicability in fabricating the frequency conversion (second, third, fourth), frequency mixing, microscopic lasing, telecommunication, optical parametric, optical switching, optical data storage etc. devices [1, 2]. ADP crystal has appealing characteristics such as ferroelectric, piezoelectric, high optical homogeneity, low cutoff wavelength, high SHG coefficient, strong thermal and physical stability owing to which research community throughout the world are trying to pursue the further advancement in inherent properties of ADP crystal by various methods. The most frequently adopted way to tailor the properties of ADP crystal is using an external additive in the form of dopant. In literature the organic (amino acids and dyes) as well as metallic ions like Fe and Cr and cesium have brought the best improving results in various distinct properties of ADP crystal.[3]. It is

noticed that, none of the researcher has reported the effect of Zn^{2+} on various characteristics of ADP crystal. Considering this exemption in literature, we make an effort to report a novel work in which the Zn^{2+} ion has been firstly used to optimize the mechanical property of ADP crystal.

II. EXPERIMENTAL PROCEDURE

The Merck make ADP salt was dissolved in double distilled water and the homogeneous solution of ADP was taken in separate beakers. The beakers were then added by 1mole of Zinc chloride ($ZnCl_2$). The mixture was then stirred well for six hours in order to achieve homogeneous doping in ADP. The solutions were then filtered using the No.1 membrane filter paper and the filtered solution was taken in a beaker. The beakers were kept in a constant water bath maintained at 34 ° C with accuracy ±0.01 ^{0}C. The single crystals have been harvested in the period of 18 to 20 days.

The ADP-Zn crystal is shown in Fig. 1.

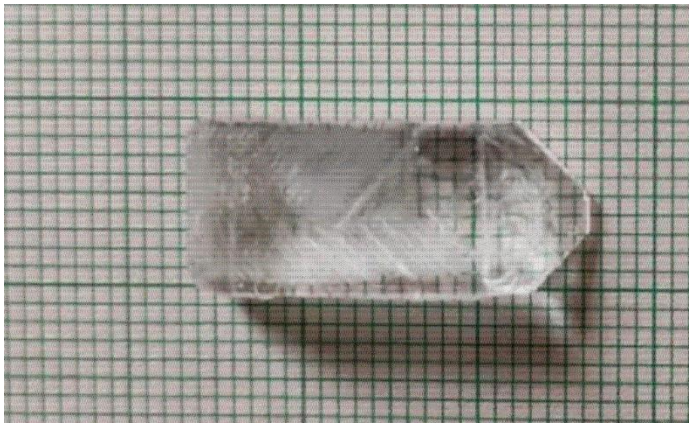

Fig. 1. Photograph of Zn-ADP single crystal

III. RESULTS AND DISCUSSION

Vicker's microhardness measurements:

The term hardness referred as a measure of the resistance against lattice destruction [4]. Microhardness study has been employed to examine mechanical characteristic of grown crystal. As hardness properties are related to the crystal structure, bonding, heat formation and Debye temperature of the material hence, mechanical study of the crystals brings out an understanding of the different effects such as yield strength, elastic stiffness etc. [5]. Mechanical behavior of the materials plays decisive role in the device fabrication. The smooth surface of the ADP and ADP-Zn crystals were subjected to Vicker's static indentation test at room temperature. Leitz Weit-zler hardness tester with loads of different magnitude was employed for the study. The indentation time was kept as 10 s for all the loads. Using the relation, $H_v = (1.8544 \times P)/d^2$ kg/mm^2 Vicker's hardness number was calculated, where H_v is Vicker's hardness number in kg/mm^2, P is the applied load in kg, d is the average diagonal length of the indentation mark in mm. The plot of load (P) vs. Vicker's hardness (Hv) for undoped ADP and ADP-Zn crystals are shown in Fig. 2(a). From the graph it is evident that the hardness of the ADP-Zn crystals is higher that the undoped ADP crystals.

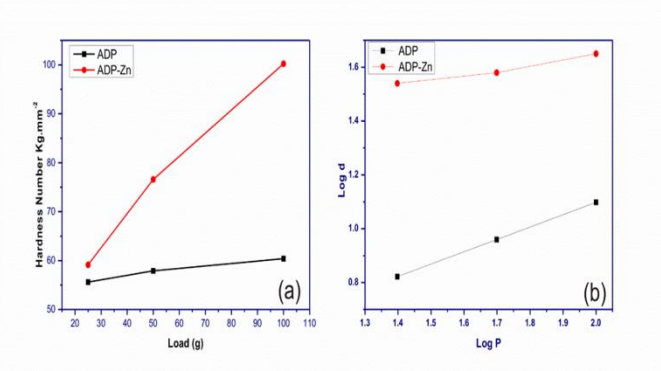

Fig -2: (a) Load dependent hardness of ADP-Zn (b) Plot of Log P Vs Log d

The work hardening index n, of studied crystals has been evaluated using the Meyer's relation given as, log P = log K1+n log d where, K1 is the material constant and n is the Meyer's work hardening index. The value of n has been calculated from the slope of plot drawn between log P and log d, shown in Fig. 2(b). The calculated value of n of both the crystals is above 1.6, this implies that the crystals belong to the category of softer materials as demonstrated by Onitsch. The Yield strength and Elastic stiffness coefficient pure and ADP-Zn crystals has been evaluated and systematically plotted in Fig 3(a) and

3(b) respectively. It has been observed that incorporation of Zn^{2+} might have facilities good bond strength between the associated neighboring atoms and hence improved yield strength and elastic stiffness coefficient of host crystal [6]. Overall enhanced mechanical performance of ADP-Zn crystal indicates that it might facilitate less wastage/breakage/cracking of material during processing the material for fabricating mechanically rigid device.

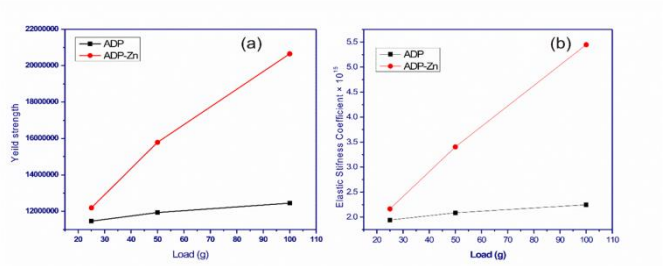

Fig -3: (a) Plot of Yield strength Vs Load (b) Elastic stiffness coefficient Vs Load

IV. CONCLUSION

The single crystals of undoped ADP and ADP-Zn have been grown by slow solvent evaporation method. The Vicker's microhardness study confirmed the enhancement of mechanical strength of host ADP crystal due to incorporation of Zn2+. Concisely, ADP-Zn crystal with superior yield strength and elastic stiffness coefficient could be decisive in designing various mechanical rigid devices applications.

V. REFERENCES

[1]. M. Yoshimatsu, "Some Observations of Imperfections in ADP Single Crystals by X-Ray Diffraction Micrography," Japanese Journal of Applied Physics, vol. 5, pp. 29-35, 1966.

[2]. M. J. Gunning, R. E. Raab, P. Góski, and W. Kucharczyk, "The quadratic electrooptic effect and estimation of antipolarization in ADP," Ferroelectrics Letters Section, vol. 24, pp. 63-68, 1998.

[3]. S. Ekadevasena, J. T. J. Prakash, and J. M. S. Gnanaraj, "Modification of structural, optical, thermal and mechanical properties of KDP crystals on the addition of Ni2+," Optik, vol. 125, pp. 2620-2624, 2014/06/01/ 2014.

[4]. G. K. Rollefson, "Chemical Kinetics. By Keith J. Laidler," The Journal of Physical Chemistry, vol. 55, pp. 759-760, 1951/05/01 1951.

[5]. C. W. Stillwell, Crystal chemistry: McGraw-Hill Book Company, inc., 1938.

[6]. B. Riscob, M. Shakir, N. Vijayan, V. Ganesh, and G. Bhagavannarayana, "Effect of Mn(II) doping on crystalline perfection, nonlinear, optical and mechanical properties of KDP single crystals," Applied Physics A, vol. 107, pp. 477-484, 2012/05/01 2012.

International e-Conference on Recent Trends in Nano-Materials and Its Applications-2021
In Association with International Journal of Scientific Research in Science and Technology
Volume 9 | Issue 2 | Print ISSN: 2395-6011 | Online ISSN: 2395-602X (www.ijsrst.com)

Studies to Determine the Young's Modulus of Monolithic Silica Aerogels

Mahendra Suhas Kavale, Subhash Shabu Karande
Assistant Professor, Department of physics, Sangameshwar College, Solapur - 413001, Maharashtra, India

ABSTRACT

Aerogel materials are not only superinsulating but also a sound proof. Such materials are very fragile in nature besides it we have examined the elastic properties of methyltrimethoxysilane (MTMS) based silica aerogels. This current research work focuses the elastic behaviour of the monolithic silica aerogels. The technique of interferometry was applied to study elastic constant of aerogels. It was observed that due to mechanical stressing, number of fringes localised on the aerogel samples and these fringes were used to determine the Young's modulus (Y) of such materials. Here, we report a new mode for determination of 'Y' of aerogel monoliths.

Keywords: Mechanical Stressing, Young's Modulus.

I. INTRODUCTION

Silica aerogels are nano-structured materials with the bulk density as low as 0.02 g/cm^3 and high porosity (> 98%) [1]. Due to the high porosity and very less solid content, determination of the various mechanical properties of the silica aerogels is the major challenge. Though methods like three point flexural techniques, Vickers and knops tests have been applied for the measurement of the mechanical properties of the aerogels, but application of even very small loads (~0.25 N) results in the cracking of the aerogel samples [2,3]. Therefore efforts have been made in the past to use non-destructive technique as like sound velocity measurements for this purpose [4, 5]. There are no reports available on the use of holographic interferometry for the determination of mechanical properties of the aerogels.

Holographic interferometry has been widely accepted as a viable tool for non-destructive testing of materials. It permits the qualitative & quantitative study of minute changes in the object contours [6]. We report here the use of double exposure holographic interferometry (DEHI) [7] to study the surface deformation of mechanically stressed aerogels. DEHI has proved to be an advantageous than the other holographic techniques in the study of transient phenomenon [8]. In this technique, there is comparison of a stressed surface state relative to its unstressed state causes interference fringes to be observed on the object, which gives information of the object deformation with a very high precision [9,10]. As this technique is enough sensitive to the determination of the order of wavelength of source [He-Ne LASER 6328 Å], application of a small stress can give rise to interferometric fringes and hence the sample under test remains intact, reusable and crack free.

II. EXPERIMENTAL

2.1. Preparation of Monolithic Silica Aerogels:

Two stage sol-gel processes was used. Alcogels were prepared by hydrolysis and polycondesation of tetraethoxysilane (TEOS). Initially, TEOS was dissolved in methanol (MeOH) in order to make it soluble in 0.05 NH_4F, Methyltrimethoxysilane (MTMS) was added to this mixture to make the aerogels hydrophobic as well as diffusely reflective. The mixture was stirred for 10 minutes and the resulting homogenous sol was transferred to 25 ml pyrex glass test tubes. The test tubes were made air tight to inhibit the evaporation of MeOH from the sol. The gelation took place at an ambient temperature of 27 ºC. In order to prevent shrinkage and cracks in the alcogels, excess amount of MeOH was poured in the test tubes after gelation. All the gels were aged at 25 ºC for 24 hours. The aged alcogels were dried supercritically in an autoclave. The details of autoclave drying conditions were given in this publication [11].

To synthesize aerogels with different physical characteristics, molar ratios of TEOS:MTMS:H_2O:NH_4F was kept constant at 1:1:4:3.6 X 10^{-3} respectively and MeOH/TEOS molar ratio (M) was varied analytically from 12 to 16, as it was observed in an earlier study that variation of M values affects the bulk density of aerogel [12-13].

2.2. Holographic Experimental Set-up:

The off axes double exposure holographic interferometry technique was used to record the holograms. In this technique, continuous comparison of the surface displacement relative to its initial position causes interference pattern observed on the object. Surface, which gives information about the object [5,6].

All the optical components used in the recording were arranged on the vibration isolation system [7]. The special type of the vibration isolation table is prepared in holography laboratory from local equipments in low cost. This system avoids all the vibrations reaching on the top of the table from ground. The cylindrical samples of aerogels having ~10 mm radius and ~30 mm height were used to study the surface deformation using DEHI technique. The aerogle sample was illuminated by 5mW He-Ne laser [λ = 6328 Å]. High quality beam splitter [70:30] was used to split the laser beam.

We used the mechanical stressing technique to study deformation. To study the effect of mechanical stressing, the object (aerogel) was placed on a rigid black painted wooden block and a weight (e.g. 1 g) was placed on it. The special pulley arrangement was used to unload the samples. The hologram of the object was recorded in this stressed state on the holographic plate. Then without disturbing the whole system, the load was removed from the object and the same holographic plate was exposed to this natural unstressed state of the object. The sufficient exposure time was adjusted depending upon the reflection from the object in both cases.

III. DETERMINATION OF YOUNG'S MODULUS

There are three different methods for the determination of Young's modulus of different solid objects. The Y of a long, thin wire can be calculated by the following equation,

$$Y = \frac{MgL}{\pi r^2 l} \qquad (1)$$

Where, M = Mass applied,
L = Length of wire,
r = radius of wire,
l = elongation produced.

In this work, we have calculated the elongation 'l', by holographic method by calculating the deformation of the silica aerogel sample after application of the load. Hence by using the holographic method the equation (1) can be modified as follows,

$$Y = \frac{MgL}{\pi r^2 a} \qquad (2)$$

Where, 'a' = surface displacement of the sample. The surface displacement of sample can be calculated by the following geometry.

3.1) Geometry for in- plane displacement of a rigid object:

To view the object from a distance R, in the following figure,

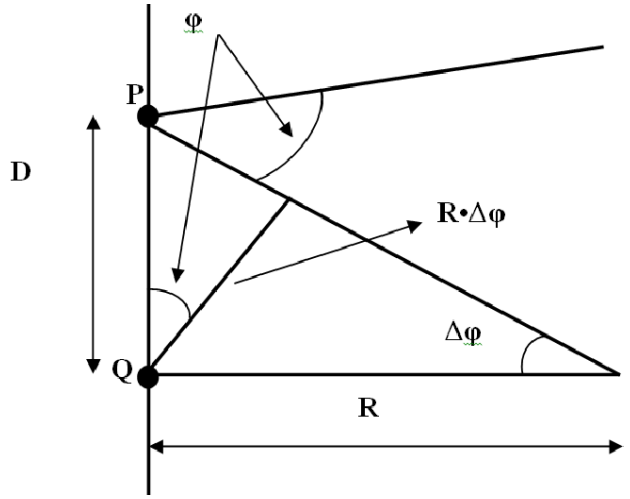

Figure 1: Geometry for in- plane displacement of a rigid object

Where, R = distance of object, φ = viewing angle.

The separation of fringes on the object is given by,

$$D = \frac{R\Delta\varphi}{\cos\varphi} = \frac{R\lambda}{a\cos(\varphi)\sin(\varphi - \partial)} \quad (3)$$

For the silica aerogel samples, the movement after the application of load is parallel to surface, hence in above equation (3), δ = π/2. Hence equation (3) becomes,

$$D = \frac{R\lambda}{a\cos^2\varphi} \quad (4)$$

Where, 'a' = surface displacement of the sample

$$\therefore\ a = \frac{R\lambda}{D\cos^2\varphi} \quad (5)$$

Here, D = Fringe separation, λ = wavelength of the source, φ = viewing angle, R = Distance of object. Using equation (2) the values of the 'Y' of the silica aerogel samples can be calculated.

IV. RESULTS

4.1. Fourier Transform Infrared Spectroscopy (FTIR):

FTIR study of the silica aerogel was carried out.

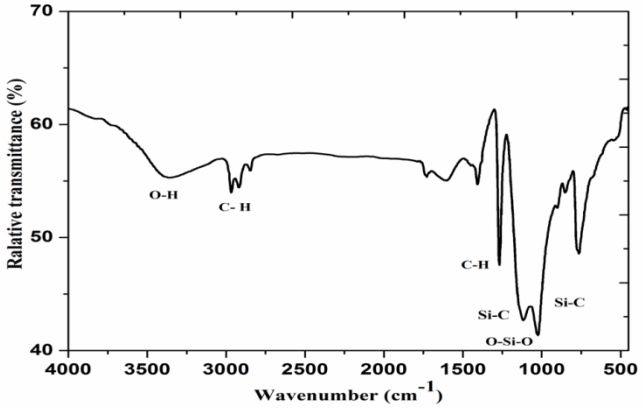

Figure 2: FTIR Study of the silica aerogel

Several characteristic absorption bands were observed in the range of 450 cm^{-1} to 4000 cm^{-1} indicating the presence of methyl groups [14]. The broad absorption band observed at 1080 cm^{-1} is a characteristic of the Si-O-Si bond present in samples. The absorption bands were observed at 2950 and 1400 cm^{-1} due to stretching and bending modes of C–H bond and the deeps observed at 765 & 1265 cm^{-1} due to the Si–C bonds. The 1265 cm^{-1} peak indicates the presence of the Si–C bonding [15]. The absorption deeps at 1600 and 3400 cm^{-1} corresponding to the polar –OH bonds

4.2. Determination of Young's modulus of silica Aerogel:

We have determined the 'Y' of the silica aerogel samples having different bulk densities and thermal conductivities of the silica aerogel monoliths. These values are reported in the table no. 1. We have used the silica aerogels having the five different densities. First the values of the surface deformations were calculated. Values of surface deformations of all the samples were also reported in table no. 1

Sample	Density 'ρ' (g/cm³)	Thermal conductivity 'k' (W/m K)	Applied load in 'g'	No of fringes.	Deformation (x 10^{-3} cm)	Youngs modulus 'Y' (x10^5 dyne/cm²)
M 9	0.1808	0.0023	2	7	5.9531	2.51
			5	13	6.6468	7.74
			10	15	7.7518	14.49
			15	17	20.23	7.68
M 17	0.1973	0.0029	1	4	3.100	2.41415
			2	12	9.300	1.61076
			5	21	10.89	4.7287
			7	23	11.37	6.1470
			10	40	14.32	9.1529
M 25	0.1566	0.0019	0.5	9	19.801	2.9946
			2	42	47.619	4.9404
M 26	0.1408	0.0019	1	7	15.90	1.531
			2	9	18.73	1.666
			3	16	46.50	1.569
M 31	0.1346	0.0016	0.5	7	18.049	1.10494
			1	10	37.35	2.8416
			2	27	75.73	2.8910

Table No:1. Physical and elastic properties of monolithic silica aerogels.

All the results have shown that as load on the sample increases, surface deformation also increases. All the values of the 'Y' calculated are reported in table no.1 and all the values are in good agreement with the standard values. The photographs of some of the silica aerogel samples are shown here.

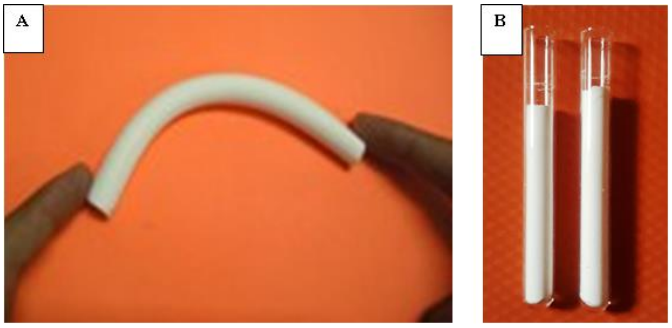

Figure 2: Photographs of synthesized silica aerogel monoliths,
[A] Flexible silica aerogel showing bending behaviour.
[B] Silica aerogels in 25 ml test tubes.

V. CONCLUSION

We have applied successfully DEHI technique for determination of 'Y' of sol-gel derived porous silica aerogel monoliths. These monoliths exhibited very low thermal conductivity. Above mentioned properties were achieved by quantifying the sol-gel chemistry and parameters during the supercritical drying of the silica aerogels. Usually, the derived porous materials are rigid in nature but this work demonstrated the new measure in the synthesis of porous, elastic and insulating silica aerogel monoliths.

VI. REFERENCES

[1]. S. S. Kistler, Nature, 127 [1931] 741.
[2]. T. Woigier, J Phalippou, Rev. Phys. Appl: C 4 – 24 (1984) 179.
[3]. K. E. Parmenter, J Milstein, J. Non-crystalline Solids, 223 (1998) 179.
[4]. M. Gronour, A Kadur, J Fricke (Ed). Aerogels, Springer, Berlin, 6 (1986).
[5]. D. Harnath, P. B. Wagh, G. M. Pajonk & A. V. Rao., Material res. Buletin, 08 (1997) 1079.
[6]. P. Mohan. C. Bhan, P Lal, R. Hradynath, Optics & Laser Tech. 4 (1982) 269.
[7]. P. Hariharan, "Optical Holography", Cambridge Univ. Press, London, P 210.

[8]. K. A. Haines and B. P. Hildebrand, App. Optics, 5 (1996) 595.
[9]. Aleksondrove E. B., Bonch. Bruevich A. M., Soviet Phy. Tech. Phys. 12 (1967) 258.
[10]. L. O. Heflinger, R. E. Brooks and R.F. Wuerker, J. Appl. Phys. 37 (1966) 462.
[11]. A. V. Rao, M. M. Kulkarni, Materials Res. Buletin 37 (9), 1667-1677, 2002.
[12]. A. V. Rao, G. M. Pajonk, N. N. Parvathy, J. of Sol-Gel Science & Technol. 3 (3) (1994) 205-217,
[13]. M. S. Kavale, D. B. Mahadik, V. G. Parale, A. V. Rao, P. B. Wagh, S. C. Gupta, AIP Conference Proceedings, 1 (144) (2012) 1283-1284.
[14]. Hegde N. D. & Rao A.V., J. Mater Sci. 42, (2007) 6965–6971.
[15]. Aelion R., Lobel A., and Eirich F., Recueil Traveux Chimiques, 69 (1950) 61-75.

International e-Conference on Recent Trends in Nano-Materials and Its Applications-2021
In Association with International Journal of Scientific Research in Science and Technology
Volume 9 | Issue 2 | Print ISSN: 2395-6011 | Online ISSN: 2395-602X (www.ijsrst.com)

Structural and Wettability Study of Electrodeposited NiO Thin Film

P. M. Kharade[1*], A.R. Babar[1], J. V. Thombare[2], S. D. Patil[3], S.D.Chavan[4], D.J. Salunkhe[5]

[1]Department of Physics, Shankarrao Mohite Patil Mahavidyalaya, Akluj, Dist-Solapur, Maharashtra, India

[2]Department of Physics, Vidnyan Mahavidyalaya, Sangola, Dist-Solapur, Maharashtra, India

[3]Department of Physics, Pratapsingh Mohite Mahavidyalaya, Karmala, Dist-Solapur, Maharashtra, India

[4]Department of Physics, D.B.F. Dayanand College of Arts & Science, Solapur, Dist-Solapur, Maharashtra, India

[5]Nanocomposite Research Laboratory, K.B.P. Mahavidyalaya, Pandharpur, Dist-Solapur, Maharashtra, India

ABSTRACT

In the present paper, nickel Oxide (NiO) thin film has been synthesized by galvanostatic electrodeposition method. The crystal structural and surface wettability study of NiO thin film was carried out using X-ray diffraction (XRD) study and contact angle meter techniques. The XRD study reveals the cubic crystal structure of NiO thin film. The surface wettability study shows NiO thin film is hydrophilic in nature.

I. INTRODUCTION

Nickel Oxide (NiO) is asemiconducting oxide material having wide band gap lies between the ranges of 3.6 eV to 4 eV [1-2]. Nickel oxide (NiO) thin film have received great interest due to good electronic, optical and magnetic properties with high chemical stability. Due to these features it is used in variety of potential applications such as, fuel cell [3], gas sensors[4], solar thermal absorbers[5], photodetectors [6], batteries [7] and catalyst [8].

The NiO thin film have been synthesized by different physical and chemical methods such as, chemical bath deposition method [9], sputtering method [10], sol-gel method [11], chemical vapor deposition method [12], pulsed laser deposition [13]. The electrodeposition method is one of the best suitable method for deposition of metal on electrode substrate. Because it is cheap, easily available, and give thin, uniform film on substrate.

In the present work, NiO thin film has been synthesized by potentiostatic electrodeposition method. The structural and surface wettability study of NiO thin film was carried out with the help of characterized by X-Ray diffraction (XRD) and surface wettability study.

II. EXPERIMENTAL DETAILS:

2.1 Substrate Cleaning

Substrate cleaning is a most important part in the deposition of thin films. If the substrate surface is contaminated, the resulting films can be non-uniform. Electrically conducting substrate is the necessary requirement of electrodeposition. These substrates were cleaned using following procedure:

1) The substrates were mirror polished using zero grade polish paper.
2) The substrates were washed with detergent and double distilled water,

3) Finally, the substrates were dried, degreased in AR grade acetone and were kept in dust free chamber.

2.1.2 Synthesis of Nickel Oxide (NiO) Thin Films:

Nickel Oxide (NiO) thin films preparation was performed using a two-electrode system. Graphite sheet was served as counter electrode. Stainless steel substrate was used as working electrode. For electrodeposition bath of Nickel oxide thin film was prepared by AR grade chemicals using double distilled water. For synthesis of Nickel Oxide (NiO) thin film electrode, we have used 0.2M Nickel nitrate aqueous solution. Nickel Oxide (NiO) thin film electrode was deposited potentiostatically on stainless steel (SS) substrates with constant potentials of 1.9 V for 20 minutes and then Nickel hydroxide was formed. For oxidation of nickel, the films were annealed at 400˚C for one hour. This oxidized film was used for further characterization.

III. RESULTS AND DISCUSSION

3.1 X-ray diffraction study:

X-ray diffraction is a powerful technique to identify the crystal structure of the electrode materials. Fig.1 shows the XRD pattern of the film on to the stainless steel substrate with 2θ range of 20 to 80°. The XRD pattern of the film revealed the formation of NiO with cubic crystal structure. The main peaks are indexed at (2θ) 37.37˚ (111), 43.6˚(200) and 62.94° (220) reflections which are in good agreement with the standard diffraction pattern of NiO cubic structure (JCPDS card no. 47-1049). In addition with this, peaks originated due to stainless steel substrate are indicated by 'SS'. Justin et al have reported similar kind of crystal structure for NiO material prepared by hydrothermal method using organic surfactants as templates [14].

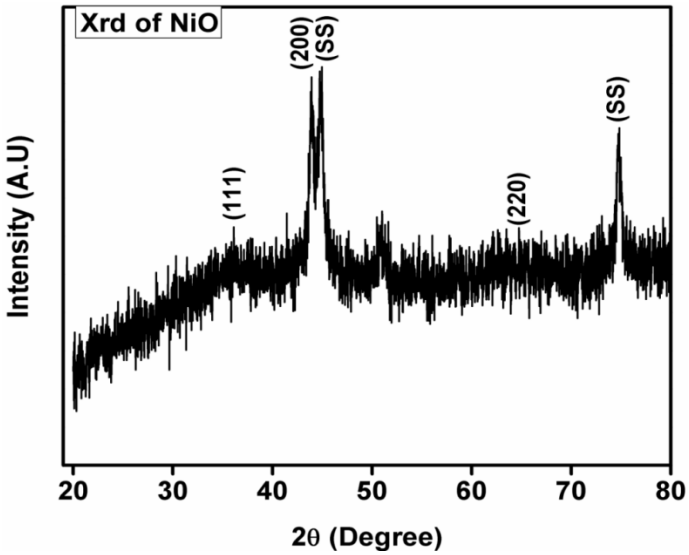

Fig.1 : X-ray diffraction study of NiO thin film.

3.2 Surface Wettability study:

Surface wettability study of the electrode was carried out with the help of water contact angle measurement with water as liquid drop.

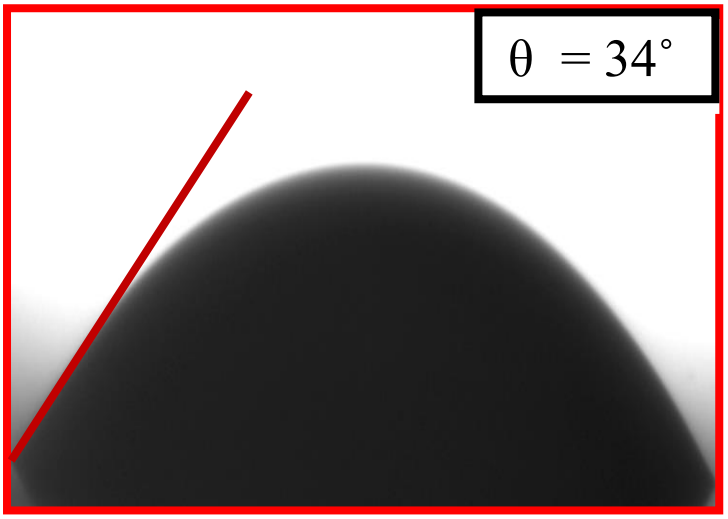

Fig.2 : contact angle of NiO thin film

The surface wettability study of film determines its ability to interact with ions when dipped into electrolyte, which is determined by measuring the contact angle with liquid electrolyte. Surface wettability of NiO thin film was studied by measuring contact angle. Fig.2 indicates the actual photograph of contact angle with film surface. The measured angle for NiO thin films is 34˚. In this study, it is observed that the NiO thin films are hydrophilic in nature and

contact angle for NiO decreases with increase in deposition cycles. The hydrophilic nature of film surface allows more interaction of electro active sites of NiO thin film.

IV. CONCLUSION

In the present report, we have synthesized nickel oxide (NiO) thin film on stainless steel substrates by using simple and economical potentiostatic electrodeposition method. The crystal structure and wettability study was carried out by using x-ray diffraction (XRD) and water contact angle measurements. The XRD study shows cubic crystal structure of electrodeposited NiO thin films. The surface wettability study shows NiO thin films are hydrophilic in nature.

V. REFERENCES

[1]. M. Guziewicz, et al., "Electrical and optical properties of NiO films deposited by magnetron sputtering," OpticaApplicata, vol. XLI, no. 2, pp. 431-440, 2011.

[2]. P. S. Patil and L. D. Kadam, "Preparation and characterization of spray pyrolyzed nickel oxide (NiO) thin films," Appl. Surf. Sci., vol. 199, pp. 211-221, 2002.

[3]. N.Shaigan, D.G.Ivey and W.Chen, "Metal-oxide scale interfacial imperfections and performance of stainless steels utilized as interconnects in solid oxide fuel Cells", J. Electrochem Soc., vol. 156, pp.B765-B770, 2009.

[4]. I. Hotovy, J. Huran, L. Spiess, R. Capkovic, S. Hascik, "Preparation and characterization of NiO thin films for gas sensor application, Vacuum 58 (2-3), (2000), pp. 300-307.

[5]. R. Cerc Korosec, P. Bukovec, B. Pihlar, A. SureaVuk, B. Orel and G. Drazie, "Preparation and structural investigation of electrochromic nanosizedNiOx films made via the sol-gel route" Solid State Ionics, vol.165, pp.191-200, 2003.

[6]. Leong-M. Choi, IM Seongil, "Ultrafiolet enhanced Siphotodetector using p-NiO films", Applied Surface Science 244(1-4), (2005), pp. 435-438.

[7]. C.M. Lambert and G. Nazri, P.C. Yu, "Spectroscopic and electrchemical studies of electrochromic hydrated nickel oxide

[8]. W. Azelee, W. Abu Bakar, M. Yusuf Othman, R. Ali , C. Yong, and S. Toemen, "The investigation of active sites on nickel oxide based catalysts towards the in-situ reactions of methanation and desulfurization," Modern Applied Science, vol. 3, no. 2, pp. 35- 43 ,2009.

[9]. E. Fujii, A. Tomozawa, H. Torii, and R. Takayama, "Preferred orientations of NiO films prepared by plasma-enhanced metalorganic chemical vapor deposition," Jpn. J. Appl. Phys., vol. 35, pp. L328-L330, 1996.

[10]. I. Hotovq, D. Buc, S. Hascik, and O. Nennewitz, "Characterization of NiO thin films preppared by reactive sputtering," Vaccum, vol. 50, pp. 41-44, 1998.

[11]. L. Cattin, B. A. Reguig, A. Khelil, M. Morsli, K. Benchouk, and J. C. Bernede, "Properties of NiO thin films deposited by chemical spray pyrolysis using different precursor solutions," Appl. Surf. Sci., vol. 254, no. 18, pp. 5814-5821, 2008.

[12]. X. H. Xia, J. P. Tu, J. Zhang, X. L. Wang, W. K. Zhang, and H. Huang, "Electrochromic properties of porous NiO thin films prepared by a chemical bath deposition," Sol. Energy Mater. Sol. Cells, vol. 92, no. 6, pp. 628-633, 2008.

[13]. K. Ravichandran and P. Philominathan, "Fabrication of antimony doped tin oxide (ATO) films by an inexpensive, simplified spray technique using perfume atomizer," Mater. Lett., vol. 62, pp. 2980-2983, 2008.

[14]. P. Justin, S.K. Meher, G.R. Rao, J. Phys. Chem. C 114 (2010) 5203.

International e-Conference on Recent Trends in Nano-Materials and Its Applications-2021
In Association with International Journal of Scientific Research in Science and Technology
Volume 9 | Issue 2 | Print ISSN: 2395-6011 | Online ISSN: 2395-602X (www.ijsrst.com)

Synthesis of MnS2 Thin Films by Chemical Route: Physicochemical Properties

R. B. Kharade[1], S. K. Jare[2,6], D. K. Sonavane[2], C. K.Kalawade[3], S. L. Kadam[1], R. N. Bulakhe[4], A. B. Bhalerao[5], R. V. Kathare[6*]

[1]P.G. Department of Physics and Research Centre New Arts Commerce and Science College, Parner, Ahmednagar, Maharashtra, India

[2]P.G. Department of Electronic Science, New Arts, Commerce and Science College, Ahmednagar, Maharashtra India

[3]Dr. Vithalrao Vikhe Patil College of Engineering, Post MIDC, Vadgaon Gupta (Vilad Ghat), Ahmednagar, Maharashtra, India

[4]Department of Polymer Science & Engineering, Korea National University of Transportation, Chungju, Republic of Korea

[5] Department of Applied Science, K. K. Wagh Institute of Engineering Education and Research, Amrutdham, Panchavati, Nashik, Maharashtra, India

[6]Karmaveer Mamasaheb Jagdale Mahavidyalaya, Washi, Osmanabad, Maharashtra, India

ABSTRACT

In present work, manganese sulfide (MnS2) thin films have been deposited by chemical route at room temperature on commercial glass substrate. Employed chemical method is inexpensive, simple and does not require any sophisticated instrument for deposition. The chemical bath is prepared from the mixture as solutions of manganese acetate tetrahydrate [C4H6MnO44H2O] as a manganese source, thiourea [(H2 N) 2 CS] as a sulfur source and ammonia solution used as a complexing agent, respectively. The structural and morphological analysis has been investigated using X-ray diffraction (XRD) and Scanning Electron Microscopy (SEM).

Keywords: DMS, chemical route, X-ray diffraction, Scanning,Electron Microscopy (SEM).

I. INTRODUCTION

Various kinds of binary and ternary chalcogenides materials are in focus of extensive research [1]. Chalcogenides materials have applications in optoelectronic devices, solar cells, photoconductors and infrared detector devices, etc. respectively. The various chalcogenides such as ZnS, Cu_2S, MnS_2, MoS_2, WS_2 are commonly used. Among all the manganese sulfide (MnS_2) is especially used in mixing with Zn and Cd to form (Zn, Mn)S and (Cd, Mn)S composites used in various applications. Manganese sulphide thin films with main advantages like wide direct band gap, cheap processing. As far as we know, there are

various methods of synthesis for managanese sulphide thin films like successive ionic layer adsorptions and reaction (SILAR), chemical bath deposition (CBD) and RF-sputtering etc. [2]. Chemical route is most feasible technique for film synthesis, since it is easy, simple and most-cost effective method of deposition [4]. In chemical route, manganese ions and a sulfur-containing organic compound (thiourea) are processed in alkaline water medium. Ammonia is used as complexing agent in deposition as it reduces spontaneous precipitation by slowly releasing of metallic ions, which avoids precipitation. In this work, MnS_2 thin film structures are reported by easy and simple chemical route at room temperature. Its structural and morphological studies are revealed by X-ray diffraction and Scanning electron microscopy, respectively.

II. EXPERIMENTAL DETAILS

Materials:

All The chemicals used are analytical grade. Manganese acetate tetrahydrate [$C_4H_6MnO_4.4H_2O$] used as a manganese source, thiourea [$(H_2N)_2CS$] used as a sulfur source and Ammonia solution was used as complexing agents and D.I. used as solvent. The pH of the solution was maintained by using ammonia solution.

Instruments:

For structural studies Philips PW1710 Diffractometer for the 2θ ranging from 200 to 800 with Cu-K_α (λ = 1.5418 A°) radiation. The Scanning Electron Microscopy (SEM) analysis is used for surface morphology study.

Glass substrate cleaning:

Commercial glass slides of dimensions 25 mm x 30 mm x 1.2 mm are used for the deposition. For better homogeneity and quality of films, cleaned slides are essential. The slides cleansed with help of detergent, after they are boiled in concentrated chromic acid (0.5 M) for 1 hour. The substrates washed with distilled water. Slides are immersed in distilled water before deposition.

Preparation of the MnS_2 thin films:

A total reactive solution prepared in a 100 ml beaker containing equimolar solutions of manganous acetate tetrahydrate (0.3M) as Mn source (50ml) and thiourea (0.3M) as a S sources (50ml). Solution is stirred well so that homogeneous solution was formed. The pH of the solution mixture was set with the help of ammonia to near about 10.6 with help of pH meter. The substrates were kept in the solution vertically at room temperature without stirring with the help of specially designed substrate holder for 24 hours. Dark brown deposited glass slides are removed gently. Finally substrates were washed in distilled water gently and dried in warm air.

III. RESULTS AND DISCUSSION

For Structural identification X-Ray Diffraction (XRD) was carried out within the range of angle 2θ between 10° to 80°. The MnS_2 thin films XRD pattern of deposited at room temperature for 24 hours deposition time is shown in Fig.1. The cubic crystal structure with five principal peaks corresponding to (2 0 0), (2 1 0), (2 1 1), (2 2 1) and (4 1 1) orientations. This XRD data is in good agreement with standard JCPDS card no.00-010-0616 and JCPDS card no. 00-010-0476 conforms cubical hauerite phase of MnS_2. Lattice constant (c) for cubical phase was determined from the relation in eq.1 [3].

$$\frac{1}{d^2_{hkl}} = \frac{4}{3}\left(\frac{h^2+hk+k^2}{a^2}\right)+\frac{l^2}{c^2} \quad (1)$$

From the position of the peak (2 0 0), determined lattice parameters a=b=c=6.09 A°, 17.4 nm is the average crystalline size of MnS_2 in the films. It was determined from line (2 0 0) by using Scherrer's formula,

$$D = \frac{0.9\lambda}{\beta\cos\theta} \quad (2)$$

where, β is the FWHM, λ is the X-ray wavelength and θ is the Bragg's angle.

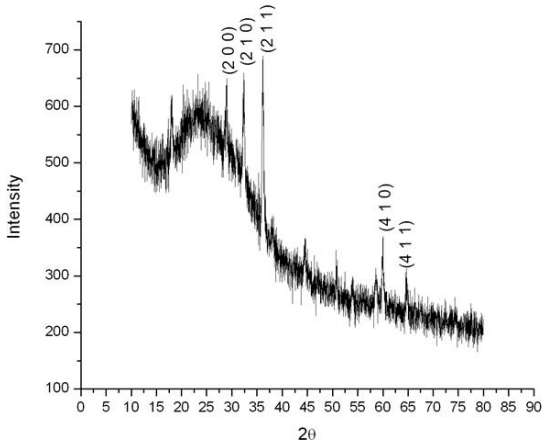

Fig.1. XRD pattern of MnS_2 thin films deposited on glass substrate.

2θ(degree)	FWHM in nm	h k l	d-spacing in (Å)
28.88	0.47	2 0 0	3.05
32.41	0.39	2 1 0	2.73
36.13	0.27	2 1 1	2.50
44.50	0.47	2 2 1	2.04
64.74	0.57	4 1 1	1.44

Using Scanning Electron Microscopy surface morphology was determined. Fig. 2 shows the SEM micrograph of MnS_2 films prepared on glass substrate for 24 h at room temperature by using simple chemical route. The film well covered and smooth all over glass substrate.

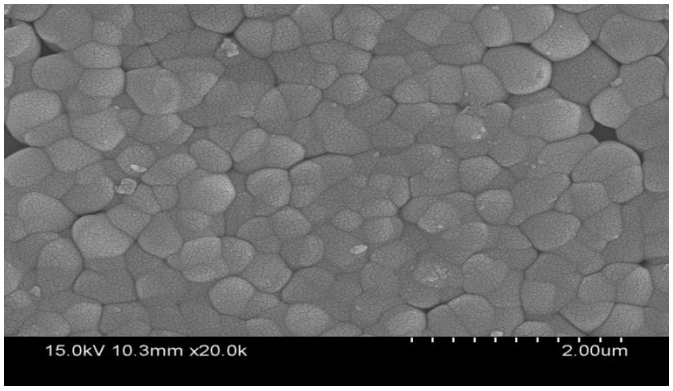

Fig.2. SEM images of MnS_2 thin films.

The films are firm and densely adhere to the surface. The grains are smaller with unequal in size and shapes. The particles are well adhering with unequal distribution the fine grain background.

IV. CONCLUSION

MnS2 thin films have been deposited sucessesfully on a glass substrate at room temperature by simple and cost effective chemical route method. From the XRD analysis, it was confirm that the film possesses a cubical structure of MnS2 of hauerite. The determined lattice parameters a=b=c=6.09A° were in a good match with the reported hauerite structured data. The SEM study showed smooth and well covered thin film on entire glass substrate.

V. REFERENCES

[1]. A. Kassim, T. W. Tee, H. S. Min, A. H. Abdullah, A.H. Jusoh,S. Nagalingam, Natural Science, 44 (2010) 446-453.

[2]. C. Gumus, C. Ulutas, Y. Ufuktepe, Optical Materials, 29 (2007) 1183-1187.

[3]. Cullity, Elements of X-ray Diffraction, Addision-Sesley Publishing Company Inc. USA.(1978) P-575.

[4]. P. R. Deshmukh, N. M. Shinde, S. V. Patil, R. N. Bulakhe, C. D. Lokhande, Chemical Engineering Journal, 223 (2013) 572-577.

[5]. D. B. Fan, H Wang, Y. C. Zhang, J Cheng, B. Wang, H. Yan, Mater Chem. Phys. 80 (2003) 44-47.

[6]. C. D. Lokhade, A. Ennaouti, P. S. Patil, M. Giersig, M. Muller, K.Diesner, H. Tributsch, Thin Solid Film. 330(2) (1998) 70-75.

[7]. A. B. Lundin, G. A. Kitaev, Inorg. Mater. (1965) 2107.

[8]. R Tepparo, P. D. Arco, A. Lichanot, Chem. Phys. Lett. 273(1-2) (1997) 83-90.

[9]. H. M. Pathan, S. S. Kale, C. D. Lokhande, S. H. Han, O. S. Jou, Mater. Res. Bull. 42(2007) 1565.

[10]. N. Khaorapapong, A. Ontam, J. Khemprasit, M. Ogawa, Appl. Clay Sci. 43 (2009) 238.
[11]. S. A. M. Hernandez, S. J. Sandoval, R. C. Perez, G. T. Delgado, B. S. Chao, O. J. Sandoval, J. Cryst. Growth, 256 (2003)12.
[12]. M. Demper, L. Chen, C. Bradford, K.A. Prior, W. Heimbrodt, Solid State Communication, 150 (2010)1092.
[13]. P. Zhao, Q. Zeng, X. He, H. Tang, K. Huang, J. Cryst. Growth. 310 (2008) 4268.
[14]. J. Lu, P.F.Qi, Y.Y. Peng, Z. Y. Meng, Z.P. Yang, W. C. Yu, Y.T. Qian, Chem. Mater. 13 (2001) 2169.
[15]. C. D. Lokhande, Mater, Chem. Phys. 27(1991)1.
[16]. R. N. Bhattaracharya, J. Electrochem. Soc. 129 (1982) 332.
[17]. I. Kaur, D. K. Pandya, K. L. Chopra, J. Electrochem Sic. 127 (1980)143.
[18]. D. K. Sonavane, S. K. Jare, R. V. Kathare, R. N. Bulakhe, J.-J. Shim, Materials Today: Proceedings 5 (2018) 7743–7747.

International e-Conference on Recent Trends in Nano-Materials and Its Applications-2021
In Association with International Journal of Scientific Research in Science and Technology
Volume 9 | Issue 2 | Print ISSN: 2395-6011 | Online ISSN: 2395-602X (www.ijsrst.com)

Electrochemical Synthesis of Manganese Oxide Thin Film for Super Capacitor

P. M. Kharade[1*], J. V. Thombare[2], S. D. Patil[3], S.S. Dhasade[2], P.B.Abhange[4], R. S. Gaikwad[5], C.S. Pawar[1], S. S. Deokar[1], D.J. Salunkhe[6]

[1]Department of Physics, Shankarrao Mohite Patil Mahavidyalaya, Akluj, Dist-Solapur, Maharashtra, India
[2]Department of Physics, Vidnyan Mahavidyalaya, Sangola, Dist-Solapur, Maharashtra, India
[3]Department of Physics, Pratapsingh Mohite Mahavidyalaya, Karmala, Dist-Solapur Maharashtra, India
[4]Department of Physics, G.M. Vedak College of Science, Tala, Raigad, Maharashtra, India
[5]Department of Chemistry, Vidnyan Mahavidyalaya, Sangola, Dist-Solapur, Maharashtra, India
[6]Nanocomposite Research Laboratory, K.B.P. Mahavidyalaya, Pandharpur, Dist-Solapur, Maharashtra, India

ABSTRACT

In the present investigation, we report synthesis of manganese dioxide (MnO2) thin film on low cost conducting substrate by electrodeposition method for supercapacitor application. The structural and surface wettability study of MnO2thin film was carried out with the help of X-ray diffraction (XRD) and contact angle meter. The supercapacitive properties of MnO2 thin film were carried out by using cyclic voltammetry (CV), charging-discharging (CD) study. The electrodeposited MnO2thin film shows specific capacitance of 430 F/g-at 10 mV/S scan rate. The specific energy and power of MnO2thin film were 7.40 kW/kg and 3.20 Wh/kg respectively. Hence, electrodeposited MnO2thin film is best electrode candidate for energy storage.

Keywords: supercapacitor, electrodeposition, MnO2, XRD, Cyclic voltammetry.

I. INTRODUCTION

In the recent years there is an urgent need of clean, renewable and sustainable energy storage devices. One such devices, supercapacitor or electrochemical capacitor plays key role in development of energy storage devices. It has higher energy density as compared to conventional capacitor and greater power densities than batteries.Supercapacitor have fascinated more attention due to outstanding electrochemical characteristics viz high power density, long capacitance retention ratio, good reversibility, environmental friendless, etc. The supercapacitor or electrochemical capacitor is broadly classified into two types depends on their charge storage mechanism such as electrochemical double capacitor and pseudocapacitor. In electrochemical double layer capacitor (EDLCs) charge storage takes place non faradically. Carbon based electrode material used in EDLCs. In pseudocapacitor charge storage takes place faradically. The conducting polymers and transition metal oxides are used as electrode material in pseudocapacitor. Manganese oxide is mostly studied as electrode material in transition metal oxide

family due to their excellent electrochemical properties such as, non-toxic, cheaper in cost, easy synthesis and variable oxidation states.It is used in catalysis, sensors, supercapacitor, rechargeable batteries and water waste treatment [1-5]. Manganese oxide electrode have been synthesized by various physical and chemical methods. Different synthesis methods gives different microstructures of manganese oxide. In supercapacitor nanocrystalline and hydrophilic electrode is mostly used for supercapacitor application. It provide higher surface area, more interaction of ions from electrode to electrolyte interface and shorten the diffusion path length which strongly improve the supercapacitive performance.

In the present work, efforts have been taken to synthesize manganese oxide electrode by potentiostatic electrodeposition method. There supercapacitive performance was tested by using cyclic voltammetry, charging-discharging studies.

II. EXPERIMENTAL

2.1. Synthesis of Manganese Dioxide (MnO_2) Thin Films:

Manganese Dioxide (MnO_2) thin filmwas carried out using a two-electrode system. Graphite sheet was served as counter electrode. Stainless steel substrate was used as working electrode. For synthesis of Manganese Dioxide (MnO_2) thin film, the aqueous bath contain 0.2M $MnCl_2$ aqueous solution. The Prior to deposition the stainless steel (SS) was used as substrate and it is well polished with zero grade polish paper rough to finish and rinsed with double distilled water and acetone. The MnO_2 thin film was deposited by using potentiostatic electrodeposition method by keeping potential of 1.8 V for 15 minutes, manganese hydroxide was formed. Further oxidation of Mn, the film was annealed at 300˚C for one hour. The colour of Mn changes from yellowish to black brown. Then oxidized film was used for further characterization.

2.2. Characterization techniques:

The as synthesized MnO_2 thin film was characterized by using different characterization techniques. The crystal structure and surface wettability study of MnO_2 thin film was carried out with help of by X-ray diffraction (XRD) techniquesusing Bruker axes D8 Advance Model with copper radiation (Kα of λ = 1.54 A˚) in the 2θ range between 20˚ to 80˚ and Rame-Hart contact angle meter respectively. The electrochemical performance of MnO_2 thin film was studied by using cyclic voltammetry and charging-discharging study. An electrochemical cell consists of three electrode systems, MnO_2thin film as a working electrode, graphite as a counter electrode and saturated calomel electrode (SCE) as a reference electrode. All electrochemical measurement was carried out using aqueous 0.5 M Na_2SO_4electrolyte solution.

III. RESULTS AND DISCUSSIONS

3.1. Structural study:

X-ray diffraction (XRD) is an important tool to analyze the crystal structural information of synthesized thin film. Fig (1) shows the XRD spectra of potentiostatically deposited MnO_2 thin film within2θ range between 20˚ to 80˚. The XRD pattern of MnO_2 thin film electrode shows tetragonal crystal symmetry. The lattice parameter observed in these case are a= b=94.815 AU and c=2.847 AU. The peaks observed in the XRD spectrum of MnO_2 thin film electrode were well matched with JCPDS data (Card No 72.1982). The additional peaks indexed (SS) in the XRD spectra is due to the stainless steel substrate only. Thus, XRD study confirms the crystalline structure of deposited MnO_2 thin film.

3.2. Surface wettability study

The surface wettability study of film determines its ability to interact with ions when dipped into electrolyte, which is determined by measuring the contact angle with liquid electrolyte. If contact angle

is less than 90°, then the film surface is said to be hydrophilic, and for greater than 90°, it is said to be hydrophobic. For more interaction of electrolyte ions with electro active site on the surface of thin film, the contact angle must be as low as possible. Wettability of MnO_2 thin film is studied by measuring contact angle. Fig. (2) shows the images of contact angle with film surface. The observed value of contact angle for MnO_2 thin films is found to be 76°. Thus, wettability study shows hydrophilic nature of MnO_2 thin film. The hydrophilic nature of electrode is feasible for supercapacitor, which allows more interaction of electro active sites of MnO_2 thin film with electrolyte [6].

3.3. Supercapacitive Study:

3.3.1. Cyclic Voltammetry (CV) Study:

Cyclic voltammetry (CV) is a most important tool to give the qualitative information about redox process and specific capacitance associated with electrode. Fig. (4) shows typical cyclic voltammogram of MnO_2 thin film at 10 mV/s scan rate within potential range of +1.2 V to -1.2 V in 0.5 M Na_2SO_4 electrolyte solution. The nature of CV curve is nearly rectangular in shape indicating the ideal pseudocapacitor behaviour of deposited MnO_2 thin film. The specific capacitance of the MnO_2 thin film was calculated by using following formulae,

Specific capacitance (C_s) = C/W ------ (1)

Where, C – capacitance in farad and W – the mass of active electrode materials in gm. The active mass of MnO_2 thin film in gm. The calculated value of specific capacitance of MnO_2 thin film is 430 F/gat 10 mV/s scan rate. The greater value of specific capacitance in present case is nanocrystalline and hydrophilic nature of MnO_2 thin film.

3.3.2. Charging-discharging study:

The electrochemical supercapacitor parameter such as coulombic efficiency, specific energy and power of the electrode was carried out with the help of charging-discharging study. Fig. (4) shows the charging-discharging (CD) study of MnO_2 thin film at 10 mA current density. The nature of charge and discharge curve is triangular in shape. There is a small voltage drop at the starting of discharge curve is due to internal resistance present between the MnO_2 thin film and electrolyte. The electrochemical supercapacitor was calculated by the following formulae:

Coulombic Efficiency=T_d/T_cx100 (2)

Specific power =(V X I_d)/W (3)

Specific energy=(V X I_d X T_d)/W (4)

Where, T_d and Tc is discharging and charging time in sec, V is voltage window volt, I_d is discharging current in A and W is the weight of active material in gm.

The coulombic efficiency of MnO_2 thin film was found to be 94% whereas the specific power and specific energy were observed to be 7.40 kW/kg and 3.20 Wh/kg, respectively.

IV. CONCLUSION

In summary, we have synthesized MnO2 thin film by potentiostatic electrodeposition method for supercapacitor application. The XRD study show the tetragonal crystal structure. The wettability study shows MnO2 thin film is hydrophilic in nature. The MnO2 thin film gives maximum specific capacitance of 430 F/g. The MnO2 thin film shows values of specific energy and specific power isbe 7.40 kW/kg and 3.20 Wh/kg respectively. Thus potentiostatistically deposited MnO2 thin film is suitable material for energy storage devices.

V. REFERENCES

[1]. D. Yan, S. Cheng, R. F. Zhuo et al., “Nanoparticles and 3D sponge-like porous networks of manganese oxides and their microwave absorption properties,” Nanotechnology, 20(2009) 105706.

[2]. Y. W. Tan, L. R. Meng, Q. Peng, and Y. D. Li, "One-dimensional single-crystalline Mn3O4 nanostructures with tunable length and magnetic properties of Mn3O4 nanowires," Chemical Communications, 47 (2011)1172.

[3]. X. Zhang, Z. Xing, Y. Yu et al., "Synthesis of Mn3O4 nanowires and their transformation to LiMn2O4 polyhedrons, application of LiMn2O4 as a cathode in a lithium-ion battery," CrystEngComm, 14(2012) 1485.

[4]. R. Ma, Y. Bando, L. Zhang, and T. Sasaki, "Layered MnO2 nanobelts: hydrothermal synthesis and electrochemical measurement," Advanced Materials, 16(2004)918.

[5]. J. Cao, Q. H. Mao, L. Shi, and Y. T. Qian, "Fabrication of γ-MnO2/α-MnO2/ hollow core/shell structures and their application to water treatment," Journal of Materials Chemistry, 21(2011) 16210.

[6]. P.M. Kharade, S.B. Kulkarni, D.J. Salunkhe, Nanoflakes like hydrophilic Mn2O3 thin film as a supercapacitor electrode, Chinese J. Phy. 55 (2017)1684.

Figure:

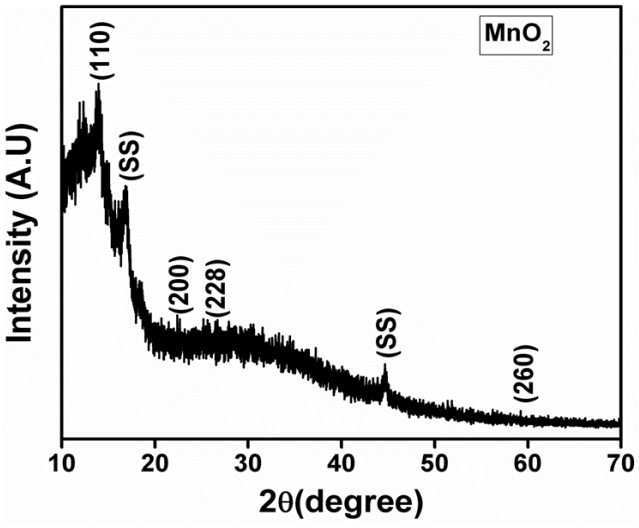

Fig. (1) XRD pattern MnO_2 thin film

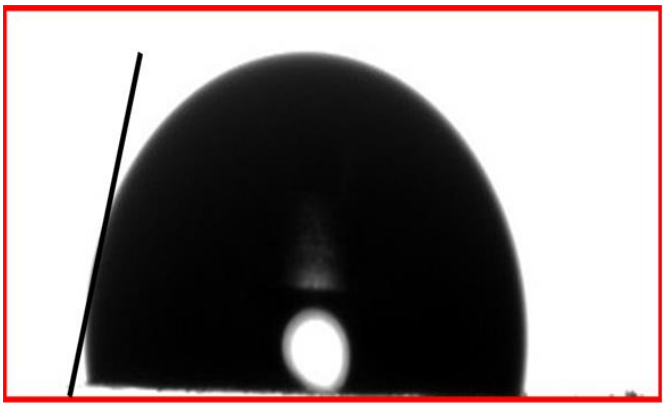

Fig. (2) Surface wettability of MnO_2 thin film

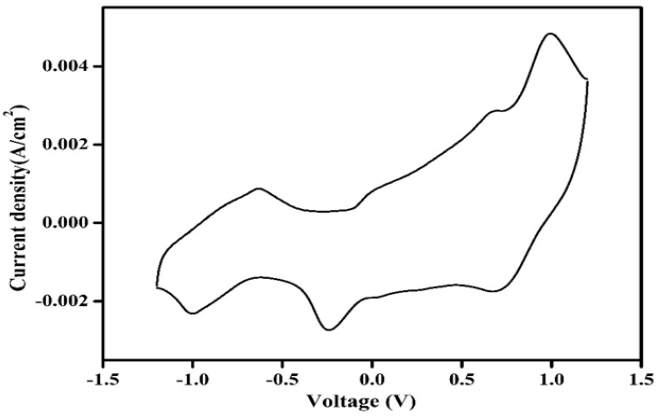

Fig. (3) CV of MnO_2 thin film

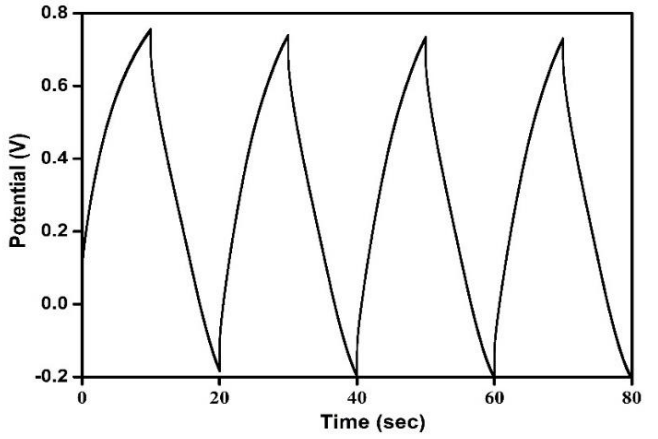

Fig. (4) Charging-discharging study of MnO_2 thin film

International e-Conference on Recent Trends in Nano-Materials and Its Applications-2021
In Association withInternational Journal of Scientific Research in Science and Technology
Volume 9 | Issue 2 | Print ISSN: 2395-6011 | Online ISSN: 2395-602X (www.ijsrst.com)

Electrochemical Synthesis of Vanadium Oxide Thin Films for Super Capacitor Application : A Review

R. S. Gaikwad[1], S. S. Dhasade[1], S. B. Patwari[2], P. M. Kharade[3], S. D. Patil[4], J. V. Thombare[1*]

[1]Vidnyan Mahavidyalaya, Sangola, Tal-Sangola, Dist-Solapur, Maharashtra-413307, India
[2]Lal Bahadhur Shastri Mahavidyalaya, Dharmabad-431809, Maharashtra, India
[3]Shankarrao Mohite Mahavidyalaya, Akluj, Dist-Solapur, Maharashtra, India
[4]Pratapsinh Mohite Mahavidyalaya, Karmala, Dist-Solapur, Maharashtra, India

ABSTRACT

The Electrodeposition of Vanadium oxide (VO) thin films are of great interest because of numerous applications in the field of electrochemical devices. Varieties of chemical and physical methods are available for synthesis of VO thin films. In the present mini review we are focusing on the synthesis of VO thin films by Electrodeposition methods and properties. We have studied the comparative study of structural and morphological properties of VO thin films. As per literature it is evident that as deposited VO thin films are amorphous in nature while upon annealing treatment VO thin films changes to crystalline nature. As deposited VO thin films have showed smooth nature but upon in-situ or ex-situ treatments morphology of VO thin films changes to nanostructures, nanoplates, inverse opal like structures etc. Also, we tried to compare the supercapacitive study of electrochemically deposited VO thin films.

Keywords: Electrodeposition, Vanadium Oxide, Thin Films, Supercapacitive Study, etc.

I. INTRODUCTION

Recently, researchers are trying to find the easy way for synthesis of thin films for suitable applications. Generally, the thin films are prepared by some physical methods and lots of thin films are prepared by chemical methods. The physical methods requires sophisticated instruments for preparation of thin films, also they require some ideal conditions such as pressure inside the instrument, vacuum, particular environment, temperature etc. So, these things waste time and other efforts. Other methods are chemical methods such as chemical bath deposition, Successive Ionic Adsorption and Reaction (SILAR) method, Electrodeposition, Sol-Gel method, Co-precipitation method, Solid State Reaction method etc. These methods have some advantages such as they do not require highly sophisticated instruments, precursors for synthesis easily available, not necessary to achieve ideal condition etc. But amongst of all chemical methods Electrodeposition is a unique chemical method for synthesis of various methods and deposited films have various applications such as supercapacitor, gas sensor, solar cell etc.

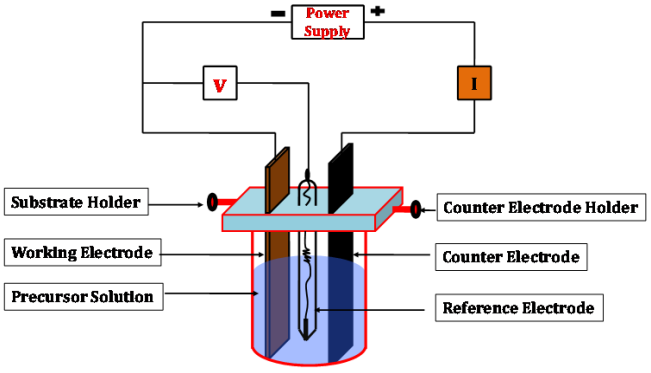

Figure 1: Schematic representation of Electrodeposition process having three electrode configurations.

In case of Electrodeposition, the depositing system consists of a deposition bath, three or two electrodes i.e. working electrode, counter electrode and reference electrode, and a power supply which provide electric field. Sometime, Electrodeposition process is mentioned as electrochemical process because materials are deposited from liquid phase (in deposition bath) to solid phase (on working electrode) by application of proper electric field. In Electrochemical synthesis, each component has its special role for making chemical change in material. Fig 1 shows the schematic presentation of Electrodeposition process.

As per requirement, researchers have made some modifications in the basic structure of Electrodeposition. There may be modification in bath such as making complex in the solution instead of just source solution. Also, there may be modification in bath temperature (i.e. at various temperatures), etc. So, Electrodeposition has variety of parameters through which we can get the proper thin film of suitable properties.

Many researchers have taken efforts to synthesis metal oxide thin films by Electrodeposition method such as NiO [1], Cu_2O [2], ZnO [3-4], molybdenum oxide [5], Manganese and Molybdenum Mixed Oxide [6], Cerium Oxide [7], ruthenium oxide [8], Vanadium Oxide/Manganese Oxide Hybrid [9] etc. Basically, electrochemical synthesis is preparing metal oxide based thin films at room temperature or as deposited films are not in oxide forms. So for proper phase or metal oxides post deposition treatments are necessary, such as annealing, sintering etc.

In the literature, we found that the VO thin films have been formed by various methods such as sol gel method [10], sputtering method [11], spray pyrolysis method [12], electron beam evaporation method [13], vacuum evaporation method [14], electrodeposition method [15], hydrothermal synthesis method [16], etc. In this review, we are focusing on the aspect of electrochemically synthesized VO thin films. Because it has some advantages over other methods, such as this method can be extended to industrial scale, even at low temperature ease of synthesis, this method is non-toxic i.e. environmentally friendly and the deposition set up requires low cost etc.

II. RESULTS AND DISCUSSIONS

A) Electrochemical synthesis of VO thin films:

The VO thin films can be electrodeposited by three different modes such as potentiostatic mode (by keeping constant applied potential across working and counter electrode), galvanostatic mode (by keeping constant applied current density across working and counter electrode) and potentiodynamic mode (by varying potentials across working and counter electrode). In the Electrodeposition of VO thin films, it is evident that every parameter is important to control the film quality. Here it is found that deposition mode, precursors and its concentrations, electrolyte either aqueous or non-aqueous, working electrode i.e. substrate, deposition time or deposition cycles etc., these parameters are very important to study the Electrodeposition of VO thin films. Here we have summarized few reports for Electrodeposition of VO thin films in Table 1.

Table 1: Electrodeposition of VO thin films

Sr. No.	Mode of deposition	Parameters	Precursors	Substrate	Reference
01	potentiodynamic	from +0.2 to -0.7 V (SCE) at 50 mV/s for several hours	NH_4VO_3	150 stainless steel mesh	[17]
02	Galvanostatic	current density of 10-12 mA/cm^2	oxovanadium sulfate solutions (0.2 mole/L, pH 1.8-2.0)	stainless steel 18H12X9T plates	[18]
03	Potentiostatic	2.5 volt for 5 min	0.05 M NH_4VO_3 aqueous solution	ITO-coated glass substrate	[19]
04	Potentiostatic	2 V vs SCE	0.25 M $VOSO_4.xH_2O$ solution in 1:1 (v/v) mixture of deionized water and ethanol	ITO/FTO coated glass	[20]
05	Potentiostatic	0.7 V vs. SCE	0.1 M $VOSO_4$	a piece of carbon cloth	[21]
06	potentiodynamic	the potential 20 times between 0 mV and 2000 mV at a rate of 50 mV/s	50 mM $VOSO_4.H_2O$ solution dissolved in 1.0 M H_3PO_4	PtIr wire	[22]
07	Galvanostatic	3 mA cm^{-2} for 1800 s	1 M aqueous Vanadium sulfate oxide hydrate solution containing 50% wt. ethanol	polystyrene sphere (PS) template	[23]

B) Structural study:

The electrodeposited vanadium oxide thin films have been characterized by x-ray diffraction (XRD) study. From the literature, it is found that the deposited films are in amorphous nature. After annealing, electrodeposited vanadium oxide film becomes crystalline in nature. Ghosh and et al have been reported that the deposited V_2O_5 samples annealed at 200 °C under ambient conditions show no characteristic peak ambient condition of V_2O_5 and after annealing at 500 °C reveals polycrystalline nature of V_2O_5 samples [24]. Raj and et al have reported the calcinations of vanadium oxide thin films for better crystallinity. They have reported the orthorhombic phase with the lattice parameters of a=11.54Å, b=4.383Å and c=3.571Å. The calculated value of crystallite size was reported to be 18 nm [25]. Tsui and et al have reported the partial reduction of V_2O_5 by annealing in air. According to their study, it is evident that the as deposited films are amorphous in nature while upon annealing the films showed monoclinic crystalline structure, possibly intermixed with nanocrystalline/amorphous phases [26]. Yu and et al have been reported that as deposited vanadium

oxide thin films are hydrated in nature and growth is along (001) direction, upon annealing at 500 °C vanadium oxide thin films were completely dehydrated and transforming to orthorhombic phase. Also, after annealing crystallite size changes from 4.2 nm to 32.1 nm and interlayer distance changes from 10.94 A° to 4.23 A° [27]. Aamir and et al have reported XRD pattern of the sample annealed at 350 °C for 4 h. They have reported orthorhombic V_2O_5 having two layers comprising of stacks of distorted VO_5 square pyramids that share edges forming zigzag double chains [28]. Le and et al have reported α and β two phases V_2O_5 films [29].

C) Morphological study:

The morphological study provides the basic structure of materials, also with the help of morphological study it's easy to correlate with other study for analysis of results. The morphological study is made with the help of SEM images.

Aamir and et al have reported the compact and agglomerated V_2O_5 with no specific morphology as they undergo irregular growth with larger particles by potentiostatic mode of electrodeposition. Also, they have reported that formation of well-defined nanoplates like morphology having particle size 200–300 nm with voids prepared by Galvanostatic mode of electrodeposition. So, here we found that the deposition method alters the morphology of vanadium oxide films [28]. The post deposition treatments such as annealing also have influence on the morphology of vanadium oxide thin films. Le and et al have reported the effect of annealing temperature on morphology of vanadium oxide thin films. They have reported that as deposited vanadium oxide thin films shows smooth surface due to amorphous nature and upon annealing at 500 °C or above temperatures the nanorods are formed and as annealing temperature increase the length of nanorods increases this is may be attributed to the high diffusion rate in the surface of the film [29]. Some researchers have tried to control the morphology of vanadium oxide films during electrodeposition, like use of template. Armstrong and et al have reported the use of opal template for control of morphology of vanadium oxide thin films. They have reported that morphology without opal template is undulating film-like structure, while with the help of opal template it becomes inverse opal like structure [20]. In case of electrodeposition, various parameters can be controlled for getting particular morphology, such as electrodeposition time. Lu and et al have reported that electrodeposition time increased from 40 seconds to 60 seconds, the morphology changed from smooth to typical sea-island like morphology [30]. Lu and Zhou have reported the combination of in-situ and ex-situ treatment on vanadium oxide thin films and they have been reported that morphology of vanadium oxide thin films without in-situ or ex-situ or both treatments are featureless. They have found that upon in-situ and ex-situ treatment, morphology changes from non porous nano-particles to nano-rods [31]. All these reports are summarized in Table2.

Table2: Effect of in-situ and ex-situ treatments for electrodeposition and its effect on morphology

Sr. No.	Effect	Morphology	Reference
01	By changing mode of electrodeposition	No specific morphology to well defined nanoplates	[28]
02	By increasing annealing temperature	Smooth surface to nano-rods with increasing length	[29]
03	By use of template	undulating film-like structure to inverse opal like structure	[20]
04	By increasing electrodeposition time	smooth to typical sea-island like morphology	[30]
05	By using template and annealing treatment	non porous nano-particles to nano-rods	[31]

D) Supercapacitive study:

Here we have summarized the supercapacitive study of electrodeposited vanadium pentoxide thin films. Supercapacitive study will be analyzed with the help of cyclic voltammetry, Galvanostatic charge-discharge (GCD) study and electrochemical impedance study. Here we are comparing the values of specific capacitance either it may be calculated from the cyclic voltammetry study or it may be calculated from GCD study. Table 3 shows the comparative study of values of specific capacitance. From this comparative study, other researcher can get the information about electrolyte, potential windows, value of specific capacitance etc.

Table 3: Comparative study of specific capacitance of electrodeposited vanadium pentoxide thin films

Sr. No.	Technique from which specific capacitance calculated	Parameters	Electrolyte	Specific capacitance	Ref.
01	Cyclic Voltammetry study	Scan rate: 2 $mV.s^{-1}$ with respect to a Ag/AgCl reference electrode Potential window: from – 0.2 V to 0.8 V	2 M KCl electrolyte	214 $F.g^{-1}$	[24]
02	Cyclic Voltammetry study	Scan rate: 10 $mV.s^{-1}$ vs SCE Potential window: from – 0.2 V to 0.6 V	0.5 M K_2SO_4 electrolyte	279 $F.g^{-1}$	[32]
03	GCD method	Current density: 1 $A.g^{-1}$	0.5 M $LiClO_4$ in PC	657 $F.g^{-1}$	[28]
04	Cyclic Voltammetry study	Scan rate: 5 $mV.s^{-1}$ vs SCE Potential window: from –1.3V to –0.1 V	1 M KCl	608 $F.g^{-1}$	[33]
05	Cyclic Voltammetry study	Scan rate: 5 $mV.s^{-1}$ vs Ag/AgCl Potential window: from – 0.2 V to 0.8 V	3 M KCl	350 $F.g^{-1}$	[34]

III.CONCLUSION

The VO thin films will be electrodeposited by three different modes like potentiostatic mode, galvanostatic mode and potentiodynamic mode. The working electrode would be any conducting substrate used in electrodeposition of VO thin films. The role of precursor and its concentration is important in electrodeposition because the oxidation potentials may be differ for precursors and its concentrations. The structural investigations showed that as deposited films are amorphous in nature, so for crystalline nature it is necessary to anneal the samples at 500 °C. So annealing of sample are prime requirement for good crystalline nature of samples. From morphological study, it is evident that the as deposited films are smooth in nature i.e. they are featureless in nature, for further use it is necessary to modify the samples by the use of in-situ and ex-situ treatments such as Electrodeposition time, Electrodeposition mode, use of template, annealing of samples etc then samples changes to nano-plates or

nanostructures etc. In supercapacitive study it is evident that the specific capacitance can be calculated either from cyclic voltammetry or galvanostatic charge-discharge study. It is evident that different electrolytes for VO thin films have different potentials windows (for CV study) and different loads of current density (for GCD study). So, this mini review will help to new researcher to get proper idea of Electrodeposition of VO thin films and its structural, morphological study along with supercapacitive study.

IV. REFERENCES

[1]. A. C. Sonavane, A. I. Inamdar P. S. Shinde, H. P. Deshmukh R. S. Patil P. S. Patil, Efficient electrochromic nickel oxide thin films by Electrodeposition, Journal of Alloys and Compounds, 489(2010) 667

[2]. Y. Tang, Z. Chen, Z. Jia, L. Zhang, J. Li, Electrodeposition and characterization of nanocrystalline cuprous oxide thin films on TiO2 films, Materials Letters, 59(2005)434

[3]. G. Machado, D. N. Guerra, D. Leinen, J. R. Ramos-Barrado, R. E. Marotti, E. A. Dalchiele, Indium doped zinc oxide thin films obtained by Electrodeposition, Thin Solid Films, 490(2005) 124

[4]. T. Yoshida, D. Komatsu, N. Shimokawa, H. Minoura, Mechanism of cathodic electrodeposition of zinc oxide thin films from aqueous zinc nitrate baths, Thin Solid Films, 451–452(2004)166

[5]. R. S. Patil, M. D. Uplane, P. S. Patil, Structural and optical properties of electrodeposited molybdenum oxide thin films, Applied Surface Science, 252(2006)8050

[6]. M. Nakayama, A. Tanaka, Y. Sato, T. Tonosaki, K. Ogura, Electrodeposition of manganese and molybdenum mixed oxide thin films and their charge storage properties, Langmuir 21(2005)5907

[7]. T. D. Golden, A. Q. Wang, Anodic Electrodeposition of Cerium Oxide Thin Films: II. Mechanism Studies, Journal of The Electrochemical Society 150(2003)C621

[8]. V. D. Patake, C. D. Lokhande, O. S. Joo, Electrodeposited ruthenium oxide thin films for supercapacitor: Effect of surface treatments, Applied Surface Science, 255(2009)4192

[9]. D. Rehnlund, M. Valvo, K. Edström, L. Nyholm, Electrodeposition of Vanadium Oxide/Manganese Oxide Hybrid Thin Films on Nanostructured Aluminum Substrates, Journal of The Electrochemical Society, 161 (2003)D515

[10]. L. Li, S. Peng, H.Y. Chen, X. Han, F. Cheng, M. Srinivasan, S. Adama, S. Ramakrishna, J. Chen, Polypyrrole-coated hierarchical porous composites nanoarchitectures for advanced solid-state flexible hybrid devices, Nano Energy, 19(2016)307

[11]. N. Ozer, C.M. Lampert, Electrochromic performance of sol-gel deposited WO3–V2O5 films, Thin Solid Films, 349(1999)205

[12]. J.K. Lee, G.P. Kim, I.K. Song, S.H. Baeck, Electrodeposition of mesoporous V2O5 with enhanced lithium-ion intercalation property, Electrochem. Commun. 11(2009)1571

[13]. S. Papaefthimiou, G. Leftheriotis, P. Yianoulis, Study of electrochromic cells incorporating WO3, MoO3, WO3-MoO3 and V2O5 coatings, Thin Solid Films, 343(1999)183

[14]. C.E. Patil, N.L. Tarwal, P.S. Shinde, H.P. Deshmukh, P.S. Patil, Synthesis of electrochromic vanadium oxide by pulsed spray pyrolysis technique and its properties, J. Phys. D, 42(2009) 025404

[15]. S. Capone, R. Rella, P. Siciliano, L. Vasanelli, A comparison between V2O5 and WO3 thin films as sensitive elements for NO detection, Thin Solid Films, 350(1999)264

[16]. J. Zheng, Y. Zhang, X. Jing, Q. Wang, T. Hu, N. Xing, C. Meng, Improvement of the specific capacitance of V2O5 nanobelts as

supercapacitor electrode by tungsten doping, Materials Chemistry and Physics, 186(2017)5

[17]. E. Andrukaitis, Lithium intercalation in electrodeposited vanadium oxide bronzes, Journal of Power Sources, 119–121(2003)205

[18]. R. Apostolova, B. Markovsky, D. Aurbach, E. Shembel, Effect of Superhalogen Anions on the Electrochemical Behavior of V2O5 Electrodes in Redox Reactions with Lithium in EC-DMC/Li-Salt Solutions, ECS Transactions, 95 (1) 183-200 (2019)

[19]. E. A. A. Arbab, G. T. Mola, V2O5 thin film deposition for application in organic solar cells, Appl. Phys. A 122 (2016)405

[20]. E. Armstrong, D. McNulty, H. Geaney, C. O'Dwyer, Electrodeposited Structurally Stable V2O5 Inverse Opal Networks as High Performance Thin Film Lithium Batteries, ACS Applied Materials & Interfaces, 7(2015)27006

[21]. M. H. Bai, L. J. Bian, Y. Song, X. X. Liu, Electrochemical codeposition of Vanadium Oxide and Polypyrrole for High Performance Supercapacitor with High Working Voltage, ACS Applied Materials & Interfaces, 6(2014)12656

[22]. J. A. Bennett, J. E. Pander III, M. A. Neiswonger, Investigating the viability of electrodeposited vanadium pentoxide as a suitable electrode material for in vivo amperometric hydrogen sulfide detection, Journal of Electroanalytical Chemistry, 654 (2011) 1

[23]. M. Chen, X. Xia, J. Yuan, J. Yin, Q. Chen, Free-standing three-dimensional continuous multilayer V2O5 hollow sphere arrays as high-performance cathode for lithium batteries, Journal of Power Sources, 288 (2015) 145

[24]. A. Ghosh, E. J. Ra, M. Jin, H. K. Jeong, T. H. Kim, C. Biswas, Y. H. Lee, High Pseudocapacitance from Ultrathin V2O5 Films Electrodeposited on Self-Standing Carbon-Nanofi ber Paper, Adv. Funct. Mater. 21(2011) 2541

[25]. D. V. Raj, V. Nandhinidevi, D. Mangalaraj, C. Viswanathan, Electrodeposition of V2O5 nanorods on current collector substrate, AIP Conf. Proc., 1447(2012)435

[26]. L. Tsui, H. Hildebrand, J. Lu, P. Schmuki, G. Zangari, Metal-insulator transition in nanocomposite VOx films formed by anodic electrodeposition, Applied Physics Letters, 103(2013)202102

[27]. D. Yu, Y. Qiao, X. Zhou, J. Wang, C. Li, C. Chen, Q. Huo, Mica-like vanadium pentoxide-nanostructured thin film as high-performance cathode for lithium-ion batteries, Journal of Power Sources, 266(2014)1

[28]. A. Aamir, A. Ahmad, Y. Khan, Z. U. Rehman, N. U. Ain, S. K. Shah, M. Mehmood, B. Zaman, Electrodeposited thick coatings of V2O5 on Ni foam as binder free electrodes for supercapacitors, Bull Mater Sci, 43(2020)273

[29]. T. K. Le, M. Kang, S. W. Kim, Room-temperature photoluminescence behavior of α-V2O5 and mixed α-β phase V2O5 films grown by electrodeposition, Materials Science in Semiconductor Processing, 94 (2019) 15–21

[30]. Y. R. Lu, T. Z. Wu, C. L. Chen, D. H. Wei, J. L. Chen, W. C. Chou, C. L. Dong, Mechanism of electrochemical deposition and coloration of electrochromic V2O5 nano thin films: an in situ x-ray spectroscopy study, Nanoscale Research Letters, 10 (2015)387

[31]. Y. Lu, X. Zhou, Synthesis and characterization of nanorod-structured vanadium oxides, Thin Solid Films, 660 (2018) 180

[32]. M. A. Sutar, M. S. Pawar, M. K. Rendale, S. K. Kandalkar, Effect of annealing on super-capacitive performance of electrodeposited vanadium-nickel oxide thin film electrode, Imperial Journal of Interdisciplinary Research (IJIR), 2(5)(2016)595

[33]. R. S. Ingole, B. J. Lokhande, Electrochemically synthesized mesoporous architecture of vanadium oxide on flexible stainless steel for high performance supercapacitor, J Mater Sci: Mater Electron, 28(2017)10951

[34]. J. D. Xie, H. Y. Li, T. Y. Wu, J. K. Chang, Y. A. Gandomi, Electrochemical energy storage of nanocrystalline vanadium oxide thin films prepared from various plating solutions for supercapacitors, Electrochimica Acta, 273 (2018) 257

International e-Conference on Recent Trends in Nano-Materials and Its Applications-2021
In Association with International Journal of Scientific Research in Science and Technology
Volume 9 | Issue 2 | Print ISSN: 2395-6011 | Online ISSN: 2395-602X (www.ijsrst.com)

Efficacy of Galvanostatically Deposited Cobalt Oxide Electrode for Supercapacitor Application

Shubhangi Gavande[1,3], Shivani Gavande[2], B. R. Karche[3]

[1]Department of Physics, Sangameshwar College, Solapur - 413003, Maharashtra, India

[2] Research Scholar, Functional Materials Research Laboratory, School of Physical Sciences, P.A.H. Solapur University, Solapur- 413255, Maharashtra, India

[3]Department of Physics, Shankarrao Mohite Mahavidyalaya, Akluj, Dist. Solapur, Maharashtra, India

ABSTRACT

Cobalt oxide electrode was electrodeposited on stainless steel substrates at room temperature using Cobalt acetate as the precursor solution by galvanostatic route. The as-deposited electrodes were annealed at 400ºC, 500ºC and 600ºC. The structural analysis was done by X-ray diffraction technique, morphological analysis by SEM and wettability studies were carried out by contact angle measurement. The electrochemical properties of the deposited thin film electrode were done in aqueous 1M Na_2SO_4 through cyclic voltammetry and galvanostatic charge-discharge analysis. The thin film electrode showed maximum Specific capacitance of 295 Fg^{-1} at 5mVs^{-1} scan rate, Specific energy 3.6Wh/kg, Specific Power 3 kW/kg and 56% Coulomb efficiency.

Keywords: Cobalt Oxide, Electrodeposition, Thin Films, Cyclic Voltammetry, Supercapacitor, Charge–Discharge.

I. INTRODUCTION

Today the world urgently needs efficient and eco-friendly energy storage device with long life, high reliability and energy efficiency with high charge-recharge capacity. One of such energy sources with good storage mechanism is the Supercapacitor which has high power density, high charge–discharge cycle life and high energy efficiency. Now, these days Supercapacitors have forced their way in to power source applications such as hybrid electric vehicles, telecommunications, particularly associated with cellular phones for a reduction of the size of the batteries and pacemakers [1].

The most extensively used active material for supercapacitor electrode are TMO's due to their good chemical stability, capricious valence etc. [2]. Co_3O_4 has been widely investigated and can be considered as a replacement for RuO_2, due to its low cost, low environmental hazardous impact, its number of stable oxidation states and subsequent high theoretical specific capacitance [3]. Cobalt oxide has been a most tempting electrode material for supercapacitor electrode due to its high theoretical SC (3560 Fg^{-1}) with good reversibility [4]. Cobalt oxide has excellent electrochemical performance [5]. The specific capacitance of as-deposited Cobalt oxide thin film electrode is found to be greater than the reported

values [6, 7], and the specific energy so obtained was found to be greater than that reported [8].

II. EXPERIMENTAL DETAILS

2.1 Preparation of Cobalt oxide thin film electrode

Cobalt oxide thin films were deposited on stainless steel substrates using aqueous 0.1 M Cobalt acetate precursor solution by galvanostatic route of electrodeposition method. The galvanostatic deposition of the thin film electrode was carried out in a three-electrode system with cobalt oxide as a working electrode, a platinum electrode as a counter electrode and saturated calomel electrode (SCE) as the reference electrode. The galvanostatic deposition resulted in accumulation of Cobalt hydroxide material on the stainless steel substrates in the form of very sticky, uniform, well-adherent and homogeneous thin films. The deposited good quality films were then annealed at 400ºC, 500ºC and 600ºC annealing temperatures, respectively to produce the necessary Cobalt oxide material deposition.

III. RESULTS AND DISCUSSION

3.1 Structural elucidation studies and compositional analysis

The structural investigation of Cobalt oxide thin film was done using X-ray Diffraction technique. The XRD pattern of galvanostatically deposited Co_3O_4 thin film at 5mAcm^{-2} current density and annealed at 400ºC, 500ºC and 600ºC annealing temperatures is illustrated in Fig.1. The diffraction pattern comprises of characteristic peaks of Cobalt oxide at 2θ values 20.05º, 31.03º, 36.6º, 38.27º, 44.12º, 50.81º, 59.21º, 65.01º, 77.18º with (111), (220), (311), (212), (400), (422), (511), (440), (533) planes of Cobalt oxide which are equivalent to simple cubic crystal structure (JCPDS No. 42-146). The diffraction pattern consists of sharp peaks with the most prominent peak at 2θ = 38.27º with (311) plane of Cobalt oxide crystal lattice. The lattice constant at this prominent peak is a = 6.802 Å and inter planar spacing is d = 2.050 Å. Except Co_3O_4 phases, no diffraction peaks corresponding to CoO or Co phases are seen which thus approves the formation of pure cubic Co_3O_4 structure [9].

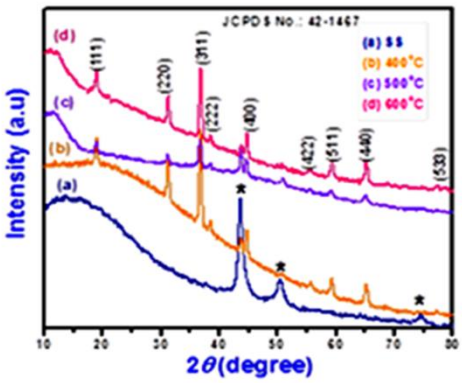

Fig.1. XRD of Galvanostatically deposited Cobalt oxide thin film

The average crystallite size of Co_3O_4 was calculated along the prominent peak of 2θ = 38.27º with (311) plane using Scherrer relation and were found to be 1.614 nm at optimized 500ºC annealing temperature.

3.2 Surface Wettability study

In the surrounding of air, the wetting of solid with water is dependent on the relation among the interfacial tensions (i.e. water/air, water/solid and solid/air). The ratio between these tensions determines the contact angle 'θ' between water droplets on a given surface [10]. A surface with water contact angle 0º means complete wetting and greater than 180º means complete non-wetting [10].

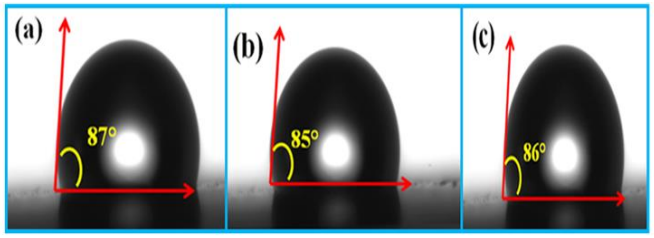

Fig.2. Contact angle of Co_3O_4 electrode at 400°C, 500°C and 600°C annealing temperatures

The hydrophilic nature (θ < 90º) denotes the supercapacitive property of the electrode material surface to make close contact with the aqueous electrolyte necessary for charge transfer between the two. The measured contact angles of Co_3O_4 electrode were 87º, 85º and 86º at 400ºC, 500ºC and 600ºC annealing temperatures respectively, as represented in

Fig. 2. This shows that the hydrophilic Co_3O_4 electrode material possesses high surface energy. It may be due to cohesive force between water droplet and hydroxide of Co_3O_4 electrode material [11]. This hydrophilic property of Co_3O_4 electrode material makes it feasible for supercapacitive energy storage devices.

3.3 Surface morphological studies

The display in Fig.3.(a), (b) and (c) is the SEM images of Co_3O_4 electrode annealed at 400ºC, 500ºC and 600ºC, respectively. The SEM images comprise of microspheres with highly porous network. The microspheres are aggregated nano particles, uniformly arranged in the form of columns with empty spaces between, giving them a spongy appearance with canal or ridges like structures throughout the sample surface, resulting in an abundant porous structure. The images clearly represent increase in annealed temperatures, increases the dense layers of spongy clusters caused due to agglomeration of nano particles. These clusters of spongy nano particles are inter-linked with each other forming a highly rough and porous surface. Such type of porous structure resulted due to the film formation based on the nucleation and coalescence. Such surface morphology has attracted increasing interest due to its large surface area which is the key factor for efficient electrode in alkaline batteries and supercapacitor devices [12].

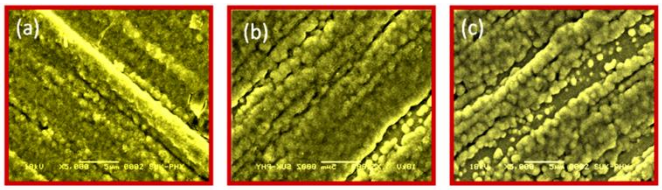

Fig.3 SEM images of Co_3O_4 electrode annealed at 400°C, 500°C, and 600°C respectively

3.4 Supercapacitive properties of Cobalt oxide electrode

3.4.1. Cyclic voltammetry

Electrochemical analyzer was used to conduct Cyclic voltammetry (CV) with saturated calomel electrode (SCE) as the reference electrode, a platinum wire as counter electrode and stainless steel as working electrode. The specific capacitance was calculated from Cyclic voltammetry.

3.4.1.1. Influence of annealing temperature on supercapacitive behaviour of Co_3O_4 electrode

The galvanostatically electrodeposited Cobalt oxide thin film electrode was annealed at three different temperatures namely 400ºC, 500ºC and 600ºC, respectively. The specific capacitance increased up to a particular temperature and then decreased. The temperature at which the specific capacitance was maximum i.e. 500ºC was taken as the optimized temperature for the electrode. The cyclic voltammetry curves for Co_3O_4 electrode at different annealed temperature in 1M aqueous Na_2SO_4 electrolyte are displayed in Fig.4. It is seen from Fig.4 that both cathodic and anodic current peaks decrease with increase in the annealing temperature. This infers that more Cobalt hydroxide constituent is converted into Cobalt oxide leading to larger capacitance of the deposited material. As the annealing temperature increases, the cathodic and anodic peak currents continue to decrease until a temperature is reached at which only non-faradaic (capacitive) current exists [13].

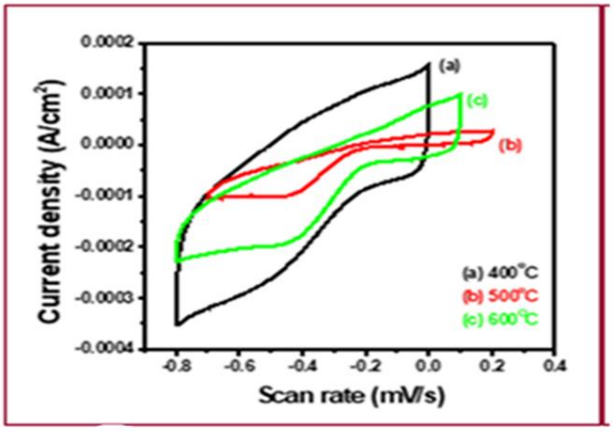

Fig.4. CV curves for Co_3O_4 electrode at different annealed temperature in 1M aqueous Na_2SO_4 electrolyte

3.4.1.2. Effect of sweep rates on Specific capacitance.

The CV plot of Co_3O_4 electrode at scan rates from 5mV to 100 mV in potential window from 0.2 V to -0.7V in aqueous 1M Na_2SO_4 electrolyte are displayed in Fig.5. The rectangular CV plots indicate the potential capacitive behaviour of electrodes.

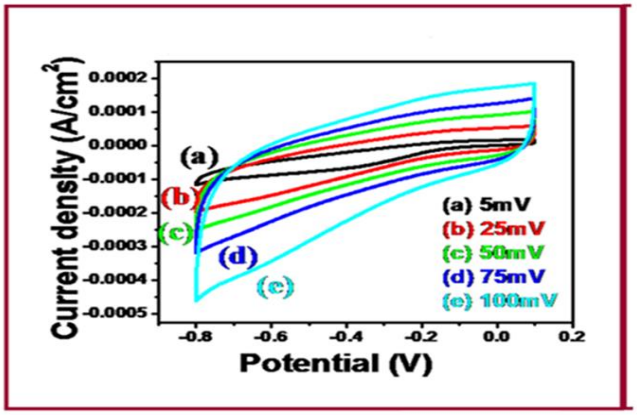

Fig.5. CV plot of The CV plot of Co_3O_4 electrode at scan rates from 5mV to 100 mV in 1M Na_2SO_4

The current under curve is slowly increased with scan rate, which reveals that the voltammetry currents are directly proportional to the scan rates, suggesting a signature of an ideal capacitive behaviour [14]. Increase in scan rates reduces specific capacitance due to decrease in diffusion time of the electrolyte ions from completely accessing the electrode surface. The decreasing tendency of the capacitance suggests that some part of the surface of the electrode material can be available at high charging–discharging rates.

The detail findings are summarized in Table 1:

Table 1

Sr. No	Annealing Temperature °C	Electrolyte	Specific energy (Wh/kg^1)	Specific power (kW/kg^{-1})	Specific capacitance (F g^{-1})	Coulomb efficiency (%)
1	400°C	Na_2SO_4	4.9	4	222	54
2	**500°C**	**Na_2SO_4**	**3.6**	**3**	**295**	**56**
3	600°C	Na_2SO_4	4.2	4	167	50

3.4.2. Charge-discharge study

The Charge-discharge study was carried out to evaluate the supercapacitive parameters of Co_3O_4 electrode like Specific Energy (SE) and Specific Power (SP). Fig.6 displays the galvanostatic charge-discharge curves for the as-deposited Co_3O_4 electrode in 1 M Na_2SO_4 electrolyte.

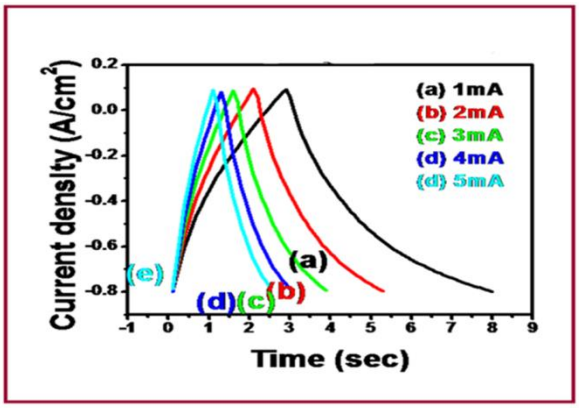

Fig. 6 . Charge discharge curves of Co_3O_4 electrode at 500°C annealing temperature in 1M Na_2SO_4 electrolyte

The curves show the outcome of two mechanisms, the internal resistance causing drop of potential and then the consecutive leisurely and firm moulder of potential indicating the capacitive property of the deposited material. The discharging time of electrode is greater than the charging time indicating good performance efficiency of the electrode. The Supercapacitive parameters such as SE, SP and Coulomb efficiency % were calculated and the findings are tabulated in Table.1 which shows maximum value of supercapacitive parameters of Co_3O_4 electrode at 500°C annealing temperature.

IV. CONCLUSION

Cobalt oxide (Co_3O_4) electrode was deposited by a simple cost-effective electrodeposition method by galvanostatic mode. The X-ray diffraction analysis revealed the as-deposited Co_3O_4 electrode material to be nano crystalline in nature with simple cubic crystal structure. The SEM investigation revealed the spongy surface with highly porous morphology which satisfies the requirement to enhance the supercapacitive performance of the Co_3O_4 electrode. The Contact angle of the material deposited was measured 87º, 85º and 86º at 400ºC, 500ºC and 600ºC attributed Cobalt oxide electrode surface to be hydrophilic in nature. The electrochemical analysis manifested maximum Specific capacitance of 295 Fg^{-1}, Specific Energy of 3.6 Wh/kg, Specific Power 3

kW/kg in 1M Na_2SO_4 electrolyte at 500°C optimized annealing temperature. All these electrochemical parameters depict that, Cobalt oxide electrode material has excellent supercapacitive properties and is a potential material for supercapacitor application.

Acknowledgments

The authors would like to express their deep gratitude to Prof. V B Patil, HOD, Director, School of Physical Sciences, Punyashlok Ahilyadevi Holkar Solapur University, Solapur, Maharashtra, India, for providing required laboratory facilities, their kind cooperation and support in completing this research work. The authors would also like to acknowledge their gratitude to Sophisticated Test and Instrumentation Centre, Kochi University 682022, Kerala, India, for their prompt, accurate and valuable cooperation in performing SEM-EDAX analysis of the research samples.

V. REFERENCES

[1]. R. Kotz, M. Carlen, 2000. Electrochim. Acta 45 2483.

[2]. Yuan, C., Yang, L., Hou, L., Shen, L., Zhang, X., Lou, X. 2012. Growth of Ultrathin Mesoporous Co3O Nanosheet Arrays on Ni Foam for High-performance Electrochemical Capacitors. Energy Environ. Sci., 5, 7883–7887.

[3]. Zheng, J. P. 1995. Hydrous Ruthenium Oxide as an Electrode Material for Electrochemical Capacitors. J. Electrochem. Soc., 142 (8), 2699.

[4]. Farhadi, S., Safabakhsh, J., Zaringhadam, P. 2013. Synthesis, Characterization, and Investigation of Optical and Magnetic Properties of Cobalt Oxide (Co3O4) Nanoparticles. J. Nanostructure Chem., 3 (1), 69.

[5]. Lokhande, C. D. Dubal, D. P. Joo. 2011. O-S. Metal Oxide Thin Film Based Supercapacitors. Curr. Appl. Phys., 11 (3), 255–270.

[6]. S. G. Kandalkar, D. S. Dhawale, Chang-Koo Kima, C. D. Lokhande, 2010. Chemical synthesis of cobalt oxide thin film electrode for supercapacitor application Synthetic Metals 160, 1299–1302.

[7]. D. Jagadale, V. S. Kumbhar, D. S. Dhawale, C. D. Lokhande. 2013. Performance evaluation of symmetric supercapacitor based on cobalt hydroxide [Co (OH)2] thin film electrodes, Electrochimica Acta 98 32– 38.

[8]. D. Jagadale, V. S. Kumbhar, R. N. Bulakhe, C. D. Lokhande. 2014. Influence of electrodeposition modes on the supercapacitive performance of Co3O4 electrodes, Energy 64, 234-241.

[9]. Gwang-Su Jang, S. Ameen, M. S. Akhtar, E. Kim and H. Shin, J. 2017. Mater Sci: inc. Nanomaterials & Polymers., Chemistry Select., 2, 8941 – 8949.

[10]. N. Singh, S. Charan, K. R. Patil, A. K. Viswanath, P. K. Khanna. 2006. Unusual formation of nano-particles of CdO and Cd (OH)2 from the reaction of dimethyl cadmium with DMF, Mater. Lett. 60 3492–3498.

[11]. A. Dhole, S.T. Navale, Y.H. Navale, Y. M. Jadhav, C. S. Pawar, S. S. Suryavanshi, V. B. Patil. 2017. Performance evaluation of galvanostatically deposited nickel oxide electrode for electrochemical supercapacitors, J. Mater. Sci. Mater. Electron. 28, 10819–10829.

[12]. D. P. Dubal, D. S. Dhawale, R. R. Salunkhe, C. D. Lokhande. 2010. J. Electrochem. Soc. 157, A812.

[13]. E. E. Kalu, T. T. Nwoga, V. Srinivasan, J.W. 2001. Weidner, Journal of Power Sources 92 163-16.

[14]. More P.D, Jadhav P.R, Ingole S. M, Navale Y. H, Patil V.B. 2017. Preparation, structural and electrochemical supercapacitive properties of sprayed manganese oxide film electrode. J Mater Sci. Mat. in Electron 28(1):707–714.

International e-Conference on Recent Trends in Nano-Materials and Its Applications-2021
In Association with International Journal of Scientific Research in Science and Technology
Volume 9 | Issue 2 | Print ISSN: 2395-6011 | Online ISSN: 2395-602X (www.ijsrst.com)

Curie temperature of Nanoparticle Sized Aluminium Substituted Copper Cobalt Ferrites

S.S. Karande[1], M.S. Kavale[1], B. R. Karche[2]

[1]Department of Physics, Sangameshwar College, Solapur, Maharashtra, India

[2]Material Science and Thin Film Laboratory, Shankarrao Mohite Mahavidyalaya, Akluj, Dist: Solapur, Maharashtra, India

ABSTRACT

The polycrystalline aluminium substituted nano-particle sized copper cobalt ferrite samples CuxCo1-xFe2-2yAl2yO4 (where x= 0.0, 0.2, 0.4, 0.6, 0.8, 1.0; y = 0.05, 0.15 and 0.25) have been prepared by standard ceramic technique. Phase formation is investigated using X-ray diffraction, Infrared absorption technique and Scanning electron microscope technique. The lattice constants of the all samples are evaluated from x-ray diffraction data. Curie temperature of samples goes on decreases with addition of aluminium and copper in the host lattice of cobalt ferrite.

Keywords : Polycrystalline, nanoparticle size, standard ceramic technique and Inverse cubic spinel, Curie temperature

I. INTRODUCTION

In a way, every material utilized today is a composite. Composite materials are a physical mixture of two or more compatible micro or macro constituent particles which differ in form and chemical composition and are essentially insoluble in each other. Composite materials are best suited for scientific applications which could not be achieved by any one component acting on its own. Ferrite / ferroelectric composites are termed as magneto electric (ME) composites due to the coupling between the electric and magnetic fields in the materials. The conversion of magnetic to electric fields in such ME composite originates from the elastic interaction between ferrite and ferroelectric subsystems [1]. In the presence of the magnetic field, the magnetostriction in the ferrite phase gives rise to mechanical stresses that are transferred to the ferroelectric phase, resulting in electric polarization of the ferroelectric phase owing to its magneto electric effect. ME materials find applications as smart materials in actuators, sensors, magnetic probes, phase inverters, rectifiers, modulators, and transducers in solid state microelectronics and microwave devices [2,3].

Spinel ferrite nanoparticles are being intensively investigated in recent years because of their remarkable electrical and magnetic properties and wide practical applications in information storage system, ferro-fluid technology, magnetiocaloric refrigeration and medical diagnosis [4]. Among the spinels, mixed Zn ferrites and especially Ni–Zn ferrites are widely used in applications like transformer cores, chokes, coils, noise filters recording heads etc. [5]. While Ni–Zn ferrite posses higher resistivity and saturation magnetization, cobalt

ferrite possess high cubic magneto crystalline anisotropy and hence high coercivity. The high coercivity is driven by large anisotropy of the cobalt ions due to its important spin orbit coupling. It is ferromagnetic with a Curie temperature (T_c) around 520°C, [6] and shows a relatively large magnetic hysteresis which distinguishes it from rest of the spinels. The synthesis of ultra fine magnetic particles has been extensively investigated in recent years because of their potential applications in high density magnetic recording and magnetic fluids [7]. Among the current methods for synthesis of mixed ferrite the combustion reaction method stands out as an alternative and highly promising method for the synthesis of these ferrites [8]. Magnetic properties measured at room temperature by vibrating sample magnetometer (VSM) reveal an increase in saturation magnetization with increase in cobalt concentration [9].

II. EXPERIMENTAL

Materials:

High purity starting materials are used as

Cobalt Oxide (CoO):- 74.9326 gm, Copper Oxide (CuO):- 74.5454 gm, Ferric oxide(Fe_2O_3):- 159.6922 gm, Aluminum Oxide (Al_2O_3):- 101.9612 gm

Preparation of ferrite:

Nano crystalline powder samples of $Cu_xCo_{1-x}Fe_{2-2y}Al_{2y}O_4$ (where x= 0.0, 0.2, 0.4, 0.6, 0.8, 1.0; y = 0.05, 0.15 and 0.25) were prepared by the standard ceramic technique. Starting materials CuO, CoO, Fe_2O_3 and Al_2O_3 of AR grade obtained from Sigma – Aldrich, India were used. These samples were heated at ramping rate of 80 ^{0}C hr $^{-1}$ at 1000^{0}C for 48 hours. XRD and IR analysis revealed the cubic spinel structure of the synthesized samples and functional groups in the samples respectively. The absence of any extra line confirms the formation of single phase ferrite. The average particle size 'D' was determined from line broadening (311) reflection using the Debye Scherer formula discussed elsewhere [10]. Calculations of lattice constant, physical density, X-ray density, porosity, site radii and ionic bond lengths on both sites were calculated by using formulae discussed elsewhere [11] and graphically shown in fig.4. Infrared absorption spectra of powdered samples were recorded in the range 350-800 cm^{-1} using Perkin-Elmer FTIR spectrum and spectrometer by KBr pellet technique and presented in (fig.2). The scanning electron microscopes are shown in fig.3

III. RESULTS AND DISCUSSION

The X-ray diffraction patterns of the samples are presented in (fig.1). Powder X-ray diffractometer of the ferrite samples reveals the single phase spinel structure, as well defined reflection is observed without any ambiguity. The diffraction peaks are corresponding to (200), (311), (400), (422), (333/511), (440) and (533) planes. The lattice constants 'a' and 'c' for all prepared samples are calculated by using prominent (311) XRD peak. The calculated and observed values of inter planer distance (d) are found in good agreement with each other for all reflections. The physical density (dB), x-ray density (dx), and porosity (p), are calculated from the formulae given by Gadkari et.al [12].

From the calculations of lattice constants 'a' and 'c' for all the prepared ferrites it is observed that c >a and tetragonality ratio (c/a) is found in the range of 1.03 to 1.07. This result is in good agreement with previous report [13-14].In this present report tetragonality ratio for copper ferrite is 1.06. It means 70% copper resides on B site and it exhibits prorate type distortions in the crystal lattice. The previous report [15] well supports the present results reported this communication. Both Fe^{3+} and Cu^{2+} are John-Teller ion which produces prolate type distortions on (B) site and hence c >a and (c/a) = 1.06. Therefore copper ferrite exhibits tetragonal spinel structure in host crystal lattice of cobalt ferrite. In addition of copper content in tetragonality ratio is found

increasing but due to addition of aluminium tetragonality ratio deceases. It means that Al^{3+} and copper suppress the tetragonal prolate type.

The crystallite sizes (t) of all the prepared samples were computed by Scherer rule utilizing the peak width at one-half intensity of the maximum intensity peak (311).

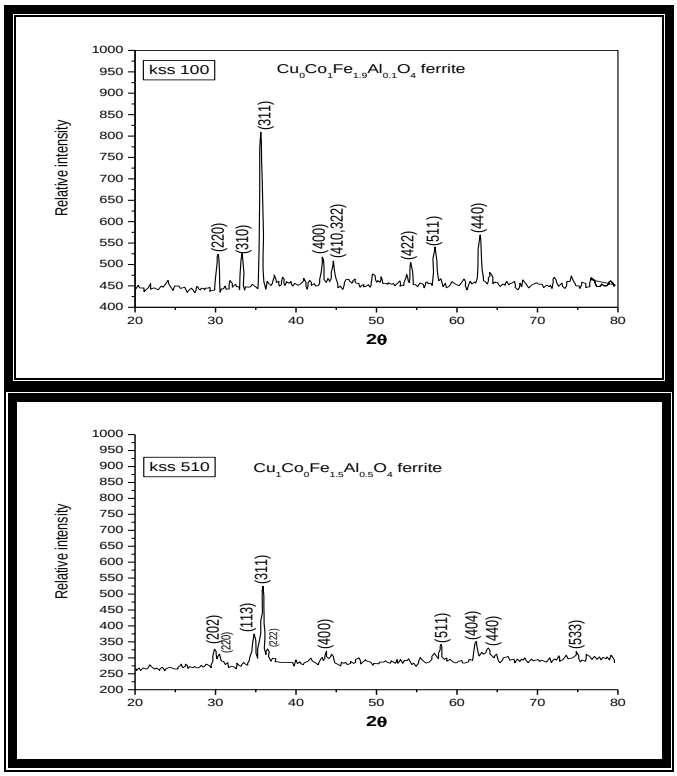

Fig: 1 XRD patterns of system $Cu_xCo_{1-x}Fe_{2-2y}Al_{2y}O_4$

The Al (y = 0.05-0.25) doped copper cobalt ferrite samples show a higher grain growth and the crystallite size (t) lies in the extent of 52.53-94.4 nm. The mean particle size calculated from diffractograms is in the range of 50 to 100 nm. That suggest the particles in the ferrites samples are fine and there is continuous grain growth in all compositions. It gives the confirmation of suitable microstructure formation in all compositions. The width of the reflection peak (311) for all the compositions is approximately the same due to the nearly equal particle size.

The infrared absorption spectra are showing two distinct absorption bands ν_1 due to tetrahedral (A) site interstitial voids near 600 cm^{-1} and other ν_2 due to octahedral (B) site interstitials voids near 400 cm^{-1}. Our results in this present communication are well supported by previous reports [16, 17].

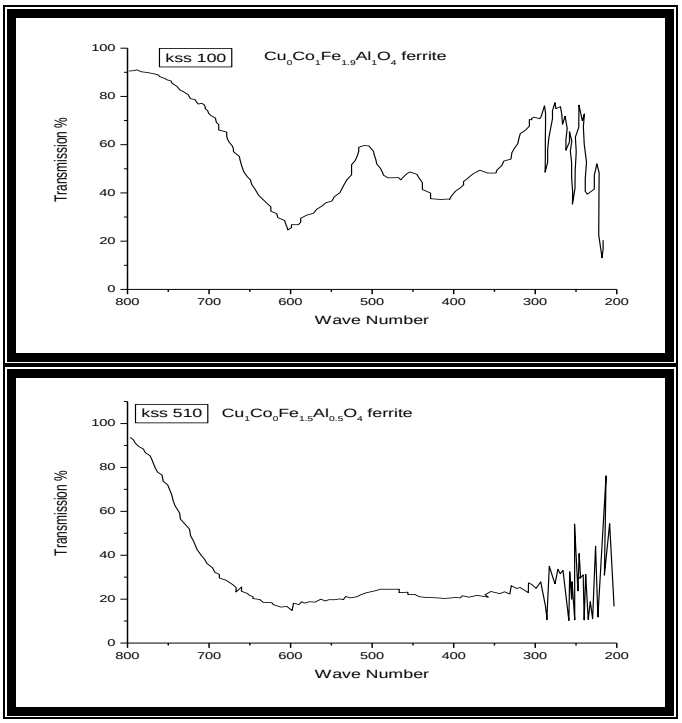

Figure 2: Absorption spectra for system $Cu_xCo_{1-x}Fe_{2-2y}Al_{2y}O_4$

The close inspection of all micrographs revealed that there is continuous grain growth with well – defined grain boundaries formed. The present system shows multi domain behavior. No exaggerated grain growth is observed in any composition. The average grain size is found to decrease with increase in Al content in copper cobalt ferrite. However in the present system the grain growth shows generally a decreasing trend with aluminum content, which is rather expected because of multi-domain behavior of these compositions in copper cobalt ferrite. Grain growth is almost accompanied with grain size, which is increasing with copper and aluminum content. So it appears that copper and aluminum content favors the grain growth. The scanning electron micrographs shown below

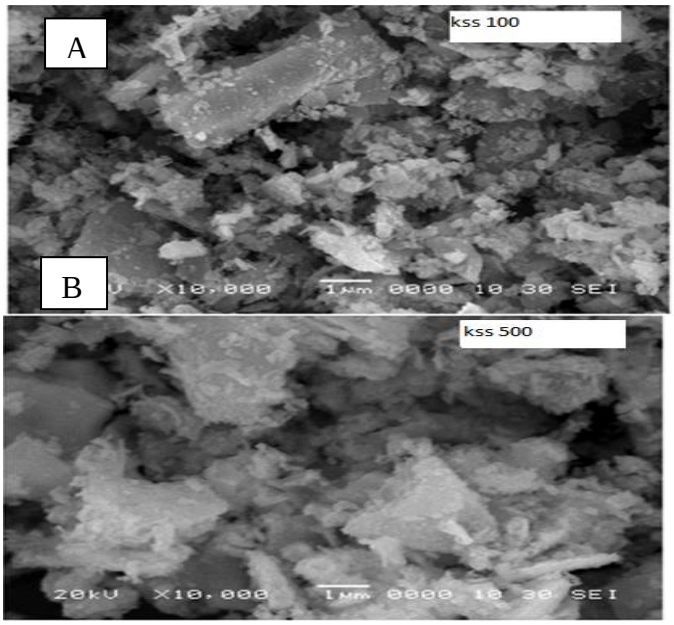

Fig: 3 (A) to (F) scanning electron microscopes of $Cu_xCo_{1-x}Fe_{2-2y}Al_{2y}O_4$:

(A) KSS 100-$Cu_0Co_1Fe_{1.9}Al_{0.1}O_4$,

(B) KSS 500- $Cu_0Co_1Fe_{1.5}Al_{0.5}O_4$

From the figures 4 it is found that Curie temperature of the compositions goes on decreases with increase in copper as well as aluminum content. It was rather expected because addition of copper replaces Fe^{3+} to B site reduces the population of Fe^{3+} on A site and hence A site becomes magnetically weak, results in the decrease in A-B interaction. Their Curie temperatures are determined by drawing tangent to the paramagnetic tail on the temperature axis. Similar type of paramagnetic tail and Curie temperatures determination has been reported [18, 19].

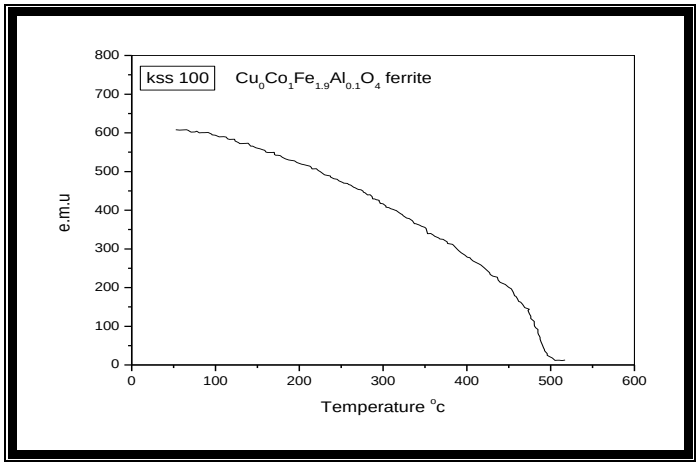

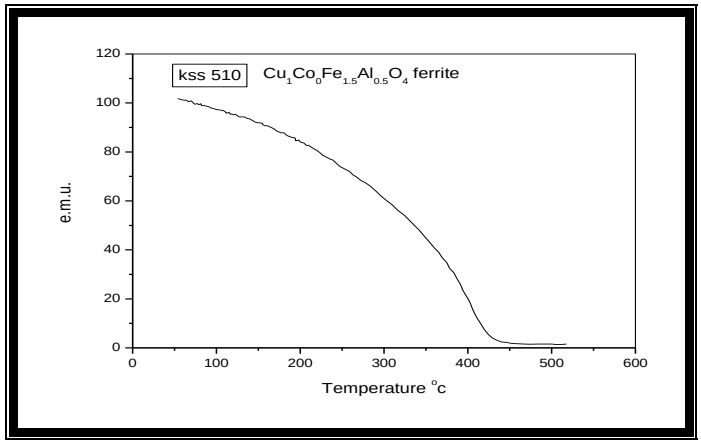

Fig 4: The curie temperatures for $Cu_xCo_{1-x}Fe_{2-2y}Al_{2y}O_4$ ferrite system

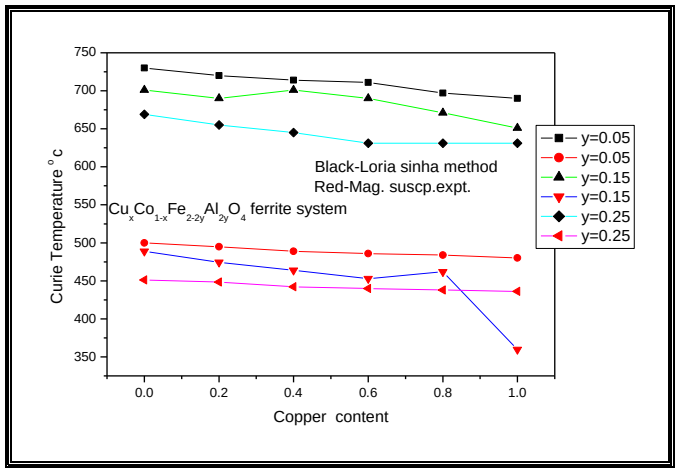

Fig4: Variation of curie temperature with copper and aluminum content for $Cu_xCo_{1-x}Fe_{2-2y}Al_{2y}O_4$ ferrite system

Curie temperature is the peculiar character of the ferromagnetic / ferrimagnetic materials. Curie temperature is the temperature at which it undergoes the phase transition from Ferro /Ferrimagnetic to paramagnetic state. The magnetic material shows spontaneous magnetization below its Curie point and no magnetization above the Curie temperature. In ferrites, Curie temperature is proportional to number of active magnetic linkages. It is affected by A-B distance and A-O-B angle. A-B interaction depends upon these distances. As these distance increases, Curie temperature decrease as suggested by Gorter and Neel [21-22] Curie temperature depends upon the Fe^{3+} ions participating in A-B interaction. When Fe^{3+} ions concentration per molecular formula unit is decreased, then Curie temperature decreased. Figure4

reveals the behaviour of Curie temperature in aluminium doped copper cobalt ferrite which is found decreasing with concentration of aluminium content indicting the decrease in ferrimagnetic properties.

IV. CONCLUSION

Copper cobalt ferrite is partially inverse spinel ferrite. Addition of Al^{3+} ions replaces Fe^{3+} on (B) site resulting in increase of lattice constant a, decrease in ionic radii(R_A) and bond length(O-A). The lattice constant obtained from XRD data shows increases. Curie temperatures of ferrite samples estimated by above mentioned three techniques are found in good agreement with each other. The curie temperature of copper cobalt ferrite decreases with aluminum and copper content.

V. REFERENCES

[1]. R. S. Devan, S. A. Lokare, S. S. Chougule, D. R. Patil, Y. D. Kolekar, andB. K. Chougule, J. Phys. Chem. Solids 67, 1524 (2006).

[2]. K. Zhao, K. Chen, Y. R. Dai, J. G. Wan, and J. S. Zhu, Appl. Phys. Lett. 87, 162901 (2005).

[3]. S. R. Kulkarni, C. M. Kanamadi, and B. K. Chougule, Mater. Res. Bull. 40, 2064 (2005).

[4]. Zhao L, Yang H, Yu L, Cui Y, Zhao X, Zou B, Feng SJ. MagnMagn Mater2006;301:445–51.

[5]. Rath C, Sahu KK, Anand S, Date SK, Mishra NC, Das RP. J MagnMagn Mater 1999;202:77–84.

[6]. Rajendran M, Pullar RC, Bhattacharya AK, Das D, Chintalapudi SN, Majumdar CK. J MagnMagn Mater 2001;232:71–83.

[7]. Ozaki M. Mater Res Bull 1989;12:35–43.

[8]. Costa ACM, Tortella E, Morelli MR, Kaufman M, Kiminami RHGA. J Mater Sci2002;37:3569–72.

[9]. M.M. Mallapur, B.K. Chougule; Materials Letters; Vol. 64 (2010); P. 231–234.

[10]. H. P. Klug, L. E. Alexander, X-ray diffraction procedure for polycrystalline and amorphous materials, Willey N.Y, 1997, 637.

[11]. A. B. Gadkari, T. J. Shinde, P. N. Vasambekar, J. Mater Sci: Mater Electron 21 2010, 96 , 103.

[12]. Prince E., Treuting R.G; Acta Crystallographica, 1956, 9, 1025.

[13]. Sagal K., Tabellen F. Rontegenstrukturanalyse, Springer, Berlin, 1958.

[14]. Borisenko A., Toropov N. A; Z. Prikl Chem, 1950, 23, 1165.

[15]. Goodenough J.B and Loeb A. L ,Phys. Rev., 1955, 98, 391.

[16]. Waldron R.D, Phy. Rev, 1955, 99(6), 1727.

[17]. K. V. S. Badarinath, Phys. Stat. Solidi (a) 1985, 91, 19-23.

[18]. Karche B. R, Khasbardar B.V., and Vaingankar A. S., J. Mag. and Mag. Mater.168 (1997) 292.

[19]. Naik A.B., Sawant S.R., Patil S.A., and Pawar J.I., Bull. Mater. Sci., 12 (3)(1989)1.

International e-Conference on Recent Trends in Nano-Materials and Its Applications-2021
In Association withInternational Journal of Scientific Research in Science and Technology
Volume 9 | Issue 2 | Print ISSN: 2395-6011 | Online ISSN: 2395-602X (www.ijsrst.com)

Room Temperature Synthesis And Characterization Of Cadmium Sulphide (CDS) Semiconductor Quantum Dots

S.I. Khan, G.K.Kande, L.D.Sonawane, A. S. Mandawade, L.J. Jondhale, P.G.Loke*

Department of Physics and Electronics, Karmveer Shantarambapu Kondaji Wavare, Arts, Science & Commerce College, Uttamnagar, CIDCO, Nashik-422008, Maharashtra, India

ABSTRACT

In present report, we synthesized CdS quantum dots (QDs) using facile chemical approach. The synthesized product crystal structure, surface morphology, energy band gap and stoichiometry are studied by various characterization techniques. X-ray diffraction (XRD) analysis shows that the confirmation of cubic structure with crystal planes (111), (220) and (311) and QDs size 3-4 nm calculated by using Debye-Scherer formula. UV-Vis-DRS spectra shows increase in energy bandgap due to quantum confinement effect. Fourier transform infrared (FTIR) spectra were used to envisage the binding of the functional group thiol and Cd-S bonding. Field emission scanning electron microscope (FE-SEM) exhibit a spherical shape of CdS QDs and Energy dispersive X-ray analysis (EDAX) which confirm purity of sample which results a stoichiometry ratio of approximately 1:1 without any impurity. Raman spectroscopy reveals the strong Raman bands 299 cm^{-1} and 600 cm^{-1} which were associated with the of 1LO and 2LO modes.

KEYWORDS: CdS QDs, X-ray diffraction, FTIR, Antibiofilm and Candida albicans.

I. INTRODUCTION

Semiconductor nanoparticles that is quantum dots QDs have been analysis over the past years due to their specific optic, electronic and catalytic properties. These properties arises from the high surface-to-volume ratio present in QDs [1-3].Cadmium sulfide (CdS) is a direct band gap semiconductor with energy band gap E_g = 2.42 eV [4,5]. The color tunability of semiconductor QDs as a function of size is one of their most attractive characteristics [6]. CdS is a promising material because of their applications in optoelectronics [7], photocatalysts [8], x-ray detectors [9], nonlinear optical material [10] and as a window material for hetro-junction solar cells [11]. Large-scale synthesis of semiconductor QDs at room temperature critically important not only for the study of their physiochemical properties but also for industrial applications point of view in the areas of catalysis, photocatalysis and microelectronics as well as it has numerous biological applications. CdS QDs have applications as an excellent photographic developer for detection of cancers and other diseases [12,13] and treatment of cancer cells [14]. The colloidal suspension of CdS QDs of size 3–5 nm are useful in ophthalmology[15]. Since, there are various methods available for the synthesis of CdS QDs such as by chemical pyrolysis deposition method [11], sol-gel method [25], chemical precipitation method [6, 4] etc.where as in our present work, CdS QDs were

synthesized by chemical method at room temperature. Although, the wet chemical synthesis method has relative advantages such as facile handling, non-hazardous, good chemical stability, size dependent optical properties, easy preparation and low cost processing.

Candida species are among the most common opportunistic pathogens that cause human fungal infections. Colonization by these species is naturally good in healthy humans but can also cause frequent infection in immune deficient individuals [16]. Although many research has found that 96% of opportunistic fungal infections are caused by Candida ablicans (C. albicans). Recent Studies made clear that hyphae play an important role in the pathogenesis of C. albicans because the hyphal form display stronger adhesion, invasion of host cells and inflammation than the yeast form [17]. C. albicans can form biofilms on almost any type of medical device, such as blood vessels, catheters, and joint prostheses [18]. Biofilm formation can improve the ability of C. albicans to resist immunity and antifungal drugs, arise in repeated infections [19-22]. Therefore, biofilm formation is another important virulence factor of C.albicans.

MATERIALS AND METHOD: Cadmium Chloride ($CdCl_2$), 1-thioglecerol ($C_3H_8O_2S$), Sodium sulfide (Na_2S) and distilled water since all the chemicals were of analytical grade and used without further purification. Experiments were done in room temperature. The distilled water was used as the solvent and 1- thioglycerol was used as the capping agent.

EXPERIMENT: Cadmium Chloride ($CdCl_2$) was dissolved in 100ml of distilled water at concentration 2mM. Then the solution was placed in reaction vessel followed by addition of18Mmol of 1-thioglecerol ($C_3H_8O_2S$) and further stirred for additional 5min, subsequently sodium sulfide (Na_2S) at concentration of 2mM was rapidly added under ambient conditions with constant stirring CdS QDs are formed with yellow color. After completion of stirring the solution was kept at room temperature. The final solution was centrifuged at 5000rpm and separated CdS QDs were washed several times with methanol and distilled water and kept for room temperature drying. The obtained yellow color CdS QDs powder further used for characterization purpose.

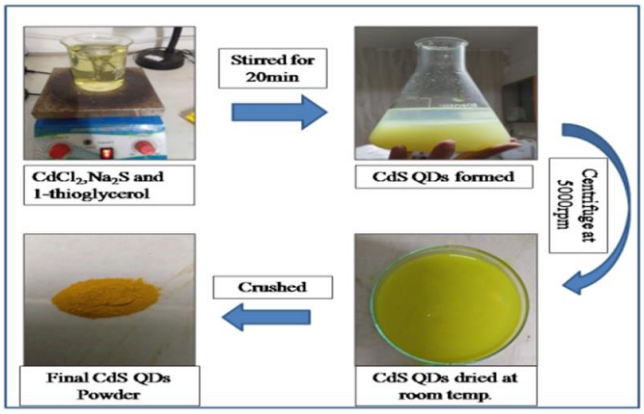

Fig. (1): Schematic diagram of CdS QDs.

MATERIAL CHARACTERISATION: The X-ray diffraction pattern of as synthesized Ag NPs was recorded in the 2θrange of 10–80°at a scanning rate of 2°/min using Rikagu(Miniflex600, Japan).The ultraviolet-visible (UV-Vis) spectroscopy study of CdS QDs was carried out by SHIMADZU Spectrophotometer in the range of 200 to 800 nm. The Fourier transform infrared spectrum was recorded by Fourier Transform Infra-red Spectrophotometer (FTIR), SHIMADZU IRAffinity-1. A drop of CdS solution was placed on freshly prepared KBr disc and scanned between 500 – 4000cm^{-1}. The scanning electronic microscopic images were captured by FESEM (FEI Nova NanoSEM- 450 instrument) with an EDS (BrukerXFlash-6I30). The Raman spectrum was recorded by Raman Spectrometer by RENISHAW Spectroscopy.

ANTIBIOFLIM ASSAY: In short, the procedure is taken from [23], in short 100µL of 10^7 cells/mL of C.albicans MTCC 227 (grown overnight in yeast peptone dextrose broth) in water were added into 96

well polystyrene plate and incubated for 3 hours for adherence of cells. The un-adhered cells were gently washed with phosphate buffer saline (PBS). 100µL of Roswell Park Memorial Institute (RPMI) medium containing different concentrations (0–100µg/L) of C-dots were added to each well, and incubated for 24 hours at 37 C. After 24 hours of incubations, the medium supernatant was removed, and the biofilm formed was gently washed with PBS and further incubated with 100µL of 5 mg/mL MTT (3-(4,5 Dimethylthiazol-2-yl)- 2,5 Diphenyltetrazolium Bromide) solution. After 6 hours of incubations, 100µL of dimethyl sulfoxide was added into each well and optical density.

X-RAY DIFFRACTION (XRD): XRD pattern of CdS QDs pattern is shown in figure 2 below. The XRD peaks found to be very broad which indicates formation of very small size QDs. The peaks are observed. These peaks positioned with 2θ values of 26.48°, 43.94° and 51.50° which corresponds to the miller indices for the crystal plane of reflection of [111], [220] and [311]the crystalline structures of synthesized CdS QDs, respectively, (JCPDS Card no.00-010-0454). The average particle size was found to be 4 nm which was estimated by using the Debye Scherrer formula i.e. particle size (D) = (k λ)/ (d cosθ) Where, D is the mean size of particle (nm), K is crystallite shape factor a good approximation is 0.9, λ is the X-ray wavelength, d is the full width at half the maximum (FWHM) in radians of the X-ray diffraction peak and θ is the Braggs' angle (deg.)[1].

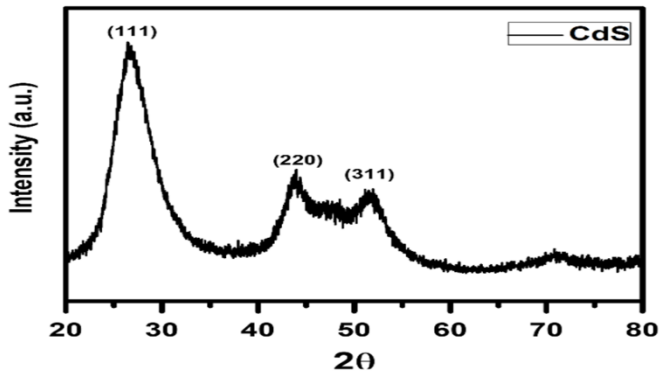

Fig.2: XRD of CdS QDs.

FOURIER TRANSFORM INFRARED SPECTROSCOPY (FTIR):

FTIR is used to determine the functional group and the type of bond present in the system. The FTIR spectrum of pure Cadmium sulfide QDs as shown in the (Fig.3). The peak at 3383cm^{-1} in the higher energy region is assigned to O-H stretching of absorption of water on the surface of cadmium sulfide QDs. The peak shift at 2358cm^{-1} corresponds to S-H thiol group and peak at 1406cm^{-1} is due to presence of S=O i.e. sulfide group. The C-O stretching vibration of absorbed methanol gives its intense peak at 1064cm^{-1}. The weak peak is observed at 879cm^{-1} due to C-H group. The alkene group which is observed at peak 1627cm^{-1}. The small peaks at 642cm^{-1}indicates the Cd-S bond[2].

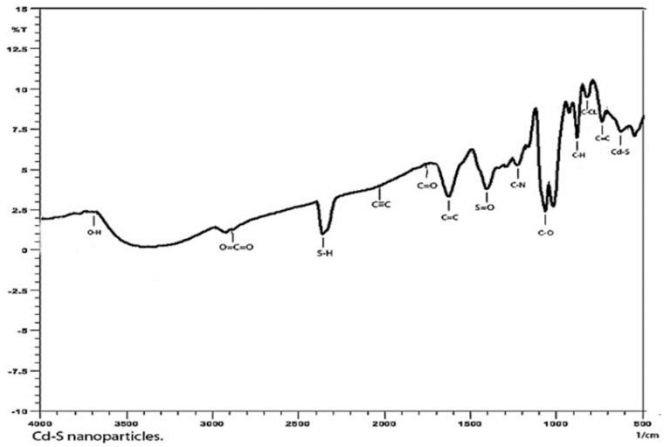

Fig.3: FTIR of CdS QDs.

UV-Visible (UV-Vis) spectroscopy: UV– Vis absorption spectroscopy is an efficient technique to monitor the optical properties of quantum-sized particles. The spectrum reveals a well-defined absorption peak at~480 nm which is considerably blue-shifted relative to the peak absorption of CdS indicating quantum size effect. The absorption peak at~480 nm is assigned to the optical transition of the first excitonic state as shown in the (Fig 4). The energy band gap (Eg) determined by using formula

$$\text{Eg (eV)} = \frac{h\nu}{\lambda} = \frac{1240}{\lambda}\text{(nm)} = \frac{1240}{480} = 2.58\text{eV}$$

Hence, the higher value of band gap indicate that quantum size quantum effect which is the larger compared with the bulk band gap[1].

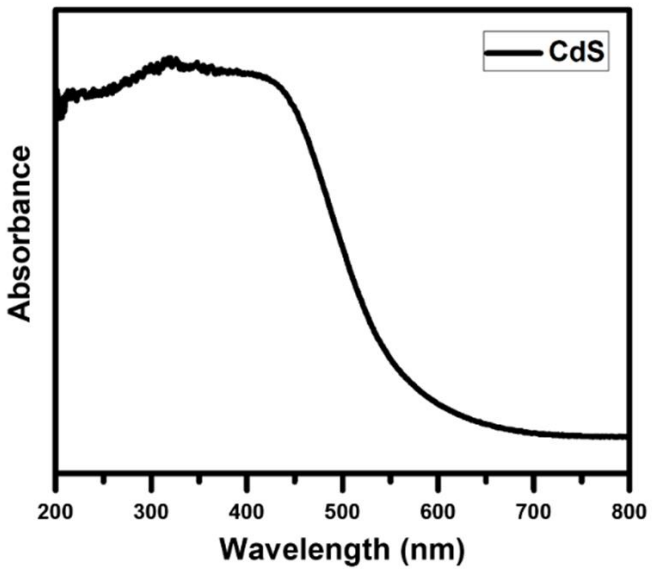

Fig.4: UV-DRS of CdS

Field Emission Scanning Electron Scanning Microscope (FESEM) and Energy Dispersive X-ray Analysis (EDAX): The synthesized samples of CdS QDs are further characterized by FESEM-EDX analysis for the evaluation of their composition and purity. As shown in (Fig. 5a) it's observed that in sample the particles are nearly spherical and morphology with uniform size. The EDX pattern for CdS QDs obtained which indicates the presence of Cd and S elements without any impurities. (Fig.5b). The atomic ratio of Cd: S is 52.61: 47.39 which can be further translated into a stoichiometric ratio of approximately 1:1.[2]

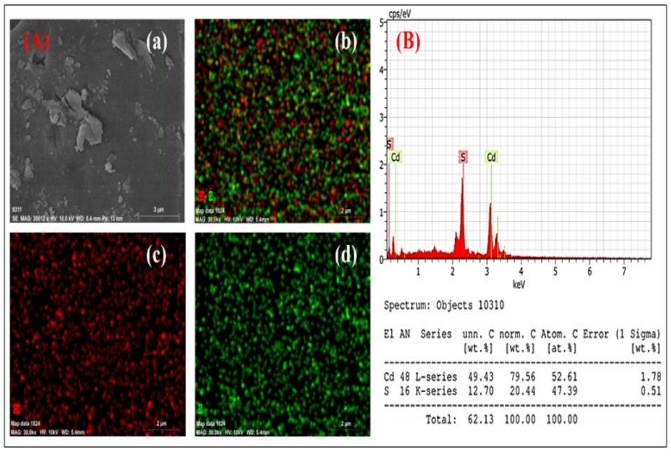

Fig.5: (A) FESEM of CdS QDs. (B)EDAX pattern CdS QDs

RAMAN SPECTROSCOPY: The presence of molecules adsorbed on particle surface was confirmed with Raman analysis, in (Fig.6).The CdS QDs demonstrated a strong Raman band 299 cm^{-1} and 600 cm^{-1}which were associated with the of 1LO and 2LO Raman modes of CdS [1].

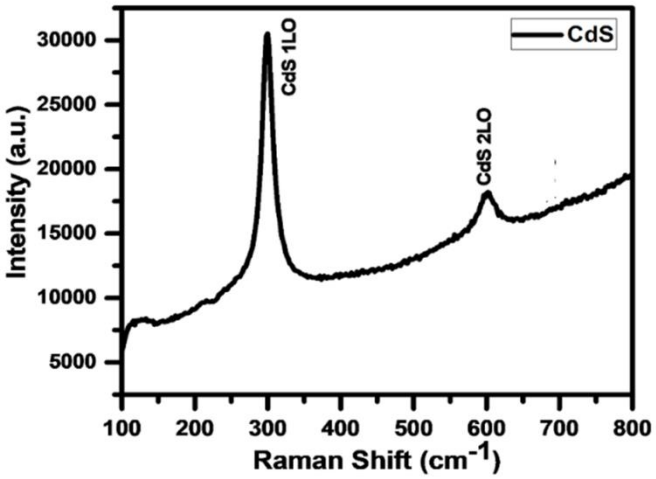

Fig.6: Raman of CdS QDs.

ANTIBACTERIAL ACTIVITY: The schematics steps of Candida biofilm formation referred from [24] Figure (7) shows schematic model which indicates multi-species biofilm formation and development of Candida infections.1) Candida cell as a part of mixed microbial community, 2) Attachment of the candida to host surface, 3) Insufficient host defense leads to proliferation of candida in multi- species bioflim embedded in self- produced polymeric matrix and with increase resistance to antimycotics C.albicans occurs in different morphological forms, 4) Hyphal cells in epithelial bioflims aid tissue invasion by C. albicans, 5) After tissue invasion, yeast cell may be disseminated in blood vessels and are expose to immune cells.

The synthesized CdS QDs are explored for C.albicans biofilms. CdS QDs shows inhibitionin Fig.:7 (B), 30×10^5 cells/mL, 40×10^5 cells/mL, 45×10^5 cells/mL and 50×10^5 cells/mL, were added 15.6 µg/mL, 51.5 µg/mL, 62.5 µg/mL and 125.0 µg/mL to each well of the 96-well polystyreneplates respectively. It reveals about 30% inhibition of biofilm and also it slow down the

biofilm formation which may perhaps contribute to various applications in biomedical field [26].

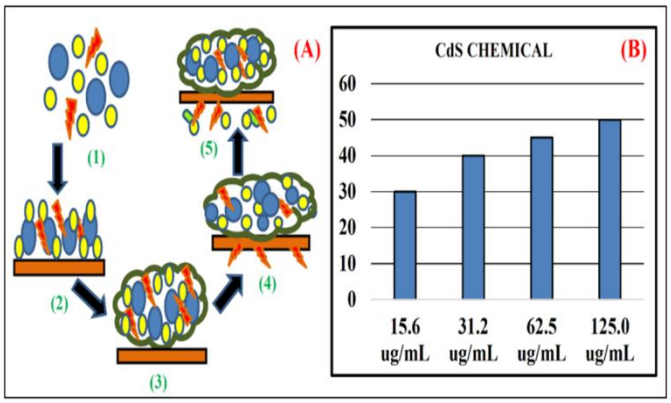

Fig.7: (A) Schematic model indicating multi-species biofilm formation and development of Candida infections.(B) Observed Inhibition of CdS QDs

II. CONCLUSION

In present study we used facile, room temperature, eco-friendly wet chemical method for synthesis of CdS QDs. From XRD, the average particle size was found to be 4 nm and cubic crystal structure.FTIR analysis reveals that small peaks at 642 cm-1 which indicates the Cd-S bond. In UV –Vis absorption spectrum shows a well-defined absorption peak at~480 nm with corresponding energy band gap 2.58 eV higher value of band gap attributed to due to quantum size confinement effect. FESEM and elemental mapping shows the spherical shape of CdS QDs. EDAX which confirm purity of sample which results a stoichiometry ratio of approximately 1:1 without any impurity. Raman spectroscopy reveals the strong Raman bands 299 cm-1 and 600 cm-1 which were associated with the of 1LO and 2LO modes.The synthesized CdS QDs are explored of C.albicans biofilms it shows about 30% inhibition of biofilm. The low temperature synthesized CdS QDs can be explore for further several applications such asbiomedical,solar cells, photographic developer and so on.

ACKNOWLEDGEMENTS: Authors would like to thanks to the Principal Dr. J. D. Sonkhaskar and Head of the Department, Dr. P. G. Loke, Department of Physics and Electronics, KSKW Arts, Science and Commerce College, Uttamnagar, CIDCO, Nashik-422008, for providing laboratory and instrumentation facility.

III. REFERENCES

[1]. G. A. Martínez-Castañón, M. G. Sánchez-Loredo, H. J. Dorantes, et al. , "Characterization of silver sulfide nanoparticles synthesized by a simple precipitation method", Mat. Lett. 59 (2005), 529-534.

[2]. C. Li and N. Murase, "Synthesis of Highly Luminescent Glasses Incorporating CdTeNanocrystals through Sol-Gel Processing", J. Surf. And Coll., 20 (2004), 1-4.

[3]. A. Schroedter, H. Weller, R. Eritja, W. E. Ford and J. M. Wessels, "Biofunctionalization of Silica-Coated CdTe and Gold Nanocrystals", Nano Lett., 2 (2002), 1363-1367.

[4]. H. L. Lee, A. M. Issam, M. Belmahi, M. B. Assouar, et al. "Synthesis and Characterizations of Bare CdSNanocrystals Using Chemical PrecipitationMethod for PhotoluminescenceApplication",Hindawi Publishing Corporation Journal of Nanomaterials 10 (2009),1-9.

[5]. R. Banerjee, R. Jayakrishnan, and P. Ayyub, "Effect of the sizeinduced structural transformation on the band gap in CdS nanoparticles",Journal of Physics: Condensed Matter, 12 (2000), 10647–10654.

[6]. Rajeev R Prabhu and M Abdul Khadar, “Characterization of chemically synthesized CdS nanoparticles”, PRAMANA – journal of physics °c Indian Academy of Sciences 65 (2005), 801-807.

[7]. R.A.M. Hikmet, V. Talapin, H. Weller, "Study of conduction mechanism and electroluminescence in CdSeO˜ ZnS quantum dot composites", J. Appl. Phys. 93 (2003), 3509–3514.

[8]. W.V. Huynh, J.J. Dittmer, A.P. Alivisatos, "Hybrid nanorod-polymer solar cells", Science 295 (2002), 2425–2427.

[9]. R. Frerichs, "The cadmium sulfide X-ray detector", J. Appl. Phys. 21 (1950), 312–317.

[10]. I.O. Oladeji, L. Chow, C.S. Ferekides, V. Viswanathan, Z. Zhao, "Metal/CdTe/CdS/ Cd1–xZnxS/TCO/glass: a new CdTe thin film solar cell structure", Sol. Energy Mater. Sol. Cells, 61 (2000), 203–211.

[11]. Deokjoon Cha, Sunmi Kim, N.K. Huang, "Study on electrical properties of CdS films prepared by chemical pyrolysis deposition", Mater. Sci. Eng. B106 (2004), 63–68.

[12]. RekhaGarg Solanki, PoollaRajaram, "Structural, optical and morphological properties of CdS nanoparticles synthesized using hydrazine hydrate as a complexing agent", Nano-Structures & Nano-Objects 12 (2017), 157–165.

[13]. A. Balandina, W.L. Wang, N. Kouklin, S. Bandyopadhyay, "Raman spectroscopy of electrochemically self-assembled CdS quantum dots", Appl. Phys. Lett. 76 (2000), 137–139.

[14]. W. Jiang, A. Singhal, J. Zheng, C. Wang, W.C.W. Chan, "Optimizing the synthesis of red- to near-ir-emitting CdS-Capped CdTexSe1–x alloyed quantum dots for biomedical imaging", Chem. Mater, 18 (2006), 4845–4854.

[15]. N. Kozhevnikova, A. Vorokh, A. Rempel, "Preparation of stable colloidal solution of CdS using ethylenediaminetetraacetic acid", Russ. J. Gen. Chem. 80 (2010), 391–394.

[16]. FanzhiKong .JiayingWang .RuiHan .ShuaiqiJi,et al., "Antifungal Activity of Magnesium Oxide Nanoparticles: Effect on the Growth and Key Virulence Factors of Candida albicans", Mycopathologia,185 (2020), 485-494.

[17]. Nicholls S, et al. "Activation of the heat shock transcription factor Hsf1 is essential for the full virulence of the fungal pathogen Candida albicans". Fungal Genet Biol, 48 (2011), 297-304.

[18]. Lo HJ, et al. "Nonfilamentous C albicans mutants are avirulent", Cell. 90 (1997), 939-49.

[19]. Jacobsen ID, et al. "Candida albicans dimorphism as a therapeutic target". Expert Rev Anti Infect Ther, 10 (2012) 85–93.

[20]. Kojic EM, Darouiche RO. "Candida infections of medical devices", ClinMicrobiol Rev, 17 (2004), 255-67.

[21]. Ranita Roy , Monalisa Tiwari , Gianfranco Donelli , Vishvanath Tiwari. "Strategies for combating bacterial biofilms: a focus on anti-biofilm agents and their mechanisms of action",Virulence, 9 (2018), 522-54.

[22]. Helena Sztajer , Szymon P Szafranski , Ju¨rgen Tomasch , Michael Reck, et al. "Cross-feeding and interkingdom communication in dual-species biofilms of Streptococcus mutans and Candida albicans", ISME J, 8 (2014), 2256-71.

[23]. Asiya F. Shaikh, Mohaseen S. Tamboli, Rajendra H. Patil, AshitaBhan, et al, "Bioinspired Carbon Quantum Dots: An Antibiofilm Agents",Journal of Nanoscience and Nanotechnology, 19 (2019), 2339–2345.

[24]. J M ten Cate , F M Klis, T Pereira-Cenci, W Crielaard, et al,"Molecular and Cellular Mechanisms That Lead to Candida Biofilm", Formation, J Dent Res 88 (2009), 105-15.

[25]. R. K. Sonker, B.C. Yadav , Vinay Gupta, Monika Tomar, "Synthesis of CdS nanoparticle by sol-gel method as low temperature NO2 sensor", Materials Chemistry and Physics 239 (2020), 121975.

[26]. Humberto H. Lara, Dulce G. Romero-Urbina, Christopher Pierce, Jose L. Lopez Ribot, et al, "Effect of silver nanoparticles on Candida ablicans biofilms: an ultrastructural study",Lara et al. J Nanobiotechnol, 13 (2015), 91.

International e-Conference on Recent Trends in Nano-Materials and Its Applications-2021
In Association withInternational Journal of Scientific Research in Science and Technology
Volume 9 | Issue 2 | Print ISSN: 2395-6011 | Online ISSN: 2395-602X (www.ijsrst.com)

Structural Study of Mn Dopant and Optical Behaviour of Fe_2O_3 Nanoparticles

S. U. Pawar, R. K. Rajure, S. D. Waghmare, R. R. Kothawale*

Nanomaterial Research Laboratory, Department of Physics, ShriShivajiMahavidyalaya, Barshi, Solapur 413-411, Maharashtra, India

ABSTRACT

Structure of Photocatalytic materials play an important role in the field of renewable energy such as artificial photosynthesis, solar cell etc. Hence, to improve photocatalytic performance via optical property is one of the challenging points in these days. Iron oxide (Fe2O3) with direct and indirect band gap has been extensively studied by many researchers in past years due to its excellent physical properties. However, in the field of photocatalysis this material is being ignored because of fast electron-hole recombination rate. This problem can be overcome by doping with suitable and appropriate amount of dopant material. In this report oval shaped Mn doped Fe2O3 nanoparticles have been successfully synthesized by simple hydrothermal method. Different (1, 2 and 3) mol% Mn were doped into Fe2O3 and its existence was confirmed by EDAX and XPS. The effect of dopant on crystal structure and morphology was studied by X-ray Diffraction and SEM, TEM respectively. The optical properties of synthesized Mn doped Fe2O3 nanoparticles were measured by diffuse reflectance spectra.

I. INTRODUCTION

Structuralstudy of nanoparticles which is intermediate between the bulk and atomic/molecular system. Nanoparticles show different properties than the bulk and atomic system which are very useful in various fields like medicine, healthcare, engineering, agriculture, electronics, defense etc. Hence the study of those properties of nanoparticles such as optical, mechanical, thermal, catalytic and magnetic is very interesting and exciting[1-2]. Various well established physical and chemical methods have been used to synthesis nano materials in different shape and size. Here nanoparticles are synthesized by simple hydrothermal method. Artificial photosynthesis replicate the natural process of photosynthesis that converts water and carbon dioxide into carbohydrates and oxygen using sun light as the energy source. Photocatalytic material play an important role in the field of renewable energy such as artificial photosynthesis, solar cell etc. Hence to improve photocatalyticperformance via optical property is one of the challenging points. Iron oxide (Fe2O3) with direct and indirect band gap has been extensively studied by many researchers in past year due to its excellent physical properties [3-6]. Fe_2O_3 has wide applications such as ferrofluide, refrigeration, magnetocaloric and biomedical fields. Metal doped nanostructure FE2O3 crystal is highly desirable. These dopant play important role to improve the optical absorption coefficient, donor density, electrical conductivity and flat band potential. In this work Mn is doped in Fe_2O_3 which is synthesized by hydrothermal method. The prepared samples were characterized for crystal structure by X-ray diffraction, surface morphology by Scanning Electron

Microscopy (SEM) and Transmission Electron Microscopy (TEM) and optical properties by Diffuse Reflection Spectra (DRS).

II. EXPERIMENTAL DETAILS

Chemicals

Ferric chloride hexahydrate($FeCl_3.6H_2O$, ~97%, Sigma Aldrich), Manganese chloride tetrahydrate ($MnCl_2.4H_2O$, >98%, Sigma-Aldrich) and sodium hydroxide (NaOH, beads, 20-40 mesh, reagent grade, 97%). All chemicals were used as received without further purification. For this experiment deionizes water is used and Millipore water purification system was used for Deionized (DI) water. These chemicals were used to synthesizes pure and Mn doped Fe_2O_3 samples.

Synthesis

Mn doped Fe_2O_3 nanoparticles were prepared by simple hydrothermal method, slightly modifying the procedure by earlier reported paper [7]. In this study, four different samples were prepared by this method among them one is pure Fe_2O_3 and remaining three are (1, 2, and 3mol %) Mn doped Fe_2O_3 nanoparticles. Initially, 2mmol of $FeCl_3$ dissolved in 10 mL of DI water and then $MnCl_2$ with different mol percentage (0, 1, 2 and 3 mol %) was inserted in a preliminary solution. The mixed solution was continuously stirred for 1 h at room temperature. After that, 4mmol of NaOH solution (in 10 mL of DI water) was added drop wise in resultant solution with vigorous stirring and kept continuous stirring for next 2 h. At the end final solution was transferred to 30 mL volume of Teflon-lined stainless steel autoclave and kept at 180°C for 8 h. Finally, synthesized nanoparticles were collected by centrifugation and washed several times with DI water.

III. CHARACTERIZATIONS

Rigaku X-ray diffractometer with CuKa radiation was used for crystal structure identification of prepared Fe_2O_3 nanoparticles. The size and morphology of obtained nanoparticles weremeasured by field emission scanning electron microscopy (FE-SEM, Hitachi S-4300) and field emission transmission electron microscopy (TEM, JEOL JEM 2100) equipped with elemental mapping, selective area electron diffraction (SAED) as well as HRTEM. An elemental composition of Fe_2O_3:Mn nanoparticles confirmed by X-ray Photoelectron spectroscopy (XPS) from VG Scientific (England) Multitab 2000 X-ray photoelectron spectrometer. A diffuse reflectance spectrum (DRS) has measured with the help of Varian Cary 5000 UV-vis-NIR spectrophotometer. Barium sulfate was used for baseline correction and obtained DRS spectra were treated by Kubelka-Munk formalism. Photoluminescence study has done by Hitachi F-7000 fluorescence spectrophotometer at room temperature using 250 nm excitation wavelength of a Xenon lamp.

IV. RESULT AND DISCUSSION

XRD pattern shown in Fig.(1) of synthesized pure and doped samples. Different peaks of the patter show well matching with pure sample in crystal structure form. Major peaks (012), (104), (110), (113), (024), (300) and (220) gives crystallinity of Mn doped Fe2O3.Molar concentration of Mn increased then well aliened structure shown in Fig.(1). InFig.(2) SEM images of synthesized Mn doped Fe_2O_3 nanoparticles with different concentration of Mn (a) without Mn, (b) 1 wt% (c) 2 wt% and (d) 3 wt% clearly shows different crystal sizes for different Mn doping. SEM shows oval and cube like structurewith proper grain size and grain boundaries. In Fig.[2 c] sample are well grown as uniform oval and cubic shapes with high density grains.

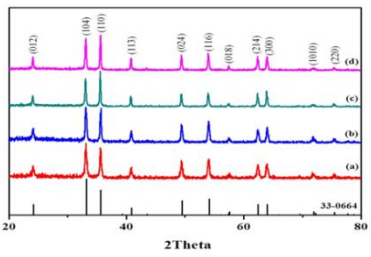

Fig.(1):- XRD spectra of synthesized (a) pure Fe_2O_3 and Mn doped Fe_2O_3 nanoparticles with different concentration of Mn (b) 1mol%, (c) 2 mol% and (d) 3 mol%.

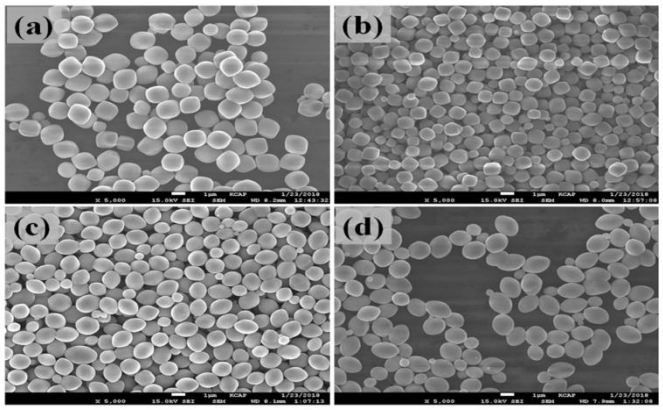

Figure 2:- SEM images of synthesized Mn doped Fe_2O_3 nanoparticles with different concentration of Mn (a) without Mn, (b) 1 wt% (c) 2 wt% and (d) 3 wt%.

In Fig.(3) (c) and (d) HRTEM images of synthesized 2mol% Mn doped Fe_2O_3 nanoparticles. TEM images show uniform Mn doped cubic crystal at 2 mol%. Fig. [3(c)] shows the selected area electron diffraction (SAED) patterns of sample 2 mol% of Mn as single cube crystal structure.Fig. [3(d)] gives the HRTEM image of clear lattice fringe of nanocubes.

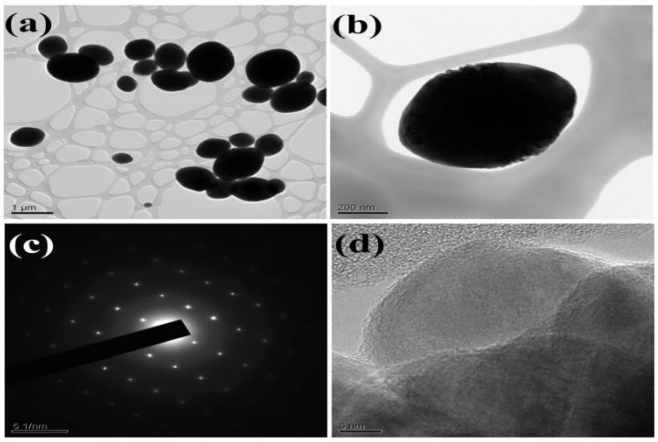

Figure 3:- TEM (a) low and (b) high magnify images, (c) SAED and (d) HRTEM images of synthesized 2mol% Mn doped Fe_2O_3 nanoparticles.

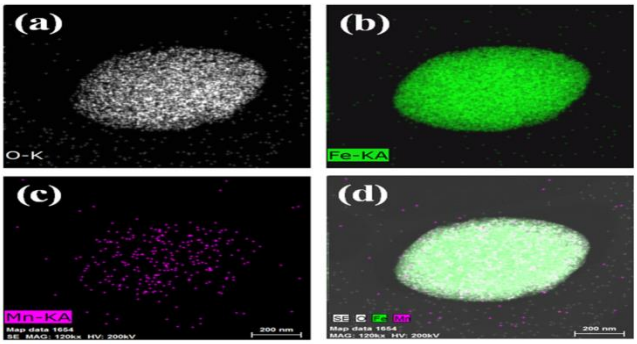

Figure 3:- TEM Elemental mapping of single particle of Fe_2O_3:Mn synthesized by 2mol% Mn doped Fe_2O_3 (a) Oxygen, (b) Iron, (c) Mn and (d) combine Fe_2O_3:Mn.

In Fig.(3) shows TEM Elemental mapping of single particle of Fe_2O_3:Mn synthesized by 2mol% Mn doped Fe_2O_3 (a) Oxygen, (b) Iron, (c) Mn and (d) combine Fe_2O_3:Mn which is oval and cube like in shape. Figure 4 shows XPS survey spectra (a), small range spectra (b) of Fe2p, (c) O1s, and (d) Mn3s elements of synthesized Mn doped Fe_2O_3 nanoparticles with different concentration of Mn (black) without Mn, (red) 1 wt% (blue) 2 wt% and (green) 3 wt% . In the spectra Fig.[4(b)] there are two peaks of binding energies of 710.4 ev for Fe2p3/2 and 723.7 ev for Fe2p1/2 i.e. distinct peaks are observed in the spectra at binding energy.

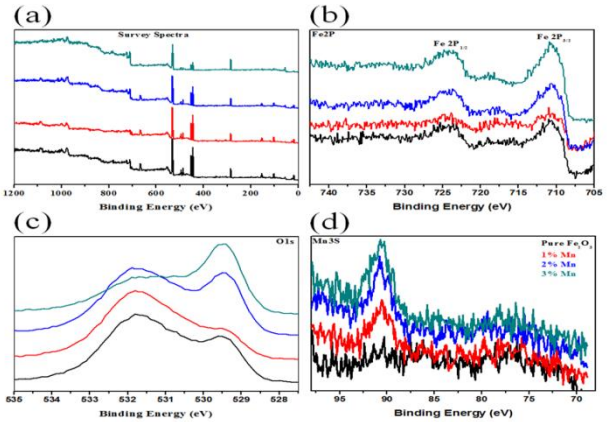

Figure 4:- XPS survey spectra (a) and small range spectra of (b) Fe2p, (c) O1s, and (d) Mn3s elements of synthesized Mn doped Fe_2O_3 nanoparticles with different concentration of Mn (black) without Mn, (red) 1 wt% (blue) 2 wt% and (green) 3 wt%.

V. CONCLUSION

In this work pure and Mn doped Fe2O3 samples were successfully synthesizes by hydrothermal method. Structural, morphological and optical Characteristic properties were studies by XRD, SEM, TEM, SAED and XPS of prepared samples. XRD study gives crystallite structure with oval and cubic in nano shape.Molar concentration of Mn increased then well aliened structure shown. Surface morphology of Mn doped Fe2O3 were uniform, oval and cubic shaped nano particles with proper grain size and grain boundaries. TEM of the samples were performed at low and high magnification, SAED gives single cubic structure of 2 mol% of Mn. Optical property related to XPS survey spectra (a), small range spectra (b) of Fe2p, (c) O1s, and (d) Mn3s elements of synthesized Mn doped Fe2O3 nanoparticles with different concentration of Mn which measure binding energy of samples.

VI. REFERENCES

[1]. A SeyedRazvi, I.K. Snook, A.S. Barnard, J.Mater Chem. 2010. 20. 416
[2]. T.K.Sau, A.L.Wang, J.Phys. Chem. B 2000, 104, 1153
[3]. Maneesha Mishra, Doo-Man Chun, Applied Catalysis A: General 498 (2015) 126–141.
[4]. V.D. Nithya, N. Sabari Arul, Journal of Power Sources 327 (2016) 297-318.
[5]. Libor Machala, RadekZboril, AharonGedanken, Journal of Physical Chemistry B 111 (2007) 4003-4018.
[6]. Heli Wang, John A. Turner, Journal of The Electrochemical Society, 157(11) (2010) F173-F178.
[7]. Hyun Gil Cha, Hyun Seok Noh, Myung Jong Kang and Young Soo Kang, New Journal of Chemistry 37 (2013) 4004-4009.

International e-Conference on Recent Trends in Nano-Materials and Its Applications-2021
In Association with International Journal of Scientific Research in Science and Technology
Volume 9 | Issue 2 | Print ISSN: 2395-6011 | Online ISSN: 2395-602X (www.ijsrst.com)

Sensitive and Selective Detection of H_2S Gas Using Al-Doped ZnO Thin-Film Sensors

Sagar M. Mane[1], Amol R. Nimbalkar[2*], Nilam. B. Patil[3], Swati Patil[4], Shankar S. Dhasade[5], Jagannath V. Thombare[5], Jae Cheol Shin[1]

[1]Department of Physics, Yeungnam University, Gyeongsan, Gyeongbuk 38541, Republic of Korea
[2]Department of Physics, DKASC College, Ichalkaranji, Maharashtra, India
[3]SIT, Polytechnic, Yadrav, Ichalkaranji, Maharashtra, India
[4]PratapsinghMohite Mahavidyalaya Karmala, Maharashtra, India
[5]Vidnyan Mahavidyalaya Sangola, Maharashtra, India

ABSTRACT

A simple sol–gel spin-coating technique is used for the synthesis of Al-doped ZnO (AZO) thin films. Then, the structural, optical,electrical,andH2S-sensing properties of the AZOthin filmsare investigated.A structural analysis confirmed the formation of a crystalline zinc oxide thin film. Moreover, the gas-sensing performance of the AZO thin films for H2S gas areinvestigatedat 250°C.Our results reveal that the ZnO thin film doped with 2 at% Al demonstratesgood sensitivity and selectivity and shows excellent reproducibility forH2S gas,therebyexhibitingasignificantenhancement in the gas-sensing properties of the Al-doped ZnO lattice.

Keywords : Selectivity, Sensors, Reproducibility, Thin Films;Sol–Gel

I. INTRODUCTION

Various natural and industrial processes around the world are known to produce colorless, extremely noxious, and flammable hydrogen sulfide (H_2S) gas with a carious-egg-like smell. H_2S is generallyproduced during natural gas manufacturing, at crude petroleum refineries, and from automobile exhausts [1]. Thelong-term lower-level exposure of H_2Shas been known tocause headaches, irritability, dizziness, fatigue, poor memory and concentration,and even death[1, 2].In light ofthese effects,it becomes important to develop and fabricate devices for the detection of H_2S gas, especially at lower concentrations.A number of factors have to be considered for gas sensor fabrication, out of which quick gas response, stability, and selectivity are the three major requirements foragas-sensing device.In the past few years, metal oxide films based onnanocrystalline ZnOhave been intensively studied as suitable materials for a gas-sensing deviceasthey havea higher surface-area-to-volume ratio, display electrical and thermal stability at higher temperatures,andare cheaper compared with other oxide materials [3].Furthermore, the creation ofan electronic defect in a ZnO film improves the influence of the partial pressure of oxygen on the conductivity ofthe film; this type of defect can be created usingan appropriate dopant[3].Various metallic dopantmaterials such as Al, Cu, Co, Sn, Fe, and In can bedoped in ZnO filmsto improveits gas-sensing performance [3, 4].The present work reports

the doping of Al in a ZnO lattice using the sol–gel fabrication of thin films and the H_2S gas-sensing properties of these films.

II. EXPERIMENTAL PROCEDURE

A synthesis procedure similar to that used in our previous study [5] was adopted forthe synthesis of Al-doped ZnO (AZO) thin films at1–4 at%. The structural analyses of the AZO thin films werestudiedusing a Bruker D2 phaser X-ray diffractometer.The optical absorption spectra of the synthesized AZO filmswere recorded using a UV–Vis-NIR V-770 (Jasco, Japan). Moreover, the DCconductivity of the synthesized AZO thin films was studiedusinga locally designed two-probe system in the temperature range 27–300°C.The gas-sensing properties of the AZO sensor films werestudied at 250°C.The AZOsensor film resistance was measured and recorded at 250°C in the presence of a test gas and ambient air by using a Keithley electrometer (6514 model, USA).The gas response (R_s) was determinedusing R_a /R_g forH_2S gas, where R_a = resistanceof the sensor in air,and R_g =resistance of the sensor in the presence of a test gas.

III. RESULTS AND DISCUSSION

A typical XRD pattern of 2 at% AZO filmat 2θ = 20to 90° is shown in Fig.1.The figure inset shows the diffraction peak (002). No effect is seen on other diffraction planes (except 002).The doping of Al confirmsthat the synthesized AZO films are crystalline with c-axis (002) plane orientation and possesshexagonal crystal structure as per JCPDS card No. 01-079-0205.In addition, it is observed that the peak intensity of (002) increases with the Al concentration up to 2 at% and reduces for higher at% doping (3 and 4 at%), whereas shifting of the peak toward a higher 2θ anglewithhigherAl concentration confirms the growth of the Al atom in the ZnO lattice. The crystallite size of the synthesized AZO films wasdetermined usingtheDebye–Scherrer formula [5]. The crystallite sizeswere found to be 32, 34, 35, 33, and 35 nm for 0, 1, 2, 3, and 4 at% AZO films, respectively.

The optical absorption of the sol–gel spin-coated AZO films was carried out with a wavelength range of 300–1000 nm. Figure 2 depictsthe plot of $(\alpha h\nu)^2$ versus photon energy ($h\nu$) for the AZO filmsaccording to Al-doping concentration (1–4 at%). From these plots, the opticalbandgap values were calculated using theTauc relation.The optical band gapvalueincreases from 3.21 to 3.26 eV as Al-doping concentration increases from 0 to4 at%, respectively.The increase inthe optical band gap with the Al doping concentration exhibits a goodcorrelation with the increase in the blueshift, which can be explained based onthe Burstein–Moss effect [6-7].

The DC conductivityof the AZO thin filmswas then measured in the temperature range 300–573K using a locally designed two-probe system.Figure 3shows thevariation in DCelectrical conductivity (σ)according to the temperature for theAZO thin films.The DCconductivity of the AZO filmsincreases exponentially with increase intemperatureand Al-doping concentration. The DCconductivity at room temperature is found to be between 4.85×10^{-7} S/cm and4.41×10^{-7} S/cm, which further increases and reaches a value between5.47×10^{-4} S/cm and 9.19×10^{-4} S/cm at 300°C for 0–4 at% AZO thin films, which confirms the semiconductor behavior of the AZO films [8].The plot of lnσ versus 1000/T for AZO thin filmsisshownin the inset of Fig.3.The activation energy was calculated from the slope of the lnσ versus 1000/T curve using the following equation:

$$\sigma = \sigma_o \exp(-E_a/KT) \quad (1)$$

where E_a= activation energy,σ_o = proportionality constant, K = Boltzmann constant,andT = temperature [9].The activation energy of the AZO thin filmsdecreases from 0.43 to 0.39 eV with increase inAl-doping concentration.These activation energy values illustrate that the excitation of thermally activated electrons from donor levels to the

conduction band is due to increase in temperature [10].

The gas response–recovery mechanism for the metal oxide sensor involves two key reactions: adsorption and desorption of O_2^-, O^-,and O^{2-} molecules by the sensing layer;these absorbed oxygen molecules trap the electrons from the conductance band and play a vital role in gas sensing.As a result,variations in the resistance of the sensor filmare observed [3].To determine the optimized Al-doping concentration in ZnO, the H_2S gas-sensing performance of AZO thin films is studiedas a function of gas concentration fora certain period oftime at 250°C.The gas response curves of the AZOfilms toward a fixed 50 ppmconcentration of H_2Sgas at 250°C are shown in Fig.4(a). Here, the 2 at% AZO sensor film demonstratesthehighestgas response compared with other films; therefore, 2 at% AZO is selected for theH_2Sgasresponse at variousconcentration levels.Figure4(b) shows the dynamic gasresponse of the 2 at% AZOfilm toward H_2S gas, which clearly shows that the sensor response improves (1.06 to 3.8) with increase in the gas concentration(5 to 50 ppm). The lower value of sensing response at lower levels of gas concentration can be attributed to H_2S gas molecules covering the sensing layer toa lesserextent, whereas at higher gas concentrations, H_2S gas molecules cover a greater part of the sensing layer area, thus resulting in maximum sensing response [4].

In general,the sensing consistency of a sensor mainly depends on the reproducibility demonstrated by the sensor material. To study the reproducibilityof the optimized Al-doped ZnO film for 2 at% doping, the gasresponse was assessed4 times at50 ppm H_2S gas concentrationat250°C,as shownin Fig.4(c).After four consecutive scans, the gas response of the 2 at% AZOfilm toward H_2Sgas remained nearly constant, which confirms the reproducibility of the as-synthesized Al-doped ZnO films for H_2Sgas sensing.The selectivity studies of the optimized 2 at% AZO film are performed at 250°C and 50 ppmfixed gas concentrationfor various gases, such as C_2H_5OH,CH_3OH, CH_3COCH_3, LPG, Cl_2, NH_3,andH_2S, as shown in Fig.4(c). From the figure, we can observe that the 2 at% AZO sensor film was comparatively sensitive,selective with higher selectivity coefficient,and showed higher gas response toward H_2S gascompared with other analyte gases.This higher sensitivity and selectivity of the Al-doped ZnO film at 2 at% makes it a promising material for the fabrication of gas-sensingdevices.

IV. CONCLUSION

AnH2Sgas sensor based on Al-doped ZnO thin films was fabricated using the less-expensive sol–gel spin-coating technique. The doping of a smaller amount of Alin a ZnO lattice results in changes in structural, optical, electrical,and H2Sgas-sensing properties. Gas-sensing studies ofa 2 at% Al-doped ZnO thin film at 250 °Crevealedthat it exhibited high gasresponse (3.8) with excellent reproducibility; it can also detect the low concentration of H2S gas with a realistic response (1.06). Therefore,weconclude that 2 at% Al-doped ZnO film is agood sensing material for H2S gas detection.

Acknowledgment

This study was supported by the National Research Foundation of Korea (NRF-2020R1A2C1015206).

V. REFERENCES

[1]. H.S. Woo, C.H. Kwak, I. D. Kim, and J.H. Lee, J. Mater. Chem. A.2, 6412 (2014).

[2]. S.S. Badadhe, I.S. Mulla, Sens. Act. B.143, 164 (2009).

[3]. S.S. Zahirullah, P. Immanuel, S. Pravinraj, P.F.H. Inbaraj, J.J. Prince, Mater. Lett.230, 1 (2018).

[4]. A.R. Nimbalkar, M.G. Patil, Mater. Sci.Semi. Pro. 71, 332 (2017).

[5]. N.B. Patil, A.R. Nimbalkar, M.G. Patil, Mater. Sci.Engg. B.227, 53 (2018).

[6]. F.K. Shan, Y.S. Yu, J.Euro. Ceram. Soc.24, 1869 (2004).
[7]. M.Vishwas, K.N. Rao, A.R. Phani, K.V.A. Gowda, R.P.S. Chakradhar, Solid State Comm.152, 324 (2012).
[8]. S.R. Aghdaee, V. Soleimanian, B. Tayebi, Superlatt. Micro.51, 149 (2012).
[9]. Y. Sahin, S.Öztürkb, N. Kılınc, A.Kösemen, M.Erkovan, Z.Z.Öztürk,App. Sur. Sci.303, 90 (2014).
[10]. Y.Caglar, M.Caglar, S.Ilican, Curr. App.Phy.12, 963(2012).

Figure captions

Fig.1XRD pattern of AZO thin films.
Fig.2$(\alpha h\nu)^2$versus hνcurves for AZO thin films.
Fig.3Plot of DC conductivity according to temperature; inset shows lnσversus 1000/T curves of AZO thin films.
Fig.4(a) Response of AZOsensor towards 50 ppm H_2S gas; (b)dynamic response, (c)reproducibility, (d) andselectivitystudy of 2 at% AZO film.

Figures

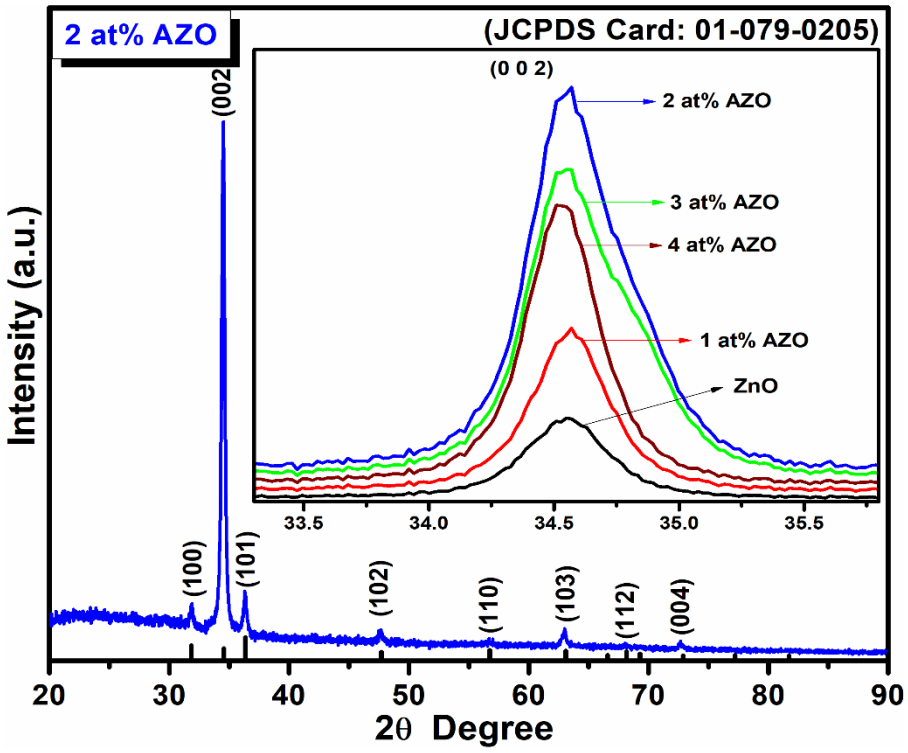

Figure: 1

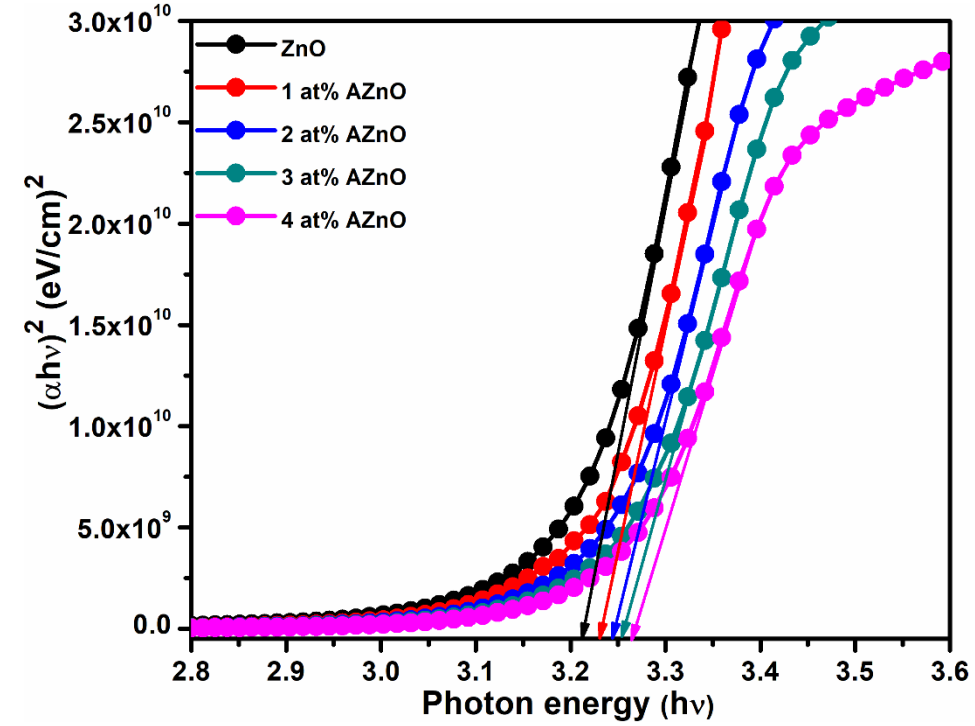

Figure: 2

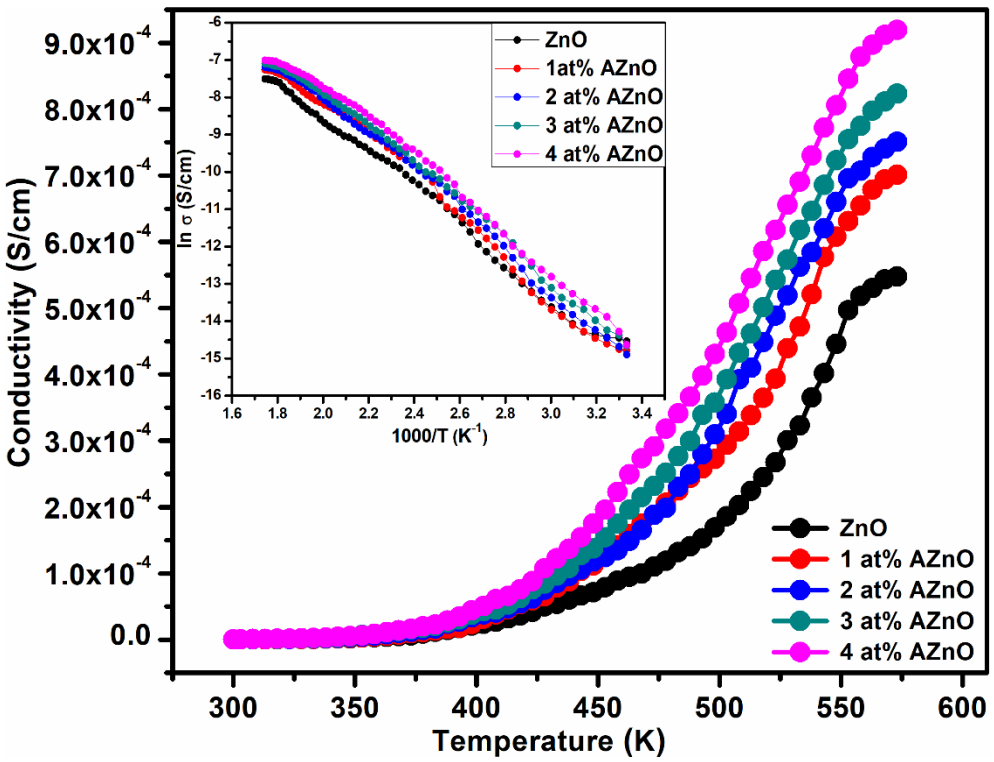

Figure: 3

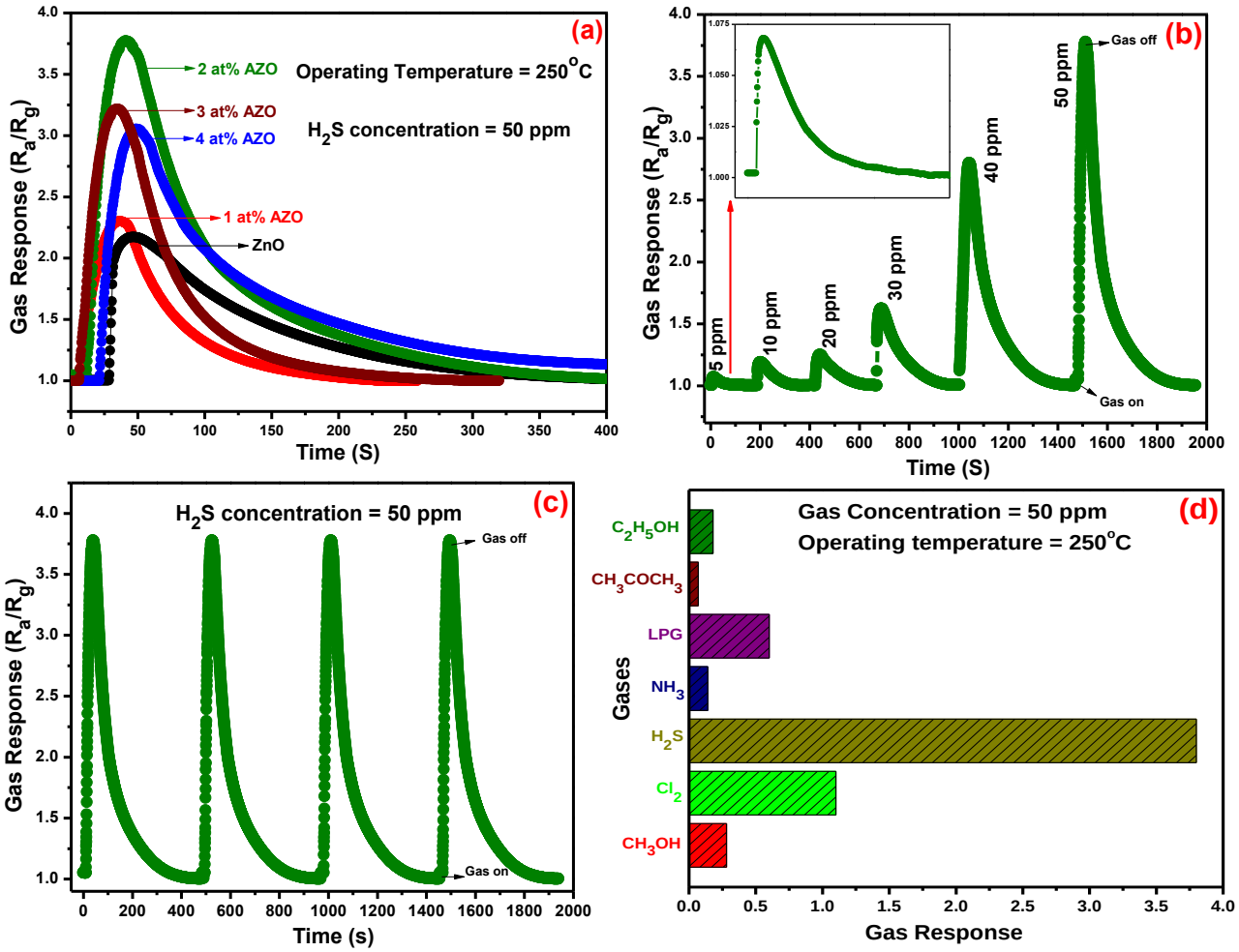
(a)
2 at% AZO
3 at% AZO
4 at% AZO
1 at% AZO
ZnO
Operating Temperature = 250°C
H2S concentration = 50 ppm
Gas Response (Ra/Rg)
Time (S)
(b)
Gas off
Gas on
5 ppm
10 ppm
20 ppm
30 ppm
40 ppm
50 ppm
Gas Response (Ra/Rg)
Time (S)
(c)
H2S concentration = 50 ppm
Gas off
Gas on
Gas Response (Ra/Rg)
Time (s)
(d)
Gas Concentration = 50 ppm
Operating temperature = 250°C
C2H5OH
CH3COCH3
LPG
NH3
H2S
Cl2
CH3OH
Gases
Gas Response

Figure: 4

International e-Conference on Recent Trends in Nano-Materials and Its Applications-2021
In Association withInternational Journal of Scientific Research in Science and Technology
Volume 9 | Issue 2 | Print ISSN: 2395-6011 | Online ISSN: 2395-602X (www.ijsrst.com)

Effect of Particle Size on the Specific Surface Area, Density, and Porosity Of $Mg_{0.8}Zn_{0.2}Cr_xFe_{2-X}O_4$

Swati Patil[1]*, P. M. Kharade[2], J. V. Thombare[3], R.S.Gaikwad[3], S. M. Mane[4], S. S. Dhasade[3]

[1]Department of Physics, Pratapsingh Mohite Mahavidyalaya, Karmala, Dist-Solapur, Maharashtra, India
[2]Department of Physics, Shankarrao Mohite Patil Mahavidyalaya, Akluj, Dist-Solapur, Maharashtra, India
[3]Department of Physics, Vidnyan Mahavidyalaya, Sangola, Dist-Solapur, Maharashtra, India
[4]Department of Physics, Yeungnam University, Gyeongsan,Gyeongbuk 38541, Republic of Korea

ABSTRACT

Particle size optimization is indispensable in many aspects for improving the properties of the materials. Here in nanoparticles of $Mg_{0.8}Zn_{0.2}Cr_xFe_{2-x}O_4$ ferritewere synthesized by the sol-gel auto-combustion method. Through the optimization of various parameters, the dimensions of the nanocrystalline ferrites are achieved within the range of 11- 54 nm. The structural changes with the substitution of Cr were analyzed using X-ray diffraction (XRD). The diffraction pattern confirms the formation of the single-phase spinel structure with cubic symmetry.The effect of particle size on parameters such as specific surface area, density, and porosity are discussed with the help of diffraction patterns. It is observed that replacing Fe^{3+} ions with the Cr^{3+} ions results in enhancement of the nanocrystalline size.

Keywords: Nanocrystalline ferrites; x-ray diffraction; sol-gel method

I. INTRODUCTION

High entropy oxide $(Co,Cr,Fe,Mn,Ni)_3O_4$based spinel structure and its microstructure was studied [1].Single-phase spinel structure nanoferrites of $Mg_{0.8}Zn_{0.2}Cr_xFe_{2-x}O_4$ were prepared by citrate–nitrate auto-combustion methodstructural, humidity sensing,impedance,conductivity and dielectric, properties of Cr^{3+} -substituted Mg–Zn ferrite cubic spinel structure was studied [2-3].Thechanges in structuralandopticalproperties of Mg-doped ZnOnanoparticlesanditsimpactonphotocatalyticefficiencyinalprazolam degradation [4] The fact of decrease in magnetization of ferrite materials is due to the increasing concentration of nonmagnetic Cr^{3+}ions that replaces magnetic Fe^{3+} ions,this results in decreasing thevalue of saturation magnetization of the Mg–Zn ferrite [5].The measured electrical properties of ferrite samples show a compositional dependencefor the AC conductivity and these materials also indicated semiconductingbehavior[6].Grain and grain boundariesof the sample will affect the conductivity of materials, at low-frequency grain boundary resistance and capacitance are contributed while at high frequency grain resistance and capacitance is contributed [7].The cubic spinel structure is maintained for all the samples of Mg-Zn ferrites by doping chromium, the crystal size increases with an

increase in doping materials[8].In the respective systems, the length between the magnetic particles of the constituent ions is decreased by increasing Al^{3+} and Cr^{3+} substitution [9].As the Cr^{3+} substitution for Fe^{3+} increases for Li-based ferrites, it will decrease curie temperature T_C and approaches the compensation temperature T_k [10].Due to the spin disorder in the surface layer of the particles,a decrease of magnetization was observed by increasing Cr doping concentration in lithium ferrite nanoparticles[11].Increasing Cr contents in Co-Fe ferrites will decrease the magnetic hyperfine fields and the Neel temperature, with further increase in the concentration of chromium ions contents size of particle will also decrease [12].Due to the smaller ionic radiiof the doped cation Cr^{3+},the lattice parameter and hence saturation magnetizationof cobalt ferrites decreases with the increase of the Crsubstitution (x) [13].The tetrahedral (A) and octahedral (B) stretching vibrations decrease with increases in Zn concentrations of Mg--Ni-Ferrites [14].TheSingle-phase cubic spinel structure of magnesium ferrite was determined by x-ray diffraction pattern and its hopping length, tetra edge, and octal edge, etc. structural parameters were also determined [15].With increasing Cr concentration in Li ferrite,X-ray density, coercivity,and porosity are increasing whereas particle size bulk density and Lattice parameter, are found to decreaseand alsothe saturation magnetization decreases linearly with increasing Cr^{3+} content[16].The saturation magnetization of lithium ferrite was studied and was found to decreases monotonically with increasing Cr-substitution content, with increasing frequency the real and imaginary parts of permittivity and permeability values decreased gradually [17].Structural and electrical properties of lithium nano ferrites were shown to be a function of composition and temperature[18].Copper doped Lithium Ferrite Nanocompositeshows the paramagnetic behavior and also it is observed that nanocomposites of ferrite exhibit the higher specific capacitance [19].P. Kharbanda et al reported homogeneousness of ferrite magnetic materialand also reported that different grain size distribution, of ferrite materials, is due to thedifference in the growth rate of individual phases in the samples [20].

II. EXPERIMENTAL

Nanocrystalline powders of $Mg_{0.8}Zn_{0.2}Cr_xFe_{2-x}O_4$were prepared by the sol-gelauto-combustion method. The A.R. grade citric acid ($C_6H_8O_7{\cdot}H_2O$), Magnesium nitrate $Mg(NO_3)_2.6H_2O$, Zinc nitrate $Zn(NO_3)_2.6H_2O$, chromium nitrate ($Cr(NO_3)_3{\cdot}9H_2O$) and ferric nitrate$Fe(NO_3)_3{\cdot}9H_2O$ were used as preparatory materials. Synthesis was carried out inthe air atmosphere without protecting by any inert gases. The molar ratio ofmetal nitrates to citric acid was taken as 1:3. The metal nitrates weredissolved together in a minimum amount of double distilled water to get aclear solution. An aqueous solution of citric acid was mixed with metal nitratessolution, then ammonia solution was slowly added to adjust the pH at 7. Themixed solution was kept on a hot plate with continuous stirring at 90 ^{0}C.During evaporation, the solution became viscous and finally formed a veryviscous brown gel. When finally all water molecules were removed from themixture, the viscous gel began frothing. After few minutes, the gelautomatically ignited and burnt with glowing flints. The decompositionreaction would not stop before the entire citrate complex was consumed. Theauto-combustion was completed within a minute, yielding the brown-coloredashes termed as a precursor. Prepared powder was then annealed at 600 ^{0}C for 6 h. Finally, a fine powder with brown color was obtained.

III. RESULTS AND DISCUSSION

X-ray diffraction:

The X-ray diffraction pattern of $Mg_{0.8}Zn_{0.2}Cr_xFe_{2-x}O_4$spinelsis shown in **Figure 1**. All Mg-Zn ferrite

samples show clearXRD reflections from the plains (220), (311), (400),(421), (422), (511), (440), and (533). The formation of the single-phase cubicspinel structure with the Fd3m space groupis in good agreement with JCPDS card number 01-071-1254. Someofthe phasesrelatedtoFe2O4Zn (ref. number 01-073-1963) and Cr2O3(ref. number 01-084-0312) are alsoobservedintheXRDpattern atthehighersubstitutionofCr3+ ions.

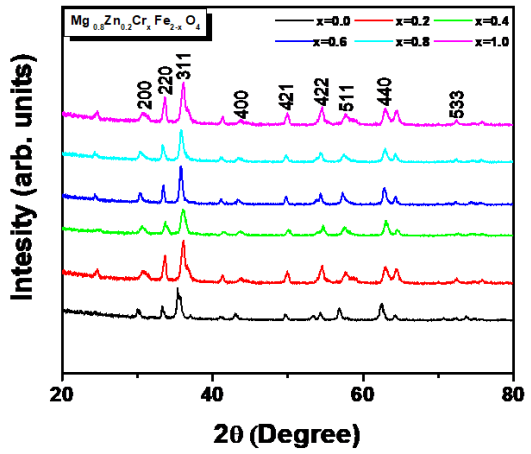

Fig. 1 XRD pattern of $Mg_{0.8}Zn_{0.2}Cr_xFe_{2-x}O_4$

These reflectionsagree quite well with powder reflections of the majority ofthe spinel systems [21]. By indexing the observed reflections of the XRD patterns the parameters of unit cell i.e. lattice constant were determined. The noticeable change in the calculated lattice constant(a) with an increase in Cr substitution is shown in **Table1**.The lattice constant(a) of all the samples was determined by using the following equation [21].

$$a = \frac{\lambda}{2}\left[\frac{\left(h^2+k^2+l^2\right)^2}{\sin\theta}\right] \quad \text{---------- (1)}$$

where ɵ is the angle of diffraction corresponding to the (hkl) plane and (hkl) are the Miller indices.The values of lattice-constant were obtained for every Mg-Zn ferrite sample using XRD data and are shown in **Table 1**. Variation of lattice constant 'a' and X-ray density 'dx' with Cr content x is shown in **Fig.3**.From the figure, it is observed that with an increase in Cr^{3+} content x, the lattice constant decreases. Thedecreaseinthelatticeconstantisrelated tothedifferenceinionicradiiofCr3+and Fe3+.Inthepresent ferrite system Fe3+ions having ionic radii,0.67 A° arereplacedbythe comparatively smallCr3+ ions having ionic radii 0.64 A°. Usingthefollowingexpression the X-ray density 'dX' was calculated

$$dx = \frac{8M}{Na^3} \quad \text{---------- (2)}$$

where 'a' isthelatticeconstant,'M' isthemolecularweightand'N' istheAvogadro's number. From **Table 1**itcanbeseenthat withincreasingtheCr3+content x,theX-ray densitydecreases.Thisdecrease in X-ray density may beduetothedecreaseinmolecularweightof the ferrite sample whichresults in thedecreaseofvolume.Thebroadening in diffractionlinesreflected bytheferritepowderisindicativeofthefineparticlenature oftheferrite.Usingthelinebroadeningofthemostintense (311)diffraction peak,the average crystallite size(t) was determined by usingtheDebyeScherrerformula [21,22].

$$t = \frac{0.9\lambda}{\beta\cos\theta} \quad \text{---------- (3)}$$

where β is thefullwidthathalfmaximumintensity measured inradian,λ is thewavelength, and ɵ is theBraggangle.**Table 1** shows thevariationofthecrystallite sizewithCrcontentx. Thecrystallitesize of ferrite powder increasedfrom10.91nmto 54.46nmwithincreasingCrcontent x.The above resultindicatesthattheaveragecrystallitesizeoftheferrite powdersismuch moredependentonthechromiumion concentrationandincreases withan increase in Cr ions,whichindicatesthatthe grain growth of ferrite powder is promoted by theadditionofchromium ion.**Fig. (2a)** and **(2b)** are the transmission electron micrographs (TEM) of x=0.8 and 1.0,respectively.It is evident from the graphs that all the synthesized particles do not have a specific shape.Both the figures confirm that most of the particles are of size about

10–54 nm. This is in close agreement with the average crystallite size obtained from XRD (**Table 1**).

Table 1

Lattice constant (a), X-ray density (dx), particle size (t),specific surface area(s),bulk density (d_B), and porosity(P) of $Mg_{0.8}Zn_{0.2}Cr_xFe_{2-x}O_4$

Comp. X	a (A^0)	dx (A^0)	t nm	s m^2/gm	d_B gm/cm^3	P %
0.0	8.381	4.6987	10.91	108.91	3.9177	16.62
0.2	8.375	4.6919	18.17	65.35	3.9777	15.22
0.4	8.368	4.6862	26.45	44.92	4.0132	14.36
0.6	8.360	4.6822	27.26	43.58	4.0463	13.58
0.8	8.355	4.6730	27.27	43.56	4.0930	12.41
1.0	8.348	4.6670	54.46	21.81	4.1218	11.68

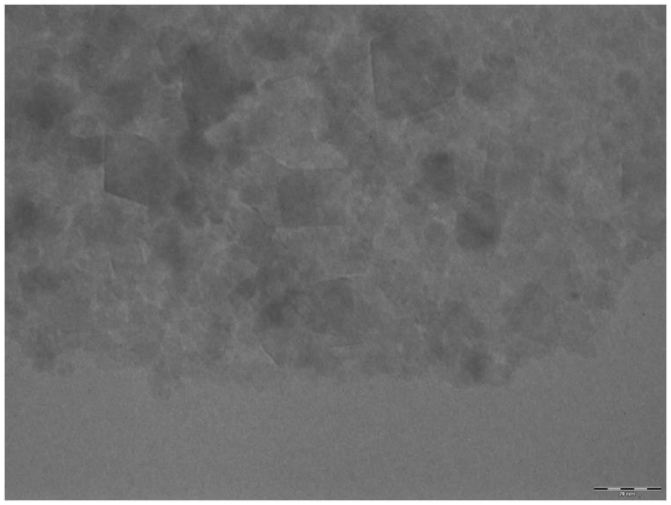

Fig. (2a) TEM image of $Mg_{0.8}Zn_{0.2}Cr_xFe_{2-x}O_4$ with X=0.8

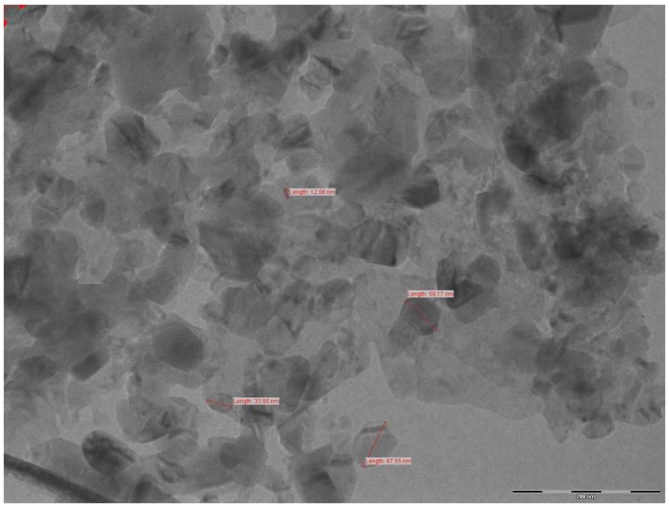

Fig. (2b) TEM image of $Mg_{0.8}Zn_{0.2}Cr_xFe_{2-x}O_4$ with X=1.0

From the diameter of the particle(D) in nanometers anddensity of the particle (ρ) the specificsurfacearea(S) was calculated using the following relation [23].

$$s = \frac{6000}{D\rho} \quad \text{---------- (4)}$$

Table 1.shows the valuesofsurfacearea. **Fig.3** shows that withincreasing Cr^{3+} content, the specific surface area decreases. Duetotheincreaseincrystallitesizeof ferrite powder thespecific surface area S decreases.

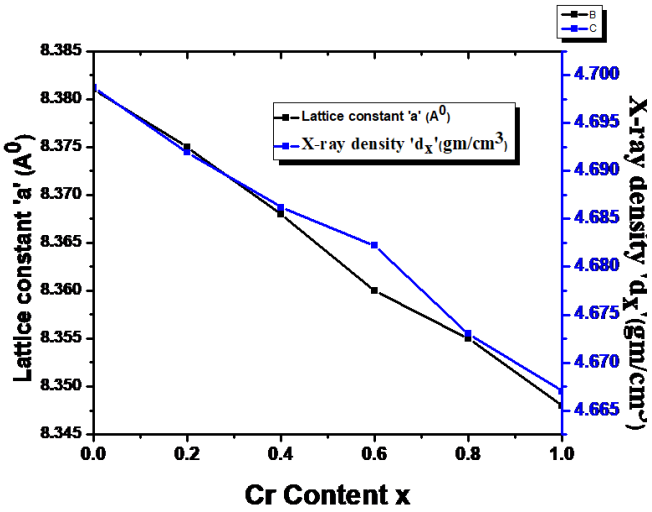

Fig.3 Variation of lattice constant 'a' and X-ray density 'dx' with Cr content x.

Byusing theArchimedes'methodthebulkdensity'dB'of thespecimenswasdetermined.The valuesofthebulkdensityareshownin **Table 1.** WithincreasingCrcontent x,thebulkdensity of ferrite

powder wasfoundtoincrease. **Fig.4** shows the variation of bulk density 'dB' and Porosity 'P' with Cr content x.

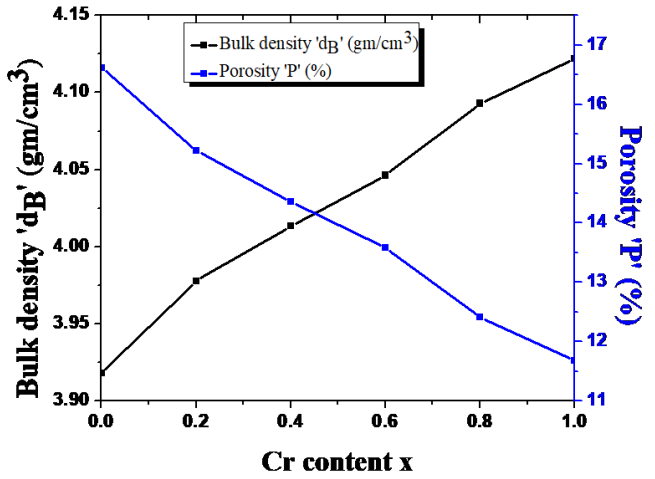

Fig.4 Variation of bulk density 'dB' and Porosity 'P' with Cr content x

Theporosity 'P' oftheferritenanoparticlescanbedeterminedusingthe followingrelation [24].

$$p = 1 - \frac{dB}{dx} \quad \text{---------- (5)}$$

IV. CONCLUSION

NanocrystallineMg-Zn ferrite powder particles are successfully synthesized by a simple sol-gel auto combustion method.The Single-phase formation of spinel structure with cubic symmetry was confirmed by XRD. The effect of particle size on parameters such as specific surface area, density, and porosity isstudied.The result indicates that the average crystallite size of the ferrite powders is much more dependent on the chromium ion concentration.With the increase in Cr^{3+} content x, the lattice constant decreases. The decrease in the lattice constant is related to the difference in ionic radii of $Cr^{3+}$and Fe^{3+}. In the present ferrite system Fe^{3+}ions having ionic radii, 0.67 A˚ are replaced by the comparatively small Cr3+ ions having ionic radii 0.64 A˚.

V. REFERENCES

[1]. Synthesis and microstructure of the (Co,Cr,Fe,Mn,Ni)3O4 high entropy oxide characterized by spinel structure,JuliuszDąbrowa, MirosławStygar, Andrzej Mikuła, Arkadiusz Knapik, Krzysztof Mroczka, Waldemar Tejchman, Marek Danielewski, Manfred Martin,Materials Letters ,216 (2018) 32-36

[2]. Improvement of physico-mechanical properties of Mg–Zn nanoferrites via Cr3+ doping,S.F. Mansour, M.A. Abdo, S.I. El-Dek,Journal of Magnetism and Magnetic Materials,422 (2017) 105-111

[3]. Synthesis and investigation of structural, dielectric, impedance,conductivity and humidity sensing properties of Cr3+-substituted Mg–Zn ferrite nanoparticle, TugbaSasmaz Kuru,Applied Physics A, 126 (2020) 419

[4]. Effect of annealing temperature on structural and optical properties of Mg-doped ZnO nanoparticles and their photocatalytic efficiency in alprazolam degradation, T.B. Ivetic, M.R.Dimitrievska, N.L.Finčur, Lj.R. Đačanin, I.O.Gúth, B.F. Abramović, S.R.Lukić-Petrović,Ceramics International, 40 (2014) 1545-1552

[5]. S.J. Haralkar, R.H.Kadam , S.SMore, SagarE.Shirsath, M.L.Mane, SwatiPatil, D.R.Mane,Substitutional effectofCr3+ ions on the properties of Mg–Zn ferrite nanoparticles,Physica B,407 (2012) 4338–4346

[6]. Structural and electromagnetic studies of Mg1-xZnxFe2O4nanoparticles synthesized via a sucrose auto combustion route,M. A. Gabal, A. A. Al-Juaid,Journal of Materials Science: Materials in Electronics,31, (2020),10055–10071

[7]. Dielectric, magnetic and humidity properties of MgeZneCr ferrites,Mehmet Kuru, TugbaSasmaz Kuru, ErtugrulKaraca, SadıkBagc,Journal of Alloys and Compounds 836 (2020) 155318

[8]. Improvement of physico-mechanical properties of mg-znnanoferrites via cr3+ doping,Journal of Magnetism and Magnetic Materials, 422 (2017) 105-111

[9]. Ion Jump Lengths Of MN-ZN-AL-FE And MG-ZN-CR-FE Nano-particles,S. J. Haralkar, S. S. More, Sagar E. Shirsath, R. H. Kadam, D. R. Mane,Indian Streams Research Journal,2 (2012) 1-6

[10]. On the magnetic compensation effect of lithium-chromium ferrites Li0.5CrxFe2.5–xO4 ($0 \le x \le 1.55$) A. Rais, A. M. Gismelseed, and I. A. Al-Omar,Phys. stat. sol. (b) 242, No. 14, (2005) 2949–2955

[11]. Effect of chromium substituted on structural and magnetic characterization lithium ferrite nanoparticles,Nguyen Thi Lan, Phuong Dinh Tam, Nguyen Phuong Duong, Than Duc Hien,Vietnam Journal of Chemistry, International Edition, 55(4) (2017) 521-526

[12]. Crystallographic and magnetic properties of CoCrxFe2˜xO4 ferrite powders, Kwang Pyo Chae, Young Bae Lee, Jae Gwang Lee, Sung-Ho Lee,Journal of Magnetism and Magnetic Materials 220 (2000) 59-64

[13]. The Effect of Cr3+ Substitution on Magnetic Properties of CoFe2O4 Nanoparticles Synthesized by Microwave Combustion Route, A. Baykal, S.Eryigit, M. Sertko, S. Unlu A. Yildiz, Sagar E. Shirsath,J Supercond Nov Magn, 2400 (2016) 29:2395

[14]. Effects of Zn Substitution on Structure Factors,Debye-Waller Factors and Related Structural Properties of the Mg1-xZnxFeNiO4Spinels,Kadhim Ahmed Khalaf, Ahmed Al-Rawas, AbbasherGismelseed, Majid Al-Ruqeishi,Salwan Al-Ani, Ahmad Al-Jubouri, Khamis Al-Ryami, Bushra Al-Jaddedi,Advances in Materials, 8(2) (2019) 70-93

[15]. Low-temperature synthesis, structural characteristic of magnesium ferrite Vinay Mahale, A V Raut, V K Surashe,S. R.Nimbhore, R G Dorik and D R Shengule,Journal of Physics: Conference Series 1644 (2020) 012013

[16]. Sol-gel synthesis of Cr3+ substituted Li0.5Fe2.5O4: Cation distribution, structural and magnetic properties, D.R. Mane, Swati Patil, D.D. Birajdar, A.B. Kadam, Sagar E. Shirsathc, R.H. Kadam,Materials Chemistry and Physics 126 (2011) 755–760

[17]. Microwave properties of chromium-substituted lithium ferrite,Yen-Pei Fu,Dung-Shing Hung,Yeong-Der Yao, Ceramics International 35 (2009) 2179–2184

[18]. Electrical Conductivity and Magnetic Properties Studies of Chromium Substituted Lithium Nano Ferrites, D. Ravinder Nayak,Poornima. B. Shetty, D. Ravinder,International Journal of Latest Technology in Engineering, Management & Applied Science 7 (2018) 2278-2540

[19]. Synthesis and Characterization of Copper Doped Lithium Ferrite Nanocomposite,P. Hajasharif, K.Ramesh, S.Sivakumar,P. Sivagurunathan,International Journal of Innovative Technology and Exploring Engineering 9 (2019) 33-37

[20]. Ferrites: magnetic materials asan alternate source of green electrical energy,Pranati Kharbanda, Tushar Madaan, Isha Sharma, Shruti Vashishtha,Parveen Kumar, Arti Chauhan, Sumit Mittal, Jarnail S. Bangruwa,Vivek Verma,.heliyon.(2019) 01151 (https://doi.org/10.1016/j.heliyon.2019.e01151)

[21]. M.V.Kuznetsov,Q.A.Pankhurst,I.P.Parkin,J.Mater.Chem.8(1998)2701.

[22]. Substitutional effect of Cr3+ ions on the properties of Mg–Zn ferrite nanoparticles,S.J. Haralkar, R.H.Kadam, S.S More, Sagar E.Shirsath, M.L.Mane, Swati Patil, D.R.Mane,Physica B 407 (2012) 4338–4346

[23]. M.George,A.M.John,S.S.Nair,P.A.Joy,M.R.Anantharaman,J.Magn.Magn.Mater. 302(2006)190.

[24]. S.M.Patange,SagarE.Shirsath,B.G.Toksha,S.S.Jadhav,K.M.Jadhav,J.Appl.Phys. 106(2009)023914

International e-Conference on Recent Trends in Nano-Materials and Its Applications-2021
In Association with International Journal of Scientific Research in Science and Technology
Volume 9 | Issue 2 | Print ISSN: 2395-6011 | Online ISSN: 2395-602X (www.ijsrst.com)

FTIR and VSM Study of Sol-Gel Synthesized Nanoparticles Of $Mg_{0.8}Zn_{0.2}Cr_xFe_{2-x}O_4$

Swati Patil[1]*, P. M. Kharade[2], J. V. Thombare[3], R.S.Gaikwad[3], Sagar Mane[4], S. S. Dhasade[3]

[1]Department of Physics, Pratapsingh Mohite Mahavidyalaya, Karmala, Dist-Solapur, Maharashtra, India

[2]Department of Physics, Shankarrao Mohite Patil Mahavidyalaya, Akluj, Dist-Solapur, Maharashtra, India

[3]Department of Physics, Vidnyan Mahavidyalaya, Sangola, Dist-Solapur, Maharashtra, India

[4]Department of Physics, Yeungnam University, Gyeongsan, Gyeongbuk 38541, Republic of Korea

ABSTRACT

In this study, spinel magnesium zinc ferrite ($Mg_{0.8}Zn_{0.2}Cr_xFe_{2-x}O_4$: x = 0.0, 0.2, 0.4, 0.6, 0.8 and 1.0) nanoparticles were synthesized by sol-gel auto combustion method. The effects of chromium ions on the functional group and magnetic properties of spinel Mg-Zn ferrites nanocomposites were investigated. Characterization methods such as Fourier transform infrared (FT-IR) spectroscopy and vibrating sample magnetometer (VSM) were used to study functional group determination and magnetic properties of ferrite materials. With the help of FTIR, the nanoregime effect on parameters such as vibration frequency, bond length, and force constant is estimated. Using the Vibrating Sample Magnetometer (VSM), the M–H loop of $Mg_{0.8}Zn_{0.2}Cr_xFe_{2-x}O_4$ has been traced and saturation magnetization (M_s), coercivity (H_C), and retentivity (M_R) studied.

Keywords: Mg-Zn ferrites; sol-gel synthesis; FTIR; VSM.

I. INTRODUCTION

Doping of Sm and Co in bismuth ferrite will influence the properties like magnetic, structural, dielectric, ferroelectric, and leakage current density [1]. Spinel structure formation and cation distribution of ferrite powder are confirmed by using Fourier transform infrared spectroscopy with the proposed data using XRD [2]. The ability of nanoporous ferrite to dissociate water molecules has been exploited to develop a green electrical energy cell, which is a combination of electrode chemistry and material science [3]. Lithium-nickel ferrite nanocrystalline particles were synthesized by a low-temperature citrate gel auto combustion method and its structural parameters like lattice parameter, X-ray density, bulk density, and porosity has determined [4] Magnetization Mg-doped lithium ferrite decreases with increases in doping percentage of magnesium and it vanishes above the comparatively high Curie temperature Tc of 900 K [5]. By using the laser diffraction technique the dispersity of the synthesized lithium ferrite powder was investigated, it is seen that there are slight decreases in the average particle size of the ferrite powder by an increase in the mechanical milling time [6]. Copper-doped cobalt ferrite

nanoparticles show a decrease in crystallite size with an increase in doping materials, while VSM results showed that the final materials are ferromagnetic and there is a decrease in magnetization due to the decrease in the value of magnetic moments of octahedral sites[7]. Cobalt doped spinel $MgFe_2O_4$ ferrite nanocomposites with improved magneto-optical and photocatalytic properties of transition metal are seen, as cobalt content increases bandgap of ferrite material goes on increases [8]. Dye-sensitized solar cell based on FeO nanorods shows conversion efficiency of 0.43%, under the light radiation of 1000 W/m^2, which is enhanced than FeO nanoparticles [9] By increasing heating rate, the average crystallite size of sintered ferrite samples decreases, during the heating period the specific surface of nanosized Mn-Zn ferrite powder strongly enhances while the density of ferrite decrease [10] The coordinates of atoms, the dimensions of the unit cell, the occupation factors of the atom, isotropic temperature factors, as well as the interatomic distances of copper doped Mg-Zn ferrite have been determined.[11] The dielectric constant of prepared spinel ferrites decreases gradually as the concentration of rare-earth ions increases in the ferrites, this is due to the exchange of electrons between Fe^{2+} and Fe^{3+} [12] By controlling the size and composition, contrast agents of Iron oxide has been developed as T_1 or T_2 for magnetic resonance imaging (MRI), they show significant interactional T_1 and T_2 contrast effects [13] Multi ferroic samples of bismuth ferrite shows the change of rhombohedral structure to a tetragonal structure after doping of Sm and CO, further it shows an increase in the symmetry and decrease in phases, Furthermore, the dielectric properties bismuth ferrites enhance with co-doping.[14] To fabricate a magnetite-based Hydroelectric Cell a chemical method is used to synthesis mesoporous magnetite nanoparticles and its ionic diffusion of dissociated ions has been confirmed, furthermore, it is observed that due to less Ohmic loss in magnetite cell current increases [15] Mn-Zn ferrite was synthesized by simple one-pot microwave combustion method, it was observed that the magnetization values of Mn-Zn ferrites increased with increasing Mn^{2+} cation, this increased values of magnetization is due to the replacement of Zn^{2+} by Mn^{2+} in the $ZnFe_2O_4$ lattice and also due to the distribution of cations at tetrahedral and octahedral sites [16] By solution combustion method single phase Cobalt copper ferrite nanopowders with increased particle size were synthesized, with an increase of Cu^{2+} ions concentration in cobalt ferrite X-ray density increase due to increase in electron density [17]

II. EXPERIMENTAL

Nanocrystalline powders of Mg 0.8Zn0.2 Crx Fe2-x O4 were prepared by the sol-gel auto-combustion method. The A.R. grade citric acid (C6H8O7·H2O), Magnesium nitrate Mg(NO3)2.6H2O, Zinc nitrate $Zn(NO_3)_2$.6H2O, chromium nitrate (Cr(NO3)3·9H2O) and ferric nitrate Fe(NO3)3·9H2O were used as preparatory materials. Synthesis was carried out in the air atmosphere without protecting by any inert gases. The molar ratio of metal nitrates to citric acid was taken as 1:3. The metal nitrates were dissolved together in a minimum amount of double distilled water to get a clear solution. An aqueous solution of citric acid was mixed with metal nitrates solution, then ammonia solution was slowly added to adjust the pH at 7. The mixed solution was kept on a hot plate with continuous stirring at 90 °C. During evaporation, the solution became viscous and finally formed a very viscous brown gel. When finally all water molecules were removed from the mixture, the viscous gel began frothing. After few minutes, the gel automatically ignited and burnt with glowing flints. The decomposition reaction would not stop before the entire citrate complex was consumed. The auto-combustion was completed within a minute, yielding the brown-colored ashes termed as a precursor. Prepared powder was then annealed at 600 ^{0}C for 6h. finally, a fine powder with brown color was obtained.

III. RESULTS AND DISCUSSION

FTIR spectroscopy:

Fig. 1 shows the FTIR spectrum of as-synthesized powder of $Mg_{0.8}Zn_{0.2}Cr_xFe_{2-x}O_4$ in the frequency range of 800–400. The positions of the ions in the crystal through the vibrational modes of a crystal can be studied with the help of an infrared absorption spectrum. It is known that the normal cubic spinels have two IR bands representing the fundamental absorption bands.

From **Fig. 1** and **Table 1** it is observed that there are two main frequency bands, namely, the high frequency band(υ_1) is observed at 529-549 cm^{-1} whereas the lower frequency band (υ_2) is observed at 422–466 cm^{-1}. The intensity of the high frequency band(υ_1) and frequency band(υ_2) appears to increase with the addition of Cr^{3+} ions. These two observed frequency bands υ_1 and υ_2 are the characteristics of all the ferrite composites and they correspond to the intrinsic vibrations of tetrahedral and octahedral $Fe^{3+}-O_2^{2-}$ complexes, respectively. It explains that the normal mode of vibration of the octahedral cluster is lower than that of the tetrahedral cluster. From FTIR data it is seen that the normal mode of vibration of the tetrahedral cluster (529 cm^{-1}) is higher than that of the octahedral cluster (422 cm^{-1}). This can be due to the long bond length of an octahedral cluster than the tetrahedral cluster[18]. This presence of a long shoulder for the A-site is indicative of the presence of other ionic states in that site. By increasing the Cr^{3+} content in ferrite powder, the vibrational frequencies $\upsilon 1$ and $\upsilon 2$ of all the compositions change. Due to the changes in bond lengths $Fe^{3+}-O_2^{2-}$ within octahedral and tetrahedral sites, the difference in frequencies between $\upsilon 1$and $\upsilon 2$ is observed. The metal-oxygen vibrational energies increases due to the decrease in the $Fe_B^{3+}-O_2^{2-}$ intermolecular distance, which arises from the increase of the number of $Cr^{3+}-O_2^{2-}$ complexes caused by the decrease in the number of $Fe^{3+}-O_2^{2-}$ complexes and the formation of Mg^{2+}/Zn^{2+} [19].

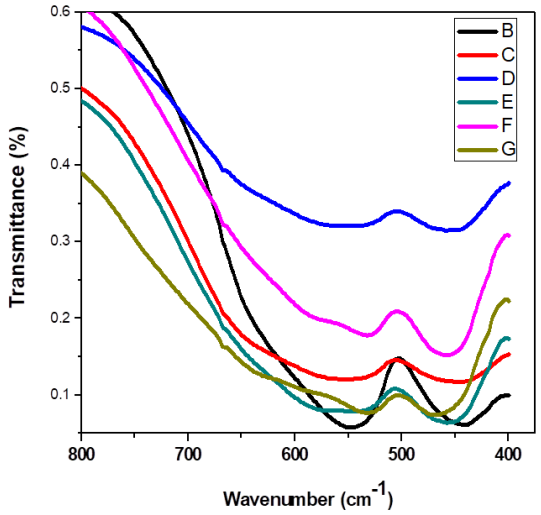

Fig.1 The FTIR spectrum of as-synthesized powder of $Mg_{0.8}Zn_{0.2}Cr_xFe_{2-x}O_4$

Comp. x	υ_1 (cm^{-1})	υ_2 (cm^{-1})	K_O x 10^4 (dyne/cm)	K_t x 10^4 (dyne/cm)
0.0	529	422	9.7603	8.5091
0.2	532	443	10.8399	8.6814
0.4	539	457	11.2090	8.6919
0.6	540	458	11.4719	8.7496
0.8	546	465	11.7285	8.8317
1.0	549	466	11.7445	8.8848

Table.1 Band position ($\nu_1$and ν_2), force constant (K_O and K_t) of $Mg_{0.8}Zn_{0.2}Cr_xFe_{2-x}O_4$.

The increasing force constant and shortening of metal-oxygen bonds of the octahedral unit is attributed to the increase in vibrational frequency (υ_2) with an increase in Cr^{3+} content in ferrite material. The force constant is the second derivative of the potential energy concerning the site radius with the other independent parameters kept constant. The force constant for the octahedral site(K_O) and tetrahedral site(K_t) were calculated by employing the Waldron method [20]. According to Waldron the

force constant K_t and K_O for respective sites are given by

$$K_t = 7.62 M_1 v_1^2 x10^{-3} \text{ dynes/cm} \text{----------(1)}$$

$$K_o = 10.62 \frac{M_2}{2} v_1^2 x10^{-3} \text{ dynes/cm} \text{----------(2)}$$

where M1 and M2 are the molecular weight of cations on the A and B sites respectively.

IV. MAGNETIC STUDIES

Substitution of Cr^{3+} ions into magnesium ferrite significantly affects the magnetic properties of ferrite materials. **Fig. 2** shows the plots of hysteresis loops for $Mg_{0.8}Zn_{0.2}Cr_xFe_{2-x}O_4$ samples. This **Fig.2** indicates that the magnesium ferrite is a soft magnetic material, which revealed minimal hysteresis. The shape and the width of the hysteresis loop depend on factors such as the porosity, grain size, and chemical composition of the compound, etc. From the field dependence of magnetization, ferrimagnetic behavior for all the samples has been observed.

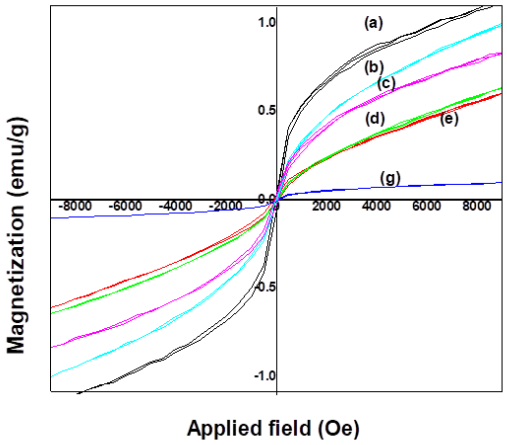

Fig. 2 Variation of magnetization with applied field measured at 300K,(a) x= 0.0, (b) x=0.2, (c) x= 0.4, (d) x=0.6, (e) x= 0.8 and(f) x= 1.0 of $Mg_{0.8}Zn_{0.2}Cr_xFe_{2-x}O_4$

From these magnetization curves (**Fig. 2)** the observed magnetic moment per formula unit,($M_{obs.}$) was determined, by extrapolating the high-field part of the curves to zero fields. In a spinel ferrite, each ion at the A site has 12 B-site ions as nearest neighbors. According to Neel's molecular field model [21], the A–B superexchange interactions dominate the intra sublattice A–A and B–B interactions. The difference of the magnetic moments of the A and B sublattices gives the net magnetic moment.[20,22]

The coercivity field, H_C reflects the coercivity for a ferromagnetic or ferrimagnetic material. This value of coercivity refers to the strength of the magnetic field required to reduce the magnetization of the ferrite magnetic sample to zero after the magnetization of the ferrite sample has reached saturation. The coercivity was observed to be significantly affected by Cr^{3+} substitution in the magnesium ferrite. It can be seen from **Fig. 3** and **Table. 2** that the coercivity increases with increasing Cr^{3+} content. According to the one-ion model, the anisotropy field in the ferrites depends on the amount of sum of effects of the different magnetic ions [23]. Values of saturation magnetization(Ms) and coercivity determined from hysteresis loops are presented in **Table 2.**

Comp. x	Ms (emu/g)	Hc (Oe)
0.0	1.1454	16.24
0.2	1.001	41.46
0.4	0.833	44.88
0.6	0.6415	56.95
0.8	0.608	61.57
1.0	0.1003	88.34

Table.2 Shows the values of magnetization(Ms), coercivity (Hc), of $Mg_{0.8}Zn_{0.2}Cr_xFe_{2-x}O_4$ with composition

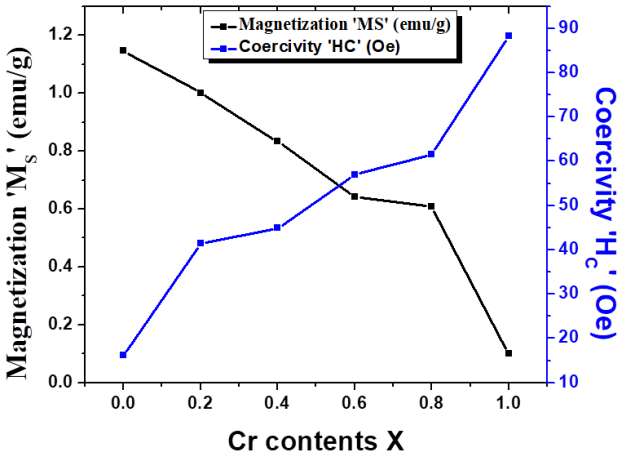

Fig. 3. Variation of saturation magnetization(M_s) and coercivity (H_C) with Cr content x.

V. CONCLUSION

The Infra-Red analysis supports the currently accepted cation distribution. With the increasing Cr^{3+} (x) content in ferrite materials, the saturation magnetization decreases linearly. The decrease in saturation magnetization is attributed to the fact that the increasing concentration of nonmagnetic Cr^{3+} ions. These nonmagnetic Cr^{3+} ions replace magnetic Fe^{3+} ions results in decreasing the value of saturation magnetization of the Mg–Zn ferrite.

VI. REFERENCES

[1]. Modified ferroelectric/magnetic and leakage current density properties of Co and Sm co-doped bismuth ferrites, Balesh Kumar Vashisth, Jarnail S. Bangruwa, Anu Beniwal, S.P. Gairola, Ashok Kumar, Nidhi Singh, Vivek VermaJournal of Alloys and Compounds, 698 (2017) 699-705

[2]. Sol-gel route of synthesis of nanoparticles of Mg Fe2O4 and XRD, FTIR and VSM study, A. Pradeep, P. Priyadharsini, G. Chandrasekaran, Journal of Magnetism and Magnetic Materials 320 (2008) 2774– 2779

[3]. Green hydroelectrical energy source based on water dissociation by nanoporous ferrite Ravinder Kumar Kotnala, and Jyoti Shah, Int. J. Energy Res. 40 (2016) 1652-1661

[4]. Structural and Electrical Properties of Li–Ni Nanoferrites Synthesised by Citrate Gel Autocombustion Method, G. Aravind, D. Ravinder, and V. Nathanial, Physics Research International, Volume 2014, Article ID 672739, 11 pages

[5]. Magnetic study of nanocrystalline Mg-doped lithium ferrite, Marek Pekala, Frank J. Berry, Hisham M Widatallah, Czechoslovak Journal of Physics, 52 (2002) 101-104

[6]. Influence of mechanical milling conditions on the dispersity of lithium ferrite, S A Lamonova, E N Lysenko and A V Malyshev, Materials Science and Engineering 93 (2015) 012035

[7]. Structural characterization and magnetic properties of undoped and copper-doped cobalt ferrite nanoparticles prepared by the octanoate coprecipitation route at very low dopant concentrations, Hypolite Mathias Kamta Tedjieukeng, Patrice Kenfack Tsobnang, Roussin Lontio Fomekong, Ekane Peter Etape, Pattayil A. Joy, Arnaud Delcortee and John Ngolui Lambia, Royal Society of Chemistry, 8 (2018) 38621–38630

[8]. Enhanced magneto-optical and photocatalytic properties of transition metal cobalt (Co2+ ions) doped spinel MgFe2O4 ferrite nanocomposites, A. Godlyn Abraham, A. Manikandan, E. Manikandan, S. Vadivel, S.K. Jaganathan, A. Baykal, P. Sri Renganathan, Journal of Magnetism and Magnetic Materials, 452 (2018) 380-388

[9]. One-Pot Low Temperature Synthesis and Characterization Studies of Nanocrystalline α-Fe2O3 Based Dye Sensitized Solar Cells, A. Manikandan, A. Saravanan, S. Arul Antony, and M. Bououdina, Journal of Nanoscience and Nanotechnology, 15 (2015) 4358–4366

[10]. Sintering of Nanosized Mn-Zn Ferrite Powders, Marko Rozman and Miha Drofenik, American Ceramic Society, 81(1998) 1757–64
[11]. Application of Rietveld Method to the Structural Characteristics of Substituted Copper Ferrite Compounds, S. Ahmed Farag, M. A. Ahmed, S. M. Hammad, A. M. Moustafa, Cryst. Res. Technol., 36 (2001) 85–92
[12]. Structural and dielectric properties of copper-based spinel ferrites, The European Physical Journal Plus, Hafiz Muhammad Tahir Farid,Ishtiaq Ahmad, Irshad Ali, Asif Mahmood, and Shahid M. Ramay, 41 (2018) 133
[13]. Interplay between Longitudinal and Transverse Contrasts in Fe3O4 Nanoplates with (111) Exposed Surfaces, Zijian Zhou,Zhenghuan Zhao,Hui Zhang,Zhenyu Wang, Xiaoyuan Chen, Ruifang Wang,Zhong Chen, and Jinhao Gao, ACS anao, 8 (2014) 7976–7985
[14]. Modified ferroelectric/magnetic and leakage current density properties of Co and Sm co-doped bismuth ferrites, Balesh Kumar Vashisth1, Jarnail S. Bangruwa, Anu Beniwal, S.P. Gairola, Ashok Kumar, Nidhi Singh, Vivek Verma, Modified ferroelectric/magnetic and leakage current density properties of Co and Sm co-doped bismuth ferrites, Journal of Alloys and Compounds, 698, (2017) 699-705
[15]. Environment-Friendly Mesoporous Magnetite Nanoparticles-Based Hydroelectric Cell Shipra Jain, Jyoti Shah, S. R. Dhakate, Govind Gupta, C. Sharma, and R. K. Kotnala, J. Phys. Chem. C, 122 (2018) 5908–5916
[16]. Enhanced Catalytic Activity and Magnetic Properties of Spinel MnxZn1–xFe2O4 ($0.0 \leq x \leq 1.0$) Nano-Photocatalysts by Microwave Irradiation Route,G. Padmapriya, A. Manikandan, V. Krishnasamy, Saravana Kumar Jaganathan, S. Arul Antony, Journal of Superconductivity and Novel Magnetism, 29(2016) 8-16
[17]. Role of Cu2+ ions substitution in magnetic and conductivity behaviour of nano CoFe2O4, D.M. Jnaneshwara, D.N. Avadhani, B. Daruka Prasad, H. Nagabhushana,B. M. Nagabhushana, S.C. Sharma, S. C. Prashantha, C. Shivakumaraha, Spectrochimica Acta Part A: Molecular and Biomolecular Spectroscopy, 132 (2014) 256-262
[18]. R.D.Waldron,Phy.Rev.99(1955)1727
[19]. O.Hemeda,M.A.Amer,S.AboulEnein,M.A.Ahmed,Phys.StatusSolidiA156 (1996) 29.
[20]. R.D.Waldron,Phy.Rev.99(1955)1727
[21]. L. Neel, Ann. Phys. 3 (1948) 137
[22]. L. Neel, C.R.Acad.,Sci.Paris230(1950)375
[23]. S.Chikazumi, S.Charap, Physics of Magnetism, John Wiley & Sons, NewYork,1964. (pp.153).

International e-Conference on Recent Trends in Nano-Materials and Its Applications-2021
In Association with International Journal of Scientific Research in Science and Technology
Volume 9 | Issue 2 | Print ISSN: 2395-6011 | Online ISSN: 2395-602X (www.ijsrst.com)

Microwave Properties of $Ca_{(1-x)}Sr_{(x)}Bi_2Nb_2O_9$ Solid Solution Prepared by Chemical Co-precipitation Method

Shivanand A. Masti

Thin Film and Material Science Division, Department of Physics, Dr. Ghali College, Gadhinglaj -416502, Maharashtra, India

ABSTRACT

Structural and microwave properties of Aurivillius-Type Structure Ceramic composition of $Ca_{(1-x)}Sr_{(x)}Bi_2Nb_2O_9$ (where x = 0, 0.2, 0.4, 0.6, 0.8 and 1.00) were investigated. The samples were prepared by co-precipitation method and the precipitate obtained is converted into thick film on alumina substrate by using screen printing method. The samples were characterized by XRD and SEM. XRD shows well defined diffraction patterns which confirm formations of compound investigation. The structure is found to be orthorhombic. The grain structure and chemical composition were examined by a scanning electron microscope (SEM). The SEM micrograph shows uniform nature of the particles. Microwave absorbance was found to be 95%, hence the material is highly useful in commercial shielding application.

Keywords: Calcium Bismuth Strontium Niobium oxide, co-precipitation method, XRD, SEM Microwave property, thick film

I. INTRODUCTION

Strontium based ferroelectric with Bismuth layered structure which is used in various electronic and technical devices. Aurivillius-type structure ceramic compounds are the materials used as high temperature piezo-electrics because of their high ferro-para electric phase transition temperature. These family materials are used in different applications like electronic, electro optical, electromechanical tuneable microwave device and system. The materials are lead-free and new candidates for substitution of widely used lead-based ceramics, owing to their environmental friendly character throughout the preparation process. Sr-based BLSFs such as $SrBi_2Nb_2O_9$ (SBN), $SrBi_2Ta_2O_9$ (SBT) and their solid solutions have been considered as one of the most promising candidates for non-volatile random access memory (NVRAM) devices [1]. The attempts have been made to improve properties of the SBNT materials by doping have been reported recently [3–6]. Many works have been focused on the improvement of the properties by appropriate substitutions [2-3], doping of the structures [4] or by non-stoichiometry [5]. Chemical methods like co-precipitation [6-8] and sol-gel [9] have been confirmed to efficiently control the morphology and chemical composition of prepared powder. The properties of these materials are significantly affected by particle size, morphology, reactivity, purity and chemical composition. The chemical method is found to be effective for preparation of ultrafine ceramic

powder with narrow particle size distribution. The A-site sublattice of the perovskite unit of the Aurivillius compounds is occupied by bismuth in $Bi_4Ti_3O_{12}$ and by lead in $PbBi_2Nb_2O_9$, but by strontium in $SrBi_2Nb_2O_9$, Dorrian et al[10] have suggested that A-site cations with one-pair electrons can have considerable influence on ferro electricity in Aurivillius compounds.

In this communication the results microwave properties of the prepared samples of $Ca_{(1-X)}Sr_{(X)}Bi_2Nb_2O_9$ under investigation are presented. The wet chemical route is employed for the preparation of powder of the sample. The precipitate obtained was converted into thick film screen painting method on alumina substrate. $Ca_{(1-x)}Sr_{(x)}Bi_2Ni_2O_9$ Powder has been investigated using different analysis techniques such as X-ray diffraction (XRD), SEM and microwave properties are reported.

II. EXPERIMENTAL

2.1. Synthesis of $Ca_{(1-x)}Sr_{(x)}Bi_2Nb_2O_9$, ceramics:

The $Ca_{(1-X)}Sr_{(X)}Bi_2Nb_2O_9$ ceramics were prepared by co-precipitation method. The chemicals used were calcium chloride ($CaCl_2$), strontium chloride ($SrCl_2$), bismuth chloride ($BiCl_2$), and niobium chloride ($NbCl_2$). The stoichiometric amount of all the chemicals was mixed together in aqueous solution. The solution is heated at 80^{0}C for 1 hour and with constant stirring the ammonium oxalate was added. The solution is converted into precipitate. The precipitate was filtered and dried in air. The mixture was homogenized by grinding it up to 4 hours in agate mortar. The mixture was heated to phase formation temperature of about 900 ^{0}C for 4 hours by making use of Muffle furnace. The sintered powder of $Ca_{(1-X)}Sr_{(X)}Bi_2Nb_2O_9$ was characterised by X-ray diffraction to ensure phase formation

2.2. Preparation of Thick Film:

The sintered $Ca_{(1-X)}Sr_{(X)}Bi_2Nb_2O_9$ powder was then mixed with binder in agate mortar to form paste of proper viscosity for thick film delineation purpose. By screen painting method the thick films were formed on alumina substrate. The prepared films were finally sintered at 900 ^{0}C to remove binder and improve adhesion of film with substrate. The prepared $Ca_{(1-X)}Sr_{(X)}Bi_2Nb_2O_9$ films were found to be strongly adherent to the alumina substrate. The films appeared to be yellowish in colour.

III. RESULT AND CONCLUSION

3.1. Structural characterization

The typical X-ray diffraction pattern of ferrite samples having general formula $Ca_{(1-x)}Sr_{(x)}Bi_2Ni_2O_9$ where x = 0, 0.2, 0.4, 0.6, 0.8 and 1.00 is shown in Figure 1. The XRD pattern was indexed using the JCPDS data for calcium strontium bismuth niobium oxide. The well defined diffraction patterns confirm the completion of chemical reaction. They show the formation of orthorhombic structure without any impurity phase.

SEM analysis

The SEM micrograph studies were carried out using SEM Model JEOL-JSM 6360 at Department of Physics, Shivaji University, Kolhapur. SEM image of $CaSrBi_2Ni_2O_9$thick film is shown in Figure 2. The micrograph shows uniform nature of the particles with some agglomeration. The average grain size is found to be 0.27μm and 0.30μm for the samples with x=0 and x=1. The grain growth in chemical methods depends upon particle size and their distribution, porosity, homogeneity in chemical composition and the sintering process.

IV. MICROWAVES PROPERTIES

4.1 Reflection Loss:

Reflection Loss (RL) study has been carried out in the frequency range 12 -18 GHz. to compare and evaluate the microwave absorption properties of $CaSrBi_2Nb_2O_9$ thick film deposited on alumina substrate. For the

measurement of RL value, samples were assembled in the Ku- Band waveguide connectors and joined to Gunn power supply. RL value of $CaSrBi_2Nb_2O_9$ thick film was calculated from the complex scattering parameter (S*11) as,

$RL = 20 \log |S_{11}|$ .... (1)

Figure 3 illustrates the variation of reflection loss with dB as the measuring unit with frequency. From this figure, it was found that $CaSrBi_2Nb_2O_9$ thick film shows maximum RL value up to -24.5dB at 12.5 GHz. In this range of frequency the absorption of microwave power is greater than 95 %. The sample under investigation shows good microwave absorption properties in Ku- Band region. It was found that the thickness of absorbent plays a vital role to enhance the microwave absorption phenomena and frequency position of microwave absorption [8]. RL value is relatively high with matching thickness ~ 20 micrometre.

4.2 Shielding Effectiveness

EMI Shielding

The total shielding effectiveness can be conveniently express in term of the S- parameters as,

$SE_T = 20 \log |S_{21}|$ ..... (2)

Shielding is conductive obstruction enveloping circuit or device to provide isolation. The SE is measure of the materials ability to attenuate the intensity of EM waves. The sample having greater SE value in decibel lowers the energy passing through that sample. EMI shielding mechanism primarily depends on the absorption of EM energy, reflection from the materials surface and multiple internal reflections of the EM radiation. For having good shielding behavior it is necessary that material should possess electrical conductivity in the range 10^{-4} to 10^{1} S/m [6]. Typical graph of total shielding effectiveness (dB) SE with Frequency is presented in Figure 6. From the graph it is seen that $CaSrBi_2Nb_2O_9$ thick film shows good shielding properties. The SE value observed is -15.1 dB at 13.8 GHz while at 15.7 GHz the observed SE value is ~16 dB which is sufficient for suppressing EM waves. The electrical conductivities of the $CaSrBi_2Nb_2O_9$ thick film is found to be 3.15×10^{-3} S/m.

V. CONCLUSION

The samples of $Ca_{(1-x)}Sr_xBi_2Nb_2O_9$ thick film prepared by co-precipitation method followed by screen printing technique. The XRD pattern was indexed using the JCPDS data for calcium strontium bismuth niobium oxide. The well defined diffraction pattern confirmed that the chemical reaction is completed. The structure of the sample was found to be orthorhombic. The SEM micrograph shows uniform nature of the particle. The average grain size is found to be 0.27μm to 0.30μm for without and with substitution of Strontium. Microwave absorbance is about 95% so formed material can be useful in commercial shielding application.

VI. REFERENCES

[1]. D. Kajewski, Z. Ujma, K. Szot, M. Pawełczyk Ceramics International 35 (2009) 2351.

[2]. A. Castro, P. Mill´an, M.J. Martinez-Lope, and J.B. Torrance, Solid State Ionics, 897 (1993) 63.

[3]. P. Dur´an-Mart´ın, A. Castro, P. Mill´an, and B. Jim´enez, J. Mater.Res., 13, (1998) 2565.

[4]. T. Takenaka and K. Sakata, Ferroelectrics, 38 (1–4), (1981) 769.

[5]. Y. Noguchi,T. Hase, andY. Miyasaka, Jpn. J. Appl. Phys, 35(9B), (1996) 4900.

[6]. S.R. Dhage, Y. Khollam, S.B. Dhespande, and V. Ravi, Mater. Res. Bull., 38, (2003) 1601.

[7]. S.R. Dhage, V. Ravi, and S.K. Date, Bull. Mater. Sci., 26, (2003) 215.

[8]. S.B. Desu, D.P. Vijay, X. Zhang, and B.P. He, Appl. Phys. Lett.,69, (1996) 1719.

[9]. C.L. Legrand, J.H. Yi, P. Thomas, Guinebretiere, and J. Pmercurrio, J. Euro. Ceram. Soc., 19, (1999) 1379.

[10]. J. F. Dorrian, R. E. Newnham, and D. K. Smith, Ferroelectrics, 3, (1971) 17.

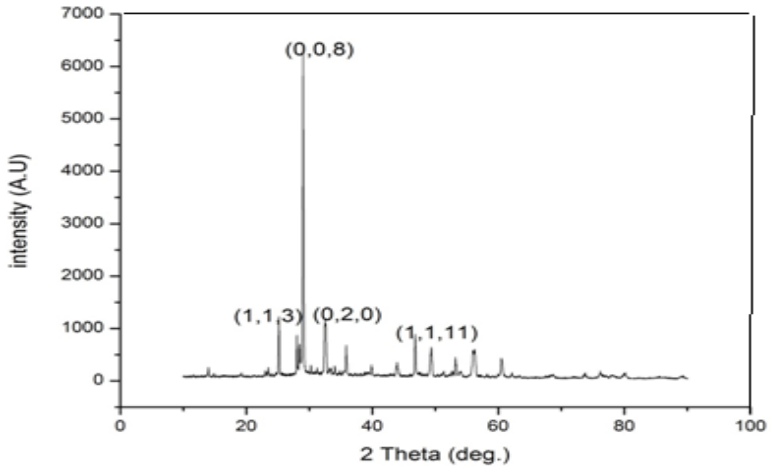

Figure 1: X-Ray Diffraction Pattern of $Ca_{(1-x)}Sr_xBi_2Nb_2O_9$ with x = 1

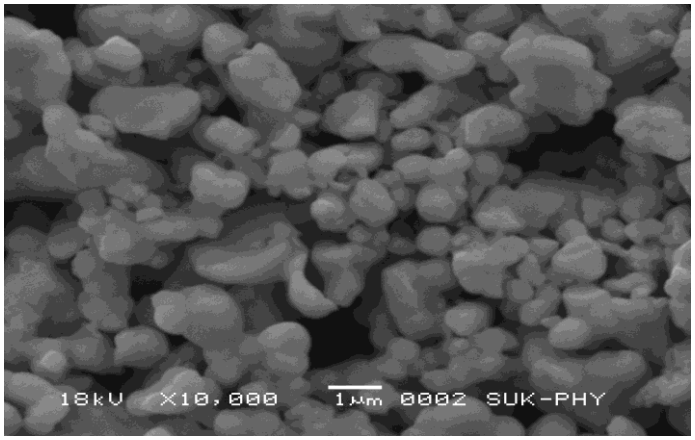

Figure 2: SEM micrograph of $Ca_{(1-x)}Sr_xBi_2Nb_2O_9$ with x = 1

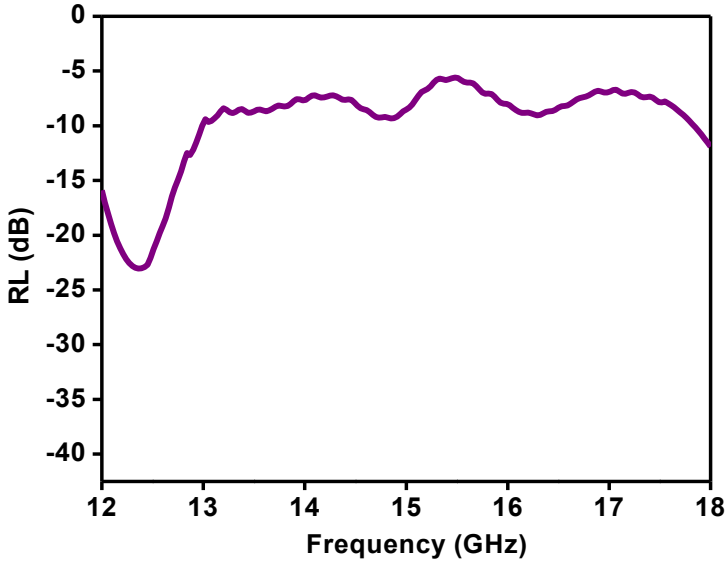

Figure 3: Reflection Loss of $Ca_{(1-x)}Sr_xBi_2Nb_2O_9$ with x = 0

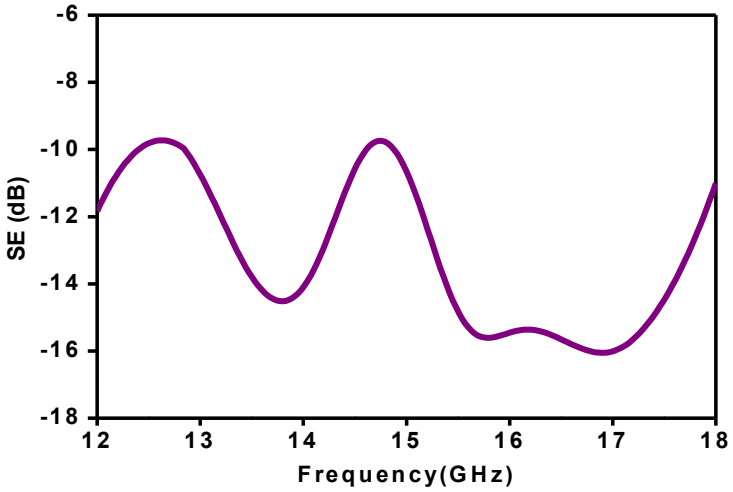

Figure 4: Shielding Effect (SE) of $Ca_{(1-x)}Sr_xBi_2Nb_2O_9$ with x = 1

International e-Conference on Recent Trends in Nano-Materials and Its Applications-2021
In Association with International Journal of Scientific Research in Science and Technology
Volume 9 | Issue 2 | Print ISSN: 2395-6011 | Online ISSN: 2395-602X (www.ijsrst.com)

Study of Structural, Morphological and Optical Properties of In_2O_3 Nano Powder Synthesised By Aloe Barbadensis Miller Extract

Sushma C. Kulkarni[1], Leena M. Mahajan[2]

[1]Department of Electronic Science, M.S.G. Arts,Science and Commerce College, Malegaon-camp, Maharashtra, India

[2]Department of Electronic Science, K.V.N. Naik Arts, Commerce and Science College Nashik, Maharashtra, India

ABSTRACT

In this study In_2O_3 nanocrystalline powder has been synthesized by simple, cost effective and ecofriendly route using Aloe Vera barbadensis Miller species available in our region having orange colour flowers. The In_2O_3 nano powder was characterized by X-ray diffraction (XRD), and transmission electron microscopy (TEM).XRD observation showed that average crystallite size 10 nm with cubic phase.Morphological observation showed a uniform size distribution of spherical particles. From TEM particle size varies from 20 to 27nm. FTIR study reveals that nano powder of In_2O_3 is single phase cubic structure. UV–visible absorption spectroscopy was utilized to deduce band gap of In_2O_3 nanocrystalline synthesized powder.

Keywords: Aloe Vera, nano crystalline, XRD, FTIR

I. INTRODUCTION

Among various semiconducting oxides In_2O_3 has attracted remarkable attention due to its interesting properties such as wide band gap (~3.6 eV), good electrical conductivity and high transparency in the visible and near infrared region [1]. It has been widely used in organic light emitting diode, solar cell, gas sensor, batteries and transparent thin films [**2**] .The core hindrance in the usage of this material is its cost. The various methods have been reported for the formation of such oxides. Researchers have focused on development of economical and environmental friendly methods for synthesis of nanoparticles (NPs), like Green method, which provides the cost effective solution for the synthesis of nanoparticles by using plant extract [3].

Although there are various methods [4, 5] reported for preparation of In_2O_3, but use of plant in synthesis of nanoparticles is novel, leading to truly green chemistry that technologist are looking for. Aloe Vera plant is used in the synthesis of oxide nanoparticles, which exhibits a super magnetic, antibacterial, anti-inflammatory, UV protective, immunomodulatory and burn healing promoting properties. Aloe Vera is used in cosmetics, drinks, detergents, as well as in stockings, diet foods, toothpaste and clothing. It is marked as a remedy for atherosclerosis, allergies, AIDS, prevention of radiation-induced dermatitis, wound healing, psoriasis, insomnia, cancer, and

several other diseases [6]. Among 400 different species, A. Vera barbadensis Miller is most popular and biologically most active

Kumar et al.[7] reported synthesis of CuO nanoparticles in monoclinic phase with average particle size of 20 nm using Aloe Vera plant extract which exhibits enhanced anti-bacterial activity against fish pathogens. Elizabeth Varghese and Mary George [8] studied photo degradation and antibacterial activity of ZnO nanoparticles synthesized using Aloe Vera plant extract. Renugadevi and Ashwini [9] reported the synthesis of silver NPs using Azadirachta indica leaf extract using microwave irradiation method. Ayeshamariam et al.[10] reported novel synthesis of In_2O_3 and ZnO NPs with particle size ranging from 10 nm to 30 nm using Aloe Vera extract solution with Indium nitrate and Zinc nitrate respectively. Maensiri et al. [11] synthesized In_2O_3 NPs of particle size 5 to 50 nm by simple method using Aloe Vera extract solution and Indium acetylacetonate.

The main goal of the paper is to present synthesis of In_2O_3 nanocrystalline powder using simple eco friendly route using Aloe Vera barbadensis Miller species available in our region.

The following section of paper discusses the experimental procedure used for the synthesis of the nanoparticles followed by results and discussions. Finally, conclusions are highlighted.

II. EXPERIMENTAL

In typical synthesis Indium (III) acetyl acetonate (Alfa Aesar, 98%) was used as starting chemical material for In_2O_3. Aloe Vera leaves of Aloe barbadensis Miller species were collected and thoroughly washed with tap water. The 35 gm pulp of leaves were finely cut and boiled in 100 ml of de-ionized water. These forms Aloe Vera extract solution.1g of Indium (III) acetyl acetonate was first dissolved in 10 ml Aloe Vera extract solution under vigorous stir at 60^0C for several hours, until dried using constant temperature magnetic stirrer cum heater. The dried precursor (brownish color) was crushed using mortar and pestle and calcined in muffle furnace at 450 ^{0}C for 2 hours in air. The dried precursor turns into yellowish colour In_2O_3 nanocrystalline powder.

Information about the crystallinity and crystal phases of the calcined powder was obtained using X-ray diffraction (XRD, Bruker D8, Advance) spectroscopy with Cu-Kα Radiation (λ =1.542 Å) for the Bragg angle ranging from 20^0 to 80^0. The grain size was determined by using Scherrer formula

$$D = \frac{0.9\,\lambda}{\beta\cos\theta} \qquad (1)$$

Where, D is the average grain size, λ = 1.541 Å, the Wavelength of X-ray radiation used and β is the angular width of the diffraction peak at the half maximum (FWHM) for diffraction angle 2θ.

An optical property of the calcined material was studied using UV-Visible spectroscopy (JASCO V-670). The morphologies and dimensions of the powder were observed by transmission electron microscopy (TEM) (Technai G20-Stwin) operated at 200 kV.

III. RESULT AND DISCUSSION

1) Fig.1 shows XRD pattern of In_2O_3 calcined powder at 450^0C. The XRD reflection can be indexed to cubic In_2O_3 (JCPDS card number 06-0416), no other peaks can be observed, revealing their phase-pure cubic structures. In_2O_3 is grown in body cantered cubic (BCC) phase with (222) plane orientation. The average crystallite size calculated using Scherrer formula was 10 nm.

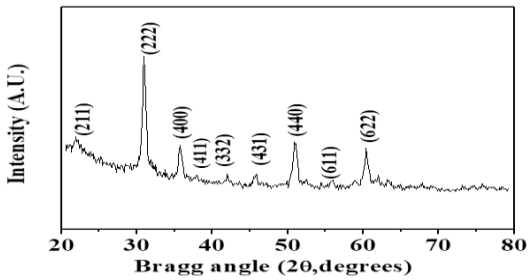

Fig.1: XRD of nanocrystalline In2O3 powder calcined at 450^0C

The morphology and structure of calcined In_2O_3 samples were investigated by TEM. The TEM bright field image of In_2O_3 is depicted in Fig.2.It shows that In_2O_3 sample calcined at 450 ^{0}C contains uniform distribution of spherical nanoparticles ranging in 20 to 27 nm in diameter. Fig.3 depicts the corresponding selected-area electron diffraction (SAED) pattern of nanocrystalline powder calcined at 450^{0}C which shows spotty ring without any other diffraction spot and rings of second phases, revealing their crystalline cubic structure. Measured interplanar spacing (d_{hkl}) from selected-area electron diffraction (SAED) pattern in Fig.3 are in good agreement with values in standard data (JCPDS:06-0416).

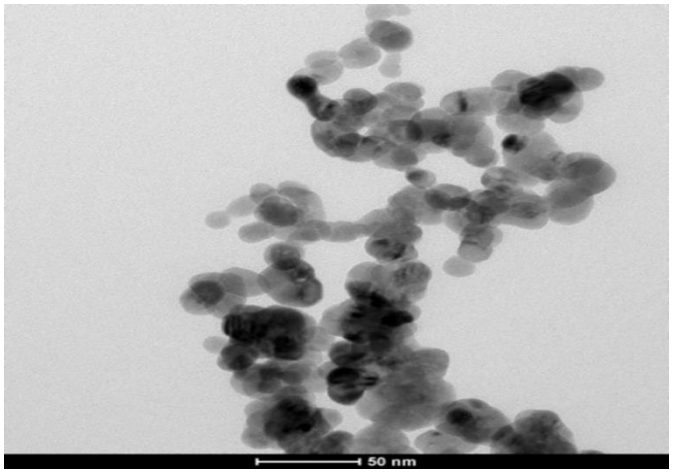

Fig.2: TEM image of In_2O_3 nanocrystalline powder calcined at 450^{0}C

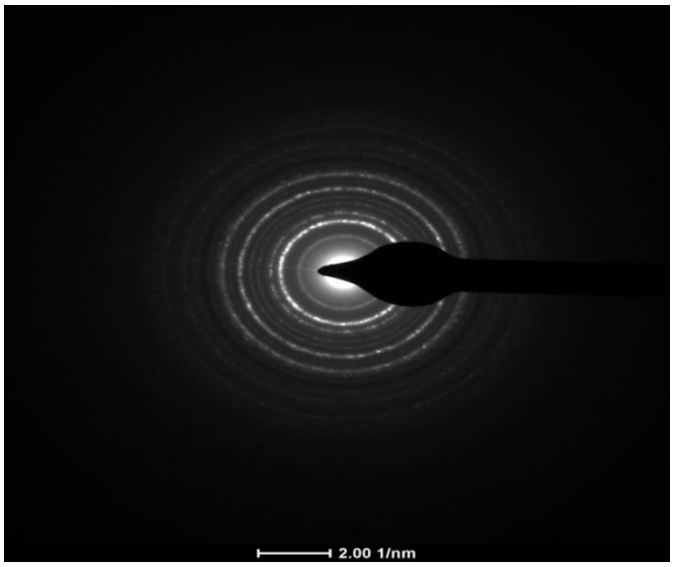

Fig.3: SAED pattern of In_2O_3 nanocrystalline powder calcined at 450^{0}C.

Fig.4 elucidates the UV-Visible spectra of calcined powder, where a symmetric peak is seen easily. An absorption peak is observed at 317 nm corresponding to the typical absorption value of In_2O_3 material. Band gap values have been estimated from the UV-visible spectra using Tauc plot method. The value of direct band gap was deduced to be 3.26 eV for In_2O_3 sample calcined at 450^{0}C which is less than reported value [12].

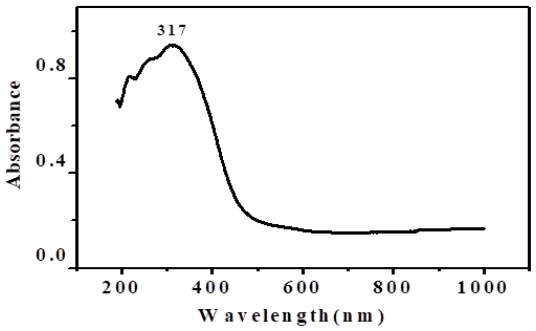

Fig.4: UV-vis-NIR spectra of nanocrystalline In_2O_3 powder calcined at 450^{0}C

IV. CONCLUSION

In this study we have reported green approach for In2O3 was synthesis using Aloe Vera plant extract. This method is simple cost effective and eco-friendly. XRD confirmed that synthesis is viable and complete and average crystallite size 10 nm..TEM analysis showed that In2O3 samples are cubic in nature. TEM shows uniform spherical distribution of nanocrystalline particles with size 20-27 nm. The optical band gap was 3.29 eV. We were successful in achieving In2O3 nanocrystalline powder for its potential in gas sensing applications.

V. REFERENCES

[1]. A Gurlo, M. Ivanovskaya, A. Pfau, U. Weimar, W. Gopel Thin Solid Films 307(1997), 288-293

[2]. D. Zhang, C. Li, S. Han, X. Liu, T. Tang, W. Jin, C. Zhou, Appl. Phys. A 77, (2003), 163–166.

[3]. Roduner, E. Chemical Society Reviews, 35(7), (2006). 583-592.

[4]. Ahmad.S, Munir. S, Ullah. A,Zeb.N, Khan.A,Bilal.M, Omer. M, Alamzeb.M,Salman. S,Ali.S, Int.J.Nanomedicine,14,(2019), 5087-5107.
[5]. Moodley.J, Krishna.S, Pillay.K, ,Govender,Adv.Nat.Sci:Nanosci Nanotechnol,(2019), 9,015011(9pp),
[6]. Ayeshamariam, A., Jayachandran, M., Kumar, P., & Bououdina, M. (2013). International Journal of Bioassays, 2(01), 304-311.
[7]. Kumar,P. V., Shameem, U., Kollu, P., Kalyani, R. L., & Pammi, S. V. N. (2015). Bio NanoScience, 5(3), 135-139.
[8]. Varghese, E., & George, M. (2015). Int. J. of Advance Science and Engineering 4(1),
[9]. Renugadevi, K., & VenusAswini, R. (2012). Asian J. of Pharmaceutical and Clinical Research, 5, 4.
[10]. Ayeshamariam, A., Kashif, M., Vidhya, V. S., Sankaracharyulu, M. G. V., Swaminathan, V., Bououdina, M., & Jayachandran, M., (2016). Int. J. Nanoelectronics and Materials 9, 49-66
[11]. Maensiri, S., Laokul, P., Klinkaewnarong, J., Phokha, S., Promarak, V., & Seraphin, S. (2008). J. Optoelectron Adv Mater, 10, 161-5.
[12]. Poznyak, S. K., Golubev, A. N., & Kulak, A. I. (2000). Surface science, 454, 396-401.

International e-Conference on Recent Trends in Nano-Materials and Its Applications-2021
In Association with International Journal of Scientific Research in Science and Technology
Volume 9 | Issue 2 | Print ISSN: 2395-6011 | Online ISSN: 2395-602X (www.ijsrst.com)

Effect of Solution Molarity on Transport Properties of $Zn_{0.55}Cd_{0.45}O$ Thin Films Prepared By Chemical Route

Suvarnalatha Shenoy[1]*, Sumanth Joishy[2]

[1]Department of Physics, Sri Bhuvanendra College Karkala, Udupi District, Karnataka - 574104, India

[2]Research Scholar, Manipal University, Manipal, India

ABSTRACT

$Zn_{0.55}Cd_{0.45}O$ films were grown on glass substrate at 673K using zinc acetate and cadmium acetate as precursor with different molar concentrations varying from 0.03M to 0.09 M. The effect of precursor concentration on structure, surface morphology, optical and electrical properties are studied by X-ray diffraction, Scanning electron microscope, UV–Vis spectroscopy and four probe Hall measurement. All deposits have shown mixed phase of hexagonal and cubic crystal structure . The crystallite size increases with increase in the molarities of the solution. The SEM observation reveals that the spheroid structure of $Zn_{0.55}Cd_{0.45}O$ grown thin film. The optical transmittance increases with a decrease in the precursor concentration and the maximum transmission in the visible region is about 80% of the film prepared with 0.03 M. The optical energy band gap and resistivity of the deposits has found to decrease with increase in molarity.

Keywords: Thin film, Molarity, Crystallite size, Resistivity

I. INTRODUCTION

ZnO and ZnO-based semiconductors have attracted considerable attention due to their potential application in the light emitting diodes (LED), blue and ultraviolet (UV) semiconductor lasers and other optoelectronic devices [1].It has a wide direct band-gap of 3.3eV, a hexagonal wurtzite structure and an even larger excitonic binding energy of 60meV [2]. To design ZnO-based devices, one of the crucial issues is the realization of band-gap engineering. CdO is II–VI compound semiconductor with a direct band-gap of 2.3eV with a cubic structure [3]. The addition of Cd into the ZnO lattice results in an improvement of the characteristics of the ternary ZnCdO to be used as transparent conducting oxides(TCO), due to its better transmittance and lower resistivity of the films [4]. Both characteristics are of crucial importance in photovoltaic solar cells where incoming photons have to be efficiently harvested by the absorbent layer located below the TCO layer. So the maximum fraction of photons has to be transmitted through the TCO layer to reach the absorber. Further, any increase of the serial resistance results in a drop of the device efficiency, therefore high conductivity is essential for TCO layers.

ZnCdO thin films can be prepared by a variety of techniques including pulsed laser deposition(PLD), electro deposition, hydrothermal synthesis, sol–gel, magnetron sputtering, spray pyrolysis technique, thermal co-evaporation [5-11]. Among these techniques, spray pyrolysis is a simple, versatile and cost effective method for the preparation of polycrystalline and amorphous thin films of oxides.

Thin film solar cell fabrication, post-deposition TA is one of the important steps which optimize compositional profile, structural, morphological, and optoelectronic properties of devices. The precursor concentration is one of the key factors in deciding the physical, chemical and other properties of any thin films. In this work we study the effect of precursor concentration on the structure, surface morphology, optical and electrical properties of pyrolized $Zn_{0.55}Cd_{0.45}O$ thin films in detail.

II. EXPERIMENTAL

The borosilicate glass is ultrasonically cleaned and used as a substrate to deposit 45% cadmium doped ZnO thin films using the chemical spray pyrolysis method. The substrate was preheated at 673K. The pyrolytic decomposition of the solutions results in the formation of good, adherent, transparent $Zn_{0.55}Cd_{0.45}O$ thin films onto preheated substrate. Parameters like nozzle to substrate distance, gas pressure and solution flow rate were kept constant which are depicted in table 1.

These samples were characterized by X-ray diffraction (XRD) using a Rigaku Miniflex 600, diffractometer with CuK_{α}radiation (1.5405Å) over the range 2Θ =20˚to80˚ at room temperature. The surface morphology and film thickness were studied using Scanning Electron Microscopy (Zeiss EVO 18-15-57) . Optical transmission measurements were carried out in the range 350–800 nm using Shimadzu-1800 UV-VIS spectrophotometer. Electrical characterization of deposit sample was studied using Hall measurement set up with Keithly source meter 6220 and magnetic field of 0.5Tesla.

Table 1: Optimized deposition condition used to prepare $Zn_{0.55}Cd_{0.45}O$ films:

Solute	Cadmium acetate dehydrate and Zinc acetate dehydrate
Solvent	Double distilled water
Concentration of solution	0.03M, 0.06M and 0.09M
Carrier gas	Compressed air 5kg(f)/cm^2
Solution spray rate	10 ml/min
Substrate temperatures	673K
Substrate to nozzle distance	24cm
Film thickness	400-450nm

III. RESULT AND DISCUSSION

Structure properties

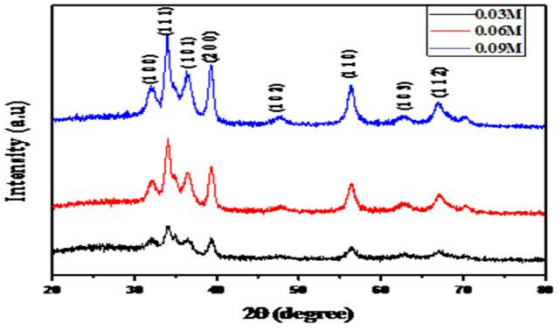

Fig. 1. XRD patterns of $Zn_{0.55}Cd_{0.45}O$ thin films of different molarity

Fig. 1 shows the X-ray diffraction patterns of the $Zn_{0.55}Cd_{0.45}O$ samples. The presence of diffraction peaks shows a polycrystalline nature with mixture of hexagonal and cubic crystal structure. The XRD peak intensities of (1 1 1) and (2 0 0) reflections were relatively higher than those of other reflections. The peak intensity has found to increase with molarity of the solution. This implies that the film grows along (1 1 1) and (2 0 0) directions which is the cubic phase of polycrystalline CdO. With the increasing of precursor concentration was found to give the common trend for all the other planes. Similar peaks were also observed by Caglar et al [12]. As seen from these results, it can be said that the crystallinity of films increases with molarity. Beevi et al [**13**] also found the increase of crystallinity with molarity for CdO films.

The crystallite size of the films was calculated using a well-known Scherrer's formula [14],

$$D = \frac{0.9\lambda}{\beta cos\theta} \quad \text{..... (1)}$$

where, constant factor K is used 0.94 for this nanostructure, β is the broadening of diffraction line measured at half of its maximum intensity (FWHM) and λ is the wavelength of the X-ray used (1.5406 Å). The crystalline size increased with molarity supporting the assumptions on the mechanism based on growth. In addition, to have more information on the amount of defects in the films, the dislocation density (δ) has been calculated by using the formula below [15]

$$\delta = \frac{n}{D^2} \quad \text{..... (2)}$$

Where, n is a factor which equals unity giving minimum dislocation density. The calculated δ values (Fig.2) indicate that the dislocations per unit volume of unit cell decreases with increase in molarity, it means with increase in molarity the defects decreases and improves the crystalline quality.

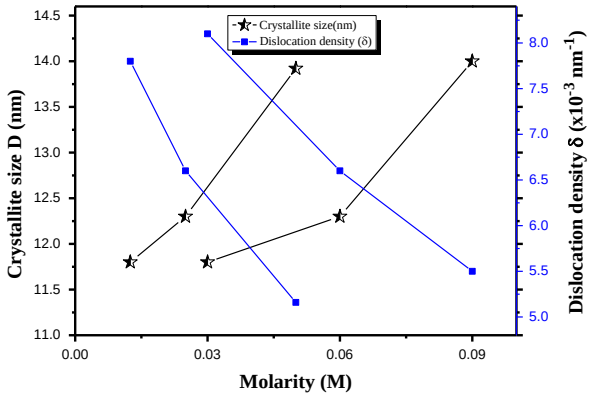

Fig. 2. Crystallite size and dislocation density versus molarity

Surface Morphology

The high magnification surface morphological study of $Zn_{0.55}Cd_{0.45}O$ nanostructures grown by chemical spray pyrolysis technique as a function of precursor concentration has been carried out using SEM micrograph shown in Fig.3. The surface morphology of the films was smooth and uniform in nature. SEM image show that all the films consist of nanoparticles and the particle size continuously increases with increasing molarity.

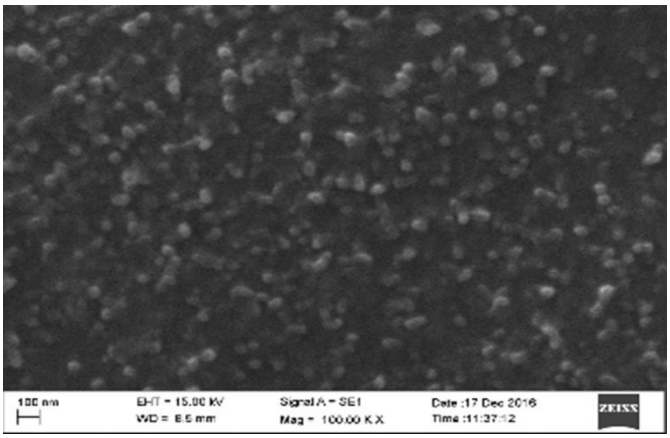

(a)

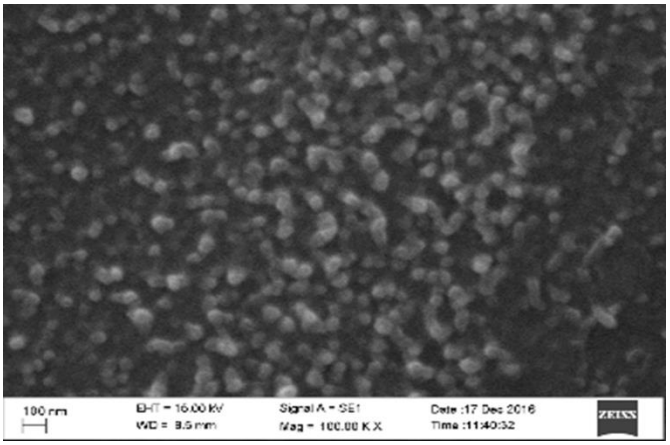

(b)

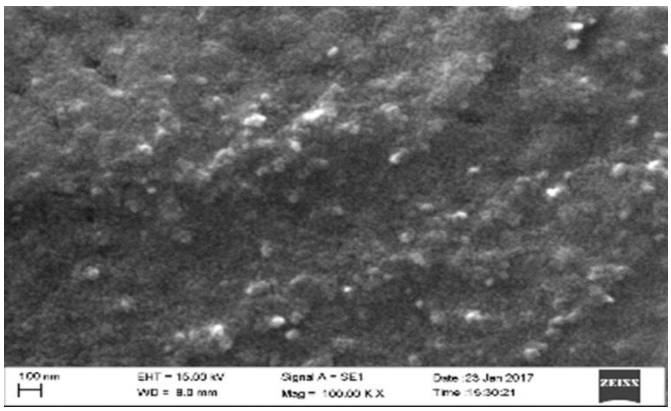

(c)

Fig. 3. SEM images of $Zn_{0.55}Cd_{0.45}O$ thin films of different molarity (a)0.03M, (b) 0.06M and (c) 0.09M

In the films of low molar concentration the density of clusters on the substrate will be low and the film exhibited an open structure. Film (b) has shown the well distributed spherical morphology. The accumulation of grains was observed on the surface of the film (c) with high density of clusters randomly

distributed on the film surface, confirming the faster nucleation. Hence, with increasing the molarity, there is a lower probability of rearrangement of the arriving material and the in homogeneity increases inducing the formation of small heaps and clusters [16].Several authors have reported the similar nanoparticle nature of the films[17-19].Therefore, it can be interpreted that crystallite structure of $Zn_{0.55}Cd_{0.45}O$ thin films are function of precursor concentration and shows symmetric change in surface morphology

Optical properties:

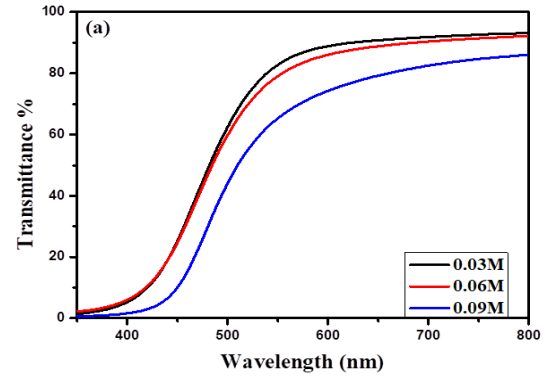

(a)

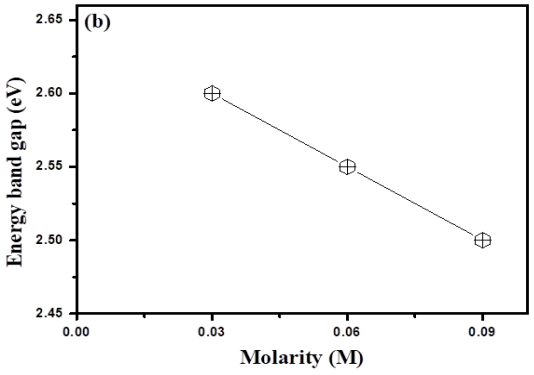

(b)

Fig.4 (a) Optical transmittance versus wavelength and **(b)** energy band gap versus molarity for$Zn_{0.55}Cd_{0.45}O$ thin films.

Fig. 4(a) shows the transmittance of film as a function of wavelength. It is observed that the transmittance is lowest in visible region about 65% for 0.09 M. Transmittance of 0.03M film is highest 80% in the visible region with compare to other films deposited using higher molarity. The dependence of α with the photon energy hυ is fitted to the relationship for the allowed direct transition

$$(\alpha h\nu) = A(h\nu - E_g)^{1/2} \quad \ldots\ldots\ldots\ldots\ldots\ldots\ldots\ldots\ldots\ldots\ldots\ldots(2)$$

Where, A is an energy-independent constant and E_g is the optical band gap. The consecutive shift in the transmission edge towards higher wavelength indicates a narrowing optical band gap. The band gap of all films varies from 2.64 to 2.46 eV. The variation of band gap may be due to the variation of strain. Strain changes inter spacing between atoms of semiconductors which affects the energy gap [20].

Electrical properties

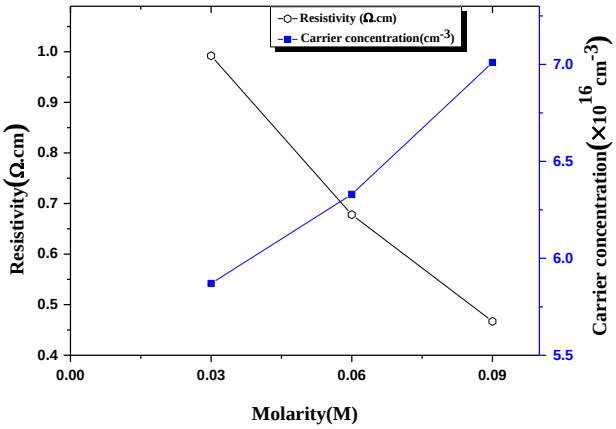

Fig. 5. Room temperature resistivity and carrier concentration versus molarity

A Hall Effect study was carried out for all the films in order to identify the type of electrical resistivity of the deposited material. The electrical resistivity was found to decrease with increase in molarity of spray solution. The deposited films were more crystalline with increasing molarity and it is well known fact that the thin film possesses relatively low resistivity when it is highly crystalline in nature [21]. The increase of grain size with molarity reduce the electron grain boundary scattering. Thus electrical resistivity decreases with molarity due to good crystallinity and large grain size. This results in increase in its free carrier concentration.

IV. CONCLUSION

The structure, surface morphology, optical and electrical properties of spray deposited $Zn_{0.55}Cd_{0.45}O$ thin films were investigated as a function of precursor concentration. The structure analysis indicated that the $Zn_{0.55}Cd_{0.45}O$ films were polycrystalline with a mixture of hexagonal-cubic phases. Spherical grain morphology was observed with uniform nature of the deposits. Optical energy band gap was decreased from 2.64 to 2.46 eV with increase of molarity. A slight increase in carrier concentration has been observed with increasing molarity. These results indicate that the Cd doped ZnO thin films are useful for optoelectronic applications in the UV and visible regions.

V. REFERENCES

[1]. Zhe Chuan Feng, Handbook of Zinc Oxides and Related Materials: Volume 1) Materials, and Volume 2) Devices and Nano-Engineering, CRC Press, NewYork, 2012.

[2]. S.J. Pearton, D.P. Norton, K. Ip, Y.W. Heo, T. Steiner, J. Vac. Sci. Technol. B 22 (2004) 932.

[3]. T. Gruber, C. Kirchner, R. Kling, F. Reuss, Appl. Phys. Lett. 83.16 (2003)3290–3292

[4]. S. Sadofev, S. Blumstengel, J. Cui, J. Puls, S. Rogaschewski, P. Schäfer, F. Hennerberger, Applied Physics Letters 89 (2006) 201907

[5]. S.Y. Lee, Y. Li, J.S. Lee, J.K. Lee, M. Nastasi, S.A. Crooker, Q.X. Jia, H.S. Kang, J.S.Kang, Appl. Phys. Lett. 85 (2004) 218–220.

[6]. M. Tortosa, M. Mollar, B. Mari, J. Crystal Growth 304 (2007) 97–102.

[7]. O. Lupan, T. Pauporte, L. Chow, G. Chai, B. Viana, V.V. Ursaki, E. Monaico, I.M.Tiginyanu, Appl. Surf. Sci. 259 (2012) 399–405.

[8]. F. Yakuphanoglu, S. Ilican, M. Caglar, Y. Caglar, Superlattices Microst. 47 (2010)732–743.

[9]. R.J. Zhang, P.L. Chen, Y.Y. Zhang, X.Y. Ma, D.R. Yang, J. Crystal Growth 312(2010) 1908–1911.

[10]. A.D. Acharya, Shweta Moghe, Richa Panda, S.B. Shrivastava, Mohan Gangrade,T. Shripathi, D.M. Phase, V. Ganesan, Thin Solid Films 525 (2012) 49–55.

[11]. Q. Wan, Q.H. Li, Y.J. Chen, T.H. Wang, X.L. He, X.G. Gao, J.P. Li, Appl. Phys. Lett.84 (2004) 3085–3087.

[12]. Yasemin Caglar, Mujdat Caglar, Saliha Ilican and Aytunc Ates, J. Phys. D: Appl. Phys. 42 (2009) 065421 (8pp)

[13]. M.M. Beevi, M. Anusuya , V. Saravanan.Int. J. Chem Eng Appl. 1(2010) 151–4

[14]. A. Singh, D. Kumar, P.K. Khanna, A. Kumar, M. Kumar, M. Kumar, Thin Solid Films. 519 (2011) 5826–5830.

[15]. M. Ali Yildirim, Aytunç Ateş, Opt. Commun. 283 (2010) 1370-1377.

[16]. N.R. Panda, B.S. Acharya ,P. Nayak ,B .P .Bag,,Ultrason.Sonochem.21(2014)582–589.

[17]. Li Gang, Xuebin Zhu, Xianwu Tang, Wenhai Song, Zhaorong Yang, Jianming Dai, Yuping Sun, Xu Pan, Songyuan Dai, Journal of Alloys and Compounds. 509 (2011) 4816–4823

[18]. A. Guru Sampath Kumar,L. Obulapathi, T. Sofi Sarmash, D. Jhansi Rani, M. Maddaiah, T. Subba Rao, K. Asokan, The Minerals, Metals & Materials Society

[19]. Munirah, Ziaul Raza Khan, Mohd. Shahid Khan, Anver Aziz, Materials Science-Poland. 32(4)(2014) 688-695.

[20]. Jeevitesh K. Rajput, Trilok K. Pathak, Vinod Kumar, L.P. Purohit, Applied surface science. http://dx.doi.org/doi:10.1016/j.apsusc.(2017).

[21]. Y.M. Lu, W.S. Hwang, W.Y. Liu, J.S. Yang, Mater. Chem. Phys. 72 (2001) 269–272.

International e-Conference on Recent Trends in Nano-Materials and Its Applications-2021
In Association with International Journal of Scientific Research in Science and Technology
Volume 9 | Issue 2 | Print ISSN: 2395-6011 | Online ISSN: 2395-602X (www.ijsrst.com)

Sodium Dodecyl Sulfonate Assisted Sol-Gel Synthesis and Characterization of Co_3O_4 Nanoparticles

Savita Vasantrao Thakare

ABSTRACT

The current work reports the synthesis and characterization of cobalt oxide nanoparticles. Stabilized Co_3O_4 nanoparticles were prepared by Sol-Gel method using $Co(NO_3)_2.6H_2O$ as a metal precursor. The synthesis of the Co_3O_4 nanoparticles was performed in the presence of anionic surfactant sodium dodecyl sulphate (SDS) The nanoparticles thus formed were characterised by powder Fourier transform infrared spectra, X-ray diffraction(XRD), scanning electron microscopy, energy-dispersive X-ray spectroscopy and transmission electron microscopy .

Keywords :-Co_3O_4 nanoparticles, Sol-Gel method, Sodium dodecyl sulfonate, XRD, SEM, TEM

I. INTRODUCTION

Nanotechnology is a field of science includes research and innovation concerned with production, utilization and manipulation of novel materials and devices on subatomic level [1]. Nanoparticles are fundamental fragment of nanotechnology. Nanoparticles include different types of inorganic nanoparticles like metals and metal oxides. In recent years, synthesizing different metal oxide nanoparticles have drawn significant amount of attention as they possess unique chemical, electronic, mechanical, magnetic and optical properties which are considerably different from those of corresponding bulk ones [2-6].

Transition metal oxides shows a broad structural variety due to variable oxidation states so being considered as promising materials for many applications [7].Cobalt oxide Co_3O_4 is an important transition metal oxide as antiferromagnetic p-type semiconductor with excellent properties such as magnetic, gas-sensing, catalytic and electrochemical ones. On account of these properties Co_3O_4 nanoparticles have been utilized applications in field of research and industry include as anode materials for rechargeable lithium batteries, solid-state sensors, heterogeneous catalysts, electrochromic and magneto resistive devices [8–12]. Thus incredible efforts have been focussed in current years to the production and exploration of properties of Co_3O_4 nanostructures

Many physical and wet chemical techniques has been applied for the synthesis of cobalt oxide nanoparticles. Now days, researchers focused on wet chemical techniques includes bottom–up approach such as sol-gel, hydrothermal, surfactant-mediated synthesis, co-precipitation, polyol, combustion, spray-pyrolysis, micro emulsion and mechanochemical methods [13-17]. Out of them Sol gel method was proved as a best process to attain the Co_3O_4 nanostructures since this method is sintering at low temperature and provides better homogeneity in addition to phase purity [18].

This research work attempt to synthesize the cobalt oxide nanoparticles with cobalt nitrate as metal precursor and SDS surfactant via the sol-gel method. This method is a more easy and low-cost process that generates nanoparticles with low sintering time. The aim of research to develop knowledge in the synthesis methods of cobalt oxide nanoparticles.

II. EXPERIMENT

Materials

Cobalt nitrate ($Co(NO_3)_2.6H_2O$) oxalic acid ($C_2H_2O_4.2H_2O$) and Sodium dodecyl sulfonate (SDS) were analytical grade and all were purchased from Sigma-Aldrich. Double distilled water was used as a solvent in all the experiments. All the solutions were prepared in double distilled water.

Preparation of Co_3O_4 Nanoparticles

The Co_3O_4 nanoparticles were synthesized by the sol gel method using Cobalt nitrate $Co(NO_3)_2.6H_2O$ (1M) used as precursor and SDS as surfactant was dissolved in 100 ml double distilled water . The oxalic acid (1M) was slowly added drop wise under continuous stirring. The light pink coloured precipitates of cobalt hydroxide was obtained. The precipitate obtained was treated in a teflon-lined autoclave at 110°C for period of 24 hours. The subsequent gel was separated via filtration and repeatedly washed by deionized water. Afterward, the washed precipitate was dried at 80 °C for 16 h. Finally, precipitate was calcined at 550°C for 4h.

III. RESULT AND DISCUSSION

Fig. 1 shows FT-IR spectrum of Co_3O_4 nanoparticles. The absorption band at 524.64 cm^{-1} was assigned to Co-O stretching vibration mode and 648.08 cm^{-1} was assigned to the bridging vibration of O- Co-O bond.

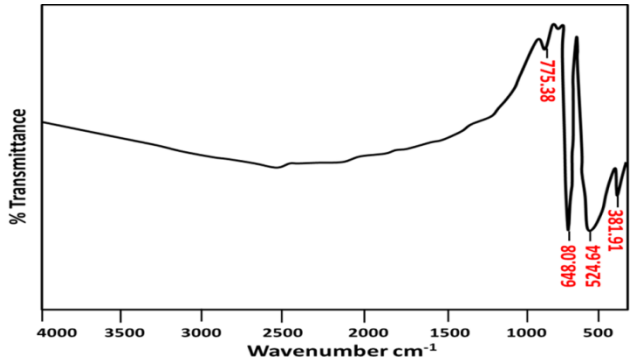

Fig 1: FT-IR spectrum of Co_3O_4 nanoparticles.

XRD patterns of the prepared Co_3O_4 nanoparticles predict that produced sample is amorphous in nature. The XRD of the Co_3O_4 nanoparticles is shown in Fig. 2. XRD pattern shows the cobalt oxide has cubic phase structure. The peak positions 2θ=18.93°, 31.33°, 36.93°, 38.66°, 44.93°, 55.79, 59.39° and 65.33° correlated to the plane of (1, 1, 1), (2, 2, 0), (3, 1, 1), (2, 2, 2), (4, 0, 0), (4, 4, 2), (5, 1, 1) and (4, 4, 0) respectively and relative intensities obtained for the Co_3O_4 nanomaterial match well with the JCPDS card No: 74-2120.

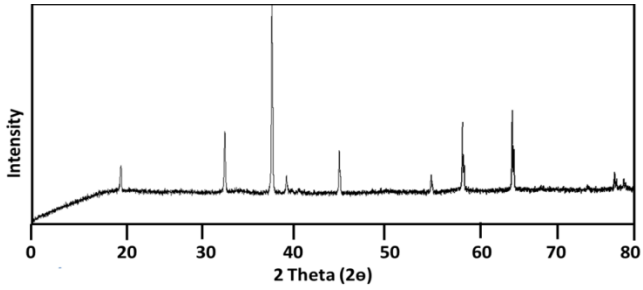

Fig 2: XRD pattern of Co_3O_4 nanoparticles.

SEM image of the Co_3O_4 nanoparticles shows that the particles are agglomerated at the surface due to the magnetic induction between the particles and evenly sized with spherical in morphology (Fig. 3a). (Fig. 3b) shows EDX spectra of cobalt oxide nanoparticles. EDX analysis confirmed that the Co_3O_4 nanoparticles were in pure form as no extra peaks were perceived.

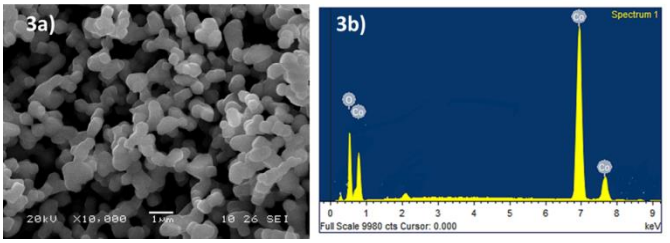

Fig 3: a) SEM image of Co_3O_4 nanoparticles b) EDX of Co_3O_4 nanoparticles.

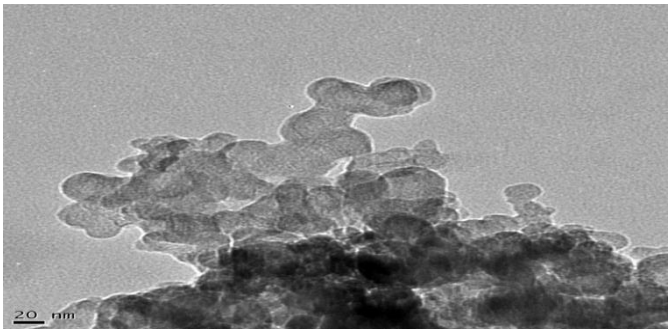

Fig 4: TEM image of Co_3O_4 nanoparticles.

Fig.4 shows TEM image of Co_3O_4 inform size and morphology of synthesized particles.Co_3O_4

nanoparticles have average size 50nm with spherical morphology.

IV. CONCLUSION

Co3O4 nanoparticles were prepared by using sol-gel technique assisted with anionic surfactant Sodium dodecyl sulfonate. The cobalt oxide nanoparticles were characterized by using FT-IR, XRD, SEM, EDX and TEM .The characterization confirms the uniform and pure cubic crystal structure of the Co3O4 nanoparticles with an average size of 50 nm. The present synthesis method of nanoparticles can be functional for large scale industrial fabrication of Co3O4 nanoparticles.

V. REFERENCES

[1]. A. L. Porter, J.Youtie, P.Shapira,D. J. Schoeneck, Refining search terms for nanotechnology, J Nanopart Res. 10 (2008)715–728.

[2]. A.V. Nikam, B.L.V. Prasad, A.A. Kulkarni, Wet chemical synthesis of metal oxide nanoparticles: a review, Cryst. Eng. Comm. 20 (2018) 5091–5107.

[3]. M. S. Chavali, M. P. Nikolova, Metal oxide nanoparticles and their applications in nanotechnology, SN Appl. Sci. 1 (2019) 607-637.

[4]. K. Murugesan, P. Sivakumar, P.N. Palanisamy, An overview on synthesis of metal oxide nanoparticles, South Asian J. Eng. Technol. 2 (2016) 58–66.

[5]. Zygmunt Sadowski, Agnieszka Pawlowska, Synthesis of metal oxide nanoparticles and its biomedical applications, nanotechnology applied to pharmaceutical technology (Springer, Berlin, 2017), pp. 91–111, Doi: https://doi.org/10.1007/978-3-319-70299-5_4.

[6]. A.Arumugan, H.S.A. Hameed, K. Gopinath, S. Gowri, V. Karthika, Synthesis of cerium oxide nanoparticles using Gloriosa superba leaf extract and their structure, optical and antibacterial properties, Mater. Sci. Eng. C 49 (2015) 408–415.

[7]. B.Ramachandra, J. S. Choi, K.S. Kim, K.Y. Choo,J.S Sung,T.H. Kim, MoVW-mixed oxide as a partial oxidation catalyst for methanol to formaldehyde. Studies in Surface Science and Catalysis, 159 (2006) 273–276.

[8]. P.N.R. Kishore, P. Jeevanandam, Synthesis of cobalt oxide nanoparticles via homogeneous precipitation using different synthetic conditions, J. Nanosci. Nanotech. 13 (4) (2013) 2908–2916.

[9]. M. R.Nasrabadi, H. R. Naderi, M. S. Karimi, F. Ahmadi, S. M. Pourmortazavi, Cobalt carbonate and cobalt oxide nanoparticles synthesis, characterization and supercapacitive evaluation, J. Mater. Sci.: Mater. Electron, 28 (2017) 1877–1888.

[10]. L. Zhang, D. Xue, Preparation and magnetic properties of pure CoO nanoparticles, J. Mater. Sci. Lett. 21 (2002) 1931–1933.

[11]. X. Xie, W. Shen, Morphology control of cobalt oxide nanocrystals for promoting their catalytic performance, Nanoscale 1 (2009) 50–60.

[12]. M. B. Durukan, R. Yuksel, H. E. Unalan, Cobalt oxide nanoflakes on single walled carbon nanotube thin films for supercapacitor electrodes, Electrochimica Acta 222 (2016) 1475–1482.

[13]. R. Manigandan, K. Giribabu, R. Suresh, L. Vijayalakshmi, A. Stephen, V. Narayanan, Cobalt oxide nanoparticles: characterization and its electrocatalytic activity towards nitrobenzene, Chem. Sci. Trans. 2 (2013) S47-S50.

[14]. C. Gruttner, J. Teller, New types of silica-fortified magnetic nanoparticles as tools for molecular biology applications, J. Magn. Magn. Mater. 194 (1999) 8-15.

[15]. W.L. Smith, A.D. Hobson, The structure of cobalt oxide, Co3O4, Acta Cryst. B29 (1973) 362-363.

[16]. K.F. Wadekar, K.R. Nemade, S.A. Waghuley, Chemical synthesis of cobalt oxide (Co3O4)

nanoparticles using co-precipitation method, Res. J. Chem. Sci. 7 (2017) 53-55.

[17]. R. Sivakami, S. Dhanuskodi, R. Karvembu, Estimation of lattice strain in nanocrystalline RuO2 by Williamson–Hall and size–strain plot methods, Spectrochim. Acta Part A: Mol. Biomol. Spect. 152 (2016) 43-50.

[18]. A. W. David and I. K. Edmond Preparing Catalytic Materials by the Sol-Gel Method, Ind. Eng. Chem. Res., 1995, 34, 2, 421–433.

International e-Conference on Recent Trends in Nano-Materials and Its Applications-2021
In Association with International Journal of Scientific Research in Science and Technology
Volume 9 | Issue 2 | Print ISSN: 2395-6011 | Online ISSN: 2395-602X (www.ijsrst.com)

Thermal Conductivity Enhancement of Nanofluid Containing Silver Nanoparticles

Vijay S Raykar
Department of Physics, G. M. Vedak College of Science, Tala, Raigad 402111, Maharashtra, India

ABSTRACT

Today due to increased work load on various electromechanical and nuclear systems a huge amount of heat is generated. To extract the heat efficiently a novel material the nanofluid has been synthesized. The synthesis is carried out using chemical route. The Silver nitrate is reduced using Trisodium with water as a base medium. The high heat absorbing property has been demonstrated by conducting an experiment in which hot water sample is cooled by nanofluid and plain water. The hot wire transient method has been used to measure thermal conductivity of nanofluid.

Keywords : Silver Nanofluids, Thermal Conductivity, Coolants, Hot Wire.

I. INTRODUCTION

Nanofluids (NFs) are opening up a new era of integrated fundamental research of heat transfer at nanoscale, covering enormous applications and enabling research activities in long term. There has been extensive interest in thermal transport study of nanofluids in recent years because of its wide use as a coolant material in high heat generating microelectronics and nuclear technologies [1], [2]. This application oriented research based on an idea that using matter at nanometer dimensions it is possible to create new materials with smart flexibility with improved physical properties. Much of the experimental effort has been oriented toward understanding effects of volume fraction [3], [4], [5] shape of nanoparticles (NPs) [6], [7], temperature [8], [9] cluster size [10], [11] aggregation [12], [13], [14] surface tension [15], pH [16] on thermal enhancement of nanofluids. There have been several recent reports in the literature, both by the authors and by other workers, of synthesizing various liquid suspensions containing nano-entities and utilizing them for heat transfer enhancement [17], [18]. The actual increased interest in the nanofluids is in the search of theory which can explain the anomalous increase in thermal conductivity (TC) [19], [20], [21], [21], [21]. Traditional questions connected with the classical nature of heat conduction in nanofluids cannot directly explain the appearance of anomalous increased thermal conductivity [22]. From a historical perspective, Maxwell first proposed the enhancement produced in the thermal conductivity of a fluid by the presence of suspended colloidal particles [6]. Nanofluids can be considered as a fluid containing nanometer sized entities. These fluids typically consist of a base fluid phase containing nanoparticles. The advantage that nanofluid is that they offer useful thermo physical and rheological properties compared to conventional coolants [12]. All of these analysis

helps directly in the search for nanofluids with desired thermal and rheological properties.

The practical problems associated with the handling of these suspensions, such as undesirable effects of sedimentation, abrasion, etc. prevented the exploitation of this promising feature in industrial heat transfer applications. The possibility of using nanometre sized particle dispersions, with suitable dispersant that should favour stability, avoid clogging effects in micro-channels and abrasion, together with enhanced thermal conductivity, appeared suddenly as a feasible solution to circumvent these problems, and attracted an extraordinary research interest, as shown by the large number of references listed in the reviews [17], [22]. Whenever we want to cool certain materials (hot) or systems (heat generating) we use the conventional coolant the water to cool it. The water absorbs the heat from such systems and gives it to sinks (atmosphere). However the heat absorbing property of water can be greatly increased with addition of nanoparticles. The metal silver is having very high thermal conductivity. But we cannot directly insert this material into water for the two reasons: 1. Silver in ordinary form settle down in to water because of its weight. 2. Low surface area available to absorb heat. Particles of silver in nanosize can overcome this problem because of its small size and low weight.

In this study, Trisodium-protected Ag water-based nanofluids have been synthesized by chemical reduction [23]. For preventing particle aggregation and controlling particle size, Trisodium has been used in the weight ratio of 1:5 and 1:10 ($AgNO_3$ to Trisodium). The nanofluids have been characterized by UV-vis spectroscopy (uses spectrophotometer and deals with the measurement of absorbance of energy), energy dispersive X-ray spectroscopy (EDX), and scanning electron microscopy (SEM). The prepared nanofluids are systematically investigated for thermal conductivity for different polymer concentrations.

II. EXPERIMENTAL TECHNIQUES

Synthesis of nanofluids

Heat-assisted chemical reduction of silver nitrate has been done with water as base fluid using Trisodium as stabilizing and reducing agent. In order to prepare Ag nanocolloids of different particle size, different weight ratios of metal salt-to-Trisodium have been selected and experimental parameters are reported in Table 1. The nanofluid with $AgNO_3$ to Trisodium weight ratio of 1:10 is denoted by "H", $AgNO_3$ to Trisodium weight ratio 1:5 by "L" hereafter.

Characterization of nanofluids

UV-vis absorption spectrum has been recorded on Nanodrop 1000 under 1-mm column in the wavelength range of 300–900 nm at room temperature. The particle size has been evaluated with scanning electron microscopy (JEOL ASM 6360A) technique.

Estimation of thermal conductivity

A transient hot wire (THW) method in which the resistance of wire (usually platinum) can be changed with an applied voltage has been used to measure thermal conductivity of nanofluids [24].

Cooling effect

Two samples of water are heated up to 70 ^{0}C. To cool these samples we have used the water in first case and silver nanoparticle solution in second case [Fig. 1]. The temperature readings are noted for every five seconds and the graph is plotted as temperature versus time [Fig.2]. From the Graph it can be seen that the temperature of the water decreases faster in nanoparticle solution case as compared to water. The high surface area of nanoparticles absorbs much heat from the sample and gives it to the walls of beaker which further pass out in to the atmosphere.

III. RESULTS AND DISCUSSION

The dark yellow to dark brown colour in different solutions indicates the presence of silver nanoparticles in the solutions [24]. Strong absorption is observed at 408 nm for samples H as shown in Fig. 3 indicating the particle size dependence and presence of silver particles in water. The slight shift of curve at 406 nm (Fig. 3) shows further reduction in particle size at temperature 323 K. Stabilization of nanofluids has been studied at room temperature and it has been found that the obtained nanofluids are stable for more than 1 month in the stationary state and more than 10 h under centrifugation at 3,000 rpm without sedimentation. Excellent stability of the obtained nanofluid is due to the protective role of Trisodium as it retards the growth and agglomeration of nanoparticles by steric effect [23]. Figure 4 shows the SEM and EDX micrograph recorded from the silver nanoparticles deposited on a glass substrate [25]. EDX analysis also showed five peaks located between 2 kV and 4 kV. Those maxima are directly related to the silver characteristic lines K and L. The carbon and oxygen spots in the examined samples confirm the presence of stabilizers composed of alkyl chains. Observation of Fig. 4 shows that Ag nanoparticles are spherical in shape and embedded in Trisodium polymer. Average particle size is about 60 nm for sample H (Fig. 4).

Measured and reported thermal conductivity of water with temperature are presented in Fig. 5. There is a close agreement between the observed and reported values of water as can be seen from the figure. It is observed that the thermal conductivity of water slightly increases with temperature as reported [26]. Measurement system has been calibrated, before use, by measuring the thermal conductivity of deionized water, benzene, and glycerol and measured thermal conductivities are 0.56, 0.16, and 0.289, respectively, at room temperature, exhibiting standard deviation from the literature values by 0.035, 0.071, and 0.050, respectively. Measurements have been recorded ten times for each sample and results have been averaged. These results demonstrate that the experimental setup used in the present study can provide reliable thermal conductivity measurement.

Figure 6 presents the thermal conductivity ratio for Ag nanofluid (thermal conductivity normalized by that of base fluid) with temperature. At temperature 323 K, thermal conductivity enhancement greater than 1.55 has been observed for sample H. With increase in temperature, nanoparticles diffuse through the polymer matrix. Thermal vibrations cause polymer to lose its structure allowing greater surface area of nanoparticles to take part in heat transfer. This also adds to increase in Brownian motion of nanoparticles causing convection to increase significantly with temperature causing thermal conductivity enhancement [27].

Figure 6 also shows estimated thermal conductivity values of silver nanofluids using Maxwell model [28]. It clearly indicates that the experimental results are significantly higher than that predicted by Maxwell model and enhancement in thermal conductivity of nanofluid cannot be explained by classical models, as this model is developed for millimeter- or micrometer-sized particle colloids without taking into account the possible influences of particle size, Brownian motion, interfacial layer at the particle–liquid interface and clustering of nanoparticles, and polymer ligand binding which are considered important mechanisms for enhancing the thermal conductivity of nanofluid. Similar differences between the experimental and classical model estimation has been reported earlier by many researchers [29].

IV. ACKNOWLEDGEMENTS

I thank Principal, G.M. Vedak College of Science, Tala, India, for granting permission to publish this work.

FIGURE CAPTIONS:

Table.1 Parameters for synthesis of silver nanofluids

$AgNO_3$ to Trisodium weight ratio	Description	Heating time and temperature
1:10	0.2 g of $AgNO_3$ with 2 g of Trisodium in 100 ml of water	15 min at 341 K
1:5	0.2 g of $AgNO_3$ with 1 g of Trisodium in 100 ml of water	15 min at 341 K

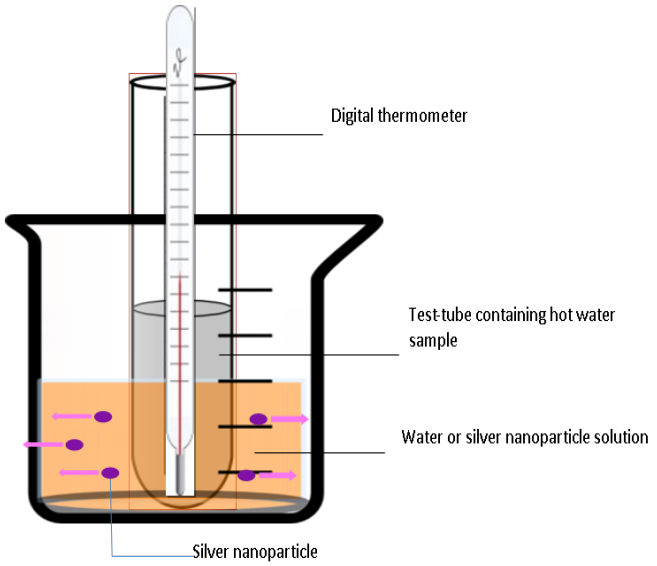

Fig.1. Experimental setup to observe the cooling effect

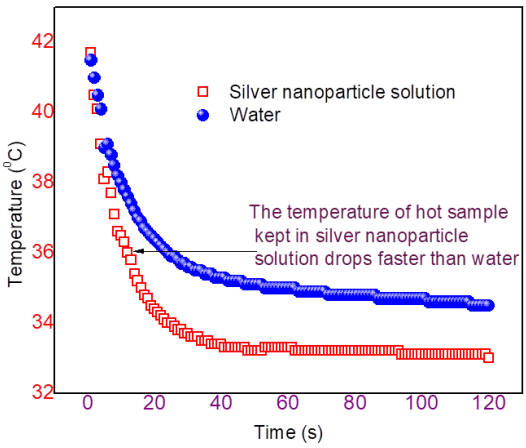

Fig.2. Temperature vs time curve for cooling of hot water sample

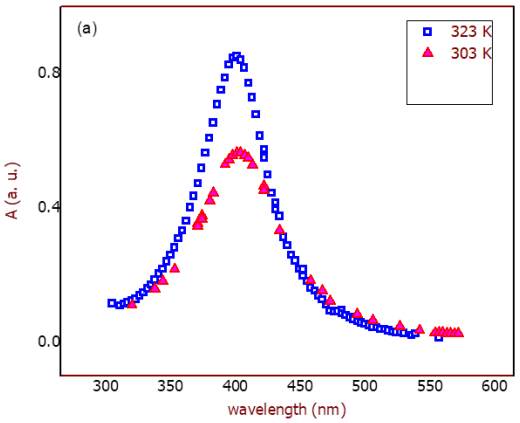

Fig.3. UV-vis absorption spectra for Ag NFs

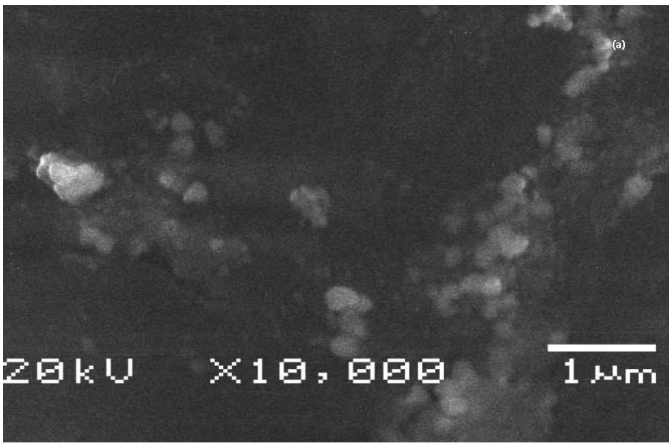

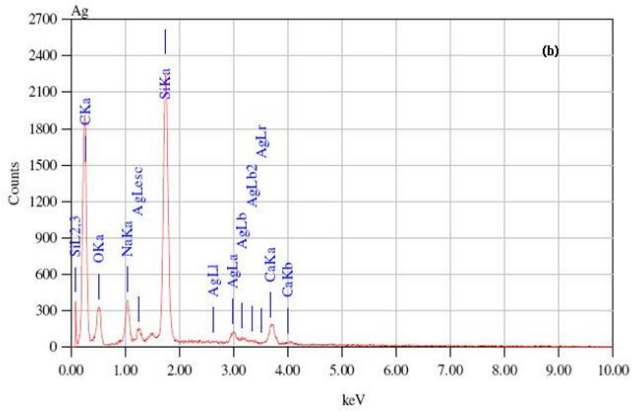

Fig.4. SEM image and EDX of silver nanoparticles

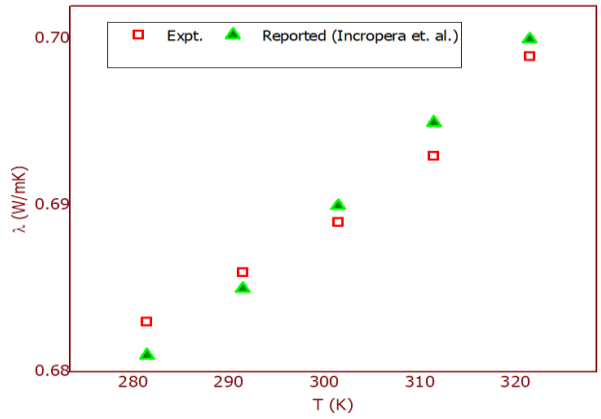

Fig.5. The temperature dependent thermal conductivity of water

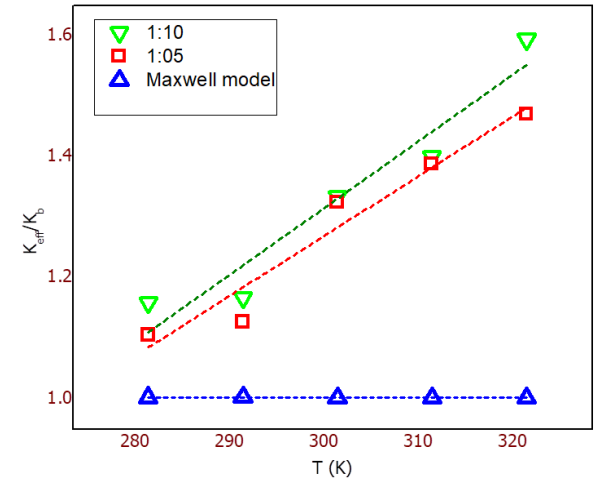

Fig.6. The temperature dependent thermal conductivity enhancement in Ag NFs

V. REFERENCES

[1]. Eastman, J., Choi, S., Li, S., Yu, W., and Thompson, L., 'Anomalously increased effective thermal conductivities of ethylene glycol-based nanofluids containing copper nanoparticles,' Applied Physics Letters, Vol. 78, No. 6, 2001, pp. 718–720.

[2]. Das, S., 'Nanofluids - The cooling medium of the future,' Heat Transfer Engineering, Vol. 27,No. 10, 2006, pp. 1–2.

[3]. Hosseini, M. and Ghader, S., 'A model for temperature and particle volume fraction effect on nanofluid viscosity,' Journal of Molecular Liquids, Vol. 153, No. 2-3, 2010, pp. 139–145.

[4]. Li, C.H., P. G., 'Experimental investigation of temperature and volume fraction variations on the effective thermal conductivity of nanoparticle suspensions (nanofluids),' Journal of Applied Physics, Vol. 99, No. 8, 2006.

[5]. Jang, S., Lee, J. H., Hwang, K., and Choi, S., 'Particle concentration and tube size dependence of viscosities of Al2O3 water nanofluids flowing through micro- and minitubes,' Applied Physics Letters, Vol. 91, No. 24, 2007.

[6]. Zhang, X., Gu, H., and Fujii, M., 'Effective thermal conductivity and thermal diffusivity of nanofluids containing spherical and cylindrical nanoparticles,' Journal of Applied Physics,Vol. 100, No. 4, 2006.

[7]. Timofeeva, E., Routbort, J., and Singh, D., 'Particle shape effects on thermophysical properties of alumina nanofluids,' Journal of Applied Physics, Vol. 106, No. 1, 2009.

[8]. Chon, C., Kihm, K., Lee, S., and Choi, S., 'Empirical correlation finding the role of temperature and particle size for nanofluid (Al2O3) thermal conductivity enhancement,' Applied Physics Letters, Vol. 87, No. 15, 2005, pp. 1–3.

[9]. Yang, B., H. Z., 'Temperature-dependent thermal conductivity of nanorod-based nanofluids,' Applied Physics Letters, Vol. 89, No. 8, 2006.

[10]. Hong, K., Hong, T. K., and Yang, H. S., 'Thermal conductivity of Fe nanofluids depending on the cluster size of nanoparticles,' Applied Physics Letters, Vol. 88, No. 3, 2006, pp. 1–3.

[11]. Zhu, H., Zhang, C., Liu, S., Tang, Y., and Yin, Y., 'Effects of nanoparticle clustering and alignment on thermal conductivities of Fe3O4 aqueous nanofluids,' Applied Physics Letters, Vol. 89,No. 2, 2006.

[12]. Prasher, R., Phelan, P., and Bhattacharya, P., 'Effect of colloidal chemistry on the thermal conductivity of nanofluids,' 2006.

[13]. Gharagozloo, P., Eaton, J., and Goodson, K., 'Diffusion, aggregation, and the thermal conductivity of nanofluids,' Applied Physics Letters, Vol. 93, No. 10, 2008.

[14]. Krishnamurthy, S., Bhattacharya, P., Phelan, P., and Prasher, R., 'Enhanced mass transport in nanofluids,' Nano Letters, Vol. 6, No. 3, 2006, pp. 419–423.

[15]. Kumar, R., M. D., 'Effect of surface tension on nanotube nanofluids,' Applied Physics Letters,Vol. 94, No. 7, 2009.

[16]. Wang, X. J., Li, X., and Yang, S., 'Influence of pH and SDBS on the stability and thermal conductivity of nanofluids,' Energy and Fuels, Vol. 23, No. 5, 2009, pp. 2684–2689..

[17]. Das, S., Choi, S., and Patel, H., 'Heat transfer in nanofluids - A review,' Heat Transfer Engineering, Vol. 27, No. 10, 2006, pp. 3–19.

[18]. Chopkar, M., Das, P., and Manna, I., 'Synthesis and characterization of nanofluid for advanced heat transfer applications,' Scripta Materialia, Vol. 55, No. 6, 2006, pp. 549–552.

[19]. Bhattacharya, P., Saha, S., Yadav, A., Phelan, P., and Prasher, R., 'Brownian dynamics simulation to determine the effective thermal conductivity of nanofluids,' Journal of Applied Physics, Vol. 95, No. 11 I, 2004, pp. 6492–6494.

[20]. Jang, S. and Choi, S., 'Role of Brownian motion in the enhanced thermal conductivity of nanofluids,' Applied Physics Letters, Vol. 84, No. 21, 2004, pp. 4316–4318.

[21]. Evans, W., Fish, J., and Keblinski, P., 'Role of Brownian motion hydrodynamics on nanofluid thermal conductivity,' Applied Physics Letters, Vol. 88, No. 9, 2006.

[22]. Eapen, J., Rusconi, R., Piazza, R., and Yip, S., J. Heat. Transf., Vol. 132, 2010, pp. 102402.

[23]. R.P. Chauhan, Ratyakshi, 'Colloidal Synthesis of Silver Nano Particles,' Asian Journal of Chemistry, Vol. 21, No. 10 (2009), S113-116.

[24]. Singh, A. and Raykar, V., 'Microwave synthesis of silver nanofluids with polyvinylpyrrolidone (PVP) and their transport properties,' Colloid and Polymer Science, Vol. 286, No. 14-15, 2008, pp. 1667–1673.

[25]. Yan, Y., Kang, S. Z., and Mu, J., 'Preparation of high quality Ag film from Ag nanoparticles,'Applied Surface Science, Vol. 253, No. 10, 2007, pp. 4677–4679.

[26]. Incropera F. P. and DeWitt D. P. 'Introduction to heat transfer,' John Wiley and Sons, Inc., New York, USA 1996

[27]. Azizian, M., Aybar, H., and Okutucu, T., 'Effect of nanoconvection due to Brownian motion on thermal conductivity of nanofluids,' 2009, pp. 53–56.

[28]. Maxwell J.C., 'A treatise on electricity and magnetism', Oxford Clarendon, UK, 1891.

[29]. Wang, X. Q. and Mujumdar, A., 'Heat transfer characteristics of nanofluids: a review,' International Journal of Thermal Sciences, Vol. 46, No. 1, 2007, pp. 1–19.

International e-Conference on Recent Trends in Nano-Materials and Its Applications-2021
In Association with International Journal of Scientific Research in Science and Technology
Volume 9 | Issue 2 | Print ISSN: 2395-6011 | Online ISSN: 2395-602X (www.ijsrst.com)

Nanoporous Mn doped Ruthenium Oxide Thin Film Electrodes for Supercapacitor applications

P. S. Joshi[1], D. S. Sutrave[2]

[1]Walchand Institute of Technology, Solapur-413006,Maharashtra, India.

[2]D.B.F. Dayanand College of Arts and Science, Solapur-413002, Maharashtra, India

ABSTRACT

Sol-gel spin coating method was adopted for preparation of Manganese doped Ruthenium Oxide thin films. In aqueous solution of M $RuCl_3$ solution, the doping percentage of Mn has been increased as 0.1, 0.2, 0.5,1 and 2at percentage. Orthorhombic structure of Crystalline RuO2 has been revealed from XRD. Formation of Nano-porous material on the steel substrate was observed from SEM. EDAX revealed successful doping of Mn in RuO_2. Changes in structural and morphological features with increasing doping of Manganese admired for supercapacitor applications. Maximum specific capacitance of 475 F/g at 10mV/s was observed for a 2% Mn doping in 0.1 M KOH electrolyte which proved its applicability in supercapacitor.

Keywords : *Mn doped RuO_2 thin films, Sol-gel spin coating, Nano-porous , Cyclic voltammetry*

I. INTRODUCTION

Ruthenium oxide (RuO_2) thin films have exposed great promise in variousapplications [1-3]. It is well known that the capacitance of RuO_2 electrode results from redox pseudocapacitance. However, the currentresponse resembles an ideal capacitor, which is a‘‘rectangular’’ shape under cyclic voltammetry. It has been widely used in supercapacitor because of its good catalytic properties [4]. Even though RuO_2 has a great advantage interms of a wide potential range of highly reversible redox reactions with high specific capacitance, it is expensive. Therefore, it is desirable to develop a processfor the preparation of thin film RuO_2 electrodes to reducetheir cost as capacitor electrodes [5].Another metal oxide Manganese oxide is of considerable importance in technological applications due to its natural abundance coupled with environmental compatibility and also intensively investigated as promising electrode material in electrochemical capacitors [6-8] .

Here attempts are made for the synthesis of Mn doped RuO_2 thin films so as to minimize the quantity of Ruthenium material and to achieve the required results. For this, sol-gel spin coating deposition technique was used which allows the uniform deposition of the gel on the substrate. Also the structural, morphological properties were studied with increasing doping concentration of Mn in RuO_2.

II. EXPERIMENTAL

The crystalline RuO_2 thin films were grown on stainless steel substrate by sol gel spin coating method by $RuCl_3{:}xH_2O$ and $Mn(II)Cl_2$ precursors. Before starting the deposition, the substrates were cleaned

with detergent, washed with double distilled water, then rinsed with acetone and dried. Six different solutions were prepared with increasing doping percentage of Mn as 0 %, 0.1 %, 0.2 %,0.5%, 1% and 2%. For the preparation of gel, isopropyl alcohol was added to the solution and stirred for 5 to 6 hours. Then the solution was settled for 24 hours for formation of gel. For uniform deposition, the substrates were spinned in aspin coater unit at 3000 rpm and annealed at 900°C. The process was repeated upto 4 deposition layers. The films were structurally characterized by X-ray diffractionin the range of scanning angle 20°–80° using diffractometer D2 PHASER using CuKα radiation (λ= 1.54 A°).The surface morphology of the film was studied by scanningelectron microscopy (SEM) (Model: JEOL JSM-6360).Electrochemical characterization of electrodes was performed in 0.1 M KOH electrolyte solution in a three – electrode cell employing Pt auxiliary electrode and a SCE reference electrode. Potential values are reported against SCE.

III. RESULTS AND DISCUSSIONS

3.1 Physical Properties

As deposited films were grey in color, uniform and well adherent to the substrate. The thickness of the films was measured in terms of their weights before and after the deposition by an electronic balance model Contech Analytical balance with 0.1mg sensitivity. The substrates were of 3 cm^2 area.

3.2 Structural Properties

The X-ray diffraction pattern of as deposited RuO_2 and Mn doped RuO_2 thin films thin films is shown in Fig. 1. The experimental data showed the crystalline nature of RuO_2 with orthorhombic structure (JCPDS Card No.-88-0323) having lattice constants of a=4.59 A, b=4.43 A°, c= 4.07A° with d=2.52, 2.21 and 1.70° corresponding to Miller Indices [011] , [020] and [211]respectively which are in good agreement with JCPDS card. Similarly orthorhombic structure of MnO_2 film (JCPDS Card No.-82-2169) with lattice constants a=9.31A°, b=4.67A°, c=2.78A° with d=2.06, 1.61, 1.30A°coresponding to Miller indices [410],[401]and [131] respectively.

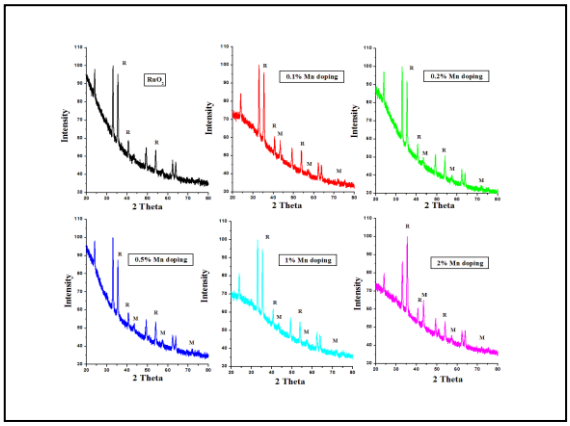

Fig. 1. X-ray Diffractogram of RuO2 and Mn doped RuO2 thin films with increasing doping concentrations.

The peaks which are not labelled correspond to stainless steel. It was observed from XRD that there is a shift in 2 theta to lower values for every observed dominant peak of RuO_2 and the intensity of corresponding peaks has also been decreased with increasing doping concentration of Mn. The change in intensity in RuO_2 as well as MnO_2 peaks with increase in doping concentration of Mn for respective 2 theta values is shown in Figure 2

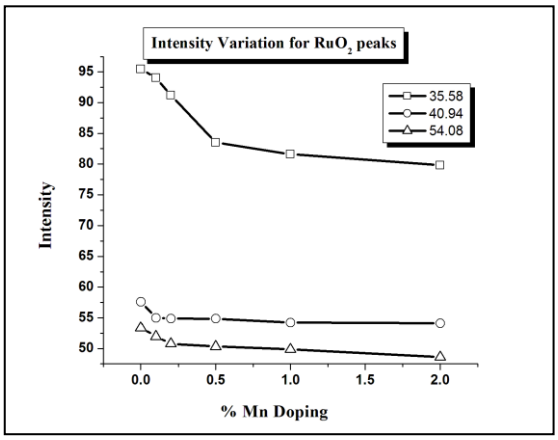

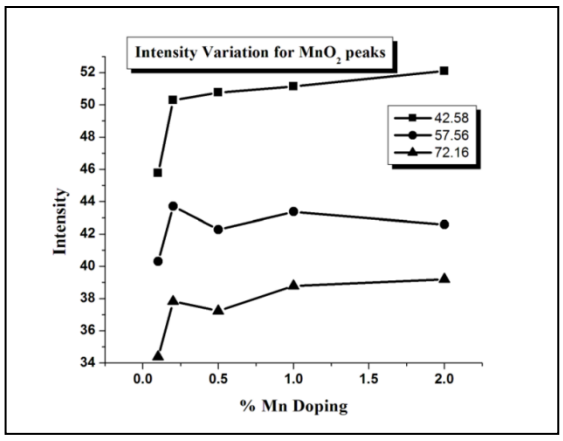

Fig 2. Intensity variation for RuO_2 and MnO_2 peaks at different 2 theta with increasing % doping of Mn.

Usually on doping, the peak intensity decreases which might be due the change in electron density or might be due to point defects.Adsorption on surface is related to intensity change and inter-layer change is indicated by change in theta value. **S**hift of Bragg peaks to lower values of the diffraction angle, increases lattice parameter. Similar results are observed for both RuO_2 and MnO_2 for every concentration.The variations in lattice constants are given in table 1.

	RuO_2			MnO_2		
	a	b	c	a	b	c
Pure thin films	4.48	4.43	3.07	9.31	4.38	2.78
Mn doped RuO_2 thin films	4.58	4.43	3.07	9.49	4.69	3.10

Table 1. Increase in lattice parameters in $RuO_2$and MnO_2 due to increase in doping percentage of Mn(2%)

3.3 Morphological Properties

The two-dimensional surface morphological study of thin films has been carried out from SEM image for 0.12 mg/cm^2 film thickness.Figure 3 shows the surface morphological images of Mn doped RuO_2 thin films with increasing doping concentration of Mn for higher magnification . The morphology showed that the substrate is well covered with RuO_2 material. The particles are well connected to each other and yet provide porosity. Macropores are distributed non-uniformly over the substrate. Diameter of pores increased with doping concentration of Mn.

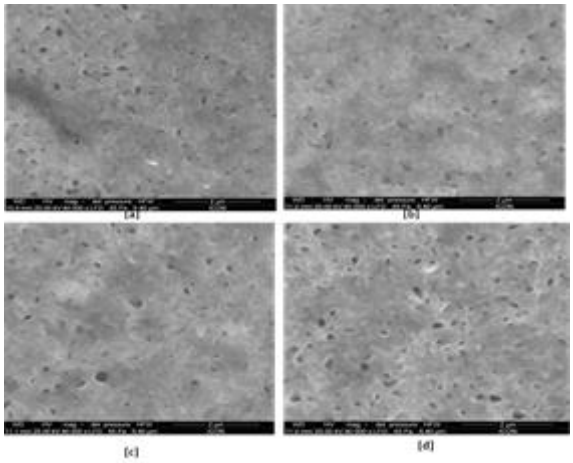

Figure 3. SEM images of Mn doped RuO2 thin film [a]0.1 % [b] 0.2 % [c]0.5% [d] 1%Mn concentration.

Fig. 4 shows the SEM image of 2 % Mn doped RuO_2 thin film on the steel substrate at 5,000 X magnification and 40,000X magnification. It showed mud-cracked morphology giving rise to high surface roughness at lower magnification. The large cracks are attributed to the presence of inner stress in forming a crystalline RuO_2 film during the high temperature preparation step. Such porous structure of electrode is desirable for efficient supercapacitor applications [9].

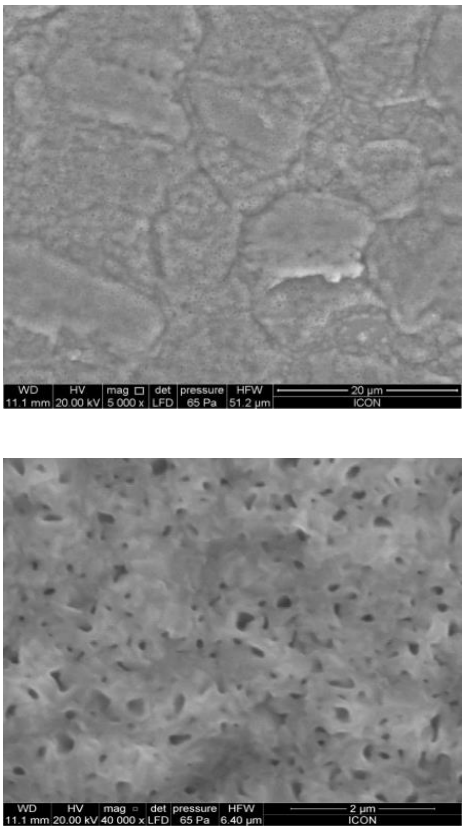

Figure 4. SEM images of 2% Mn doped RuO_2 thin film

3.4 EDAX

EDAX is a characterisation technique that provides elemental composition of various constituent elements in a material. In EDX spectrum of Mn doped RuO2films as in figure 5 it shows the incorporation of Mn in RuO_2.There was increment in the weight percentage of Mn with increase in doping percentage.

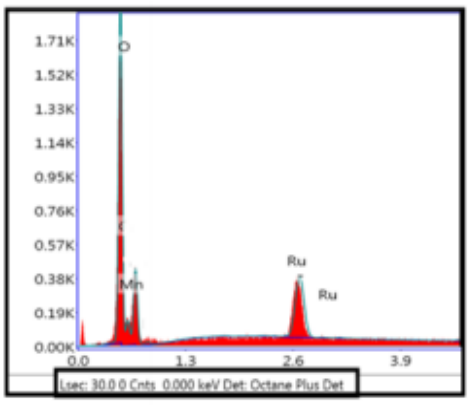

Figure 5. EDX Spectrum of Mn: RuO_2 thin film

3.5 Electrochemical Properties

Cyclic Voltammetry was used to determine the electrochemical properties of the spin coated Mn doped RuO_2 thin films. The electrode potential was scanned between 0 to 0.8 V in both anodic and cathodic directions and current response was measured indicating the typical pseudocapacitive behaviour. Figure 6. Shows the CV plot of 2% Mn doped RuO_2 thin film. An ideal capacitive nature of electrode includes a rectangular type of voltammogram, symmetric in anodic and cathodic directions and a large magnitude of the current. It was found that the current under the curve slowly increased with scan rate. This indicates that the voltammetric currents are directly proportional to the scan rates, indicating an ideal capacitive behaviour [10].

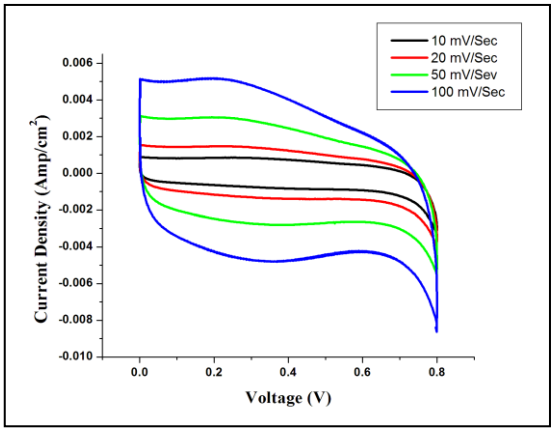

Figure 6. Cyclic voltammogram of 2 % Mn doped RuO2 Thin Film Electrode.

The specific capacitance of the electrode was obtained dividing the capacitance by the weight dipped in the electrolyte. Specific capacitance increased with increasing the doping percentage of Mn and decreased with scan rate. The reason for decrease in capacitance with scan rate is given elsewhere [11].The doping concentration and specific capacitance values are detailed in table 2.

Table2. Specific capacitance values for increasing doping concentration of Mn for different scan rates.

	Mn doping Concentration				
scan rate (mV/Sec)	0.1% (F/g)	0.2% (F/g)	0.5% (F/g)	1% (F/g)	2% (F/g)
10	256	265	295	364	475
20	219	219	260	335	398
50	191	183	213	299	313
100	169	159	182	273	257

It showed maximum specific capacitance of 475 F/g. It is noteworthy that the maximum specific capacitance value obtained in this study is comparable to that obtained for ruthenium oxide thin films by other methods [12-14] . This suggests that doping of Mn is beneficial so as to achieve the betterspecific capacitance values with a cost-effective sol-gel method.

IV. CONCLUSION

The crystalline, nano-porous Manganese doped ruthenium oxide(RuO_2) thin films have been successfully synthesized using sol-gel spin coating method on stainless steel substrate. The doping percentage of Mn was increased. The films showed high porosity with increase in percentage doping of Mn. The thin film electrode of 2 % doped Mn showed maximum specific capacitance of 475 F/g . Capacitance increased with doping percentage of Mn and decreased with scan rate. It may be assumed that pore structure for 2 % Mn doped thin films is suitable for supercapacitor applications.

V. REFERENCES

[1]. M. Deepa, A.K. Srivastava, K.N. Sood, S.A. Agnihotry, Nanotechnology,17 (2006) 2625

[2]. V.R. Shinde, T.P. Gujar, C.D. Lokhande, Sens. Actuators B 120 (2007) 551.

[3]. S. Karuppuchamy, K. Nonomura, T. Yoshida, T. Sugiura, H. Minoura,Solid State Ionics 151 (2002) 19

[4]. D.S Sutrave, P.S Joshi, S.D Gothe, S.M Jogade,International Journal of Chemtech Research, 6- 3,(2014),1991.

[5]. B.O Park ,C.DLokhande, H.S Park , K..D Jung, O.S Joo ,J Power Sources 134,(2004), 148

[6]. S. C. Pang and M. A. Anderson, Journal of Materials Research, 15-10,(2000),2096.

[7]. S. F. Chin, S. C. Pang, and M. A. Anderson, Journal of the Electrochemical Society, 149-4 (2002),A379

[8]. S. F. Chin and S. C. Pang, Materials Chemistryand Physics, vol. 124-1(2010),29.

[9]. B.O. Park, C.D. Lokhande, H.S. Park, K.D. Jung, O.S. Joo, J. Power Sources 134 (2004) 148

[10]. C.C. Hu, T.W. Tsou, Electrochem.Commu.4 (2002)105.

[11]. P.S Joshi, D.S Sutrave, International Advanced Research Journal in Science Engineering and Technology, DOI 10.17148.

[12]. U.M Patil, S.B Kulkarni, V.S Jamadade, C.D Lokhande, J Alloys Comp 509,(2011)1677

[13]. C.C Hu ,Y.H Huang , J Electrochem Soc 146, (1999) 2465

[14]. V.DPatake,C.DLokhande (2007) Appl Surf Sci 254:2820

International e-Conference on Recent Trends in Nano-Materials and Its Applications-2021
In Association with International Journal of Scientific Research in Science and Technology
Volume 9 | Issue 2 | Print ISSN: 2395-6011 | Online ISSN: 2395-602X (www.ijsrst.com)

Sol-gel spin coated Nickel oxide (NiO) thin film Electrode for Electrochemical Pseudocapacitor Applications

Sagar S. Gaikwad[1], Sangam S. Gaikwad[2], Dattatray S. Sutrave[3], Bhanudas R, Karche[4]
[1, 2, 3] D.B.F Dayanand College of Arts and Science, Solapur, Maharashtra
[4] S. M. MohiteMahavidyalay, Akluj, Maharashtra, India

ABSTRACT

The nickel oxide (NiO) thin films were prepared from nickel chloride precursor by sol–gel dip coating method. The films were characterized in support of their structural, compositional, morphological, and optical and electrochromical measurement using X-ray photoelectron spectroscopy, Field effect scanning electron microscopy, and cyclic voltammetry. XPS measurements discovered that the films exhibited existence of NiO phase. FESEM images showed porous micro granules nature of NiO thin film. The pseudocapacitive properties are tested using cyclic voltammetry, charge–discharge and electrochemical impedance Spectroscopy. The maximum value of specific capacitance obtained is 152Fg^{-1}.

Keywords : Nickel Oxide, X-Ray Photoelectron Spectroscopy, Field Effect Scanning Electron Microscopy, Cyclic Voltammetry

I. INTRODUCTION

Corresponding to the double-layer capacitor of electrochemical capacitor technology is that based on redox pseudo-capacitance concerning oxidation state changes in metal oxides[1], such as amorphous phase of hydrated ruthenium oxide (RuO) [2], MnO2[3], NiO [4], Co_3O_4 [5], are regularly reported with their relatively different microstructures. Conducting polymers such as polypyrrole [6], polyaniline [7], and polythiophene [8] are reported as the electrode materials in pseudocapacitor. The RuO2 is outstanding electrode material, exhibits exceptional electrochemical properties such as high conductivity, a variety of oxidation states and superior electrochemical stability. Since the toxicity and price of RuO2 hold back its potential application in pseudocapacitors. The metal oxides like MnO_2, MoO, CuO, NiO and Co_3O_4 have good electrochemical properties with low cost and abundance in nature. Amongst these metal oxides; NiO is reported with greater values of electrochemical parameters. In fact, the values of specific capacitance of NiO are mainly recognized to the morphology and Corresponding surface area of the material. The fine nanoparticles of NiO have been reported by Yeager et al. [10] as a pseudocapacitive electrode with the value of specific capacitance 243 Fg^{-1}. The single- crystalline NiO nanoplatelet arrays as supercapacitor electrodes have reported by Li et al. [11]. The loose-packed nanoflakes of NiO for supercapacitors have been reported by Lang et al. [13].Nickel oxide has been

expansively prepared by thermal treatment of electrodeposited [12] and sol–gel derived [13] NiO thin films for pseudo-capacitor applications. There are number applications of NiO thin films collectively with LCD, LED, and memory devices and in energy conversion systems like solar cells, Li-ion batteries and supercapacitors [14, 15]. There are various methods to synthesize NiO thin films, in general physical vapor deposition(PVD), electron beam evaporation, electrodeposition, spray pyrolysis, chemical bath deposition, Successive ionic layer adsorption and reaction (SILAR), and Sol-Gel dip coating are used [16].Sol-Gel method is preferred because of its advantages such as low cost, possibility for large area deposition[17]. It offers a low-temperature method for deposition of materials on large area that both inorganic and organic in nature. Sol–gel deposition of NiO.

In the present work, NiO thin films were synthesized using sol–gel dip coating method from nickel chloride precursor and structural morphological properties and electro chemical properties were studied and are reported in this paper.

II. Experimental details

2.1 Synthesis of NiO thin film electrode

The Nickel Oxide (NiO) thin films were synthesized by sol gel method using Nickel Chloride ($NiCl_2.6H_2O$) as a precursor of Nickel oxide and isopropyl alcohol as a starting material and reagent respectively.

A 0.1 M precursor solution was prepared by mixing nickel chloride and 50ml double distilled water and it was stirred well using magnetic stirrer until it became transparent solution, then isopropyl alcohol was added slowly [18]. The prepared solution was stirred again for 6 hours at temperature 50^0 C and then aged for 24 hours to the gel in the viscous form and the gel is deposited on SS substrate by spin coating unit. Before deposition the steel substrate was mirror polished by zero grade polish paper and then kept in ultrasonic bath for 10 mins. The deposited sample was the rotated at 2000rpm for 2min and the film were annealed at 500^0C for 30mins.

2.2 Material characterizations

The XRD pattern was carried out using X-ray diffractometer A D2 PHASER diffractometer with source CuKα1 with λ =1.54184, the 2θ angle is varied from 30^0 to 80^0. The surface morphology has been carried out from FESEM image using FESEM: FEI NoavaSEM 450 Instrument. The XPS measurements were carried out by a Thermo K alpha+ spectrometer using micro focused and monochromated Al Kα radiation with energy 1486.6 eV. The electrochemical supercapacitive performance of the NiO electrode was studied with the help of cyclic voltammetry (C-V) plots.

III. Result and Discussion

Fig-1 shows the XRD patterns of NiO thin film. The deposited films were uniform and well adherent to the substrate. The main peaks present at (2θ) 37.25 (111), 43.23 (200), 62.83 (220), reflections which are matched with the standard diffraction pattern of NiO cubic structure (JCPDS 47–1049) [19].

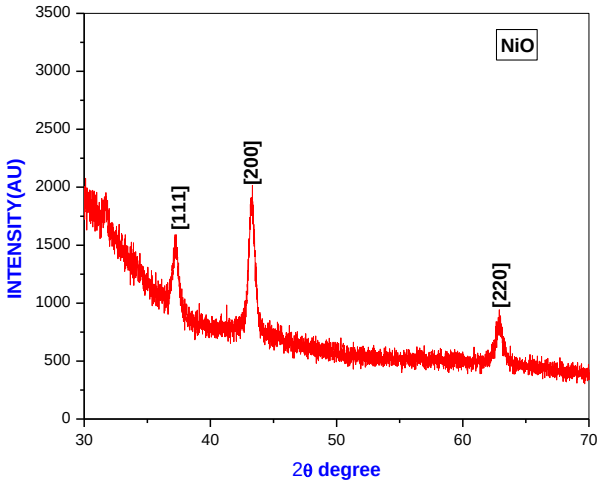

Figure 1 XRD pattern of NiO Thin Film electrode.

IV. Surface morphological studies

Surface morphology of NiO thin films deposited on stainless steel substrate (SS) substrates by sol-gel spin coating method. The resultant morphology observed under microscopy is shown in Fig 2. It is observed that the SS substrate is well covered with NiO material with smooth and porous micro granules which are advantageous for electrolyte penetration into the film structure which increase the electro chromic performance. In supercapacitors, increased amount of charge can be stored on the highly extended surface area created by large number of pores. Nanocrystalline and porous materials as electrode material exhibit good electrochemical performance because these materials possess both a high surface area and pores [20,21]. EDS demonstrates that Ni, O elements were contained, indicating the formation of NiO, which is reliable with the XPS data. The average weight percentages of O (83.36%) and Ni (16.64%) elements.

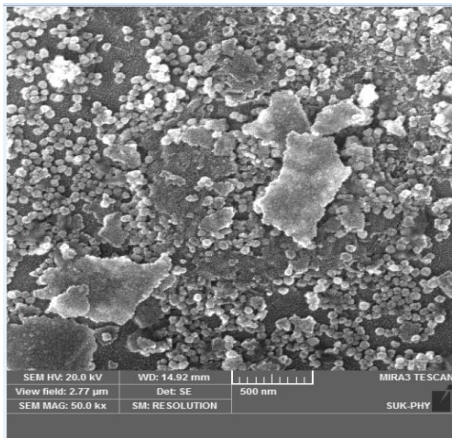

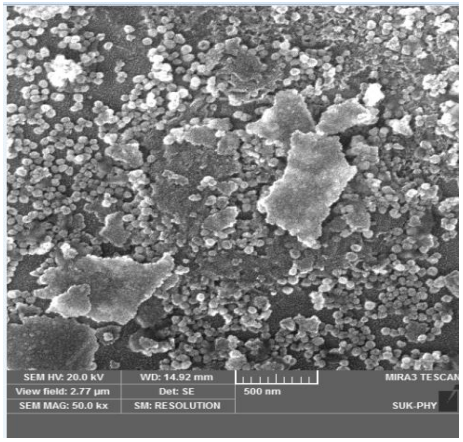

(a)

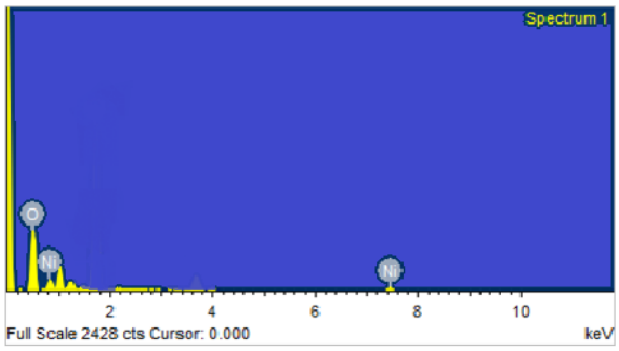

(b)

Fig 2: (a) FESEM image, (b) EDS of NiO Film

V. X-ray photoelectron spectroscopy

X-ray photoelectron spectroscopy (XPS) technique is used to investigate the chemical state of elements present in NiO nanoplatelets as shown in Fig. 3a The Ni 2p spectral peaks in XPS were deconvoluted by way of Gaussian curves.

The Ni2p signal could be deconvoluted into four peaks in the range of 850 to889 eV. Figure 4b shows, the peaks centered at 857.34 and 862.94 eV are featured to Ni2p3/2, and the peaks located at 874.89 and 882.75 eV are featured to Ni2p1/2. This shows highly determined Ni 2p core level spectrum of NiO. The peak of Ni (2p3/2) at a binding energy of 862.94 eV with their associate shake-up satellite peaks at 882.75 eV showed the presence of Ni^{2+} cations. This observation confirmed the NiO pores compiled of pure NiO phase [18]. The Ni (2p3/2) and Ni (2p1/2) peaks are separated by 17.55 eV, which furthermore confirms the formation of only NiO relatively than any additional phase of nickel oxide [22].

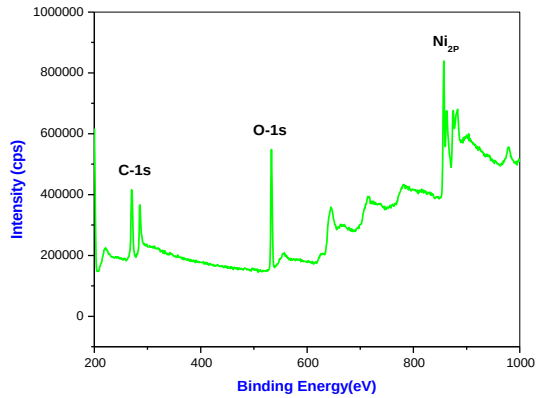

(a)

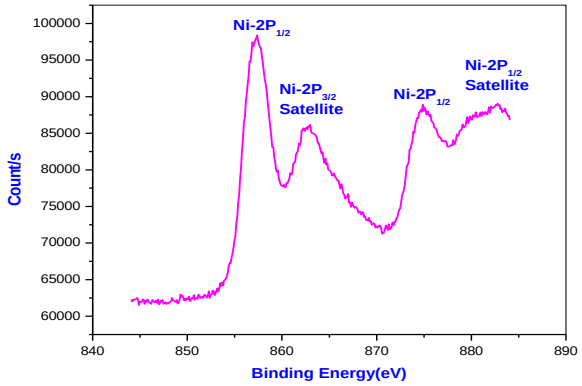

(b)

Fig. 3 (a) Survey XPS spectrum of NiO nanoplatelets grown on SS substrate,(b) Ni 2p core- level spectrum.

VI. Surface wetabillity

Surface wettabilities were evaluated by water contact angle measurements, Surface wettability test which involves the interaction between a liquid and a solid in contact, (sagar bhise). Wettability measurement was carried out for investigating electrolyte/nickel oxide electrode interaction. In general, if the wettability is high, contact angle (θ) will be small and Fig shows the digital photograph of water contact measurement on NiO electrode surface is considered as hydrophilic. As water contact angle is75 ° (less than 90° means more wettability), the Nickel oxide films are hydrophilic in nature. This was because of the strong cohesive force between the oxide present in the nickel oxide compound and water droplet. Generally, low contact angle increases the electrochemical performance [23].

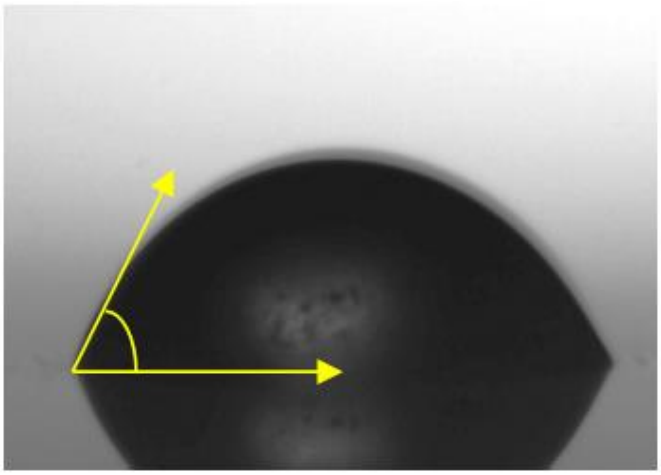

Fig.4 Contact angle image of NiO film electrode

VII. Electrochemical measurements

The elctrochemical performance of sol-gel deposited NiO thin film electrode was tested using cyclic voltameterry measurement. The capacitance (C) was calculated using following relation

$$C = I / (dV/dt) \quad \text{.....(1)}$$

Where I is the average current in ampere and dV/dt is the voltage scanning rate.

The SC of NiO electrode was calculated using following relation;

$$SC = C/ W \quad \text{.....(2)}$$

Where W is the mass of NiO film dipped in electrolyte.

VIII. Effect of scan rate

The CV curves of NiO electrode in 0.1M KOH electrolyte at different scan rates within voltage range of -0.8 to 0.8 are shown in Fig 5. The measurements were performed with NiO thin films as working

electrode and platinum wire as counter electrode and Saturates Calomel Electrode (SCE) as a reference electrode in 0.1M KOH electrolyte. From the cyclic voltametery (CV) curves, the area under curve increased gradually with the scan rate. This indicates that the current is directly proportional to the scan rate, representing an ideal capacitive behavior [24]. The maximum specific capacitance of 152 Fg^{-1} obtained at minimum scan rate of $10mVs^{-1}$.

Obtained results are better than the value previously reported by Wu et al (138 F g^{-1} in 0.5M KOH by electrochemical deposition) [25], Zheng et al (131.6 F g^{-1} in 2M KOH by Hydrothermal method and followed by thermal decomposition) [26].

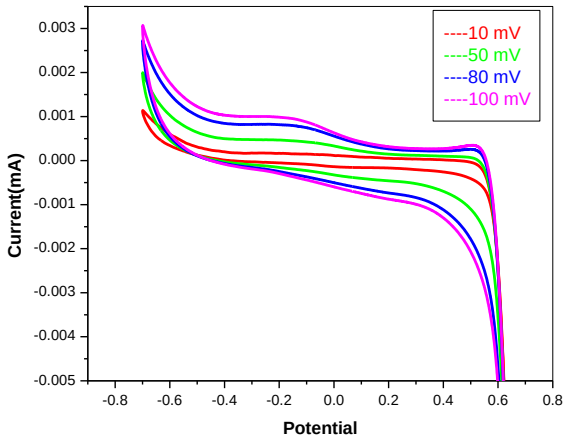

Figure 5: Cyclic voltameterry of NiO electrode in 0.1M KOH electrolyte

IX. Galvanometric charge–discharge studies

In addition, the electrochemical performances of the annealed NiO thin films were studied by galvanostatic charge–discharge cycles (GCD), as shown in Fig. 6. The GCD study was performed at 1 $mAcm^{-2}$ current density between -1.2 to +0.6 V potential windows in 0.1 M aq. KOH. The quick drop in the potential at the starting of the discharge cycles is due to the small equivalent series resistance (ESR) of NiO. The electrochemical parameters such as specific capacitance, energy, and power density of the materials are calculated from the curve by using the equations below [26].

$$C_{sp} = \frac{I_d \times T_d}{m \times dV} \quad (3)$$

$$E.D = \frac{0.5 \times Csp \times dV^2}{3.6} \quad (4)$$

$$P.D = \frac{E.D \times 3600}{T_d} \quad (5)$$

C_{sp} is the specific capacitance of the material, I_d is the discharged current density, T_d is the time required for discharging the device, m is the mass of deposited active material, and dV is the potential window.

The specific capacitance is calculated of energy density, and power density from GCD is 165 Fg^{-1}, 50 $Whkg^{-1}$, 0.72 $kWkg^{-1}$ at $1mAcm^{-1}$.

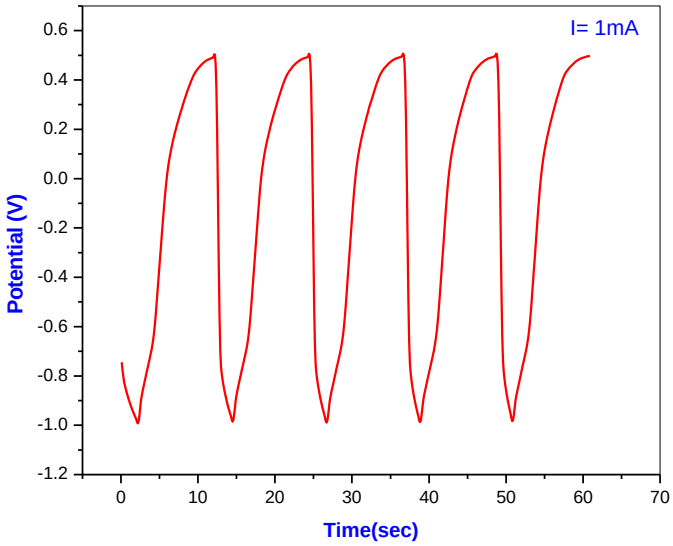

Figure 6: the charge–discharge measurements of NiO electrode in 0.1M KOH electrolyte

X. Conclusion

In this work, we have successfully synthesized NiO thin film electrodes using Sol-Gel method and studied electrochemical supercapacitor application. The XRD pattern confirmed cubic nature of NiO. It was found from the FESEM image that NiO film surface was well-covered with spherical micro granules. The presence of characteristics bonds of NiO were confirmed by XPS analysis. Contact angle measurement revealed the hydrophilic nature of NiO

surface as surface water 75° contact angle was smaller than 90°. The NiO electrode exhibited specific capacitance of 152 F g^{-1}. Energy density and power density from GCD 50 $Whkg^{-1}$, 0.72 $kWkg^{-1}$ at 1$mAcm^{-1}$.

These results reveal that sol gel deposited NiO thin film can be a good candidate as electrode material for electrochemical supercapacitor.

XI. REFERENCES

[1]. M.S. Halper, J.C. Ellenbogen, Supercapacitors: A Brief Overview, MITRE, March, 2006.

[2]. V.D. Patake, C.D. Lokhande, Oh Shim Joo, Appl. Surf. Sci. 255 (2009) 4192– 4196.

[3]. D.P. Dubal, D.S. Dhawale, R.R. Salunkhe, C.D. Lokhande, J. Electrochem. Soc. 157 (2010) A812–A817.

[4]. U.M. Patil, R.R. Salunkhe, K.V. Gurav, C.D. Lokhande, Appl. Surf. Sci. 255 (2008) 2603–2607.

[5]. X. Xia, J. Tu, Y. Mai, X. Wang, C. Gu, X. Zhao, J. Mater. Chem. 21 (2011) 9319– 9325.

[6]. D.P. Dubal, S.H. Lee, J.G. Kim, W.B. Kim, C.D. Lokhande, J. Mater. Chem. 22 (2012) 3044–3052.

[7]. V. Gupta, N. Miura, Electrochem. Solid State 8 (2005) A630–A632.

[8]. B.H. Patil, A.D. Jagadale, C.D. Lokhande, Synth. Met. 162 (2012) 1400–1405.

[9]. H. Xia, Y.S. Meng, G. Yuan, C. Cui, L. Lu, Electrochem. Solid-State Lett. 15 (2012) A60–A63.

[10]. M.P. Yeager, D. Su, N.S. Marinkovic, X. Teng, J. Electrochem. Soc. 159 (2012) A1598–A1603.

[11]. J. Li, W. Zhao, F. Huang, A. Manivannan, N. Wu, Nanoscale 3 (2011) 5103-5109.

[12]. E.E. Kalu, T.T. Nwoga, V. Srinivasan, J.W. Weidner, J. Power Sources 92 (2001) 163.

[13]. Imenez-Gonzalez AE, Cambray JG. Surf Eng 2000; 16:73–6.

[14]. A. A. Yadav, J. Mater. Sci.: Mater. Electron. 27 (2016) 1866-1872.

[15]. M. Jlassi, I. Sta, M. Hajji, H. Ezzaouia, Appl. Surf. Sci. 308 (2014) 199-205.

[16]. B. Sasi, K.G. Gopchandran, P.K. Manoj, P. Koshy, P. Prabhakara Rao, V.K. Vaidyana, Vacuum 68 (2003) 149-154.

[17]. S. M. Jogade, D. S. Sutrave, S.D. Gothe, International Journal of Advanced Research in Physical Science 2 (2015), 36.

[18]. P.S Joshi, D.S Sutrave, International Journal for Research in Applied Science and Engineering Technology,Ruthenium Oxide: Thin film and Electrochemical Properties, 4-V-III, (2016),765-772.

[19]. M.S. Wu, Y.A. Huang, C.H. Yang, J.J. Jow, Electrodeposition of nanoporous Nickel oxide film for electrochemical capacitors, Inter. J. Hydrogen Energy 32, 4153 (2007).

[20]. L. Chengzhi, L. Delong, W. Wenhui, Z. Yupeng, P. Chunxu, Preparation of porousmicro–nano- structure NiO/ZnO heterojunction and its photocatalytic property, RSC Adv. 4, 3090 (2014).

[21]. K.C. Liu, M.A. Anderson, J. Electrochem. Soc.,1996, 143,124.

[22]. Sutrave D. S, Joshi P. S, Gothe S. D, Jogade S.M,2014, Structural and Morphological properties of Ruthenium oxide Thin Films deposited by Sol-Gel Spin coating, International Journal of ChemTech Research,6, 1991-1993.

[23]. O. Bockman, T. Ostvold, G. A. Voyiatzis, G. N. Papatheodorou, Raman spectroscopy of cemented cobalton zinc substrates, Hydrometallurgy, 55, 93 (2000).

[24]. Y.H. Navale, S.M. Ingole, S.T. Navale, F.J. Stadler, R.S. Mane, Mu.. Naushad, V.B. Patil, Electro- synthesized fibrous polyaniline electrode as an active electrochemical supercapacitor material. J. Colloid Interf. Sci. 487, 458 (2017).

[25]. M.S. Wu, C.Y. Huang, K.H. Lin, Electrophoretic deposition of nickel oxide electrode for high-rate electrochemical capacitors, J. Power Sour. 186, 557 (2009)

[26]. Y.Z. Zheng, H.Y. Ding, M.L. Zhang, Preparation and electrochemical properties of nickel oxide as a supercapacitor electrode material. Mater. Res. Bull. 44, 403 (2009)

International e-Conference on Recent Trends in Nano-Materials and Its Applications-2021
In Association with International Journal of Scientific Research in Science and Technology
Volume 9 | Issue 2 | Print ISSN: 2395-6011 | Online ISSN: 2395-602X (www.ijsrst.com)

Exploration of Structural and Electrochemical Properties of (Sn-Ru)O2 Composite Electrode for Supercapacitor Application

[1]Madale. S. G, [1]Gaikwad. S. S, [1]Sutrave. D. S, [2]Jogade. S. M, [3]Karche. B. R

[1]D. B. F. Dayanand College of Arts and Science, Solapur, Maharashtra, India

[2]Sangameshwar College, Solapur (Autonomous), Maharashtra, India

[3]S. M. Mohite Mahavidyalay, Akluj, Maharashtra, India

ABSTRACT

The (Sn-Ru)O_2 composite electrode material was synthesized through Sol-gel spin coat method from $SnCl_2 \cdot 2H_2O$ and $RuCl_3 \cdot 2H_2O$ solutions. The obtained products were characterized using X-ray Diffractometry, Scanning Electron Microscopy (SEM), Cyclic Voltammetry (CV) and Chronopotentiometry (CP). XRD revealed the crystalline structure of thin film electrode by exhibiting peaks of both SnO_2 and RuO_2 corresponding to different planes. Porous morphology has been observed from SEM micrographs. Electrochemical studies were carried out to examine the specific capacitance of (Sn-Ru)O_2 electrodes in 0.1 M KOH electrolyte at various scan rates. The estimated electrode specific capacitance was determined to decrease with an increase of scan rate. The maximum specific capacitance of $1574 Fg^{-1}$ was obtained at scan rate of $10 mVs^{-1}$.

Keywords : (Sn-Ru)O_2, Spin Coating, XRD, SEM, CV, CP

I. INTRODUCTION

Electrochemical capacitors or supercapacitors have the considerable attraction in recent years due to the growing demand of power sources. Supercapacitors have the wide range of applications in various areas such as hybrid electric vehicles, telecommunications, digital communication devices particularly associated with cellular phones for a reduction of the size of the batteries, electrical tools, pulse laser technique, uninterruptible power supplies etc. [1-4].

Recently, extensive research is focused on the supercapacitor behaviour of metal oxide electrodes. Among the various metal oxides, the hydrous form of RuO_2 has shown excellent supercapacitive behaviour [5-8].

Even though RuO_2 is more promising material for supercapacitors, it has some drawbacks of very high cost and toxic nature, which limits its commercial use. Therefore, several studies are carried out by combining RuO_2 with other materials such as VOx, TiO_2, NiO, WO_3, SnO_2 etc., to minimize the use of Ru precursors and hence to decrease the cost of the precious metal. It is observed that addition of SnO_2 in RuO_2 matrix increases the utilization of Ru species and enhance the electrochemical stability [9-13].

In the present study we have adopted Sol-gel spin coat method which has various merits of deposition of metal oxides such as simple and inexpensive, excellent material utilization, efficiency, good control

over deposition process etc. [14]. In the present investigation, we report on the synthesis of (Sn-Ru)O_2 composite film and its structural and electrochemical properties.

II. MATERIALS AND METHODS

Preparation of (Sn-Ru)O_2 composite film

The (Sn-Ru)O_2 mixed thin film is deposited on stainless substrates by Sol-gel Spin Coat method. The cationic solutions of 0.05M were prepared by using stannous chloride ($SnCl_2 \cdot 2H_2O$) and ruthenium trichloride ($RuCl_3 \cdot 2H_2O$) with a complexing agent isopropyl alcohol. Equal proportions of both solutions were mixed continuously on magnetic stirrer for 6 hours by keeping the magnetic stirrer temperature at 50^0C.

III. CHARACTERIZATIONS

3.1 Structural Analysis by XRD

Structural analysis was carried out by D2 PHASER diffractometer with steps one degree per minute using source CuKα1 with λ =1.54184 Å. The 2θ angle is varied from 10^0 to 90^0. The fig.1 shows the XRD pattern for (Sn-Ru)O_2 composite thin film. XRD pattern exhibited crystalline nature with orthorhombic structure for both SnO_2 and RuO_2 phase [15, 16]. The XRD pattern showed peaks of both oxides and dominating peak is observed for RuO_2 phase. The details of all the peaks, planes and lattice constants are given in table.1 and 2 respectively. The values of lattice parameters were calculated by the XRD data, which are in good agreement with the standard data as in JCPDS cards [15,16].

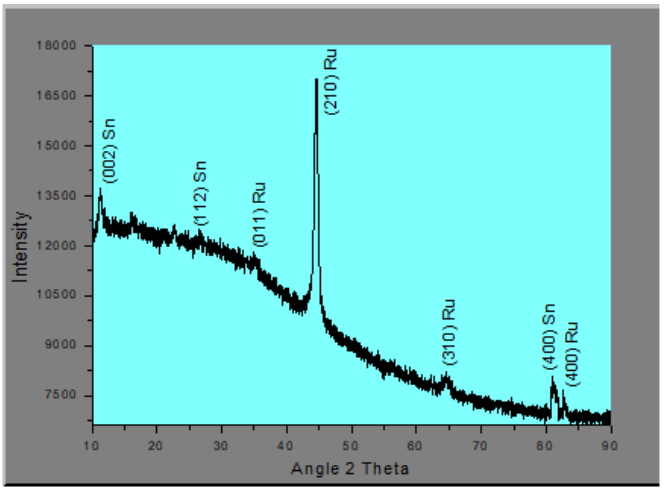

Fig.1 XRD pattern of (Sn-Ru)O_2 thin film electrode

Table. 1 Observed and standard 'd' values for different peaks

Phase	Plane	Standard 'd'	Observed 'd'
SnO_2	(002)	7.933	7.904
	(112)	3.312	3.324
	(400)	1.184	1.185
RuO_2	(011)	2.537	2.562
	(210)	2.002	2.033
	(310)	1.417	1.442
	(400)	1.122	1.164

Table. 2 Standard and observed Lattice constants from XRD analysis

Phase		Lattice constants		
		a	b	c
SnO_2	Standard	4.737	5.708	15.865
	Observed	4.739	5.778	15.801
RuO_2	Standard	4.654	4.181	3.240
	Observed	4.865	4.431	3.093

3.2 Morphological Analysis by SEM

Surface morphological study has been carried out by Scanning Electron Microscopy (SEM) using a JEOL JSM-6360 instrument.

The SEM images revealed the formation of thin film which is well adherent to the substrate. Fig-2 shows SEM micrograph of (Sn-Ru)O_2 at x10,000

magnification and an enlarged insight image. From the SEM image the irregularly arranged agglomerates forming a rough surface with porous morphology is observed. The porosity prompts possibility of better electrochemical supercapacitor behaviour of (Sn-Ru)O_2 thin film electrode [17].

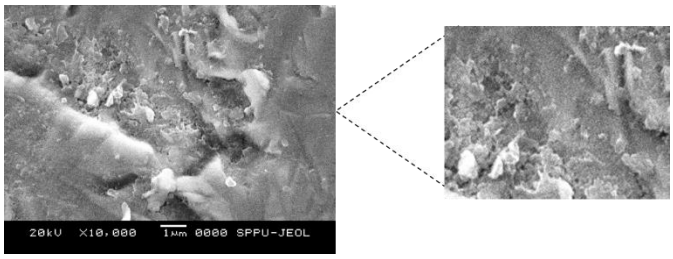

Fig. 2 SEM morphology of (Sn-Ru)O_2 thin film electrode

3.3 Compositional Analysis by EDAX

The compositional analysis of the as deposited (Sn-Ru)O_2 composite thin film electrode was carried out using EDAX technique by Quanta 200 ESEM instrument. The typical EDAX pattern given in fig. 3 shows the formation of (Sn-Ru)O_2 on the substrate.

From the obtained data it was found that the Sn and Ru were present in the sample. EDAX analysis showed that the atomic and weight percentage of Sn and Ru are approximately in the same proportions.

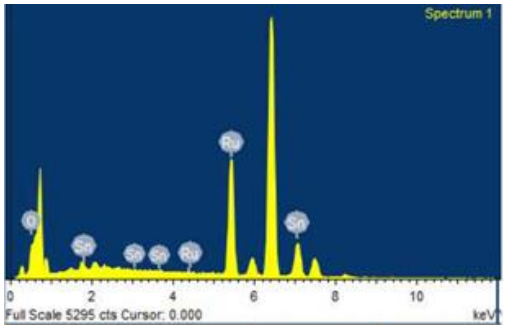

	O	Ru	Sn
Weight %	89.32	5.73	4.95
Atomic %	77.92	11.26	10.82

Fig. 3 Atomic and weight percentage of elements by EDAX

3.4 Electrochemical Analysis by Cyclic Voltammetry (CV)

The electrochemical properties of the (Sn-Ru)O_2 composite thin film electrode were determined using cyclic voltammetry. The measurements were performed with (Sn-Ru)O_2 composite thin film electrode as working electrode and platinum wire as counter electrode and SCE as a reference electrode in 0.1 M KOH electrolyte. Fig. 4 shows the cyclic voltammograms with potential window -1V to 1V at various scan rates 10, 20, 50, 80 and 100mV/sec. From CV analysis, the electrode exhibited maximum specific capacitance of 1574Fgm^{-1} at 10mVs^{-1} scan rate. S. N. Pusawale et al. obtained specific capacitance of 1010F/g for SnO_2-RuO_2 mixed thin films prepared by SILAR method [9]. Hu et al. used the modified sol–gel process for deposition of ruthenium–tin oxide composites with a maximum specific capacitance of 690 F/g [10]. Wang and Hu adopted a mild hydrothermal process to synthesize hydrous ruthenium oxide-tin oxide composites (Ru–Sn)O_2 nH_2O where a maximum specific capacitance is 830 F/g [12]. A composite tin oxide-ruthenium oxide supercapacitor electrode synthesized by cyclic voltammetric plating of RuO2 onto a porous and highly conductive SnO_2 showed a specific capacitance of 930 F/g [13]. A specific capacitance of 150 F/g was observed for SnO_2–RuO_2 composite thin films prepared by chemical bath deposition [14]. As compared to the previous research done on (Sn–Ru)O_2 oxide, our present work obtained maximum specific capacitance of 1574Fgm^{-1}.

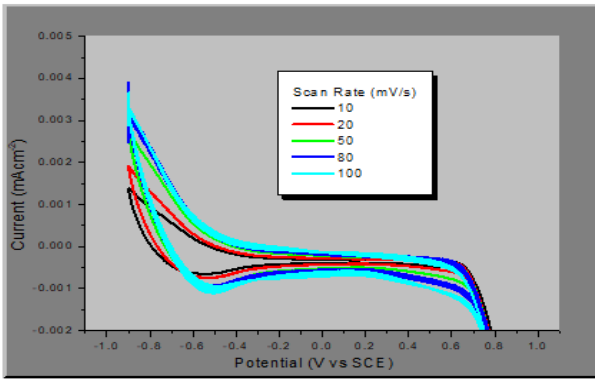

Fig. 4 CV curves of (Sn-Ru)O_2 thin film electrode

The electrode exhibited a common trend of decreasing specific capacitance value against an increasing scan rate. It is well known that for very low scan rates, the specific capacitance values are higher because the ions have a much longer time to penetrate and reside in all the available electrode pores and form electric double layers, which are needed to generate higher capacitance [18]. Despite this common trend, the (Sn-Ru)O_2 composite electrode displays higher specific capacitance values throughout the whole scan region, clearly indicating its superiority over the pure electrodes. This is in good agreement with the values shown in table.3

Scan Rate (mV/s)	Specific Capacitance (F/gm)
10	**1574**
20	1066
50	653
80	496
100	430

Table. 3 Specific capacitance values for different scan rates

3.5 Charge-discharge Analysis by Chronopotentiometry (CP)

Chronopotentiometric charge-discharge is the most reliable and accurate method for evaluating supercapacitor properties of electrodes. Typical charging and discharging curves for (Sn-Ru)O_2 composite electrode was measured between the voltage range of -0.6V to 0.4V in 0.1 M KOH electrolyte as shown in fig. 5.

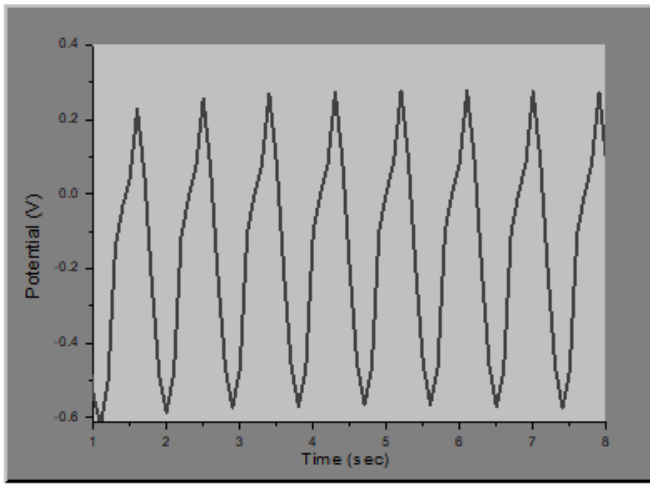

Fig. 5 Charge – discharge curves of (Sn-Ru)O_2 composite electrode

From CP, the supercapacitive parameters such as specific energy, specific power and coulombic efficiency were calculated using,[19]

$$\text{Specific energy S.E} = \frac{V \times I_d \times T_d}{W} \quad (1)$$

$$\text{Specific energy S.P} = \frac{V \times I_d}{W}, \text{ and} \quad (2)$$

$$\text{Coulombic efficiency } \eta \ (\%) = \frac{T_d}{T_c} \text{X } 100 \quad (3)$$

Where, I_d and T_d are the discharge current and discharge time, respectively. The W is the mass of the film. From calculations, the electrode exhibited specific energy 2.61Wh/kg and specific power 20KW/kg. The columbic efficiency was fond to be 88.7%.

IV. CONCLUSION

The present study shown a successful synthesis of (Sn-Ru)O_2 composite thin film electrode as confirmed by the different characterizations such as XRD, SEM, Cyclic Voltammetry and Chronopotentiometry. XRD revealed the formation of (Sn-Ru)O_2 metal oxide which is crystalline in nature and orthorhombic structure, the XRD pattern include dominating peaks of both metal oxides. SEM image revealed irregularly arranged agglomerates forming a rough surface with porous morphology. Cyclic Voltammetry and

Chronopotentiometry techniques revealed that (Sn-Ru)O_2 oxide electrode exhibited good electrochemical behaviour by contributing 1574F/gm specific capacitance. The electrode exhibited specific energy 2.61Wh/kg, specific power 20KW/kg and columbic efficiency of 88.7% by chronopotentiometric behaviour.

V. REFERENCES

[1] Kotz. R, Carlen. M, Principles and applications of electrochemical capacitors, J. lectrochim. Acta 45, 2483–2498 (2000)

[2] Lam. L. T, Louey. Development of ultrabattery for hybrid-electric vehicle applications, Journal of Power Sources, 158(2), 1140-1148 (2006)

[3] Miller. T. A, Electrochemical capacitor thermal management issues at high-rate cycling, Electrochim Acta, 52(4), 1703-1708 (2006)

[4] Conway. B. E, Plenum Publishers, New York, 1st Edition (1999)

[5] Zheng. J.P, Cygan. P. J, Jow. T. R, Hydrous ruthenium oxide as an electrode material for electrochemical capacitors. J. Electrochem. Soc. 142, 2699–2703 (1995)

[6] Michell. D, Rand. D.A, Woods. R, A study of ruthenium electrodes by cyclic voltammetry and X-ray emission spectroscopy. J. Electroanal. Interfacial Electrochem. 89, 11–27 (1978)

[7] Deshmukh. P.R, Pusawale. S. N, Jagdale. A. D, Lokhande. C.D, Supercapacitive performance of hydrous ruthenium oxide (RuO2·nH2O) thin films deposited by SILAR method. J. Mater. Sci. 47, 1533–1546 (2012)

[8] Burke. L. D, Whelan. D. P, The behaviour of ruthenium anodes in base, J. Electroanal. Interfacial Electrochem. 103, 179–187 (1979)

[9] Pusawale. S. N, Deshmukh. P. R, Jadhav. P. S, Lokhande. C. D, Electrochemical properties of chemically synthesized SnO2-RuO2 mixed films, J. Materials for Renewable and Sustainable Energy, 8:1 (2019)

[10] Hu. C.C, Wang. C.C, Chang. K.H, A comparison study of the capacitive behaviour for sol–gel-derived and co-annealed ruthenium– tin oxide composites. J. Electrochim. Acta 52, 2691–2700 (2007)

[11] Wang. C.C, Hu. C.C, Electrochemical and textural characterization of binary Ru–Sn oxides synthesized under mild hydrothermal conditions for supercapacitors, J. Electrochim. Acta 50, 2573–2581 (2005)

[12] Wu. N. L, Kuo. S. L, Lee. M. H, Preparation and optimization of RuO2-impregnated SnO2 xerogel supercapacitor, J. Power Sources 104, 62–65 (2002)

[13] Pusawale. S. N, Deshmukh. P. R, Gunjakar. J. L, Lokhande. C. D, SnO2–RuO2 composite films by chemical deposition for supercapacitor application. J. Mater. Chem. Phys. 139, 416–422 (2013)

[14] Jogade. S. M, Gaikwad. S. S, Sutrave. D. S. CV analysis of manganese doped cobalt oxide thin film electrodes for supercapacitor application Asian Journal of Research in Chemistry and Pharmaceutical Sciences. 140-146, 4(4) (2016)

[15] Joshi. P. S, Sutrave. D. S, Study of Ruthenium Oxide, Manganese Oxide and Composite (Ru:Mn)O2 thin film Electrodes Assembled by Layer by Layer Spin Coating Method, J. Material Science Research India Vol. 13(1), 43-49 (2016)

[16] Farma. R, Deramanl. M, Awitdrus. I. A, Talib. R. Omar, Manjunatha, Int. J. Electrochem. Sci., 8, 257 – 273(2013)

[17] Sutrave. D. S, Jogade. S. M, Gothe. S. D, MnO2, Co3O4 and MnO2:Co3O4 Stacked Thin Film Electrodes for Supercapacitor, International Journal for Research in Applied Science & Engineering Technology (IJRASET) Volume 4, Issue IV (2016)

International e-Conference on Recent Trends in Nano-Materials and Its Applications 2021(RTNA-2021)

Organised by

Department of Physics in Collaboration with
Internal Quality Assurance Cell (IQAC)
Sangola Taluka Shetkari Shikshan Prasarak Mandal Sangola's Vidnyan Mahavidyalaya, Sangola
Tal-Sangola, Dist-Solapur, MH-413307, India

Publisher

Technoscience Academy

Website : www.technoscienceacademy.com

Email : editor@ijsrst.com Website : http://ijsrst.com